

University of Stuttgart - Institute for Modelling Hydraulic and Environmental Systems
Department of Stochastic Simulation and Safety Research for Hydrosystems
Prof. Dr.-Ing. Wolfgang Nowak



Pfaffenwaldring 5a, 70569 Stuttgart

<http://www.iws-ls3.uni-stuttgart.de>

Master's Thesis

Bayesian Model Selection for Hydro-Morphodynamic Models

Farid Mohammadi

Matriculation Number: 2925918

Examiners: Prof. Dr.-Ing. Wolfgang Nowak
Dr.-Ing. habil. Sergey Oladyshkin
Supervisors: Dr. Dipl.-Ing. Rebekka Kopmann
Dr. Dipl.-Ing. Anneli Guthke

Stuttgart, May 2017

Acknowledgements

The present master thesis is the document to support Farid Mohammadi's candidature for the academic degree Master of Science (M.Sc.), in which his research and findings on the topic of "*Bayesian Model Selection for Hydro-Morphodynamic Models*" is comprehensively elucidated. This study was a cooperation between the Department of Stochastic Simulation and Safety Research for Hydrosystems (LS3) at University Stuttgart and the Federal Waterways Engineering and Research Institute (BAW) in Karlsruhe.

The author would like to thank his supervisors; Dr.-Ing. habil. Sergey Oladyskin, Dr.-Ing. Rebekka Kopmann and Dr. Dipl.-Ing. Anneli Guthke. Without their passionate participation and input, this research study could not have been successfully conducted. They were always cooperative whenever the author ran into a troubles or had a question concerning his research or writing. They consistently allowed this study to be his own work, but steered him in the right direction whenever they felt the necessity.

Finally, the author expresses his profound gratitude to his family and friends for their constant motivation and continuous support throughout the process of researching and writing this thesis, as well as all years of his study. Also, he kindly appreciates the help of Betsaida Fernandez and Diego Motavita for their valuable supports. This accomplishment would not have been conceivable without them.

Stuttgart, May 2017

Farid Mohammadi

Author declaration

I declare that I have developed and written the enclosed thesis completely by myself and that I have not used sources or means without declaration in the text. Any thoughts from others or literal quotations are clearly marked. The thesis was not used in the same or in a similar version to achieve an academic grading or is being published elsewhere. The enclosed electronic version is identical to the printed versions.

Stuttgart, May 2017

Signature

Farid Mohammadi

Abstract

A good grasp of hydro-morphodynamic processes plays a major role in modern river management to accommodate its often-conflicting functions. In the last century, a variety of models has been developed to improve our perception of sediment transport and the resulting changes in river bed topography, using several empirical formulations. Therefore, there is a demonstrated need to establish a framework that helps the river engineer to select the closest model to the measurements.

This study suggested a Bayesian Model Selection (BMS) framework to direct the modeler towards the most robust and sensible representation of the hydro-morphodynamic conditions of the river under investigation. The proposed framework employs Bayesian Model Evidence (BME) resulting from Bayesian Model Averaging (BMA) as a model evaluation yardstick for ranking competing models. BMA performs a compromise between bias and variance, i.e. it blends a measure for goodness of fit with a penalty for unacceptable model complexity. This approach requires many model simulations, which are computationally expensive. However, this issue can be deminished by a mathematically optimal response surface via the aPC technique projects the original model. This response surface, also known as a reduced (surrogate) model, can exhibit the reliance of the model on all relevant parameters for calibration at high-order accuracy.

The proposed framework was implemented in the model selection of two test cases; namely a test case model, based on an experiment done by Yen and Lee (1995) and a river model of a 10-km stretch of the lower Rhine, provided by the Federal Waterways Research Institute (BAW) in Karlsruhe. The results demonstrated that the proposed framework was acceptably able to detect the most desirable model in which a good agreement existed between the simulation results and measurement data when the complete knowledge of initial parameters lacked. Further, the BMS framework could direct us to the most probable parameter regions for the task of optimization via probability density distributions of uncertain variables. Overall, this research fills a void in the literature with respect to selection of sediment transport equation for representation of hydro-morphodynamics of natural rivers. The suggested approach provides an objective guidance in the model selection to assist even less experienced users by reducing the professional expertise required for further optimization tasks.

Keywords: Hydro-morphodynamics, Bayesian model selection, Bayesian model evidence, Response Surface, Arbitrary Polynomial Chaos expansion.

Contents

List of Figures	3
List of Tables	10
1 Introduction	14
1.1 Hydro-Morphodynamics	14
1.2 Overview of Hydro-morphodynamic Investigations	15
1.3 Advancement of Sediment Calculations	16
1.4 Comparison of Transport Models	17
1.5 Challenges in Hydro-Morphodynamic Modeling	19
1.6 Goals of this Study	20
1.7 Outline	21
2 Hydro-Morphodynamic Modeling	23
2.1 Hydro-Morphodynamic Model	23
2.2 Detailed Study of Selected Equations	26
2.3 Channel Bend Model of Yen and Lee (1995)	41
2.4 The River Rhine Model	45
2.5 Summary	56
3 Bayesian Model Selection Framework	57
3.1 Surrogate Model Construction	57
3.2 Bayesian Updating of Surrogate Model	62
3.3 Bayesian Model Selection	65
3.4 Properties of BMS Framework	68
3.5 Summary	69
4 Bayesian Model Selection for Channel Bend Experiment	71
4.1 Setup and Implementation	71
4.2 Bayesian Model Ranking	73

4.3	Uncertainty Analysis of BMS for Channel Bend	89
4.4	Summary	91
5	Bayesian Model Selection for the Lower Rhine Model	92
5.1	BMS for Twin Experiment of the Lower Rhine Model	92
5.2	BMS of the Real Lower Rhine Model	115
5.3	Summary	131
6	Summary and Conclusions	132
6.1	Thesis Summary	132
6.2	Conclusions	134
6.3	Recommendations for Further Investigations	137
A	Appendix I: BMS for the Channel Bend Model	138
B	Appendix II: BMS for the Lower Rhine Model	149
B.1	BMS for Twin Experiment	149
B.2	BMS of the the Real Lower Rhine Model	162
	References	170

List of Figures

2.1	Definition of the exposure height (Wu et al. 2000)	38
2.2	Bend channel geometry	42
2.3	Bend channel geometry	43
2.4	Inflow hydrograph	43
2.5	Measurement profiles (Source: Yen and Lee (1995))	44
2.6	The Study area of the lower Rhine model (Source: Google Maps, 2017)	45
2.7	Model boundaries, velocities, grid of the lower Rhine model (Source: Backhaus (2013))	47
2.8	Friction zones of the lower Rhine model	48
2.9	Sieve analysis curve of grains and the fractions	49
2.10	Inflow hydrograph of the lower Rhine model	51
2.11	Outlet water level of the lower Rhine model	51
2.12	Bed evolution from 2002 to 2004 (Source of the aerial photo: WSV)	53
2.13	Averaged bed evolution from 2002 to 2004	54
2.14	Averaged bed evolution from 2004 to 2006	54
2.15	Synthetic bed evolution for calibration period	55
2.16	Synthetic bed evolution for validation period	56
3.1	Research methodology flowchart	70
4.1	Simulation output vs. response surface (calibration-Meyer-Peter-Müller model)	73
4.2	The posterior PDF of parameters (calibration-Meyer-Peter-Müller model)	74

4.3	Simulation output vs. response surface (validation-Meyer-Peter-Müller model)	75
4.4	The Posterior PDF of parameters (Validation-Meyer-Peter-Müller Model)	76
4.5	Simulation output vs. response surface (calibration-Einstein-Brown model)	77
4.6	The posterior PDF of parameters (calibration-Einstein-Brown model)	78
4.7	Simulation output vs. response surface (validation-Einstein-Brown model)	78
4.8	The posterior PDF of parameters (validation-Einstein-Brown model)	79
4.9	Simulation output vs. response surface (calibration-Mod. Engleund-Hansen model) . . .	80
4.10	The posterior PDF of parameters (calibration-Mod. Engleund-Hansen model)	80
4.11	Simulation output vs. response surface (validation-Mod. Engleund-Hansen Model) . . .	81
4.12	The posterior PDF of parameters (validation-Mod. Engleund-Hansen model)	82
4.13	Simulation output vs. response surface (calibration-Van Rijn model)	82
4.14	The posterior PDF of parameters (calibration-Van Rijn model)	83
4.15	Simulation output vs. response surface (Validation-Van Rijn model)	84
4.16	The posterior PDF of parameters (validation-Van Rijn model)	84
4.17	Simulation output vs. response surface (calibration-Wu model)	85
4.18	The posterior PDF of parameters (calibration-Wu model)	86
4.19	Simulation output vs. response surface (validation-Wu model)	86
4.20	The posterior PDF of parameters (validation-Wu model)	87
4.21	Bayesian model evidence vs. iterations for channel bend model in calibration step (Log-scale)	88
4.22	Performance range of the BME values after calibration	90
4.23	Box plot for the BME values after validation	90
5.1	Simulation output vs. response surface (calibration-Meyer-Peter-Müller model)	95
5.2	The posterior PDF of parameters (calibration-Meyer-Peter-Müller model)	95
5.3	Simulation output vs. response surface (validation-Meyer-Peter-Müller model)	96
5.4	The posterior PDF of parameters (validation-Meyer-Peter-Müller model)	97

5.5	Simulation output vs. response surface (calibration-Einstein-Brown model)	98
5.6	The posterior PDF of parameters (calibration-Einstein-Brown model)	99
5.7	Simulation output vs. response surface (validation-Einstein-Brown model)	99
5.8	The posterior PDF of parameters (validation-Einstein-Brown model)	100
5.9	Simulation output vs. response surface (calibration-Mod. Engelund-Hansen model) . .	101
5.10	The posterior PDF of parameters (calibration-Mod. Engelund-Hansen model)	101
5.11	Simulation output vs. response surface (validation-Mod. Engelund-Hansen model) . .	102
5.12	The posterior PDF of parameters (validation-Mod. Engelund-Hansen model)	103
5.13	Simulation output vs. response surface (calibration-Van Rijn model)	104
5.14	The posterior PDF of parameters (calibration-Van Rijn model)	105
5.15	Simulation output vs. response surface (validation-Van Rijn model)	105
5.16	The posterior PDF of parameters (validation-Van Rijn model)	106
5.17	Simulation output vs. response surface (calibration-Hunziker model)	107
5.18	The posterior PDF of parameters (calibration-Hunziker model)	107
5.19	Simulation output vs. response surface (validation-Hunziker model)	108
5.20	The posterior PDF of parameters (validation-Hunziker model)	109
5.21	Simulation output vs. response surface (calibration-Wu model)	110
5.22	The posterior PDF of parameters (calibration-Wu model)	110
5.23	Simulation output vs. response surface (validation-Wu model)	111
5.24	The posterior PDF of parameters (validation-Wu model)	112
5.25	The posterior PDF of parameters with measurement error of 0.025 (validation- Wu model)	113
5.26	Bayesian model evidence vs. iterations for twin experiment of lower Rhine model in calibration step (Log-scale)	114
5.27	Simulation output vs. response surface (calibration-Meyer-Peter-Müller model)	117
5.28	The posterior PDF of parameters (calibration-Meyer-Peter-Müller model)	118
5.29	Simulation output vs. response surface (validation-Meyer-Peter-Müller model)	119

5.30	The posterior PDF of parameters (validation-Meyer-Peter-Müller model)	119
5.31	Simulation output vs. response surface (calibration-Van Rijn model)	120
5.32	The posterior PDF of parameters (calibration-Van Rijn model)	121
5.33	Simulation output vs. response surface (validation-Van Rijn model)	121
5.34	The posterior PDF of Parameters (validation-Van Rijn model)	122
5.35	Simulation output vs. response surface (calibration-Hunziker model)	123
5.36	The posterior PDF of parameters (calibration-Hunziker model)	123
5.37	Simulation output vs. response surface (validation-Hunziker model)	124
5.38	The posterior PDF of parameters (validation-Hunziker model)	125
5.39	Simulation output vs. response surface (calibration-Wu model)	126
5.40	The posterior PDF of parameters (calibration-Wu model)	126
5.41	Simulation output vs. response surface (validation-Wu model)	127
5.42	The posterior PDF of parameters (validation-Wu model)	128
5.43	Bayesian model evidence vs. iterations for real lower Rhine model in calibration step (Log-scale)	129
5.44	Simulated bed evolution with Hunziker model with bed evolution from 2002 to 2004 .	130
A.1	Prior likelihood weights before iterations (calibration-Meyer-Peter-Müller model) . . .	138
A.2	Prior likelihood weights after iterations (calibration-Meyer-Peter-Müller model)	139
A.3	Posterior likelihood weights after rejection sampling (calibration-Meyer-Peter-Müller model)	139
A.4	Prior likelihood weights (validation-Meyer-Peter-Müller model)	140
A.5	Prior likelihood weights before iterations (calibration-Einstein-Brown model)	141
A.6	Prior likelihood weights after iterations (calibration-Einstein-Brown model)	141
A.7	Posterior likelihood weights after rejection sampling (calibration-Einstein-Brown Model)	142
A.8	Prior likelihood weights (validation-Einstein-Brown model)	142
A.9	Prior likelihood weights before iterations (calibration-mod. Engelund- Hansen model) .	143

A.10	Prior likelihood weights after iterations (calibration-mod. Engelund- Hansen model)	143
A.11	Posterior likelihood weights after rejection sampling (calibration-mod. Engelund- Hansen model)	144
A.12	Prior likelihood weights (validation-mod. Engelund-Hansen model)	144
A.13	Prior likelihood weights before iterations (calibration-Van Rijn model)	145
A.14	Prior likelihood weights after iterations (calibration-Van Rijn model)	145
A.15	Posterior likelihood weights after rejection sampling (calibration-Van Rijn model)	146
A.16	Prior likelihood weights (validation-Van Rijn model)	146
A.17	Prior likelihood weights before iterations (calibration-Wu model)	147
A.18	Prior likelihood weights after iterations (calibration-Wu model)	147
A.19	Posterior likelihood weights after rejection sampling (calibration-Wu model)	148
A.20	Prior likelihood weights (validation-Wu model)	148
B.1	Prior likelihood weights before iterations (calibration-Meyer-Peter-Müller model)	149
B.2	Prior likelihood weights after iterations (calibration-Meyer-Peter-Müller model)	150
B.3	Posterior likelihood weights after bootstrap-filtering (calibration-Meyer-Peter-Müller model)	150
B.4	Prior likelihood weights (validation-Meyer-Peter-Müller model)	151
B.5	Prior likelihood weights before iterations (calibration-Einstein-Brown model)	152
B.6	Prior likelihood weights after iterations (calibration-Einstein-Brown model)	152
B.7	Posterior likelihood weights after bootstrap-filtering (calibration-Einstein-Brown model)	153
B.8	Prior likelihood weights (validation-Einstein-Brown model)	153
B.9	Prior likelihood Weights before iterations (calibration-Mod. Engelund-Hansen model)	154
B.10	Prior likelihood weights after iterations (calibration-Mod. Engelund-Hansen model)	154
B.11	Posterior likelihood weights after bootstrap-filtering (calibration-Mod. Engelund- Hansen model)	155
B.12	Prior likelihood weights (validation-Mod. Engelund-Hansen model)	155

B.13	Prior likelihood weights before iterations (calibration-Van Rijn model)	156
B.14	Prior likelihood weights after iterations (calibration-Van Rijn model)	156
B.15	Posterior likelihood weights after bootstrap-filtering (calibration-Van Rijn model) . . .	157
B.16	Prior likelihood weights (validation-Van Rijn model)	157
B.17	Prior likelihood weights before iterations (calibration-Hunziker model)	158
B.18	Prior likelihood weights after iterations (calibration-Hunziker model)	158
B.19	Posterior likelihood weights after bootstrap-filtering (calibration-Hunziker model) . . .	159
B.20	Prior likelihood weights (validation-Hunziker model)	159
B.21	Prior likelihood weights before iterations (calibration-Wu model)	160
B.22	Prior likelihood weights after iterations (calibration-Wu model)	160
B.23	Posterior likelihood weights after bootstrap-filtering (calibration-Wu model)	161
B.24	Prior likelihood weights (validation-Wu model)	161
B.25	Prior likelihood weights before iterations (calibration-Meyer-Peter-Müller model) . . .	162
B.26	Prior Likelihood Weights after Iterations (calibration-Meyer-Peter-Müller model) . . .	162
B.27	Posterior likelihood weights after bootstrap-filtering (calibration-Meyer-Peter-Müller model)	163
B.28	Prior likelihood weights (validation-Meyer-Peter-Müller model)	163
B.29	Prior likelihood weights before iterations (calibration-Van Rijn model)	164
B.30	Prior likelihood weights after iterations (calibration-Van Rijn model)	164
B.31	Posterior likelihood weights after bootstrap-filtering (calibration-Van Rijn model) . . .	165
B.32	Prior likelihood weights (validation-Van Rijn model)	165
B.33	Prior likelihood weights before iterations (calibration-Hunziker model)	166
B.34	Prior likelihood weights after iterations (calibration-Hunziker model)	166
B.35	Posterior likelihood weights after bootstrap-filtering (calibration-Hunziker model) . . .	167
B.36	Prior likelihood weights (validation-Hunziker model)	167
B.37	Prior likelihood weights before iterations (calibration-Wu model)	168

B.38	Prior likelihood weights after iterations (calibration-Wu model)	168
B.39	Posterior likelihood weights after bootstrap-filtering (calibration-Wu model)	169
B.40	Prior likelihood weights (validation-Wu model)	169

List of Tables

2.1	Roughness coefficients of different zones	48
3.1	The description of BMS toolkit's inputs	69
4.1	The morphodynamic models used in the test case of channel bend	72
4.2	The selected uncertain parameters and their ranges (channel bend)	72
4.3	The BME comparison after the validation (channel bend)	88
4.4	The statistical characteristics of the BME values after validation (Channel Bend)	91
5.1	The morphodynamic models used in the twin experiment of lower Rhine model	93
5.2	The selected uncertain parameters and their ranges (twin experiment)	93
5.3	The accuracy of parameter inferences after calibration and validation step	112
5.4	The impact of measurement error on parameter inferences after validation step	114
5.5	The BME comparison after the validation for the twin experiment of the lower Rhine model	115
5.6	The morphodynamic models used in the real model of the lower Rhine	116
5.7	The selected uncertain parameters and their ranges (real lower Rhine model)	116
5.8	The BME comparison after the validation for the real lower Rhine model	129

Nomenclature

Symbols

u, v	Flow velocities in x- and y directions, respectively
g	Gravitational acceleration
Z	Free surface elevation
S_h	Source or sink of fluid
S_x, S_y	Source or sink terms in dynamic equations
ϑ_t	Momentum coefficient
ρ	Density of water
ρ_s	Sediment density
s	Relative density
C_d	Quadratic friction coefficient
k_s	Nikuradse bed roughness
n	Non-cohesive bed porosity
Z_f	Bed evolution
Q_b	Volumetric rate of the sediment transport (bed-load) per unit width
θ_c	Dimensionless critical Shields parameter
θ'	dimensionless skin friction parameter
χ	Bed slope
ϕ_s	Angle of repose of the sediment
ψ	Angle of the current to the upslope direction
α	Angle between the direction of solid transport and the flow direction
δ	Direction of bottom stress in relation to the flow direction
T	Deviation coefficient
β_2	Parameter of deviation
Φ_s	Non-dimensional current-induced sand transport rate
d_{ch}	Characteristic sand diameter for uniform grains
μ	Correction factor for skin friction
τ_0	Bottom shear stress
q	Water discharge per unit width
I	Slope of the channel
R_b	Hydraulic radius of channel

R'_b	Hydraulic radius due to grain resistance
u^*	Bed shear velocity
ν	Kinematic viscosity of flow
R^*	Boundary Reynolds number
K	Strickler coefficient
C_D	Bottom drag coefficient
κ	Von Karman constant
δ_b	Saltation height
c'	Chezy-coefficient related to grains

Abbreviations

MPM	Meyer-Peter and Müller
FEM	Finite Element Method
DTM	Digital Terrain Model
SedDB	Sediment Data Bank
WSV	German Federal Waterways and Shipping Administration
PCE	Polynomial Chaos Expansion
aPC	arbitrary Polynomial Chaos
PCM	Probabilistic Collocation Method
KDE	Kernel Density Estimation
PDF	Probability Density Function
BMA	Bayesian Model Averaging
BME	Bayesian Model Evidence
BMS	Bayesian Model Selection

1 Introduction

Rivers are present in nature in a variety of forms, such as straight, sinuous, meandering, and braided, because of interacting processes among water flow, sediment transport, and vegetation. Anthropogenic activities can severely modify these processes often resulting in undesired and unforeseen consequences at a variety of spatial and temporal levels. This modification causes safety problems, environmental hazards, as well as environmental degradation, with massive resources and economic damages for the entire society. Therefore, modeling of hydro-morphodynamics, also known as river morphodynamics, is vital to understand how the mentioned interacting processes work. The results can assist decision-making at multiple levels that can promote environmentally friendly and cost-effective river basin and land management.

However, modeling the complex interactions of hydro- and morphodynamic processes is driven by various physical and numerical parameters, and many processes are reproduced using empirical formulations. Generally, several formulations for the same process (e.g. bed load transport equation) exist and the modeler must be aware of the limitations of these models to be able to reproduce the real behaviors of the river.

The current chapter starts with Section 1.1 that contains the definition of the term hydro-morphodynamics and the necessity of its modeling. In Section 1.2, an overview of hydro-morphodynamic investigations is provided. Section 1.3 briefly highlights the development of morphodynamic models; i.e. sediment transport models, over the course of time. A comparison of transport models is presented in Section 1.4 followed by the challenges of model selection in Section 1.5. The objective of this study is elaborated in Section 1.6. At last, the outline of the present study is presented in Section 1.7.

1.1 Hydro-Morphodynamics

Modern river management must accommodate numerous functions, such as flood protection and provision of safe and efficient navigation, floodplain agriculture, ecology, and recreation. Thus, a good grasp of hydro-morphodynamic processes, which assess the hydraulic regime

and sediment transport in rivers, plays a significant role to serve its often-conflicting functions, especially for multi-function rivers in densely populated areas.

Hydro-morphodynamics comprises of hydrodynamics and morphodynamics. Both terms will frequently be used throughout this study, and are worth defining from the outset. Hydrodynamics is a part of fluid mechanics that is concerned with forces applying on or exerted by fluids and is widely used in engineering practices to study how energy and forces interact with fluids. A river hydrodynamic model uses a series of equations to explore how the conservation laws of mass, energy, and momentum apply to the incompressible liquid, water. These models enable a river engineer to investigate the processes in water bodies and provide predictions at various scale levels. These levels are as follows: (I) in planning and design - to assess the effectiveness and the impact of river engineering works, to satisfy planning and design specifications; (II) in operational forecasting - e.g. information required about the rise of flood levels to decide whether detention basins must be deployed or whether there is a need for emergency measures such as evacuation or forced inundation; (III) in maintenance - to sustain the river for flood conveyance and navigation.

On the other hand, river morphodynamics is the study of river bed topography in response to erosion and sedimentation. The understanding of river morphodynamics is essential for proper management and prediction of critical erosion and sedimentation processes occurring in streams, such as bank erosion, sediment balance in dam regulation, sediment wave propagation, interactions with man-made structures (bridges, weirs), silting up of reservoirs, sediment mining, degradation/aggradation, planform changes.

1.2 Overview of Hydro-morphodynamic Investigations

The first observation of water flow and sediment transport was carried out during the Renaissance period by Leonardo da Vinci (1452-1510), the Italian artist and engineer (Wu, 2008). Since then, scientists and engineers conducted many studies on river processes. Water flowing in natural rivers is capable of scouring riverbeds, carrying particles (heavier than water) and depositing materials, resulting in the bed topography changes. In this phenomenon sediment transport is of great importance. The reasons include but are not limited to risk assessment of scouring of bridges, weirs and channel banks; estimation of the siltation in an upstream reservoir of a dam; prediction of possible bed form changes of rivers and estuaries (Apsley, 2014).

The development of sediment transport models has been insignificant, in comparison with the other branches of science, and the proposed theories have not been able to predict the actual

sediment discharges accurately. The reason stems from the dependency of sediment discharge, in a complex way, to several parameters related to flow and sediment. These parameters include depth, width, density, energy gradient, temperature, viscosity, and turbulence of the flowing water, as well as the size distribution, shape, density, cohesiveness, and concentration of the moving particles. Consequently, presenting a mathematical model which accounts for all these wide-ranging parameters in longitudinal and lateral directions, to predict the amount of moving material, is a strenuous task.

Due to this difficulty, almost all the existing sediment load predictors have been derived under certain simplifications and assumptions that are seldom met in natural rivers. Hence, in general, a fraction of the inaccuracies in sediment discharge estimations can be accredited to the underlying assumption (Habibi, 1994; Papanicolaou et al., 2008).

Another source of difficulty in the development and assessment of sediment load predictors is the presence of uncertainty in sediment transport data. This uncertainty is largely because of limitations in measurement equipment and the significant temporal and spatial variations of concentration and transport rates of sediment particles in natural channels. Traditional measurement procedures of bed bathymetry, grain size distribution, bed morphology and velocity, and shear stress distributions use limited point or cross-sectional measurements. They are, thus, applicable to a limited spatial and temporal resolution and prevent satisfactory model calibration and verification (Papanicolaou et al., 2008). Therefore, the current primary effort aims at reducing the uncertainty in the morphodynamic model results.

1.3 Advancement of Sediment Calculations

The sediment transport investigations are founded upon the premise that a particular relationship exists between hydraulic parameters, and bed material characteristics of a stream, and the rate at which the flow transports the particles. In the period of over a century since du Boys (1879) presented the first "modern" equation, a plenty of formulae has been introduced. For the first few decades, the focus of most studies maintained on the estimation of bed load transport. Afterward, from 1937 with the induction of the concept of turbulence in fluid mechanics mostly by Prandtl and von Karman, more efforts were made for the formation of suspended and total material load equations.

Bed load is the fragment of the bed material that migrate periodically during flood events, either via rolling or sliding motion or via jumping in the river channel. Many fluvial research and management applications require estimates of bed load because it controls the three-dimensional

morphology of streams. The bed load transport formulae appear based on four fundamental concepts: (I) critical bed shear stress or flow discharge, e.g. du Boys (1879), Meyer-Peter and Müller (1948) and Schoklitsch (1934), (II) stochastic and probability concepts for sediment movement, e.g. Einstein (1950) and Misri et al. (1984), (III) energy exchange of the flow, e.g. Bagnold (1966) and Celik and Rodi (1991) and (IV) dimensional and regression analysis, e.g. Rottner (1959) and Ackers and Rodney White (1973).

The development of most bed load transport formulae could be regarded mainly in two stages. Firstly, a theoretic relationship is obtained which attempts to relate the bed load transport rate to hydraulic and sedimentological quantities. In the former case, this typically contains the derivation of an equation which describes the transport conditions that are observed in a suite of experimental and, sometimes, field data e.g. Schoklitsch (1934), Rottner (1959), Parker and Klingeman (1982), and Bathurst (2007). However, in the latter the formation of a relationship from fundamental mechanical or physical principles, e.g. Yalin (1963). Secondly, the basic equation regularly has been revised taking into account its performance against data of initial analysis, e.g. Meyer-Peter et al. (1934) or, by the improvement of coefficients and factors of the formulae by available data, e.g. Ackers and Rodney White (1973).

Numerous bed load transport formulae originate from the original author's experimental data, which usually have been accompanied by data obtained by one or several other investigators, commonly including that of Gilbert (1914), e.g. Schoklitsch (1934). Moreover, the capability of a formula has been regularly evaluated based on its agreement with a limited amount of field data (Müller, 1937). Thus, most formulae owe their origin to a relatively limited data set, though their effectiveness has been established via comparatively few field data. It is a matter of concern that there seem to be more bed load formulae than reliable datasets by which to test them. Consequently, none or even few formulae have been either widely accepted or recognized as being particularly appropriate for designated application.

1.4 Comparison of Transport Models

A considerable importance has been attached to independent evaluations of the performance of the various sediment transport equations, particularly to those assessments, which have included field data. According to López et al. (2014), key components that affect the performance of equations are inherent bed load transport variability, the changing alluvial conditions of the river bed and sampling efficiency. While the scarcity of reliable field data apparently has not eased verifications of bed load transport formulas, there has been some attempts to evaluate their performance.

Johnson (1943) was perhaps the first person to launch a comparison of the performance of bed load transport formulas, through least squares regression, using observed (flume) data. He concludes that the selection among the examined methods (the du Boys, Chang, MacDougal, Meyer-Peter, O'Brien, and U.S. Waterways Experiment Station formulae) might be made merely based on the "comfort" of the variable measurements, required for the calculation.

Since the first comparison of Johnson (1943), several evaluations of the performance of bed load transport formulae, using both field and laboratory data have been published subsequently. These studies are included but not limited to Hubbell and Matejka (1959), Jordan (1965), Cole et al. (1973), Shulits and Hill (1968), White et al. (1973), Carson and Griffiths (1987), Yang and Wan (1991), Chang (1994); Reid et al. (1996), Batalla (1997), Martin (2003), Martin and Ham (2005). Batalla (1997) concludes that the degree of accuracy between observed and predicted values differs significantly from one formula to another. Moreover, he reports the percentage of observations in which the discrepancy ratio between observed and predicted rates fell in a range between 0.5 and 2.0. The reported percentage ranges from 25% (van Rijn) to 38% (Brownlie), 52% (Meyer-Peter and Müller), 65% (Engelund -Hansen), and 68% (Ackers and White). Similarly, most evaluations deduced that no formula performs reliably satisfactory; this can be accredited to the limitations of the test data and the restrictions of the experiment and the physical characteristics of the transport phenomenon (López et al., 2014).

Most efforts to assess the performance of bed load transport formulae have been commenced through the simple comparison of the calculated (bed-load) sediment transport rate with the measured bed-load transport rate of either a laboratory flume or a natural stream. However, Carson and Griffiths (1987) thoroughly examined some assumptions underlying the entire approach to computing gravel bed load, as well as the form of some renowned equations. Also, they specified research directions, which is essential to present a more comprehensive understanding of the river behavior.

Gomez and Church (1989) conducted one of the most comprehensive evaluations of bed load formulae. Given the results and recommendations of their study, the following notes can be made:

- (I) In spite of being evaluated over a relatively wide range of hydraulic conditions, the performance of many of the formulae has not been evaluated outside the range of grain sizes from which they were derived (mostly sand to fine gravel size range).
- (II) It seems to have been little effort to select test data which is consistently related to the hydraulic and sedimentological conditions which the formulae were explicitly intended to describe (e.g. steady flow and equilibrium sediment transport conditions). The authors assert that laboratory data commonly refer to flume studies with significant sidewall effects, or poorly

defined hydraulic and sedimentological parameters, and the sediment discharge measurements, which more accurately describe the total or suspended load instead of the observed bed load transport rate.

Overall, most evaluations conclude with a recommendation or representative formula, but no universal relationship between bed load discharge and hydraulic conditions has been established yet (Habersack and Laronne, 2002).

1.5 Challenges in Hydro-Morphodynamic Modeling

Several failures, such as bridge collapse (pier foundation erosion), the formation of sand bars in estuaries and navigable rivers, destruction of banks and levees, stemmed from the incapability of engineers to predict hydro-morphodynamic conditions of rivers such as sediment motion. Despite the improvement in the description of physical processes, the degree of accuracy in morphodynamic model results remains challenging to assess and is also less than that of hydrodynamics alone (Villaret et al., 2013).

Bed-load transport rates are extremely challenging to predict. Robert (2003) argues that the complexity and irregularity of natural coarse-grained surfaces lead to the hurdle in the prediction of bed-load transport rates. He declares that this complexity results in specific problems in defining the initiation of bed-load transport for a wide range of particle sizes, the effects of bed-forms on shear stress zoning and on bed-load movement itself (e.g. downstream migration of sand bed-forms), the high spatial variability of local tractive forces applied on the bed surface owing to spatial segregation in grain sizes, deformation in local flow gradients, bed undulation, and various features associated with channel configurations, such as meander bends, dunes, bars, etc. There are also significant practical hurdles related to the calculation of the moving distance of individual grains and the spatial and temporal scales at which these convoluted problems need to be addressed.

Bed-load transport is a vastly spatially and temporally inconsistent phenomenon, and the functions that correspond flow intensity to bed load demonstrate this variability. Such relations have an uncertainty that can be reflected in some orders of magnitude (Gomez and Church, 1989). This uncertainty originates partially from the highly local and unsteady nature of the driving forces but is also connected to varying rates of sediment supply from upstream, the configuration and the river bed structure (Wilcock, 2001; Di Cristo et al., 2006; Greco et al., 2012).

The recently developed sediment transport models are not as comprehensive as a hydraulic engineer desires. According to Papanicolaou et al. (2008), some of the limitations of most sediment

transport models are as follows:

(I) Under the assumption that sediment entrainment is triggered by the excess shear stress instead of the near-bed flow turbulent characteristics, shear stress, in most entrainment formulas is determined by assuming uniform flow conditions (Gomez and Church, 1989; Almedeij and Diplas, 2005). Nevertheless, recent studies have shown that turbulent sweeps, outward interactions, and ejections are the main triggering mechanisms of sediment transport.

(II) The conventional approach in sediment transport models, for example, excess shear stress models (settling velocity models) is to calculate the transport rate by using a single characteristic grain size, such as the median (Raudkivi, 1998). It is likely that this approach underpredicts or overpredicts the transport rate of individual fractions when bimodal or multimodal distributions are present on the river bed. The reason is that it does not account for differential transport of sediment particles with a different size or density.

(III) Most multidimensional models deal with flow and sediment processes as entirely uncoupled or semi-coupled within one computational time step (or even during a sequence of time steps in some cases). Thus, the effect of changes in bed elevation and bed material size distribution on the flow field can be considered approximately.

Although bed load transport equations are abundant and used extensively in both applied and theoretical studies, acute testing of such equations in the literature remains limited. Testing the predictive abilities of these formulae over intermediate temporal scales (approximately decadal) and spatial scales (a length of at least several kilometers) remains noticeably more demanding due to lack of field data on bed load transport rates at these levels. According to Wilcock (2001), the absence of sufficient field data to analyze bed load transport complexities (e.g. variability) is identified as the crucial reason why the expectation to obtain the high predictive power of equations under selected conditions cannot be satisfied. According to Gomez and Church (1989), there are more bed load equations in existence than there are reliable data to test them.

To sum up, there is no consensus among researchers in the literature on the selected methods, concerning choice of the best representative equation, since each equation has its limitations and the range of application within the selected data set (Martin, 2003; Sinnakaudan et al., 2006). These challenges hinder a simple model selection for a less experienced engineer.

1.6 Goals of this Study

An issue in many hydro-morphodynamic studies is the determination of the best model that describes the morphodynamic condition of a river in any modeling exercise. It is widely accepted

that no model can be labeled as ideal for the range of existing morphodynamic conditions.

Evaluating the relative performance of competing models can often be challenging given the limited available data. Another complication stems from difficulties in obtaining a unique set of the model parameters. The choice of model parameters demands a substantial degree of expertise from end-users to adapt the model to their application correctly. Hence, a necessity of a framework that allows the modeler to rank different available models according to their capability of future predictions is obvious.

To respond to the mentioned necessity, the present thesis is aimed in constructing a Bayesian model selection framework and to evaluate its applicability in the selection of the most suitable hydro-morphodynamic numerical model. Bayesian model selection uses concepts of probability theory and numerical integration to obtain a model ranking. The proposed framework is aimed at providing objective guidance in model selection to assist even less experienced users in related engineering and management questions by reducing the professional expertise required for manual calibration.

The description of specific goals follows below.

I: To design the framework as a programming routine in Python 2.7 that ranks the competing hydro-morphodynamic models, digitalized by Telemac2D-Sisyphe, after their assessments according to the Bayes' theory.

II: To evaluate the framework using test cases considering different available variants of a hydro-morphodynamic model in Telemac2D-Sisyphe.

1.7 Outline

The structure of present thesis titled "Bayesian Model Selection for Hydro-morphodynamic Models" entails acknowledgments, thesis' declaration and abstract; also, lists of content, figures and tables, nomenclature, the six main chapters, annexes, and the bibliography.

Chapter 1 is devoted to the introduction of this thesis that briefly contains the definition and main features of hydro-morphodynamics, an overview of hydro-morphodynamic modeling, advancement of sediment calculations, followed by the performed studies on model comparisons to shed some light on the performance of each sediment transport equation. All the information has been derived through citations taken from research articles. Further, it addresses the restrictions and challenges of hydro-morphodynamic model selection. The last section of this chapter explains how the present study intends to overcome these challenges as goals definition.

Chapter 2 discloses the main features of hydro-morphodynamic models. First, it provides the description of governing equations, computational modules setup within the initial and boundaries conditions, and the numerical solution proposed by the Telemac-2d-Sisyphe. The second section of this chapter presents a detailed study of selected sediment transport equations implemented in this study. Then, the chapter continues with the description of the two considered case studies. This description entails the geometry, the boundary conditions, and the measurement data.

Chapter 3 describes the methodology of the current study. It introduces the mathematical definitions and explanations of the method for calculation of Bayesian Model Evidence (BME) according to the Bayesian theory, which serves as the basis for the selection of competing hydro-morphodynamic models. Also, it comprises the introduction of a stochastic model reduction technique, called "Response Surface," and how it shows the dependence of each model on the parameter space using few of its evaluations. Additionally, the Bayesian updating to improve the response surfaces is presented. At last, bootstrap filtration is enclosed, which sieve poorly performed parameter sets from the rest.

Chapter 4 entails the setups and the results of Bayesian model selection (BMS) for the channel bend experiment of Yen and Lee (1995). Furthermore, it covers the assessment of the parameter behavior of the individual hydro-morphodynamic model as well as uncertainty investigation of the selected evaluated morphodynamic models.

Chapter 5 presents BMS for the second examined case study, namely the numerical model of the 10-km stretch of the lower Rhine with two different scenarios. First section includes the settings and results for a benchmarked test case using synthetic measurements, also known as Twin Experiment. Then, the results for a real scenario; i.e. using the authentic two-year period measurements for calibration and validation steps is given in the second section.

Chapter 6 summaries the thesis, and presents the conclusions of the present study, followed by some suggestions for future research work.

2 Hydro-Morphodynamic Modeling

In morphodynamic modeling of river systems, empirical relations (models) normally calculate the entrainment, transport, and deposition of sediment to derive morphological changes, i.e. river bed evolution. These models can be computationally demanding because the boundaries of the flow field can vary owing to the coupling between flow field and channel morphology, which entails frequent re-computation of flow conditions. Moreover, the aforementioned empirical models are abundant, and this creates a great challenge for the modeler in the selection of the most appropriate model, which can simulate the real behavior of the river.

The following chapter starts with a description of the hydro-morphodynamic model (Telemac-2d-Sisyphe) in Section 2.1, followed by a detailed study of the selected bed-load transport equations in Section 2.2. Subsequently, the description of the selected case studies to be implemented in the Bayesian selection framework, is presented. It must be noted that we restrict ourselves to the channels with fixed banks, carrying non-cohesive sediment. First, a test case model of a channel bend, based on an experiment done by Yen and Lee is described in Section 2.3. At last, Section 2.4 addresses the real river case study of the river Rhine.

2.1 Hydro-Morphodynamic Model

The hydro-morphodynamic model used in this study has been built in the TELEMAC-MASCARET (www.telemac.org) simulation software, which is an open-source integrated suite of solvers for simulation in the field of free surface flow (Hervouet, 2000). It is the product of a consortium of core organizations: Artelia (formerly Sogreah, France), Bundesanstalt für Wasserbau (BAW, Germany), Centre d'Etudes Techniques Maritimes et Fluviales (CETMEF, France), Daresbury Laboratory (United Kingdom), Electricité de France R&D (EDF, France), and HR Wallingford (United Kingdom).

The modules used in this study are as follows: (I) The hydrodynamic module (TELEMAC-2D) that focuses on free-surface maritime or river hydraulics. (II) The morphodynamic module

(SISYPHE) that is part of the hydro-informatic finite element system (TELEMAC) and describes sediment transport processes and the resulting changes in the riverbed. These two modules are internally coupled, i.e. the relevant hydrodynamic variables are exchanged between hydrodynamic and morphodynamic modules. The technical set-up of the modules and their specifications are summarized in the subsequent section.

2.1.1 Governing Equations

Shallow Water Equations: The hydrodynamic module (TELEMAC-2D) solves the shallow water equations also known as Saint Venant equations, which is the depth-integrated derivation of the Navier-Stokes equations in a two-dimensional domain under the condition that horizontal scale is much greater than vertical length scale.

$$\begin{cases} \frac{\partial h}{\partial t} + \vec{u} \nabla h + h \nabla (\vec{u}) = S_h, \\ \frac{\partial u}{\partial t} + \vec{u} \nabla u = -g \frac{\partial Z}{\partial x} + S_x + \frac{1}{h} \nabla (h \vartheta_t \nabla u), \\ \frac{\partial v}{\partial t} + \vec{v} \nabla v = -g \frac{\partial Z}{\partial y} + S_y + \frac{1}{h} \nabla (h \vartheta_t \nabla v), \end{cases} \quad (2.1)$$

where h denotes water depth (m). u, v are flow velocities in x- and y directions, respectively (m/s), Z is free surface elevation (m), and S_h is source or sink of fluid (m/s). S_x, S_y represent source or sink terms in dynamic equations (m/s²), and ϑ_t is momentum coefficient (m²/s). In Equation 2.1, the variables h, u and v are unknown, and they are in Cartesian coordinate system (Lang, 2010).

Bed Shear Stress: In the momentum equation in Equation 2.1, the bed shear stress is represented as a source or a sink term of momentum (S_x, S_y) within the domain. In the sediment transport processes, the bed shear stress plays a major role and, it is calculated by:

$$\tau = \frac{1}{2} \rho C_d u^2, \quad (2.2)$$

where ρ is the density of water, u is the flow velocity on the river bed and C_d is a quadratic friction coefficient, which can be defined by the Nikuradse bed roughness k_s :

$$C_d = 2 \left[\frac{k}{\log\left(\frac{12h}{k_s}\right)} \right]^2, \quad (2.3)$$

where k is the Von-Kármán constant (0.4), and h is water depth (m).

Bottom Evolution: Near-bed flow fields govern local rates of sediment transport. These flow fields are mostly ruled by the bottom topography and the changes in bed evolution. To calculate the bed evolution, the morphodynamic module, SISYPHE, solves the Exner equation:

$$(1 - n) \frac{\partial Z_f}{\partial x} + \nabla \cdot Q_b = 0, \quad (2.4)$$

where n is the non-cohesive bed porosity, Z_f is the bed evolution, and Q_b is the volume of sediment transport (bed-load) per unit width (m^2s^{-1}). Equation 2.4 specifies that variation of sediment bed thickness can be computed from a simple mass balance and it is plausible for equilibrium conditions (Tassi, 2014). The detailed study of considered sediment transport formulae that predict the bed load is presented in Section 2.2.

Bed Slope Effect: Slanting riverbed leads to an increase of bed load transport rate in the downslope direction, and to a reduction of the rate in upslope bed load direction. Accounting for the bed slope effect, we can implement a correction of sediment transport rate to the magnitude as well as the direction of the transport via the Soulsby's formula (Equation 2.5).

$$\frac{\theta_c}{\theta_{co}} = \frac{\cos \psi \sin \chi + (\cos^2 \chi \tan^2 \phi_s - \sin^2 \psi \sin^2 \chi)^{0.5}}{\tan \phi_s}, \quad (2.5)$$

This formula makes a correction in the critical shear stress θ_{co} as a function of bed slope χ , angle of repose of the sediment ϕ_s , and angle of current to upslope direction ψ with θ_c the modified threshold bed shear stress. Moreover, the modification of sediment-transport-rate direction owing to the slope bed effect is taken into account by:

$$\tan \alpha = \tan \delta - T \frac{\partial Z_f}{\partial n}, \quad (2.6)$$

where α is the angle between the direction of solid transport and the flow direction, δ is the direction of bottom stress in relation to the flow direction, and n , here, is the coordinate along the axis perpendicular to the flow. The deviation coefficient (T) is calculated according to Talmon et al. (1995) and depends on the Shields parameter and an empirical coefficient (parameter of deviation) β_2 :

$$T = \frac{1}{\beta_2 \sqrt{\theta}}. \quad (2.7)$$

Secondary Current Effects: Direction of bed load movement diverges from the main flow direction because of helical flow effect. Engelund (1974) proposed an expression to account for this fact based on the assumption that the mean water depth, the bed roughness, and the bottom shear stress are constant in the cross-section. According to this formula, the angle between bed load movement and main flow direction is defined as:

$$\delta = \frac{7h}{r}, \quad (2.8)$$

where h is the mean water depth (m), and r is the local radius of the bend curvature (m) that is computed based on the cross-sectional variation of the free surface.

$$r = -\rho \alpha' \frac{U^2}{g \frac{\partial Z_s}{\partial y}}, \quad (2.9)$$

in which the recommended α' for considerably rough beds is 0.75, and for smooth beds 1.0.

In the morphodynamic module (SISYPHE), there is a possibility of the introduction of a new sediment transport formula in addition to the existing equations. This user-defined equation can be added as a new subroutine to the Fortran file used in SISYPHE. Further information about the computational procedures of TELEMAC-2D and SISYPHE modules is available in Hervouet (2007) and Tassi (2014), respectively.

2.2 Detailed Study of Selected Equations

After a thorough review of the literature, six widely used sediment transport predictors are selected for detailed investigation.

- Meyer-Peter and Müller formula (1948)
- Einstein-Brown formula (1950)
- Modified Engelund-Hansen formula by Cholley and Cunge (1979)
- Van Rijn formula (1984)
- Hunziker formula (1995)
- Wu fomula (2000)

In the following sections, the non-dimensional current-induced sand transport rate (Φ_s) is expressed by:

$$\Phi_s = \frac{Q_b}{\sqrt{g(s-1)d_{ch}^3}}, \quad (2.10)$$

where s is the relative density ($s = \frac{\rho_s}{\rho}$), ρ_s is the sediment density; d_{ch} is the characteristic sand diameter for uniform grains. The characteristic sand grain diameter (d_{ch}) can be initially introduced as d_{50} , which is a diameter for which 50% of grains are larger. Moreover, the non-dimensional sand transport rate (Φ_s) is a function of a non-dimensional parameter (θ'), defined by

$$\theta' = \frac{\mu \tau_0}{(\rho_s - \rho)gd_{ch}'}, \quad (2.11)$$

with the correction factor for skin friction μ , and the bottom shear stress τ_0 .

2.2.1 Meyer-Peter and Müller Formula (1948)

Meyer-Peter and Müller (1948) formulated an empirical equation for prediction of bed load transport in open channel flows. Their formula is one of the most commonly used bed load predictors.

In 1934, Meyer-Peter, Favre, and Einstein introduced a relationship to estimate the transport rate of uniform grains of gravel. In their experimental investigations, only two grains sizes of gravel with diameters of 5.05 mm and 28.60 mm were considered. The proposed relationship is as follows:

$$q_b^{2/3} = 250q^{2/3}I - 42.5d_s, \quad (2.12)$$

in which q_b represents bed load transport rate per unit width ($kg/s.m$), q is water discharge per unit width ($m^3/s.m$), d_s is the diameter of bed material (m), and I is the slope of the channel. However, this equation is not applicable to the majority of alluvial streams, because it is restricted to rivers with rather coarse uniform materials. Therefore, they extended their experiments to include non-uniform and smaller sediment grains.

Formulation of the transport Equation: Meyer-Peter and Müller (1984) developed the following empirical equation for bed load transport of non-uniform particles, using a wider range of data and the outputs of the previous studies:

$$\frac{(n_s/n)^{2/3}R_bI}{(s-1)d_m} = 0.047 + 0.25\rho^{1/3}(q_b/\rho_s)^{2/3} / [(\gamma_s - \gamma)^{1/3}] d_m, \quad (2.13)$$

where n and n_s are Manning coefficients defined by $v = \frac{1}{n}R_b^{2/3}I^{1/2}$, $v = \frac{1}{n_s}R_b^{2/3}I'^{1/2}$, respectively. n_s is calculated by:

$$n_s = d_{90}^{1/6} / 26, \quad (2.14)$$

in which d_{90} is the grain size for which 90% of sediments are finer.

Meyer-Peter and Müller (1948) discovered that the total shear stress is not accountable for sediment transport in the presence of an undulated bed; a part of the shear stress, however, is consumed to overcome the form resistance, and the bed load transport is a function of the remaining part. Thus, they divided the slope I as $I = I' + I''$, where I' is the portion of the total energy slope required to overcome the grains' resistance and induce bed load motion, and I'' is the rest of the energy slope needed to overpower bed undulation resistance.

Einstein (1950) divided the hydraulic radius into two parts instead of one slope, then the relationship between the two parts of the hydraulic radius can be derived from:

$$R'_b = \left(\frac{n_s}{n}\right)^{3/2} R_b, \quad (2.15)$$

where R'_b represents the hydraulic radius due to grain resistance. Equation 2.13 can be rewritten, using Equation 2.15 as:

$$\Phi_b = \begin{cases} 0 & \text{if } \theta' < \theta_c \\ \alpha_{mpm}(\theta' - \theta_c)^{\frac{3}{2}} & \text{otherwise} \end{cases}, \quad (2.16)$$

with α_{mpm} a coefficient (= 8 by default), θ_c the dimensionless critical Shields parameter (= 0.047 by default). The characteristic sand grain diameter was originally chosen to d_{64} by Meyer-Peter and Müller. This classical bed-load formula has been validated for coarse sediments in the range $0.4\text{mm} < d_{50} < 29.0\text{mm}$, and it is based on the concept of initial entrainment. The Equation 2.16 has basically the same form as du Boys (1879) formula in the sense that the transport rate is related to an effective shear stress ($\theta' - \theta_c$).

Advantages and Disadvantages: Most of the data used in the calibration of Meyer-Peter-Müller's formula were obtained from flows with little or no suspended load and for coarse sands and gravels. Hence, it is suggested that this procedure should be used for the similar flow and sediment conditions.

Equation 2.16 gives zero bed-load transport for θ' of 0.047. This implies that there is no sediment transport for values less than 0.047 and motion of the bed material begins when θ' reaches the value of 0.047. Therefore, according to Meyer-Peter and Müller the dimensionless critical shear stress (θ_c) has a constant value of 0.047, and the quantity ($\theta' - 0.047$) is regarded as the effective or extra shear stress responsible for bed load transport. However, Misri et al. (1984), in their experimental studies, found that bed load transport is not zero even for 0.047. This is due to the fact that the critical dimensionless shear stress for smaller particles is not constant and is significantly smaller than 0.047, as can be seen from the Shields' diagram. The reason that Meyer-Peter and Müller reached a constant value of 0.047 for θ_c is that they used mainly large particle sizes in their experimental studies.

2.2.2 Einstein-Brown Formula (1950)

The Einstein-Brown bed-load equation is a modification of Einstein Formula (1942). The Einstein theory has been described in detail in various studies, e.g. Yalin (1977); Raudkivi (1998);

Simons and Sentuerk (1977); Graf (1971); Garde and Ranga Raju (1977), and Vanoni (2006). Therefore, in the following section, only a short description of the theoretical concept is presented.

The methods employed in Einstein's formula (1942) to predicting bed and suspended load are different. His renowned bed-load function is based on physical principles and probability theories, whereas, suspended sediment transport is calculated from a deterministic approach through the depth integration of the product of local concentration and flow velocity. However, the computation of suspended load is affected by the bed-load through the injection of reference concentration from the bed-load function into the suspended sediment integration.

In his bed-load function, Einstein regarded the bed load transport as the movement of sediment particles in a thin layer with the thickness of two times of the particle diameter exactly above the bed. The fluctuating lifting force transfers these grains by saltation, and then the particles jump a longitudinal distance of approximately 100 particle diameters. The jumping length was assumed to be autonomous of the hydraulic conditions and associated with the sediment size.

The Einstein theory is based on dividing the bed material mixture into several size classes. Firstly, the transport rate of each size class is computed, and then the total sediment discharge is calculated by adding the individual rates. The method results in complex and burdensome computations; nevertheless, the procedures are unambiguous.

The main difference between the Einstein's method of bed-load calculation and the previously published methods of du Boys (1879), and Meyer-Peter and Müller (1948) is that Einstein did *not* utilize any concept for the incipient motion of sediment. Furthermore, the bed-load transport in Einstein theory is associated with the fluctuations of turbulence rather than to the average values of the forces that are exerted on the sediment particles by the flow.

Einstein's bed-load formula incorporates all relevant variables of water and sediment transport, yet, the method has not produced acceptable accuracy in most applied river engineering projects because the experimental data obtained in the laboratory was only used in the calibration.

Formulation of the transport Equation: The Einstein equation is as follows:

$$\begin{aligned}
 A \left[\frac{\Phi_s}{F(D_*)} \right] &= f(B \Psi) , \\
 \Psi &= \frac{1}{\theta'} , \\
 F(D_*) &= \left(\frac{2}{3} + \frac{36}{D_*} \right)^{0.5} - \left(\frac{36}{D_*} \right)^{0.5} , \\
 D_* &= d \left[\frac{(\rho_s - 1)g}{\nu^2} \right]^{1/3} ,
 \end{aligned} \tag{2.17}$$

Einstein assumes that the probability f to be some function of particle weight over the average lift on the particle. He settled on $f(x) = \exp(-x)$ for the functional relationship between Φ_s and Ψ . He proposed $A = 0.465$, and $B = 0.391$ by fitting with measurement data:

$$f(\theta') = \exp(-0.391/\theta') . \tag{2.18}$$

Numerous sediment transport researchers modified Einstein's stochastic model, and similar equations were developed. However, Rouse, Boyer and Laursen have developed one of the most popular modifications of Einstein's formula, which is known as the Einstein-Brown relationship (Brown, 1950). In this correction, Brown (1950) fitted a new curve to Einstein's data, with the function of $f(x) = x^{-3}$, instead of $f(x) = \exp(-x)$, Brown's curve was as follows:

$$f(\theta') = 40(\theta')^3 . \tag{2.19}$$

It is believed that his curve applies well for high value of bed shear stress θ' . However, Einstein's and Brown's curves are often used together, forming the Einstein-Brown bed load equation. This formula is presented in Equation 2.19, which is recommendable for gravel ($d_{50} > 2mm$), and large bed shear stress ($\theta > \theta_c$). The solid transport rate is expressed as:

$$\begin{aligned}
 \Phi_s &= F(D_*)f(\theta') , \\
 f(\theta') &= \begin{cases} 2.15 \exp(-0.391/\theta') & \text{if } \theta' \leq 0.2 \\ 40\theta'^3 & \text{otherwise} \end{cases} .
 \end{aligned} \tag{2.20}$$

The Einstein-Brown equation is rather closer to reality for low θ (large Ψ) than DuBoys and other excess shear models, because it shows some transport for $\theta < \theta_c$, while excess shear models show none. A major drawback of the Einstein-Brown formulation, however, is that there are no bed-form effects.

2.2.3 Modified Engelund-Hansen Formula by Cholley & Cunge (1980)

Engelund and Hansen (1967) assumed that there was a definite relationship between the rate of sediment discharge and the energy dissipation of the flow. They introduced a new approach for the prediction of transport rate of *total bed material load*. Data from four suites of experiments in a large laboratory flume were used to calibrate the proposed equation. Due to the limitation in data for calibration, the formula is recommended for fine sediments, in the range $0.15\text{mm} < d_{50} < 1.00\text{mm}$. Furthermore, the equation is a function of mean flow velocity, water surface slope, hydraulic radius, the median diameter of bed material mixture, and relative density of sediment particles.

Engelund and Hansen's research is based on a simple transport mechanism in dune bed area, where sediment particles are eroded from the stream-side and deposited on the lee side of the dunes. They propose that the moving sediment in the presence of dune beds is raised to a height equivalent to the dune height (h). The energy (per unit time and width) needed for this action can be expressed as $(\rho_s - \rho)gq_t h$, where q_t represents the volumetric transport rate of bed material per unit width of the channel.

Formulation of the transport Equation: Assuming that the particle velocity is proportional to the friction or the shear velocity $u^* = \left(\frac{\tau_0}{\rho}\right)^{0.5}$, and the effective shear stress $(\tau' - \tau_c)$, which is transferred from the fluid to the moving grains, Engelund and Hansen developed the following equation:

$$(\rho_s - \rho)gq_t h = \alpha(\tau' - \tau_c)L\left(\frac{\tau_0}{\rho}\right)^{0.5}, \quad (2.21)$$

where τ_c denotes critical bed shear stress at which the bed material particles start to move, τ' is bed shear stress due to the grain roughness only, L is length of the dune, τ_0 stands for flow shear stress at the bed, and α is a dimensionless coefficient to be determined experimentally. Equation 2.21 can be rearranged to derive the following:

$$fq_t \left(\frac{h}{f.L}\right) = \alpha \frac{(\tau' - \tau_c)}{(\rho_s - \rho)gd_{50}} \left(\frac{\tau_0}{\rho}\right)^{0.5} d_{50}, \quad (2.22)$$

d_{50} is used here as the median diameter of the bed material, and f is the function factor of the bed, derivable from Darcy-Weisbach equation for open channel flows, $f = 2g \times (4R) \frac{I}{V^2}$, where R is the hydraulic radius of flow cross section, and V is average flow velocity.

Dimensionless forms of τ' , and τ_c can be written as following, using the definition of the

Shield's parameter $\left(\theta' = \frac{\mu \tau_0}{g(\rho_s - \rho)d_{50}}\right)$:

$$\begin{aligned}\theta'_c &= \frac{\mu \tau_c}{g(\rho_s - \rho)d_{50}} = 0.06, \\ \theta'_* &= \frac{\mu \tau'}{g(\rho_s - \rho)d_{50}}.\end{aligned}\tag{2.23}$$

By replacing τ_0 , τ' , and τ_c in Equation 2.22, the following expression is obtained:

$$fq_t \left(\frac{h}{fL}\right) = \alpha(\theta'_* - 0.06)\sqrt{\theta'_*} \sqrt{g \left(\frac{\rho_s}{\rho} - 1\right) d_{50}^3}.\tag{2.24}$$

By introducing the dimensionless sediment discharge parameter Φ_s :

$$\Phi_s = \frac{q_t}{\sqrt{g \left(\frac{\rho_s}{\rho} - 1\right) d_{50}^3}},\tag{2.25}$$

into Equation 2.24, and by showing that $\left(\frac{h}{fL}\right)$ is constant for a value of θ'_* , they derived the expression $\theta'_* - 0.06 = 0.4\theta'^2$. Therefore, the transport equation becomes:

$$f\Phi_s = \text{const.} \times \theta'^{5/2}.\tag{2.26}$$

The validity of a transport formula of this type is tested by comparison with four sets of experiments in a large laboratory flume, reported in Guy et. al. (1966), and the calibrated form of Equation 2.26 is:

$$\Phi_s = 0.1 \times \theta'^{5/2}.\tag{2.27}$$

Advantages and Disadvantages: Engelund and Hansen's derivation is directly based on bed load transport phenomenon. Their initial assumption (the sediments are elevated to the dune height in the presence of a dune bed) is valid when only bed-load particles are considered. However, this assumption is used for developing total load equation, which includes both bed and suspended loads.

Another questionable assumption is that the particle velocity, for the whole sediment material in transport, is proportional to the bed shear velocity u^* . This hypothesis is also typically applicable to the bed-load particulate matters and cannot describe the velocity of suspended solids properly. In general, the velocity of suspended particles in the direction of the flow is strictly proportional to the velocity of the surrounding fluid (Bagnold, 1966; Toffaleti, 1969; Van Rijn, 1984).

Moreover, the dimensionless critical shear velocity (θ'_c), is replaced with a constant value of 0.06. Nonetheless, this value is not constant, according to Shields (1936), and is function of both flow and sediment characteristics, such as bed shear velocity u^* , kinematic viscosity of flow ν , flow density ρ , sediment density ρ_s , and particle size d_s . Conversely, the constant value of (θ'_c) is only applicable for the large particle size, where boundary Reynolds number (R^*) is nearly greater than 100, i.e. for particles which typically move within the bed load layer.

Modification of the Engelund-Hansen Formula: The classic method of Engelund and Hansen (1967) has been revised by Cholley and Cunge (1980) to rectify the drawback of the dimensionless critical Shield's parameter (θ'_c), to account for different transport regimes, and to suggest a threshold for incipient motion of sediment particles. The proposed formulation is as following:

$$q_t = 0.05 f_n \left[\frac{(s-1)d_{50}^3}{g} \right]^{1/2} k^2 H^{1/3} \theta_*^{5/2}, \quad (2.28)$$

where f_n is the fraction in the bed of sediment class n , and K is the Strickler coefficient. Moreover, the Strickler coefficient can be replaced by setting $k^2 H^{1/3}$ equal to g/C_D , in which the bottom drag coefficient (C_D) can be derived using the following equation:

$$C_D = \left[\frac{\kappa}{\ln(z_b/z_0)} \right]^2 \quad \text{or} \quad C_D = \left[\frac{\kappa}{\ln(H/z_0) - 1} \right]^2. \quad (2.29)$$

Here, κ is the Von Karman constant, z_b represents the height of the first velocity node above the bed, z_0 is the roughness height (or skin roughness length defined in the sediment transport model), and H the total water depth.

Considering the Equation 2.10 for non-dimensional current-induced sand transport rate (Φ_s), the bottom drag coefficient (C_D), the modified version of Engelund-Hansen formula can be expressed as:

$$\Phi_s = \frac{0.1}{C_D} \hat{\theta}^{5/2}, \quad (2.30)$$

in which the dimensionless bed shear stress $\hat{\theta}$ is computed as a function of the dimensionless skin friction parameter θ' :

$$\hat{\theta} = \begin{cases} 0 & \text{if } \theta' < 0.06 \text{ (flat bed regime - no transport)} \\ \sqrt{2.5(\theta' - 0.06)} & \text{if } 0.06 < \theta' < 0.384 \text{ (dune regime)} \\ 1.065 \times \theta'^{0.176} & \text{if } 0.384 < \theta' < 1.08 \text{ (transition regime)} \\ \theta' & \text{if } 1.08 < \theta' \text{ (sheet flow regime)} \end{cases}. \quad (2.31)$$

2.2.4 Van Rijn Formula (1984)

van Rijn (1984) develops his bed-load equation based on the product of the saltation height, the representative velocity of bed-load particles, and the concentration of sediment materials in the bed layer. Moreover, in his later researches, he proposes an approach to estimate suspended load via the depth integration of the product of the vertical profiles of flow velocity and sediment concentration, and a simplified procedure for computation of sediment loads. His equations are mostly based on a revision of existing equations implementing numerical and regression analysis techniques with plenty of field and lab data.

Formulation of the Transport Equation: According to van Rijn (1984), in the bed-load transport, the particles are displaced by rolling, and saltating along the bed surface. The transport rate (q_b) of the bed load is defined as the following:

$$Q_b = u_b \delta_b c_b , \quad (2.32)$$

where u_b is the particle velocity, δ_b the saltation height, and the bed-load concentration is denoted by c_b . By numerically solving the equation of the motion for a spherical saltating particle, the following relationships for calculation of the saltation height (δ_b), and the particle velocity (u_b):

$$\frac{\delta_b}{D_{50}} = 0.3 D_*^{0.7} T^{0.5} , \quad (2.33)$$

$$u_b = \left[\left(\frac{\rho_s}{\rho} - 1 \right) \times g D_{50} \right]^{0.5} \times 1.5 T^{0.6} .$$

Here, dimensionless particle diameter (D_*) and dimensionless transport stage parameter (T) can be calculated from the following equations (Ackers and Rodney White, 1973; Yalin, 1963):

$$D_* = D_{50} \times \left[\frac{\left(\frac{\rho_s}{\rho} - 1 \right)}{\vartheta^2} \right]^{1/3} , \quad (2.34)$$

$$T = \frac{(u'_*)^2 - (u_{*,cr})^2}{(u_{*,cr})^2} .$$

The critical shear velocity ($u_{*,cr}$) according to Shields can be obtained from:

$$u_{*,cr} = \left[\left(\frac{\rho_s}{\rho} - 1 \right) \times g D_{50} \times \theta_{cr} \right]^{0.5} . \quad (2.35)$$

In addition, Van Rijn used Chezy formula to compute bed shear velocity related to grains (u'_*) defined as:

$$u'_* = \left(\frac{\sqrt{g}}{c'} \right) \times \bar{u} , \quad (2.36)$$

in which c' is Chezy-coefficient related to grains, \bar{u} is mean flow velocity.

Van Rijn assumes that bed-load transport can be defined accurately as a function of two dimensionless parameters D_* and T . By analyzing 130 sets of measured bed load transport in laboratory flumes, with particle diameters ranging from 0.2 mm to 2.0 mm, he shows that the bed load concentration C_b can be derived through:

$$\frac{Q_b}{\sqrt{g(s-1)d_{50}^3}} = \frac{0.053 T^{2.1}}{D_*^{0.3}} \quad \text{or} \quad \Phi_s = \frac{0.053 T^{2.1}}{D_*^{0.3}}. \quad (2.37)$$

Equation 2.33 is dimensionally homogeneous and provides the bed-load transport rate Q_b per unit width of channel in volumetric ratio. The equation has been verified with 580 datasets from bed-load transport in experimental flumes and natural rivers carrying sand sediment particles. Van Rijn concludes that the results demonstrate that near 77% of predicted bed load discharges are within 0.5 - 2.0 times of the measured transport rates.

Advantages and Disadvantages: One advantage of Van Rijn's theory is that the energy slope (or water surface) has been removed from the sediment transport rate computations. Energy slope is one of the most significant variables that influences all the physical characteristics of open channel flows. Nonetheless, it is rather sensitive to minor changes in water surface elevation, which are not simply determined, and its measurement, especially for natural rivers during the flood events, is utterly demanding. The replacement of energy slope via Chezy formula sounds rational for large-scale natural streams. On the other hand, for experimental flumes and small-scale streams, this alternative is irrelevant and may inject errors into the computations, because in such cases, the conditions are controlled and measurement of the water surface slope is manageable (Habibi, 1994). What is more, the proposed expressions of bed-load transport rate, i.e. Equation 2.37 is valid for the sand grains (diameter between 0.2 mm and 2.0 mm). However, in natural streams with high energy slope, near-bed grains mostly include gravel particles, which are larger than 2.0 mm of diameter.

2.2.5 Hunziker Formula (1995)

The formula of Hunziker (1995) is an adaptation of the Meyer-Peter Müller formula to account for fractional transport calibrated with the experiments of Gunter (1971) and Suzuki and Hano (1991) with grain diameters from 0.9 to 4.0 mm. The principle of this transport function is the concept of same incipient motion for all sediments. As per all sediment formulae that assume threshold conditions for the onset of erosion, the transport within the idea of this method only initiates if the dimensionless shear stress of the flow is greater than the dimensionless threshold.

According to Parker (1992) and Wilcock (1992), the transport model was selected to be surface based, and the transport capacity of each fraction is calculated as a function of the mean grain size of the surface layer. This procedure ensures incipient motion of all grains at the same threshold value.

The model applies the mixing layer concept suggested by Hirano (1971), in which the mixing layer is supposed to be equal to the surface layer. It was concluded that using the basic structure of the MPM formula, and multiplication of the excess shear stress with the hiding function, the identical mobility condition for the mobile armor case was satisfied without any further correction. The applied structure differs from previous approaches, where either the total shear stress or the critical shear stress are corrected by the hiding function (Sutherland, 1992).

Formulation of the Transport Equation: The basic structure of the transport equation for a fraction in a dimensionless form is expressed by:

$$\Phi_b = p_1 \times 8 \left[\varphi_i (\theta'_{dms} - \theta_{cdms}) \right]^{1.5}, \quad (2.38)$$

in which p_i is the fraction of class i in the surface or mixing layer. The dimensionless Shields factor referred to the mean surface grain size is defined by:

$$\theta'_{dms} = \frac{\tau'_0}{\rho g (s-1) d_m} \quad (2.39)$$

where τ'_0 represents the reduced bed shear stress accounting for bed form losses. The modified critical Shield's parameter for any grain class within the surface is determined by:

$$\theta_{cdms} = \theta_{cr} \left(\frac{d_{mo}}{d_m} \right)^{0.33}, \quad (2.40)$$

where θ_{cr} the critical Shields parameter ($\theta_{cr} = 0.047$), d_m and d_{mo} are the mean grain size of the surface layer and subsurface layer in meter, respectively.

The hiding function (φ_i) is computed using:

$$\varphi_i = \left(\frac{d_i}{d_m} \right)^{-\alpha}, \quad (2.41)$$

with d_i the grain size of class i and α is a constant.

Hunziker (1995) states that, in the particular case of uniform bed sediment, the procedure used in the Meyer-Peter Müller (MPM) formula to correct for bed forms led to a significantly large form drag. The reason for this is the inaccurate parameterization of skin friction implemented in MPM formula; namely, $K_r = 26/D_{90}^{1/6}$. This result is in accordance with the earlier results of Jaeggi (1984), Smart and Jaeggi (1983). According to Jaeggi (1984), the parameter k_r had

been calibrated using the Nikuradse (1933) tests and the effect of form roughness evidently overestimated during the development of the original MPM formula. In light of this finding, Hunziker (1995) used an alternative bed-form correction proposed by Yalin and Scheuerlein (1988). The intention of this correction was to account not only for bed-form effects, but to consider also the effect of moving particles in bed-load transport. As a result, Hunziker (1995) derived the following improved MPM relation,

$$\phi = 5 \times (\tau_{H-YH}^* - 0.05)^{1.5}, \quad (2.42)$$

where τ_{H-YH}^* represents dimensionless boundary shear stress, after including the same sidewall correction procedure used by Meyer-Peter and Müller (1948) but now implementing the bed-form correction of Yalin and Scheuerlein (1988) instead of the original bed-form correction considered by Meyer-Peter and Müller.

Equation 2.36 involves reducing the coefficient 8 to a value of 5, in comparison to the original equation of Meyer-Peter and Müller (Equation 2.16), taking into account the form roughness by an appropriate relation, and discarding the parameter $(k_s/k_r)^{1.5}$. In Equation 2.42, the value of the parameter, representing critical shear stress has been marginally raised from 0.047 to 0.05. However, this value is constant only for hydraulically rough conditions.

Using the new constant in the MPM expression (Equation 2.27), the volumetric sediment transport for each sediment class presented in Equation 2.23 is replaced by:

$$\Phi_s = p_1 \times 5 \left[\varphi_i (\theta'_{dms} - \theta_{cdms}) \right]^{1.5} \text{ if } \theta'_{dms} > \theta_{cr}. \quad (2.43)$$

As mentioned before, the critical Shields parameter is calculated as a function of the dimensionless mean grain size D_* . It is worth noting that according to Hunziker, stability problems may occur outside the parameter range $\alpha \leq 2.30$, and $d_i/d_m \geq 0.25$.

Advantages and Disadvantages: The valuable conclusion of Hunziker (1995); i.e. MPM formula over-corrected for form drag, is, however, incomplete and obscured by additional factors, such as α . It is incomplete in the sense that it specifies that some form of correction for form drag, the one according to Yalin and Scheuerlein (1988), is still required even for data without bed forms, which does not hold according to Wong and Parker (2006).

2.2.6 Wu Formula (2000)

This equation is particularly recommended for the calculation of graded sediment since, in its derivation, the different fractions were explicitly implemented. In Wu et al. (2000), the authors

argue that the hiding and exposure effect in the modeling of non-uniform sediment transport needs to be considered. The argument stems from the fact that the coarse particles on the bed in non-uniform sediment movement are readily entrapped in comparison with the uniform sediment of equal sizes, due to a higher possibility of exposure to the flow.

In their study, they assumed that sediment particles have a spherical shape with different diameters as shown in Figure 2.1, and defined the exposure height Δ_i , for a particle with diameter d_i , as the height difference between the apexes of particle and its upstream neighbor. The particle d_i is regarded as being at exposed state, if $\Delta_i > 0$, otherwise it is at hidden state.

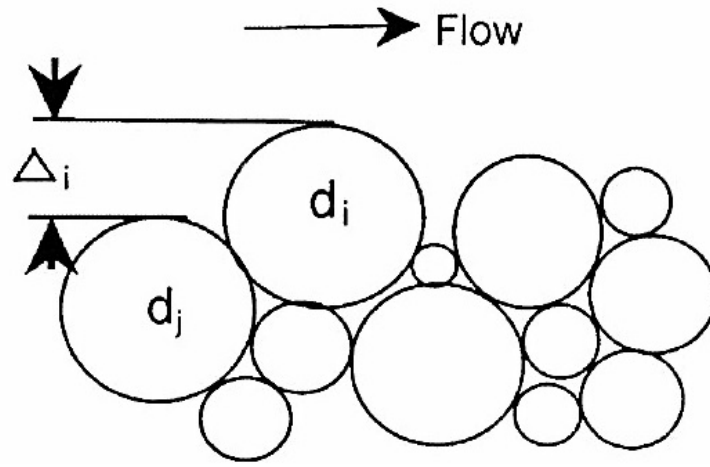


Figure 2.1: Definition of the exposure height (Wu et al. 2000)

Δ_i is a random variable, due to randomly sediment particle distribution on the bed, and assumed to follow a uniform probability distribution f , expressed by:

$$f = \begin{cases} \frac{1}{d_i + d_j} & -d_j \leq \Delta_i \leq d_i \\ 0 & \text{otherwise} \end{cases} . \quad (2.44)$$

The probability of particles d_j residing in the front of particles d_i can be assumed to be the total rate of fraction of particles d_i in the bed material, p_{bj} . Thus, the total hidden and exposed probabilities of particles d_i , can be obtained by:

$$p_{hi} = \sum_{j=1}^N p_{bj} \frac{d_j}{d_i + d_j}, \quad (2.45)$$

$$p_{ei} = \sum_{j=1}^N p_{bj} \frac{d_i}{d_i + d_j},$$

where N denotes the total number of particle size fractions of non-uniform sediment mixtures, p_{hi} and p_{ei} are the total hiding and exposing probabilities of particles d_i . They show in their

study that there is a correlation of $p_{hi} + p_{ei} = 1$ between p_{hi} and p_{ei} . This correlation can be defined via the hiding and exposure factor using laboratory and field data:

$$\xi_i = \left(\frac{p_{ei}}{p_{hi}} \right)^{-0.6} . \quad (2.46)$$

An expression for determining the critical bed shear stress for incipient motion of non-uniform sediment was derived by introducing the hiding and exposure factor in Equation 2.46:

$$\frac{\tau_{ci}}{\gamma_c - \gamma} = \theta_c \left(\frac{p_{ei}}{p_{hi}} \right)^{-0.6} , \quad (2.47)$$

where τ_{ci} is the critical shear stress for particle d_i in non-uniform sediment mixtures, and θ_c is interpreted as the non-dimensional critical shear stress for the related uniform sediment or the mean size of bed materials. Using field and laboratory data, θ_c was determined to be equal 0.03.

The authors adopted the threshold equation suggested by Parker et al. (1983) for the incipient motion of non-uniform sediment as the reference transport threshold to ascertain the critical shear stress,

$$W_{ri}^* = \frac{q_{bi} (\rho_s / \rho - 1) g}{p_{bi} u_*^3} , \quad (2.48)$$

where W_{ri}^* represents a reference transport parameter, q_{bi} is the volumetric bed load transport rate of the fraction i per unit width, and p_{bi} shows the gradation of the fraction i of bed material.

Characteristic parameters and relationship: The type of formulas, which relate the bed load transport rate of non-uniform bed-load to the excess shear stress ($\tau_b - \tau_c$), can be written as:

$$\Phi_b = f_3 \left(\frac{\tau_b}{\tau_c} - 1 \right) , \quad (2.49)$$

where Φ_b is a non-dimensional bed-load transport rate, q_b is the bed load transport rate per unit width, and τ_b is the total bed shear stress due to grain roughness. By extending Equation 2.49, the non-dimensional fractional bed load transport rate Φ_{bi} is defined as:

$$\Phi_{bi} = \frac{q_{bi}}{p_{bi} \sqrt{g(s-1)d_i^3}} , \quad (2.50)$$

in which q_{bi} denotes the transport rate of the i th fraction of bed load per unit width (m^2/s). The bed shear stress is calculated by $\tau_b = \gamma R_b J$, where R_b is the hydraulic radius of channel bed, and J is the energy slope. However, the bed load transport corresponds only to the grain shear stress τ_b' , when sand ripples and dunes exist and is calculated by $\tau_b' = \gamma R_b' J$, where R_b' is the hydraulic radius of the grain roughness on the bed. Therefore, the following expression calculates the grain shear stress by using the Manning's formula for uniform flow:

$$\tau_b' = \left(\frac{n'}{n} \right)^{3/2} \times \tau_b . \quad (2.51)$$

The non-dimensional excess bed shear stress ($T_i = \frac{\tau'_b}{\tau_{ci}} - 1$) is used as an independent parameter in the expression of Φ_{bi} .

Regression function: To establish the relationship between Φ_{bi} and T_i , the authors utilized some collected data and to calculate τ'_b , n was determined by $n = R_b^{2/3} J^{1/2} / U$. With the help of the least square curve fitting, the following expression for the fractional transport rate of non-uniform bed load was derived:

$$\Phi_{bi} = p_i \times 0.0053 \left[\left(\frac{n'}{n} \right)^{1.5} \left(\frac{\theta_m}{\xi_i \theta_c} - 1 \right) \right]^{2.2}, \quad (2.52)$$

where p_i represent the fraction, θ_c is equal to 0.003, n' and n are respectively the Manning's roughness coefficient correspond to grain roughness and channel bed, ξ_i is the hiding and exposure factor (Equation 2.46), and θ_m is the calculated shields parameter for d_m . Finally, they concluded that the proposed hiding and exposure correction factor could account for not only the influence of sediment particle size but also that of bed-material gradation.

In conclusion, most of discussed formulae assume threshold conditions for the inception of erosion (e.g. Meyer-Peter and Müller, and van Rijn). Other methods are based on similar energy concept (e.g. Modified Engelund-Hansen) or can be a derivation from a statistical approach (e.g. Einstein-Brown). Ultimately, the available formulae can be viewed merely as scale equations of the flow. On this account, it is perhaps not astonishing that so many variations have been presented so far, and adjudicating their merits remains challenging. It is also noteworthy to mention that the physics of bed load transport remains incompletely analyzed. Therefore, there is no reason to postulate that any one of the existing formulae necessarily represents a complete or even a close correlation with the measurements.

2.3 Channel Bend Model of Yen and Lee (1995)

Yen and Lee (1995) conducted sets of experiments in a laboratory channel bend to investigate bed topography and transverse sediment sorting in an alluvial channel bend under unsteady flow conditions with non-uniform sediment. Five experiments, with the same primary sediment-size gradation but with dissimilar inflow hydrographs, were performed in an 180° channel bend with a constant radius of curvature. For the purpose of this study, we select the hydrograph of run number 4 and the corresponding collected measurement data (Yen and Lee, 1995).

Model Geometry: The channel, illustrated in Figure 2.2, is 1m wide and has a central angle of 180 degrees. Two straight reaches of 11.5 m long connect the channel to a stilling basin in the upstream and a sediment-settling tank in downstream. A weir controls the water depth at the downstream end to produce relatively uniform flow along the bend with the base flow discharge. Before each run of the experiment began, a layer of sand around with thickness 20 cm and a mean diameter of 1.0 mm had been placed on the bed.

Numerical Model: The numerical model of the bend channel embodies an unstructured, triangular mesh with 709 nodes and 1050 elements to be solved by Finite Element Method (FEM) as shown in in Figure 2.3.

Inflow Hydrograph: A triangular-shaped hydrograph was considered with the base flow of $Q_{bf} = 0.02 \frac{m^3}{s}$, and a peak discharge of $Q_{peak} = 0.053 \frac{m^3}{s}$ in a period of 300 minutes as shown in Figure 2.4. The peak of the hydrograph applied in the present experiment was adjusted at the point of the first third of total duration. A sluice gate, whose opening was set at a step of 1 mm each time, manually operated the discharge. Additionally, a weir at the outflow controlled a constant water depth of $h_{bf} = 5.44 \text{ cm}$ and $h_{peak} = 10.30 \text{ cm}$. Measurements of water levels taken by point gauge at the upstream end revealed that the error of discharge laid within 20.5% of the set values. (Yen and Lee, 1995)

Measurements: The results of the physical experiment are the measurements of bed topographic evolution, taken by point gauge. These results were obtained at the end of hydrograph, for the run of experiments after termination of the flow, and complete but gradual drainage of water. These evolution measurements define the erosion and deposition of sediment near the bed of the channel at the cross sections of 90 and 180 degrees of the bending channel after 300 minutes of time; normalized with the initial water depth $h_0 = 0.054 \text{ m}$.

As seen in Figure 2.5, the evolution profiles illustrate non-smooth slopes, which are proper of nature systems, tools, and human errors. The representative cross-section in channels presents a high sediment deposition in the inner bank and erosion in the outer bank. As indicated in Yen

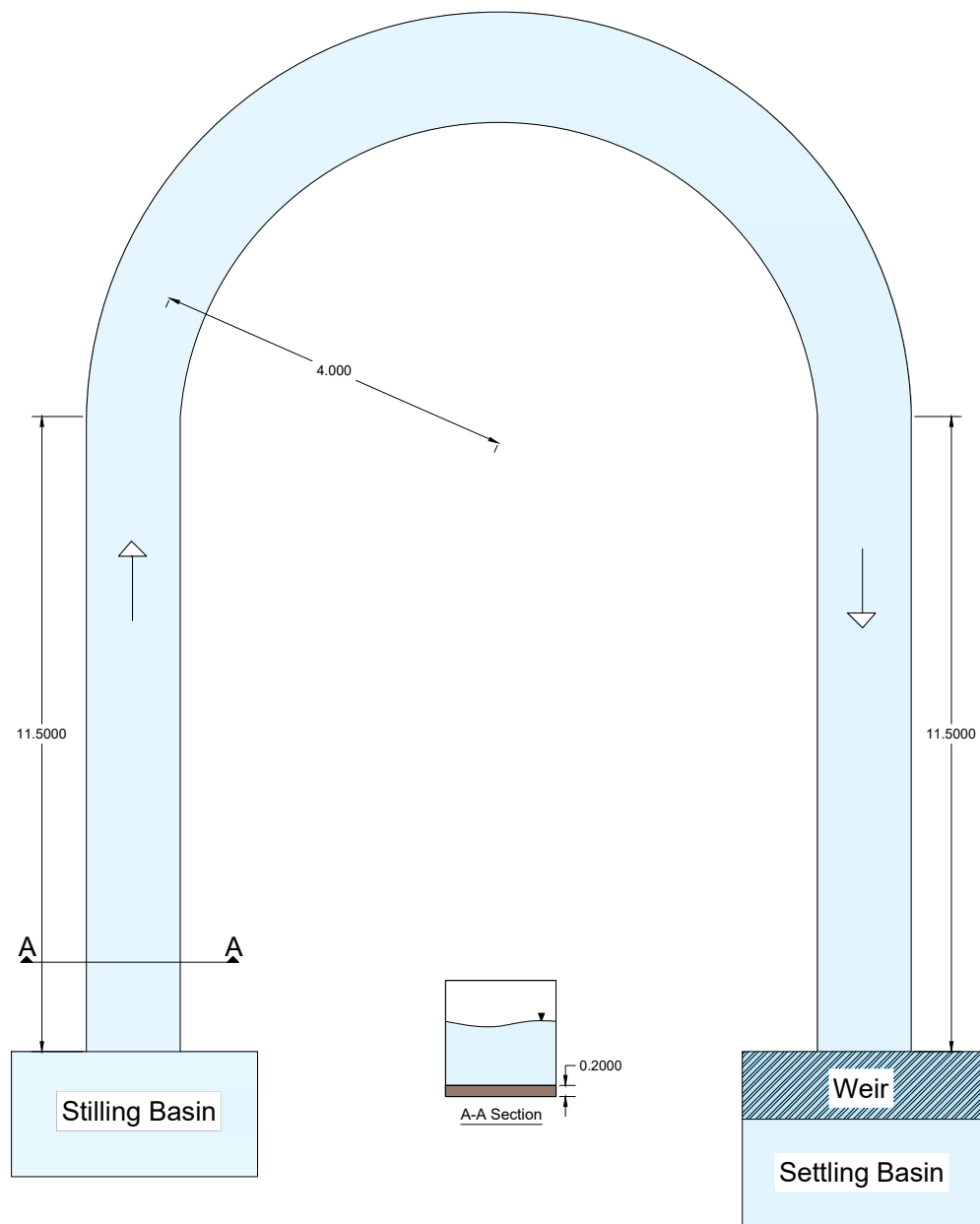


Figure 2.2: Bend channel geometry

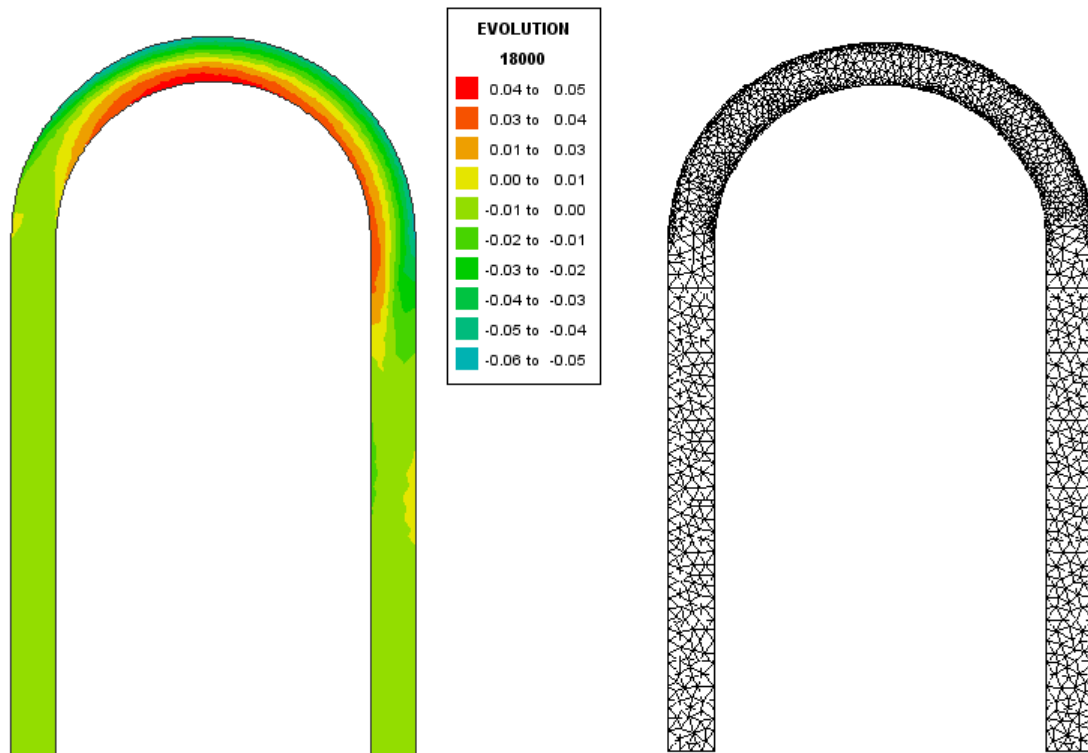


Figure 2.3: Bend channel geometry

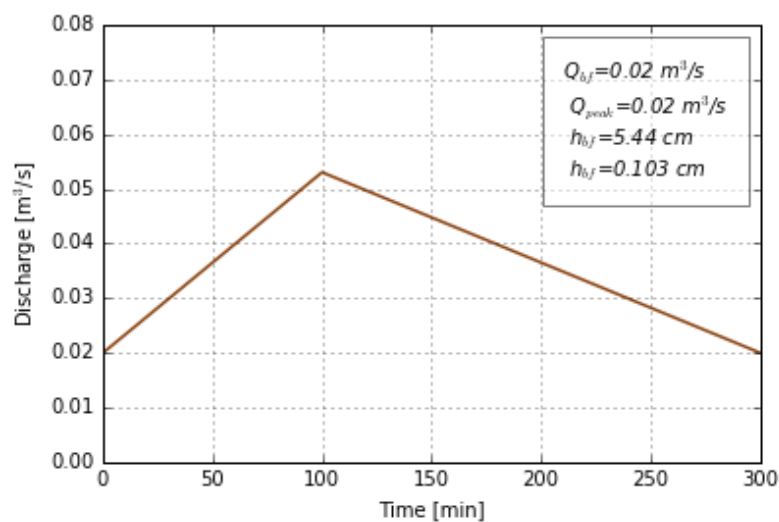
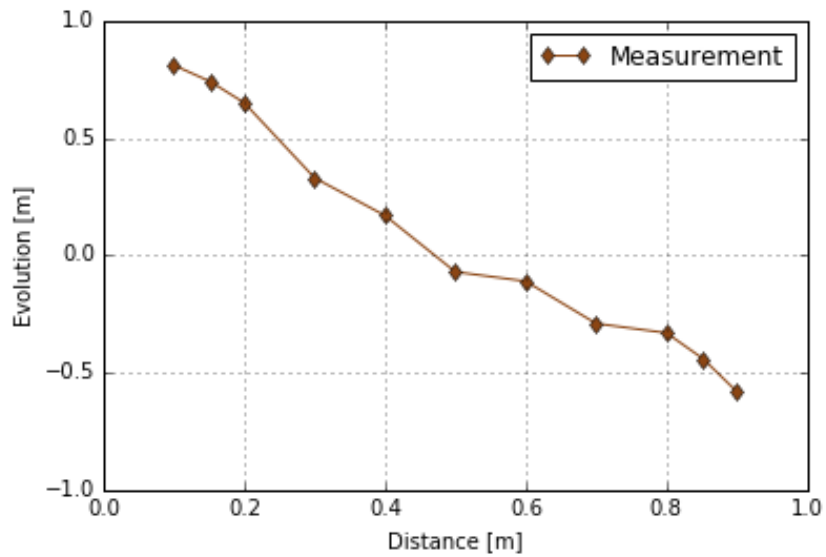
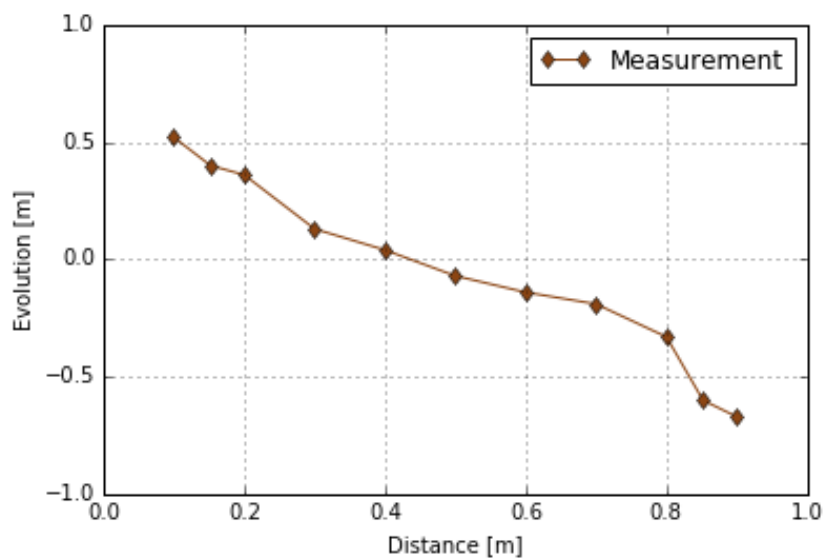


Figure 2.4: Inflow hydrograph

and Lee (1995), this configuration specifically occurs at 90° , in which a higher slope of the bed evolution and more deposition of sediment in the inner bank exist. However, the bed evolution at the 180° cross section clearly shows that a smoother slope and deeper scour depth emerged in the outer bank.



(a) Evolution at 90 degree



(b) Evolution at 180 degree

Figure 2.5: Measurement profiles (Source: Yen and Lee (1995))

2.4 The River Rhine Model

Meandering channel sections present a particularly difficult challenge for modeling sediment transport. They are characterized by high levels of sedimentation on inside bends and erosion on outside bends. The dynamic conditions in curved channels mean that the shape of the banks and riverbed is constantly changing, thus influencing the flow characteristics. This change may affect especially the inland navigation and flood situations.

Study area: The central reach of the Lower Rhine at Düsseldorf/Neuss (Rhine-km 739.0 to Rhine-km 749.0, see Figure 2.6) is implemented as a complex hydro- and morphodynamic model. An intense meandering with two close meandering curves and active bed-load transport

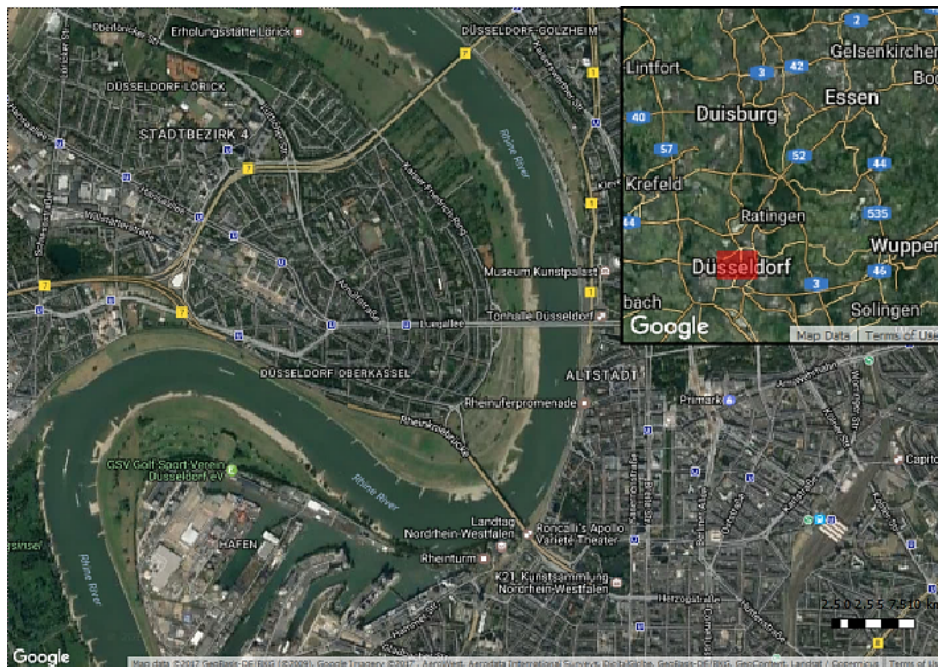


Figure 2.6: The Study area of the lower Rhine model (Source: Google Maps, 2017)

characterize this section of the river. In the first upper-stream curvature, a mean radius of approximately 800 m exist with a flow section of 2.5 km; the counter-curvature is directly connected with an average radius of approximately 600 m to 1.5 km of flow section. A further river curve follows, which has a much larger radius of 2.5 km and ends in a nearly straight river course. The river stretch is about 400 m wide, and the width reduces to 220 m between the two bends. Along the 10 km long section of the river, there is an average gradient of about 0.17 ‰, which corresponds to a slope which is characteristic of the entire Rhine bottom (Messing, 2008).

The Rhine flows freely in this section, i.e. neither in the upper nor lower stream is there a congestion control by transverse structures. However, the morphology of the Lower Rhine is,

among other things, through the construction of the Rhine and the canalization of the tributaries (for example, the Neckar and the Moselle) is profoundly affected. Additionally, for a long time dumping and dredging of bed material has been performed to provide safe inland navigation.

Model Geometry: A comprehensive database was used to create the model geometry. In addition to laser scan data, information was also available on the groynes, longitudinal and bridge structures in the study area. The Digital Terrain Model (DTM) based on this data includes, in addition to the main river channel, the adjacent floodplains to the dikes.

-Digital Terrain Model-Floodplain: The terrain model is based on aerial mapping data from January 1997 (aerial mapping data of 639km-760km from 17.01.97 - BAW-97953). These were available for the floodplain as a grid with a resolution of 1 m x 1 m.

-Digital Terrain Model-Main channel: The model geometry in the area of the river channel was modeled based on the cross section profile data from the year 2000 at a distance of 100 m each.

-Digital Terrain Model-Groynes: The position and height of the groynes were taken from the groyne cadaster, plan data, and floodplain data.

Numerical Model: A two-dimensional numerical sediment transport model was established by the Federal Waterways Engineering and Research Institute (BAW) as a component of the "artificial grain-feeding of bed material on the central Lower Rhine" project, aiming at improving the efficiency of future hydrological design and optimizing the measures economically.

The numerical model of the 10 km Rhine section has an unstructured, triangulated grid with 41277 nodes and 81684 elements. The grid elements can be categorized into three groups. The edge length in the riverbed is 10-15 m, while a finer resolution of about 5-10 m was selected for the groynes and banks. Moreover, the elements with an edge length of approximately 50 m represent the floodplains. The model was extended up- and downward by 500 m, to obtain a stable flow pattern in the inlet and outlet region. The terrain geometry was adopted, only the groynes were removed manually in this 500 m. In this way, numerical instabilities, particularly because of the groynes, are avoided at the inlet cross-section.

For the 2D model considered, the floodplains are first defined as "rigid bed." In these areas, there can be no erosion of the original site. However, it is possible for material to deposit here, for example, when the flood is running off and is eroded again during a next flood wave.

While the inlet and outlet cross-sections for the hydraulics (Telemac-2D) have been completely opened, the bed load (Sisyphé) is only entered or discharged in the main river channel. In this way, during a flood, the whole flow is not forced through the main channel, but can also overflow the floodplains. Further, a so-called "equilibrium condition" realizes the entry of bed

load in the inlet cross-section, i.e. the theoretical transport rate on the edge nodes is calculated, and the load is transported into the model area, but the height of the nodes remains unchanged.

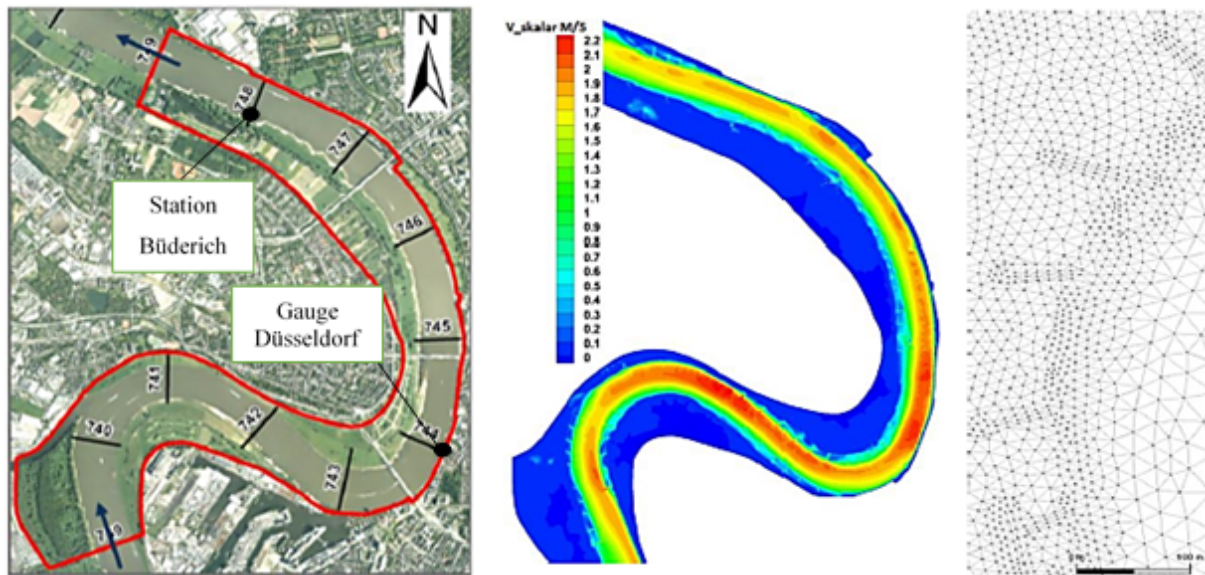


Figure 2.7: Model boundaries, velocities, grid of the lower Rhine model (Source: Backhaus (2013))

Roughness: Different roughness zones were defined for the model area (see Figure 2.8), to determine the natural flow resistance. Their spatial definition, as well as roughness value assignment, was carried out in the floodplain area using existing orthophotos and local approaches taking into account the respective vegetation and surface conditions. In the river main channel, different bottom samples could be used for the roughness coverage within the model area. Since these samples showed only slight differences among one another, the entire flow tube was provided with a similar roughness value. Thus, the roughness values defined for the individual zones as part of the model calibration. These five different zones categorize the domain of the river stretch: the main channel, the floodplain, the groynes, the vegetation area and residence area.

The Nikuradse roughness coefficients, obtained in the calibration process, for all zones, are presented in Table 2.1.

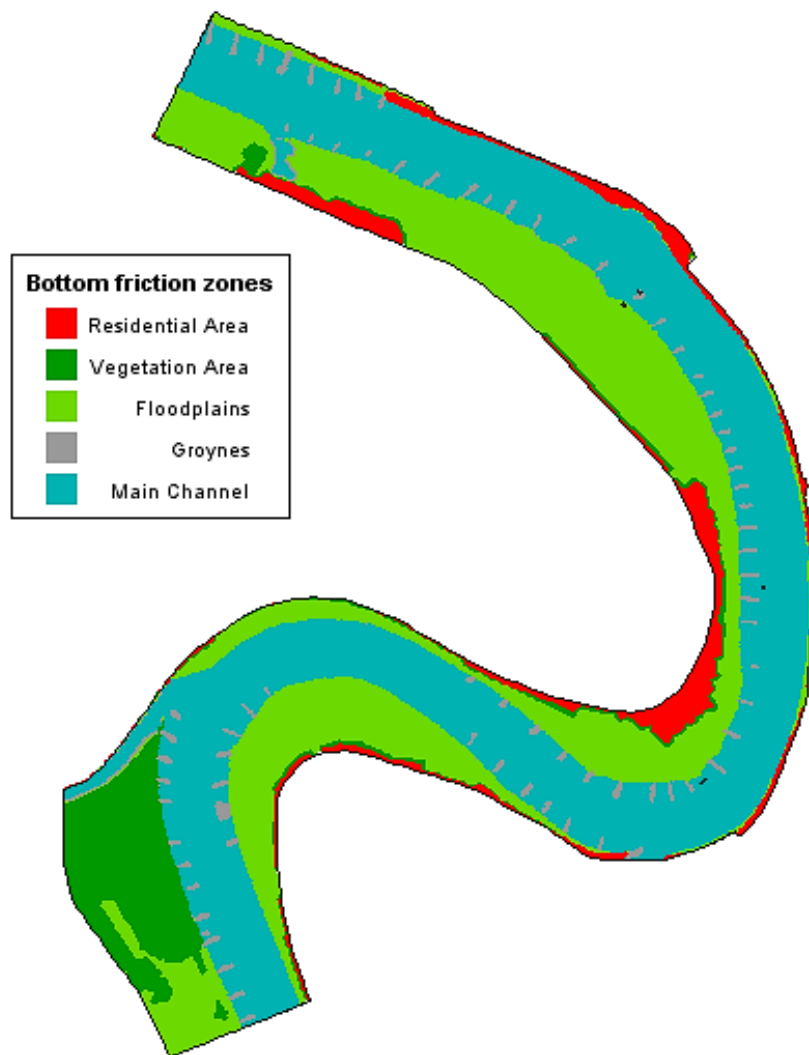


Figure 2.8: Friction zones of the lower Rhine model

Table 2.1: Roughness coefficients of different zones

Zones	Description	Nikuradse roughness factor (k_s)
K_1	Main channel	0.1
K_2	Floodplains	0.5
K_3	Groynes	0.3
K_4	Vegetation area	0.8
K_5	Residential area	1.0

Sedimentological data: The Sediment Data Bank of the BfG "SedDB" (www.geoportal.bafg.de) offers the possibility to get an overview of the data collected on the waterways and evaluated data of the soil samples, as well as impact and suspended matter measurements. It also provides direct access to the parameters recorded in a variety of measurement campaigns. Within the framework of the "Erfolgskontrolle Geschiebebewirtschaftung" (ECG), sampling is carried out on a regular basis (6 times per year) for the detection of the bed and suspended matter load at the sites of the lower Rhine. These data are subsequently entered into the SedDB. With the aid of the obtained knowledge, the grain distribution and its variation within the model range could be analyzed. Within the framework of the numerical investigations, a grain distribution averaged by the soil samples present in the model area was used.

With the help of the natural measurement data already from the SedDB, a mean initial grain distribution was established for the model area. This initial grain distribution, which is shown in the numerical model according to Figure 2.9 were divided into ten fractions as the basis for the subsequent study of different morphological and hydraulic parameters.

Morphological Factor: To ensure the comparability of the 2D models, these models are based on an identical mesh grid. As the 10 km long model with 41277 nodes requires a considerably large computational time, a new approach to reducing the computation time was implemented. Wurms and Schröder (2012) reduced the required computation time by approximately the same

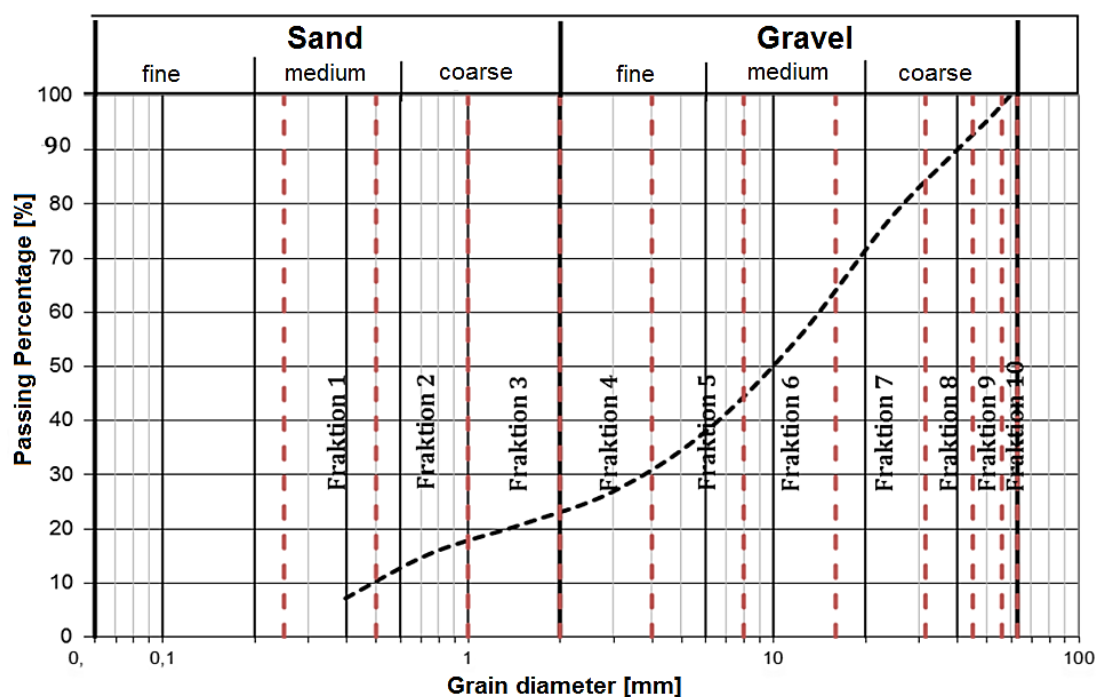


Figure 2.9: Sieve analysis curve of grains and the fractions

factor using the so-called morphological factor. The concept provides that the hydrograph is compressed and a factor, that falls between 2 to 10, simultaneously multiplies the transport rate. The results of the first attempts to implement this approach also in the "Neuss-Düsseldorf" model showed that deviations of up to 15% of the transport load occur in comparison to that of the original model with no factor (Backhaus, 2013). Therefore, the approach of the morphological factor is pursued further in this work.

Hydraulic Boundary Conditions: As the hydrodynamic boundary conditions, the discharge values are set at the upstream model edge (inlet edge) and the water level at the downstream model edge (outlet edge) in the control file. The inlet and outlet boundaries include the entire through-flow area (the river main channel as well as the floodplains). In the part of the inlet side, the two control structures in nature have been removed within the first 500 m. Due to this undisturbed starting range, possible numerical instabilities should be prevented, and the adjustment of a near-natural flow situation should be made possible.

An important hydrological variable for the bed-load transport and thus for the erosion phenomena is the discharge. This variable is determined for the boundaries of the investigation area via a so-called key curve that describes a functional relationship between the water level of the gauge Düsseldorf (Rhine-km 744.2) and the associated flow (See Figure 2.10). The hydrograph starts on 27th of June 2002 and finishes on the fifth of May, 2004. The discharge data at the inlet boundary were derived every one hour from the gauge located in Düsseldorf (See Figure 2.7). Then, these values have been delayed by minus 30 min, because the Düsseldorf gauge is situated approximately 5.7 km downstream of the inlet edge. The measurements at the Buderich station (Rhein-km 749.5) can calculate the connection between discharge and transport. The outlet water level data also originated from the 60 min values of the measurement location Buderich, which is located at about 5.3 km upstream of the outlet edge. The water level values are therefore shifted by plus 30min, and lowered down by 0.90 m (corresponds to a slope gradient of 0.17 ‰).

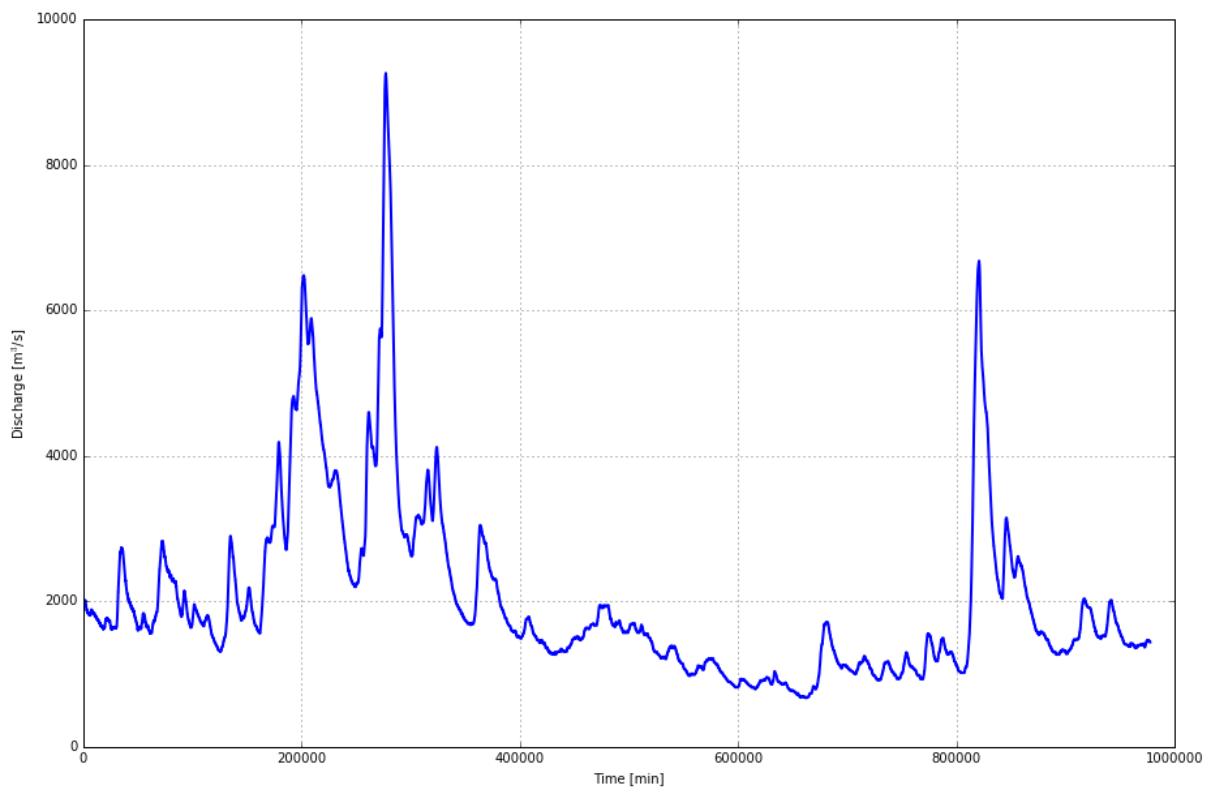


Figure 2.10: Inflow hydrograph of the lower Rhine model

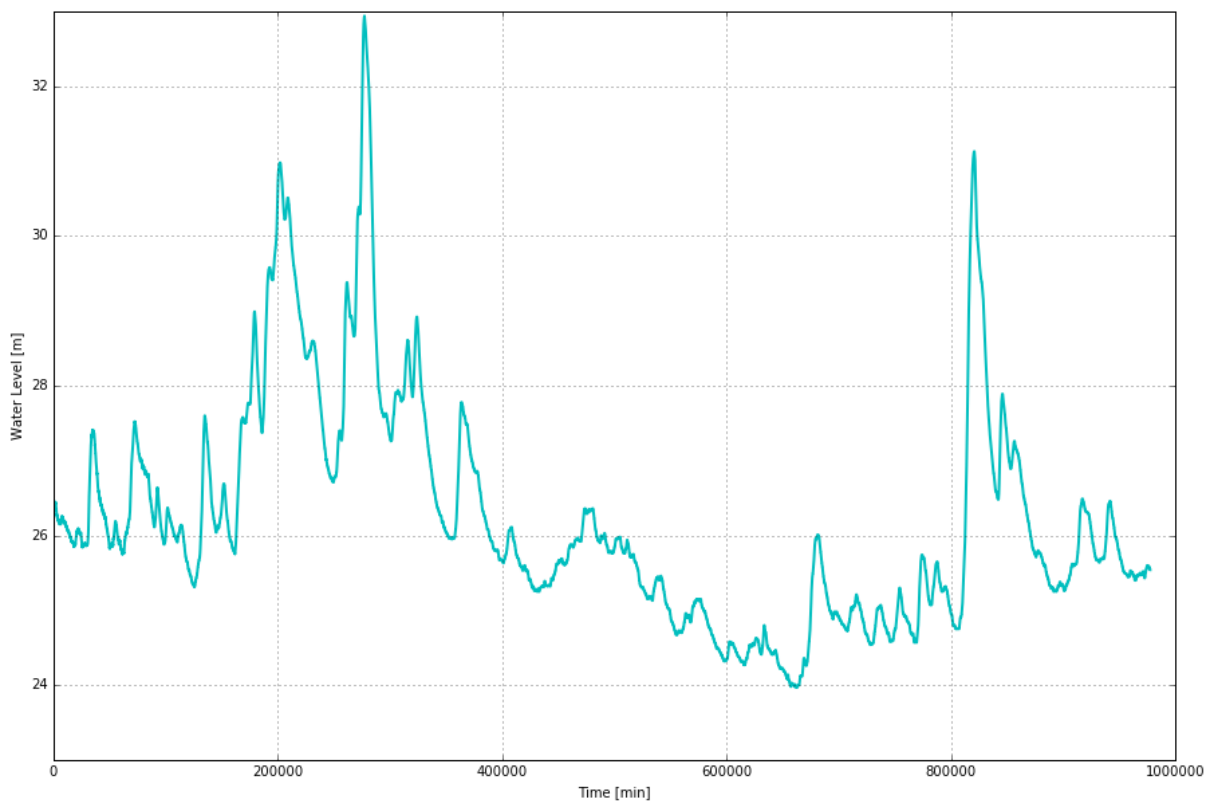


Figure 2.11: Outlet water level of the lower Rhine model

The hydrograph and water level, illustrated in Figure 2.10 and Figure 2.11 are compressed by a factor of four in time, to accelerate the simulation process (the real morphological values are received in one-hour period).

Morphodynamic Boundary condition: The definition of the morphodynamic boundary conditions occurs in the numerical model by assuming an equilibrium boundary condition at both model edges (inlet and outlet edge).

The inlet boundary was defined in such a way that only a bed-load entry occurs in the decisive bedload carrying region within the main river channel because the transport quantities via the floodplains are negligible and their detection in the model would lead to an overestimation of the bed-load entry. On the lower model margin, on the other hand, the morphodynamic boundary condition was determined according to the hydrodynamic boundary condition over the entire through-flow region.

Initial Conditions: A primary calculation was performed to calculate the *initial hydrodynamic conditions*. A stationary calculation was carried out from an unvarying initial water level. The hydrodynamic boundary conditions (inflow and water level) corresponded to the initial conditions of the actual calculation. The stationary result subsequently served as initial hydrodynamic conditions.

The determination of the *initial morphodynamic conditions* also took place using an initialization step. Assuming a uniform initial grain distribution within the entire model area, a morphodynamic simulation was carried out over two years (2000 to 2002) to allow an adaptation of the grain distribution to the local flow and transport processes. A uniform grain size distribution were used as initial distribution for the actual calculations.

Bed Evolution Measurements: For the hydro-morphodynamic calibration, hydraulic and morphological data were available over a period of two years. These data set give information on the river bed is given by the so-called "bed Eco-Sounding", which were available for the years 2000-2010 every two years. These elevation data, which have been measured for all hectometer profiles of the investigation area, serve as a basis for the linear interpolation of the vertical positions between the profiles.

The bed evolution from 2002 to 2004 is presented in Figure 2.12. The blue regions correspond to the eroded areas and the deposition zones are presented with red color. Comparing the measurements with every nodes in the unstructured grid of the numerical model is not useful, because the bed evolution at a specific place for a specific time can not be predicted. However, the mean bed level change is obtainable with a certain reliability. Hence, an average bed evolution for each 100 meters of river reach was taken into account.

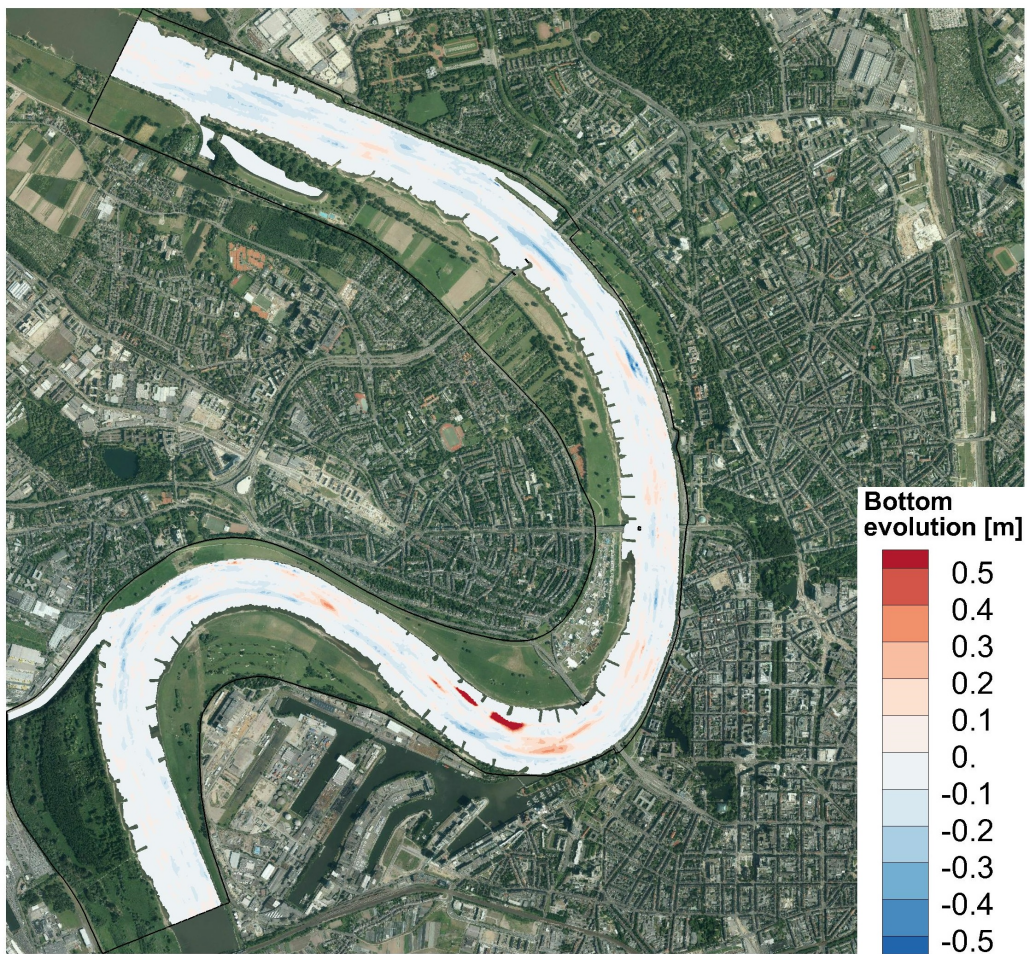


Figure 2.12: Bed evolution from 2002 to 2004 (Source of the aerial photo: WSV)

Each measurement point is in the center of a region, whose dimensions correspond to a length of 100 meters and the width of the river stretch. The measurement value is the river bottom elevation from which the averaged bed morphological evolution over the analogous area is computable. The averaged bed evolution for the calibration period (2002-2004) and for the validation period (2004-2006) are presented in Figure 2.13 and Figure 2.14, respectively. The x-axis show the distance from the inlet (Rhine-km 738.5)

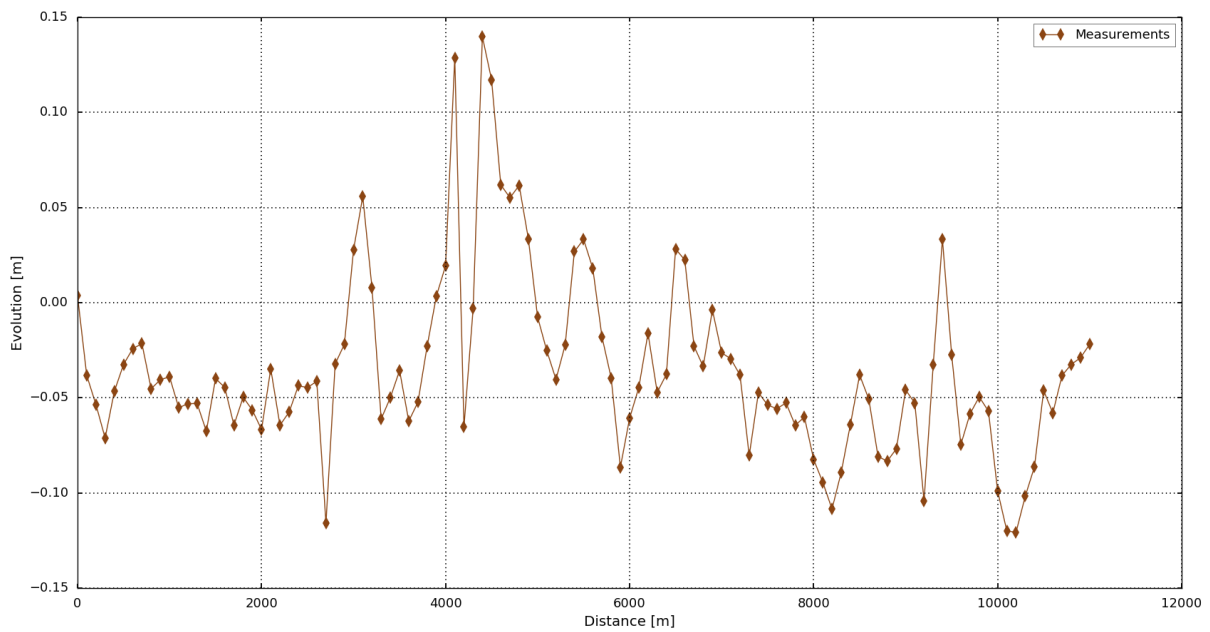


Figure 2.13: Averaged bed evolution from 2002 to 2004

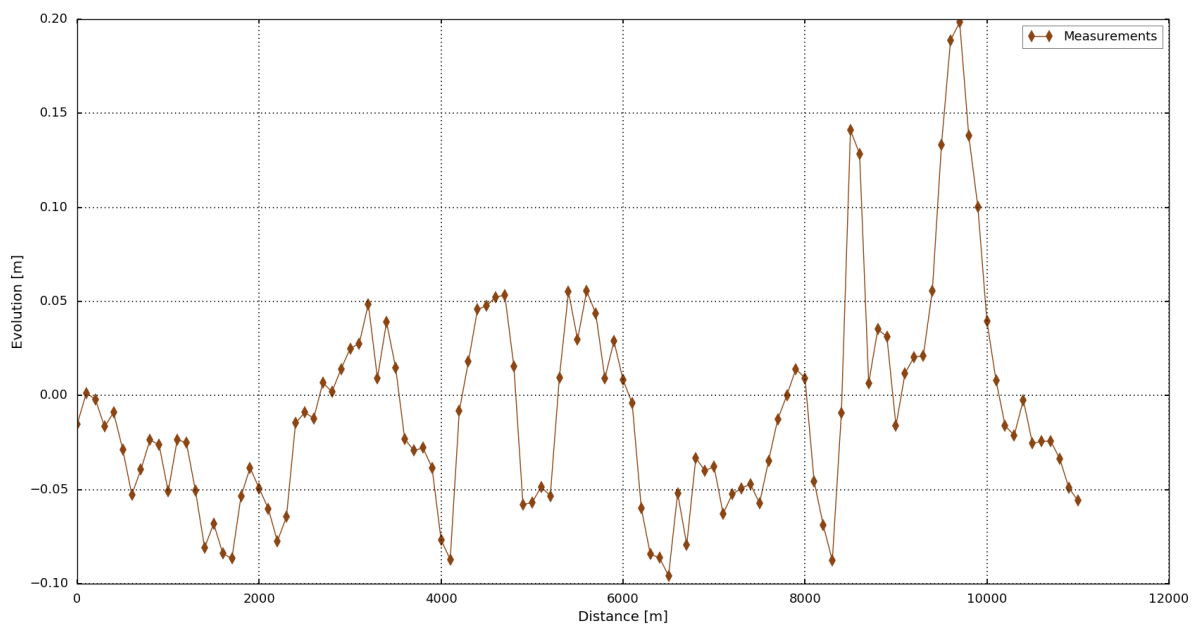


Figure 2.14: Averaged bed evolution from 2004 to 2006

Twin Experiment: A twin experiment (generated synthetic measurement data) is considered to verify the ability of the framework in ranking the competing morphological models (sediment transport variants in Telemac-2d-Sisyphé). For this purpose, we postulate certain calibration parameters and a "true" sediment equation and run the simulation. Subsequently, we accept the simulation result as the measurement to be used in the Bayesian selection framework. The goal is to infer if the framework can identify the best sediment formula and guide the user to the

presumed calibration parameters.

Bed Evolution Measurements: Since in the twin test, there is no restriction of data availability concerning the calibration and the validation processes, we divide the total simulation period into two intervals; namely, the calibration period and the validation period. The hydro-morphodynamic model of the lower Rhine with the variant of Wu equation was simulated for the duration of about 34 days. The intermediate bed morphological evolution (17 days), shown in Figure 2.15, is used as the measurements of the calibration process and the final output (after 34 days) is implemented in the validation scheme.

Similar to the real measurements, each observation point in Figure 2.15 and Figure 2.16 is located in the center of an area which dimensions correspond to a length of 100 meters and the width of the fairway stretch. The measurement value is the averaged bed morphological evolution over the analogous area.

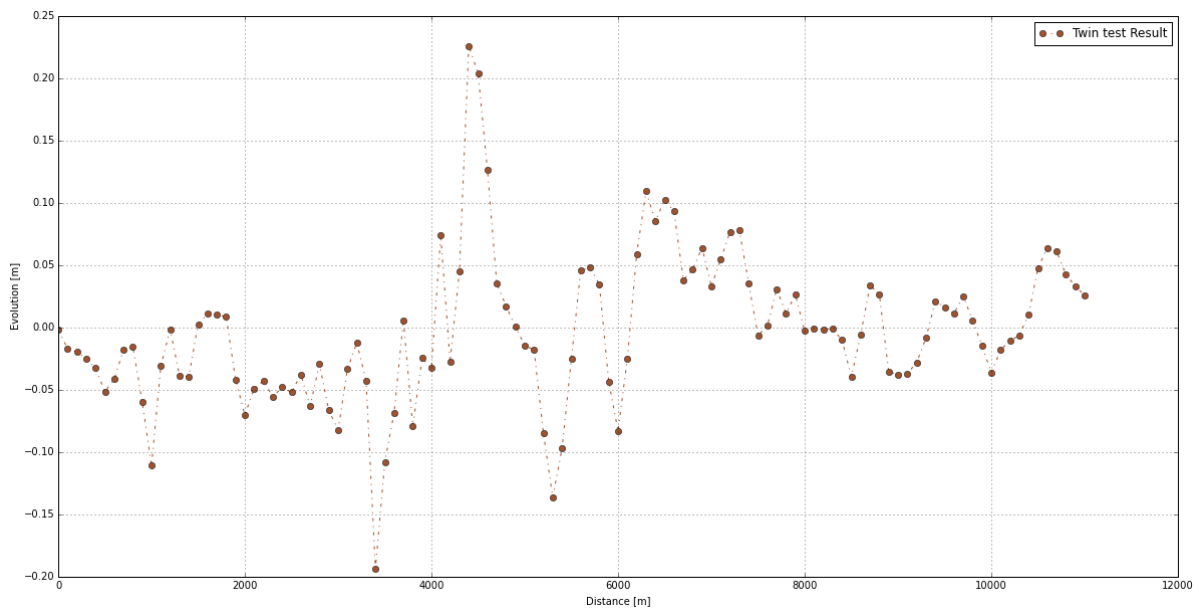


Figure 2.15: Synthetic bed evolution for calibration period

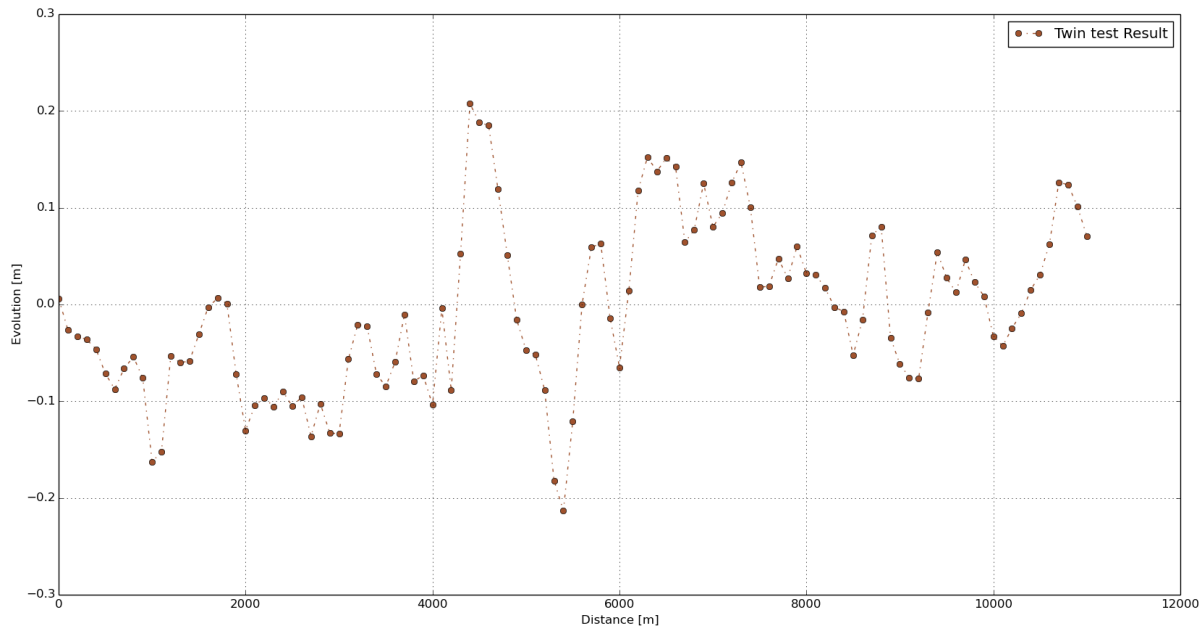


Figure 2.16: Synthetic bed evolution for validation period

2.5 Summary

This chapter introduced the description of the hydro-morphodynamic model (Telemac). All the equations and parameters necessary to compute the bed evolution have been mentioned in Section 2.1. Firstly, the shallow water equations derive the hydrodynamic conditions, and then the morphodynamic module calculate the sediment transport rate to be used for its final output, which is the bed evolution, calculated by Exner equation (Equation 2.4). Section 2.2 provided a detailed analysis of the selected sediment transport formulae in this study. Additionally, bed slope effect and secondary current effect modify the bed evolution. This procedure is repeated at every time step, and the coupling between the hydrodynamic (Telemac2d) and morphodynamic (Sisyphé) modules is also taken into account.

Two case tests have been described in this chapter. A test case model, based on an experiment done by Yen and Lee (1995) and a real river case study of the river Rhine. The channel bed model of Yen and Lee (1995) has been inspired by a laboratory experiment in a 180° channel bend to investigate bed topography and crosswise sediment sorting in a channel bend under unsteady flow conditions. The results of the physical experiment are the measurements of bed topographic evolution. The second case study is performed on a river model from the central reach of the Lower Rhine at Düsseldorf/Neuss (Rhine-km 739.0 to Rhine-km 749.0). The numerical model of the 10 km Rhine section has an unstructured, triangulated grid with 41277 nodes and 81684 elements and five different roughness zones.

3 Bayesian Model Selection Framework

The greatest challenge in the hydro-morphodynamic modeling is the selection of reliable and feasible models that can adequately describe real behaviors of surface flows and simultaneously account for uncertainty. To address this issue, the present thesis proposes a framework that provides objective guidance in model selection to assist even less experienced users in selection of the most suitable hydro-morphodynamic model by reducing the professional expertise required for manual calibration.

The current chapter presents the methods implemented in the proposed Bayesian Model Selection (BMS) framework. Bayesian model selection uses concepts of probability theory and numerical integration to obtain a model ranking. First, a stochastic model reduction techniques is discussed in Section 3.1. Moreover, the improvement method of this response surface is addressed in Section 3.2. Subsequently, Section 3.3 introduces the concept of Bayesian model selection based on the posterior distribution of sensitive parameters. This chapter finishes with a description of the properties of the BMS toolkit in Section 3.5, in which the fixed terms in different components of the framework are defined.

3.1 Surrogate Model Construction

Since required simulation results for such a framework is computationally expensive, a model of the outcome is considered instead. The model reduction is established using so-called surrogate models (response surface). This model shows the dependence of original model's output on the design variables via projections on the orthonormal polynomial basis. In other words, the surrogate model is a black box that simply reproduce the model outputs in a limited context and does not require to be acquainted with the internal properties of the original model. Hence, the response surface of a simple case may not represent the model with different conditions. This indicates that a trade-off between a wide context of applicability and large computational time is needed.

Consideration of alternative system representation significantly enhances the sureness of the modeler and reduces the potential bias in modeling. Even though building response surface is conceptually straightforward, it is known to be computationally demanding, because the statistical accuracy of their predictions relies on the number of considered realizations. Therefore, an alternative methodology, discussed in Section 3.1.1, is implemented, which requires only a few model evaluations to create a response surface.

3.1.1 Data-Driven Polynomial Chaos Expansions

The alternative approach for construction of a response surface is Polynomial Chaos Expansion (PCE). In general, all PCE techniques are efficient approximations and advanced approaches to statistical regression to exhibit the dependence of a model to alteration of variables via a response surface that is defined using an orthonormal polynomial basis in the parameter space (Li and Zhang, 2007). In other words, a high-dimensional polynomial approximately represents the reliance of model output on all related input parameters. The PCE offers an accurate high-order method of counting for nonlinear effects in stochastic analysis. One of the excellent characteristics of PCE is the high-order approximation of error propagation (Oladyshkin and Nowak, 2012a) along with its computational speed compared to Monte-Carlo method (Oladyshkin et al., 2011a).

The PCE methods postulate a correct knowledge of the probability density functions of all input parameters and they are optimal only if they are applied to a finite number of certain parametric probability distributions. However, the information regarding the statistical distribution of input parameters is, unfortunately, scarce, especially in environmental engineering and sciences (Red-Horse and Benjamin, 2004). Moreover, another source, which introduces new subjectivity into the analysis and may result in bias, is to build probability density functions of any particular shape from samples of limited size or scattered information. In a related application study (Oladyshkin et al., 2011b), the authors illustrate that new subjectivity in data interpretation could strictly affect uncertainty quantification and risk assessment, and thus lead to failure. Hence, there was a demand for further adaptation of the chaos expansion technique to a larger assortment of distributions.

Given the mentioned challenges, Oladyshkin and Nowak (2012b) present the generalization of PCE to arbitrary Polynomial Chaos (aPC) expansion that accommodates a broad spectrum of arbitrary distributions with arbitrary probability measures. The distributions not only can be either discrete, continuous, or discretized continuous, but they can also be delineated either analytically (as probability density/cumulative distribution functions), numerically as histograms

or as raw data sets. The aPC adjusts to arbitrary probability distribution shapes of input parameters and can even work with unidentified distribution forms when only a few statistical moments can be derived from limited data or expert judgment (Oladyshkin et al., 2011b; Oladyshkin and Nowak, 2012a).

Multi-dimensional aPC: Let us consider a stochastic process in the probability space (Ω, A, Γ) with space of events Ω , σ -algebra A , and probability measure Γ . The stochastic model is $Y = f(\omega)$ with multi-dimensional model input ω , i.e. $\omega = \{\xi_1, \xi_2, \dots, \xi_N\} \in \Omega$ and model output Y . Here, N is equal to the total number of input (uncertain) parameters. The model output Y can be expressed via a multivariate polynomial expansion (response surface) as follows:

$$Y(X, \omega) \approx \tilde{Y}(X, \omega) = \sum_{i=1}^P c_i(X) \phi_i(\omega). \quad (3.1)$$

Here, the coefficients c_i denote the reliance of the model output Y at the measurement location (X) on the input parameters $\xi_1, \xi_2, \dots, \xi_N$. The value P in Equation 3.1 depends on the total number of input parameters N and on the order of the expansion d according to the combinatory formula $P = (N+d)!/(N!d!)$. Moreover, the function ϕ_i illustrates the multi-variate orthogonal polynomial basis for $\xi_1, \xi_2, \dots, \xi_N$. Here, a surrogate model of first order is considered.

Assuming the independence of the input parameters, the multi-dimensional basis can be created as a simple product of the corresponding univariate polynomials:

$$\phi_i(\omega) \approx \prod_{j=1}^N P_j^{(\alpha_j^i)}(\omega), \quad (3.2)$$

$$\sum_{j=1}^N \alpha_j^i \leq M, \quad i = 1, \dots, N,$$

where α_j^i is a multivariate index that contains the combinatory information how to count all possible products of individual univariate basis functions. In fact, the index α can be seen as $P \times N$ matrix, which contains the corresponding degree (e.g. 0, 1, 2, etc.) for parameter number j in expansion term k .

The set of polynomials $\{P_j^{(0)}, \dots, P_j^{(d)}\}$ shapes an orthogonal basis of degree d in the space of parameter ω_j . Generally, the polynomial $P_j^{(k)}(\omega_j)$ of degree k in an individual parameter ω_j can be expressed as a simple linear combination of the different powers i of ω_j :

$$P_j^{(k)}(\omega_j) = \sum_{i=1}^P P_{i,j}^{(k)} \omega_j^i, \quad k = 0, \dots, d, \quad j = 0, \dots, N, \quad (3.3)$$

where $P_{i,j}^{(k)}$ is the coefficient for the power $i = 0, \dots, k$ within the polynomial $P_j^{(k)}(\omega_j)$.

According to Oladyshkin et al. (2013), an orthogonal polynomial basis can be defined for any arbitrary polynomial measures, as ω_j has finite statistical moments, such as mean, variance, skewness, etc. up to order $2d - 1$.

The following relation defines the $P_j^{(k)}$ coefficients within the basis polynomial in Equation 3.3:

$$\begin{bmatrix} \mu_{(0,j)} & \mu_{(1,j)} & \cdots & \mu_{(k,j)} \\ \mu_{(1,j)} & \mu_{(2,j)} & \cdots & \mu_{(k+1,j)} \\ \vdots & \vdots & \cdots & \vdots \\ \mu_{(k-1,j)} & \mu_{(k,j)} & \cdots & \mu_{(2k-1,j)} \\ 0 & 0 & \cdots & 1 \end{bmatrix} \begin{bmatrix} P_{0,j}^{(k)} \\ P_{1,j}^{(k)} \\ \vdots \\ P_{k-1,j}^{(k)} \\ P_{k,j}^{(k)} \end{bmatrix} = \begin{bmatrix} 0 \\ 0 \\ \vdots \\ 0 \\ 1 \end{bmatrix}, \quad (3.4)$$

where $\mu_{(k,j)}$ denotes the i th non-central (raw) statistical moments of the random variable ω_j . It is apparent from Equation 3.4 that statistical moments are the sole source of information needed about the input distributions and propagated in all polynomial expansion-based stochastic approaches (Oladyshkin and Nowak, 2012a). In the current study, an orthonormal basis is taken into account.

3.1.2 Collocation Method

There are many different methods to compute the unknown coefficients $c_i(X)$ of the expansion in Equation 3.1. The objective of the available methods is to derive $c_i(X)$ from the weighted residual minimization or projection point of view. In this study, the non-intrusive Probabilistic Collocation Method (PCM) is applied because it does not enforce any rearrangement, or simplification on the initial flow model, i.e. no change in the system of the governing equations. In other words, this approach can consider any simulation model as a black-box, that means the commercial software can be used without any modifications required. The fundamental conception of this method was presented by Villadsen and Michelsen (1978).

Collocation Approach and Formulation: The main idea of the collocation method is to match the unknown coefficients c_i to model outputs Y_i evaluated with different parameters sets ω_j . A given N -dimensional set of parameters ω_j is named as a collocation point in the multidimensional parameter space. The number of collocation points ω_j is equal to the number P of unknown coefficients c_i in the formulated chaos expansion in Equation 3.1. It requires P (from combinatory formula) model evaluations in total, which leads to the following:

$$M_{\Phi}(\omega)V_c(X) = V_Y(X), \quad (3.5)$$

where V_c is the $P \times 1$ vector of unknown coefficients c_i , V_Y is the $P \times 1$ vector holding the model output $Y_i(\omega_i)$ for each collocation point ω_i , and the $P \times P$ matrix M_{Φ} contains the P Hermite

polynomials $H_j(\omega_i)$ evaluated at the P collocation points. It is worth mentioning that the matrix $M_\Phi(\omega)$ is space- and time-independent and can be produced once for the given expansion degree and parameter number, whereas the $V_c(X)$ vectors and $V_Y(X)$ are space- and time-dependent.

Selection of Collocation Points: The efficiency of PCM strongly (the solution $V_c(X)$ in Equation 3.5) rests on the selection of collocation points (Li and Zhang, 2007). Villadsen and Michelsen (1978) assert in their book that the best selection of collocation points agrees with the roots of the polynomial of one degree higher than the order considered in the chaos expansion. Thus, the resulting polynomial surface is precise at the collocation points and applies a polynomial interpolation or extrapolation on interior and exterior of the domain with collocation points, respectively. Moreover, the number of available points in the multi-dimensional case, is larger than the required number of collocation points. Therefore, a principal strategy for the selection of collocation points must be considered from the available strategies, which are as follows: (I) totally random and (II) selection based on the distribution of the input parameters. In this study, the second option is implemented. The focus is on the best estimation of the mean stochastic characteristics and hence, the selection of the collocation points from the most plausible section of the input parameters' distributions.

The scheme used in this study, which is analogous to Gaussian quadrature, entails selecting the collocation points from the roots of the next higher order orthogonal polynomial for each uncertain parameter at a given order of polynomials. These points are the ones from which we derive the approximation of the real model via a response surface (see e.g. Villadsen and Michelsen (1978); Webster et al. (1996); Tatang et al. (1997)).

Let us consider the polynomial order is d , then the number of available collocation points is $(d + 1)^N$, which is continuously greater than the required number of collocation points. For example, in case of the first-order PCM, the P sets of collocation points; denoted as $(\xi_{1,1}, \xi_{2,1}, \dots, \xi_{N,1}), (\xi_{1,2}, \xi_{2,2}, \dots, \xi_{N,2}), \dots, (\xi_{1,P}, \xi_{2,P}, \dots, \xi_{N,P})$, are essential. They are selected from all the combinations of the two roots of the second-order Hermite polynomial.

Here we show how to make the selection of the P sets of collocation points. The first set of collocation point always contains the roots with the highest probability for each random variable. Note that we sort the roots based on closeness to the mean value in the case of uniform probability. The other sets of collocation points are picked by maintaining as many of the variables with high probability as possible (Li and Zhang, 2007). The P sets of collocation points for a given type of polynomial chaos of known N and d are independent of physical problems at hand. As for integration points in Gaussian quadrature, the selection of collocation points only must be done once and can, henceforth, be arranged in advance.

Since the polynomial chaos expansion is a black box model, Webster et al. (1996) suggest the

consideration of a linear approximation as a first guess for the response surface. Therefore, a linear response surface is considered to approximate the model throughout this study.

Post-processing computations: When the coefficients have been estimated, the polynomials in Equation 3.1 can represent the initial model. This procedure implies that the computational cost of evaluating different statistical quantities is significantly reduced.

Each model output $Y(X)$ has its own response surface, and consequently its coefficients in space and the mean value of the output $Y(X)$ can be represented via coefficient $c_1(X)$. The following expression calculates the variance.

$$\sigma_Y^2(X) = \sum_{i=2}^P c_i^2(X) . \quad (3.6)$$

Monte Carlo simulation can be directly performed on the constructed polynomial to evaluate more complex statistical quantities. By doing so, the probability density function and cumulative distribution function of the model output can be readily obtained.

3.2 Bayesian Updating of Surrogate Model

The aPC method presented in Section 3.1 builds a response surface; also known as surrogate model $\tilde{Y}(\omega)$, that approximates the original simulation model $Y(\omega)$. In fact, this reduced model is exceptionally faster than the original model, because the reduced model is solely a polynomial and has functional properties owing to the orthogonal basis. Once a surrogate model has been created, inverse modeling (also known as history matching) to the available observations becomes an exceptionally significant subject to enhance the model quality. The reliability of history matching, however, increases with the number of available observations.

Conventionally, an iterative manual approach of trial and error is implemented to adjust the simulation models to reproduce past measurements in the field of river engineering. However, such a manual process requires a remarkably sound expertise of the investigation's processes. Moreover, the non-trivial and non-linear relations of the matched parameters within the model can significantly complicate the history matching process (Oliver et al., 2001).

Another important issue regarding history matching methods is that they can yield non-unique solutions (Oliver et al., 2008), i.e. several simulated models and parameter sets can fit the observation data similarly well. Nevertheless, stochastic approaches can deal with such type of uncertainty arising during the matching process without the necessity to limit the parameter space artificially. In fact, their outputs are a probability distribution of possible parameters

sets instead of a single best parameter set. However, stochastic approaches are more expensive than classical optimization-based calibration methods, as they need to examine the full range of possible model results with numerous model runs.

Methods based on response surfaces or other surrogate models have recently been integrated with more precise forms of Bayesian updating that apply Bayesian theory (see e.g. Smith and Geffland (1992)) in practice for model updating and forecasting. In the current section, a fully accurate Bayesian updating is implemented to match the response surface $\tilde{Y}(\omega)$ to available measurements in a data vector y_o of past or real-time observations of system behavior. This approach not only provides the essential flexibility to deal with arbitrary distributions of model parameters, including high-order statistical moments, but it can also handle the conditional parameter distributions that occur after Bayesian updating. In addition, Bootstrap filtering is the most direct yet straightforward numerical implementation of Bayes theorem, which can consider arbitrary non-linear model equations and arbitrary distribution forms as opposed to (Ensemble) Kalman Filters (Evensen, 2009). Henceforth, Bootstrap filtering is a suitable match for combination with the aPC technique.

3.2.1 Bayesian Updating

In this Section, Bayesian updating via weighted bootstrap (see e.g. Smith and Geffland (1992)) is applied to fit the surrogate model $\tilde{Y}(\omega)$ to available measurements in a data vector y_o past observations of system behavior. According to Bayes and Price (1763), Bayes' theorem is defined as follows:

$$f(\omega|y_o) = \frac{f(y_o|\omega)f(\omega)}{f(y_o)}, \quad (3.7)$$

where $f(\omega)$ denotes the joint prior PDF for the vector of model parameters ω , $f(y_o)$ is the prior probability of y_o , used as normalization constant, $f(y_o|\omega)$ is the conditional PDF of y for given ω , i.e., the likelihood of the parameters, and $f(\omega|y_o)$ is the conditional PDF of ω for given y_o , which is intended to be approximated rapidly and precisely. Bay's theorem (Equation 3.7) can be rewritten the following expression:

$$p(\Theta_k|M_k, y_o) = \frac{p(y_o|M_k, \Theta_k)p(\Theta_k|M_k)}{p(y_o|M_k)}, \quad (3.8)$$

where $p(y_o|M_k)$ represents a model-specific normalizing constant for the posterior of the parameters (Θ) , $p(\Theta_k|M_k, y_o)$.

To set up the Monte Carlo framework for calibration and model ranking, we have produced a set of predictions based on N_{MC} random realizations of parameters for each competing model. These realizations were drawn from uniform priors $p(\theta_k|M_k)$ of uncertain parameters.

On the common assumption that the measurement errors are independent and have Gaussian distribution, the likelihood function $p(y_o|M_k, \Theta_k)$ is defined as following:

$$p(y_o|M_k, \Theta_k) = 2\pi^{-N_s/2} |R'|^{\frac{1}{2}} \exp \left[-\frac{1}{2} (y_o - \tilde{Y}(\Theta_k))^T R^{-1} (y_o - \tilde{Y}(\Theta_k)) \right], \quad (3.9)$$

where R is the diagonal (co)variance matrix of size $N_s \times N_s$ (N_s refers to the length of the measurement dataset) with standard deviation of measurement error (ε). Though other arbitrary error distributions could be considered, the assumption on the measurement error distribution remains throughout the study.

Likelihood weights are assigned to each realization of Θ_k using Equation 3.9. To update the surrogate model $\tilde{Y}(\Theta_k)$ (or $\tilde{Y}(\omega)$) through an iterative procedure, the realization Θ_k with the highest probability (likelihood) is chosen and the original (hydro-morphodynamic model in Telemac-2d-Sisyphé) is executed. The result of this run, then, is used as new information for reconstructing the response surfaces at the measurement locations.

When the prior information is far from the reality, it is likely that the surrogate model is highly imprecise and produces wrong outcomes. This imprecision stems from the fundamental principle of all chaos expansion methods that the approximation error is the lowest where the highest (prior) probability density occurs, that means significant errors may befall in less probable regions. Avoiding this, an advanced iterative approach for aPC-based Bayesian updating is considered that allows performing updating task even where the prior assumptions on model parameters are offset from the reality. In this method, the response surface is reiterated to become more precise in the relevant areas of high posterior probability.

3.2.2 Bootstrap Filtering

Likelihood weights, which represents the probability of the parameter set being able to reproduce the measurements, have assigned to the samples from the prior distribution of parameters (realizations) using Equation 3.9. In bootstrap filtering (also known as rejection sampling), the purpose is to filter poorly performed realizations. It accommodates the quantification of the post-calibration parameter and the predictive uncertainty and is more accurate than ensemble Kalman filtering or linearized methods, as stated in Oladyshkin et al. (2013). To do so, a number N_p of realizations of parameter vectors $\Theta_{k,i}$ are drawn from the prior PDF $p(\Theta_k|M_k)$:

$$\Theta_{(k,i)} \sim p(\Theta_k|M_k), \quad i = (\overline{1, N_p}), \quad (3.10)$$

where N_p is an adequately large number. Additionally, assigning relative importance weights w_i to each realization $\Theta_{(k,i)}$ by the following expression:

$$w_i = \frac{p(y_o|M_k, \Theta_{k,i})}{\max\{p(y_o|M_k, \Theta_{k,i})\}}, \quad (3.11)$$

where $\max\{p(y_o|M_k, \Theta_{k,i})\}$ is the biggest individual values $p(y_o|M_k, \Theta_{k,i})$ available over all realizations $i = (1, N_p)$.

Then, realization $\Theta_{k,i}$ is acknowledged as a valid ensemble member of the posterior distribution, if $w_i \geq u_i$ is satisfied for a random number u_i drawn from the uniform distribution in the interval of $(0, 1)$.

Weight disproportion, which leads to weight collapse, is a typical issue encountered in the filtering schemes; however, including a resampling step can mitigate this problem. This step can be considered before the second filtration (filtration of the prior distribution for validation), where it is likely that no realization remains after the first filtration. Note that the posterior distributions of uncertain parameters are considered as prior knowledge of parameters for the validation process.

Sample Enlargement: In the bootstrap filtering step, the particles with negligible weights are removed from the prior distributions of uncertain parameters. Then, the objective of this step is to enlarge the parameter set in the proximity of the remaining particles that possess higher likelihood weights.

In this case, Kernel Density Estimation (KDE) method to estimate probability density function of a random variable is used as the basis for drawing new samples of random numbers. In this scheme, a small amount of zero-centered random noise is added onto each observation.

3.3 Bayesian Model Selection

In this section, a statistical framework, called Bayesian selection that can provide objective guidance in model selection is explained. This framework ranks the plausibility of competing models according to Bayes' theorem. Bayesian Model Averaging (BMA) (see Draper (1995); Hoeting et al. (1999)) is a formal statistical approach with remarkable features. These features are included but not limited to allowing the user to compare alternative conceptual models, to test their adequacy, combine their forecasts into a more robust output estimation, and quantify the contribution of conceptual uncertainty to the general prediction uncertainty (Schöniger et al., 2014). An updated posterior model parameters' probabilities from the corresponding

prior beliefs are used as model weights for ranking of the competing models. These posterior probabilities are based on the ability of each model in reproducing the measurement data.

According to Schöniger et al. (2014), BMA implicitly follows the principle of parsimony or Occam's razor, in which the posterior model weights indicate an optimal trade-off between model goodness of fit and complexity. Hence, it plays a significant role in the quantification of model prediction uncertainty, which reinforces the foundation for managerial purposes and risk assessment. BMA ranks competing models without averaging them. Therefore, Bayesian selection will be used in the following section to avoid any confusion.

3.3.1 Bayesian Selection

In this section, the formulation of the Bayesian selection is presented according to Hoeting et al. (1999). Let us consider N_m credible, competing models M_k . The posterior predictive distribution of a desired realization Θ_k given the vector of observed data y_0 can be expressed as:

$$p(\Theta_k|y_0) = \sum_{k=1}^{N_m} p(\Theta_k|y_0, M_k)P(M_k|y_0), \quad (3.12)$$

with $p(\Theta_k|y_0, M_k)$ representing a conditional probability distribution and $P(M_k|y_0)$ being discrete posterior model weights.

In Bayes' theorem, the model weights can be calculated by:

$$P(M_k|y_0) = \frac{p(y_0|M_k)P(M_k)}{\sum_{i=1}^{N_m} p(y_0|M_i)P(M_i)}, \quad (3.13)$$

where $P(M_k)$ is subjective credibility of model M_k accounting for its plausibility in the set of models before any observed data have been considered. In Hoeting et al. (1999), the authors state that a "reasonable and neutral choice" for the choice of $P(M_k)$ could be equally likely priors $P(M_k) = 1/N_m$, where little prior knowledge about the advantages of the different models under investigation exists. In this study, subjective credibility of each model follows the assumption of equally likely priors of $P(M_k) = 1/N_m$. The denominator in Equation 3.13 normalizes all model weights by a normalizing constant of the posterior distribution of the models.

In Equation 3.13, $p(y_0|M_k)$ quantifies the BME term, also referred to as marginal likelihood or prior predictive of the observed data based on the prior distribution of the parameters (Kass and Raftery, 1995):

$$p(y_0|M_k) = \int_{\Omega_k} p(y_0|M_k, \Theta_k)p(\Theta|M_k)d\Theta_k, \quad (3.14)$$

where Θ_k denotes the vector of parameters of model M_k with a dimension equal to the number of parameters $N_{(p,k)}$, Ω_k is the corresponding parameter space, $p(y_0|M_k, \Theta_k)$ is the likelihood of

a realization of the model M_k to have produced the observed data set y_o (calculated by Equation 3.9) and $p(\Theta|M_k)$ represents their prior distribution of each model. To rank the competing models, if $p(y_o|M_k)$ is computed under the assumption of equal model priors ($P(M_k) = 1/N_m$), the model that maximizes marginal likelihood is the one with the highest probability of being the "true" given observed data.

The BME term can either be assessed by integration over the full parameter space Ω_k (Equation 3.14, mentioned in Kass and Raftery (1995) as Bayesian integral, or by the posterior probability distribution of the parameters $p(\Theta_k|M_k, y_o)$ via rewriting Bayes' theorem (Equation 3.8) with respect to the parameter distribution instead of model distribution.

Generally, three approaches exist for solving Equation 3.14; namely *Analytical Evaluation*, *Mathematical Evaluation* and *Numerical Evaluation*. The first method can be considered under strongly limiting assumptions, whereas the other two approaches are more preferable. A full description of all three methods can be found in Schöniger et al. (2014). They conducted a thorough comparison of nine ways to assess Bayesian model evidence. In the present study, the focus is on the numerical evaluation approach in the computation of the BME.

Numerical Evaluation: Evans and Swartz (1995) offers a rigorous review of numerical methods to assess the Bayesian integral (Equation 3.14). They stated that traditional integration schemes; e.g. adaptive Gaussian quadrature, are the algorithms of choice for low-dimensional applications. Another review on strengths and limitations of numerical methods that can also be applied to highly complex models is given by Schöniger et al. (2014).

In this thesis, *Simple Monte Carlo integration* (Hammersley, 1960) is considered. According to Schöniger et al. (2014), this method is the most suitable approach since it is bias-free and dispense with any assumptions on the shape of the parameter distribution. This approach evaluates the integrand at randomly chosen points in parameter space ($\Theta_{(k,i)}$), which are randomly drawn from their prior distribution $p(\Theta_k|M_k)$. The Bayesian integral (or expected value over parameter space) in Equation 3.14 is then determined as the mean value of the evaluated likelihoods calculated by Equation 3.9 (also referred to as arithmetic mean approach):

$$p(y_o|M_k) = \frac{1}{N_P} \sum_{i=1}^{N_P} p(y_o|M_k, \Theta_{k,i}), \quad (3.15)$$

with N_P representing the number of Monte Carlo (MC) realizations and $p(M_k, \Theta_{k,i}|y_o)$ denoting the conditional PDF of y for given realization $\Theta_{(k,i)}$ for model M_k .

Schöniger et al. (2014) point out: "For large ensemble sizes N_p and a friendly overlap of the parameter prior and the likelihood function, this method will provide very accurate results. For high dimensional parameter spaces, however, a sufficient (converging) ensemble might come at a high or even prohibitive computational cost."

3.4 Properties of BMS Framework

The procedure mentioned in the previous sections is repeated for all the competing models to produce a ranking using the BME values. In the subsequent section, the terms and the inputs that will be utilized in the toolkit are addressed.

Measurement Error: Measurement errors can be subdivided into two components, namely random error, and systematic error. Random errors are errors in measurement that results in inconsistency of the measurable values when various measures of an unchanging attribute or quantity are taken. However, Systematic error is also known as a nonzero mean error, because its effect is not diminished when observations are averaged. These errors are not determined accidentally but are introduced by an inherent observation inaccuracy in the system. The measurement error in Equation 3.9 needs to be defined by the user. This value can be described as a desired criterion for calculation of likelihood weights based on the proximity of their simulated value to the measurements using the response surface.

Uncertain Parameters: As discussed in Section 1.5, many morphodynamic models include empirical formulations, i.e. their formulations consist of experimentally determined variables and coefficients based on limited available datasets. These datasets were mostly from controlled experiments or real data from rivers but under certain conditions, which might not include the actual situations in nature. Therefore, the presented framework incorporates uncertain parameters, which the user categorizes as uncertain.

Prior Knowledge of Uncertain Parameters: In optimization schemes, it is likely that wrong prior knowledge about the selected sensitive parameters hinders the optimization procedure, and navigate us to less probable scenarios. As mentioned before, the framework is attuned to any assumption on the bounds and distribution of chosen parameters.

Sample Size: This term refers to the number of the prior parameter sets or realizations that significantly contribute to the posterior distribution. These realizations receive likelihood weights after the construction of the surrogate models.

Iteration: The sole objective of the iteration on the improvement of response surface (surrogate model) is to adjust these models to the observed bed evolutions. In each iteration, new information acquired from the previous response surface is included in the adjustment process.

Stochastic Calibration: The calibration is conducted by simulating the hydro-morphodynamic models in the Telemac-2d-Sisyphe, using the best parameter set that possesses the largest likelihood.

Stochastic Validation: The validation process also follows the same routine of stochastic calibration. Note that the stochastic approach in calibration and validation is not similar to that of river engineering, i.e. the surrogate model remains the same as constructed in calibration stage, but the calibrated parameter set may vary in the validation step.

Table 3.1 presents the user defined inputs required for the BMS Toolkit. All the inputs of each case study will be presented in their associated sections in Chapter 4 and Chapter 5.

Table 3.1: The description of BMS toolkit's inputs

Name of inputs	Remark(s)
Monte-Carlo size	Total number of the realizations
Uncertain parameters	Uncertain parameters must exist in all competing models.
Parameter ranges	Lower and upper bound of parameters must be meaningful.
Measurement error	Criterion for weighting the realizations
No. of iterations	Number of the modifications of the initial surrogate model

3.5 Summary

This chapter presented the methods implemented in the proposed Bayesian framework for model selection. Figure 3.1 shows a summary of the research methodology.

The framework is composed of three main steps. In step 1, a mathematically optimal response surface approximates each hydro-morphodynamic model's outputs through the aPC technique. The response surfaces are constructed at all observation points. Afterward, likelihood weights is assigned to each parameter set based on the closeness of the response surfaces to the observation points.

Step 2 entails matching the reduced model from the previous step to the observation data using iterations. Here, the aim is to improve the response surfaces by including the parameter set with the highest importance index to the sets of collocation points to rebuild the response surfaces and reassign the likelihoods to get the posterior distributions of realizations. Further, this step contains bootstrap filtering. With this method, realizations with lower likelihoods comparing to the other sets are discarded. The probability density distribution of the filtered posterior parameter sets can be used for any inferences of the most probable region of calibration parameters for further task of optimization.

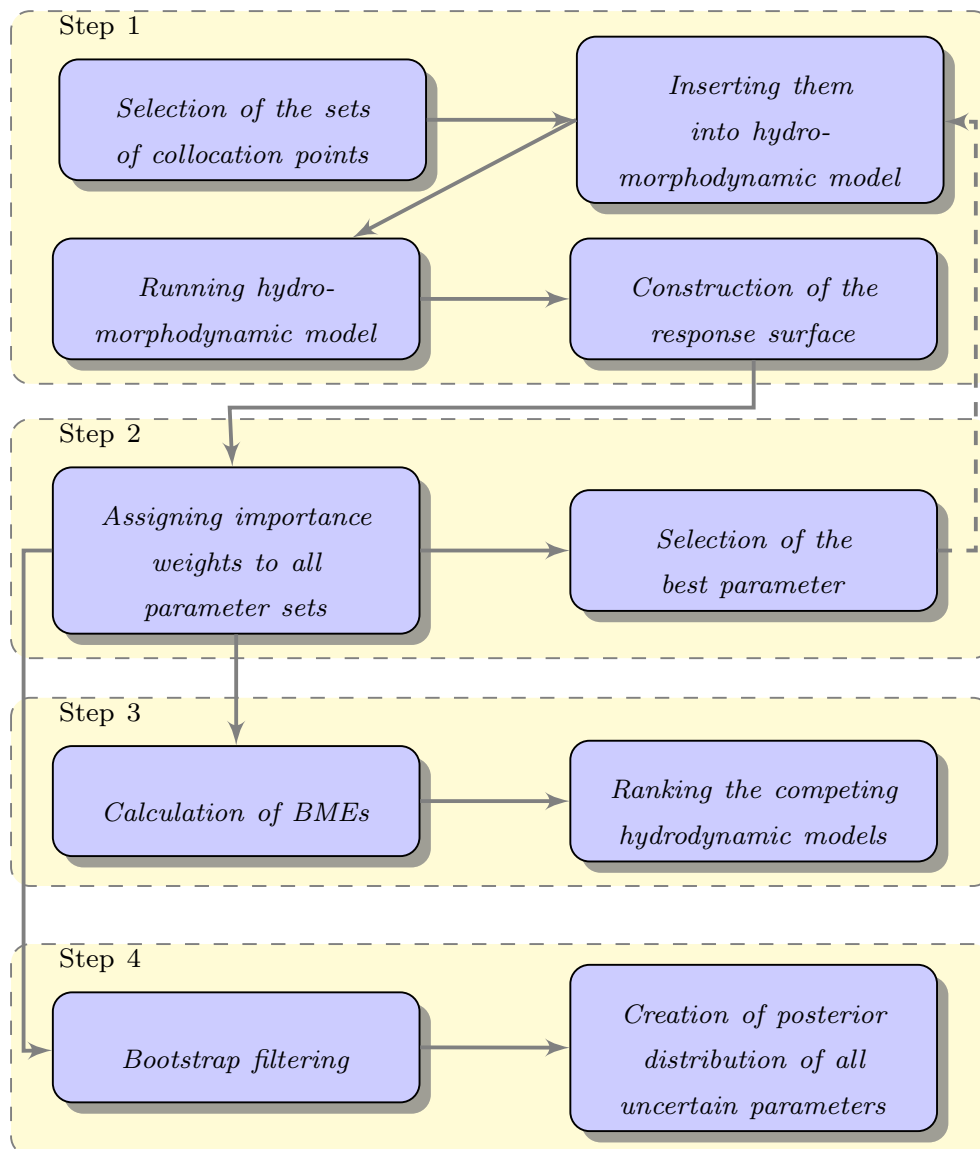


Figure 3.1: Research methodology flowchart

Step 3 consists of calculation of the Bayesian Model Evidence (BME). From the resulting posteriors in step 2 that provides a comprehensible post data summary of the residual uncertainty, BME value of each model is calculated.

The procedure mentioned above is repeated for all the competing models to produce the ranking. With this combination, a statistical method for model selection is obtained that is accurate, yet has an acceptable computational speed that is sufficient to be implemented in the real-time application.

4 Bayesian Model Selection for Channel Bend Experiment

The abundance of the existing morphodynamic models hinders the model selection for less experienced engineers. To eliminate the problem in selection of hydro-morphodynamic models, the proposed Bayesian Model Selection (BMS) framework presented in this study intends to serve as guidance in the model selection of the hydro-morphodynamic models. This proposed approach can also suggest the most likely region of uncertain parameters for the task of history matching.

Assessing the performance of the BMS framework, it was first implemented in the hydro-morphodynamic numerical model for the channel bend from Yen and Lee (1995). The following chapter begins with the setup and implementation of Channel Bend test case in the framework (Section 4.1). Subsequently, the results of the BMS in the model selection of the hydro-morphodynamic model of the Yen and Lee's experiment are demonstrated in Section 4.2. Lastly, Section 4.3 includes the uncertainty analysis of the BMS for the same test case.

4.1 Setup and Implementation

The geometry, initial conditions and all relevant information of the channel bend model have been explained in detail in Section 2.3. All the considered morphodynamic models, uncertain parameters and their selected ranges, stochastic calibration and validation scenarios, and other BMS toolkit's inputs are subsequently summarized.

Examined Hydro-Morphodynamic Models: In Sisyphé module, the volume of the sediment transport (bed-load) per unit width (Q_b) in Exner Equation (Equation 2.4) is computed via different bed load transport formulae, i.e. different hydro-morphodynamic models when coupled with Telemac-2D.

The selected formulae in the current test case is summarized in Table 4.1. More details about

each formula and the conditions and assumptions under which they have been developed were discussed in Section 2.2.

Table 4.1: The morphodynamic models used in the test case of channel bend

Name of the bed load Equation	Year	Mode of Transport
Meyer-Peter-Müller	1948	Bed-load
Einstein-Brown	1950	Bed-load
Modified Engelund-Hansen	1980	Total-load
Van Rijn	1984	Bed-load
Wu	2000	Bed-load

Chosen Uncertain Parameters and their Bounds: Under the assumption of insufficient knowledge on the distribution of the selected uncertain parameters, the uniform distributions were preferred for all parameters. Moreover, the bounds were introduced to coincide with mostly physically meaningful parameter limits. The selected hydro-morphological parameters and the corresponding ranges are shown in Table 4.2.

Table 4.2: The selected uncertain parameters and their ranges (channel bend)

ID	Uncertain Parameter's Name	Lower Bound	Upper Bound	Unit
P ₁	Sediment diameter	0.00095	0.00115	m
P ₂	Friction Coefficient	0.0024	0.0036	m
P ₃	Roughness Coefficient of Boundaries	0.001	0.006	m
P ₄	Ratio Between Skin Friction and Mean Diameter	1.00	6.00	-
P ₅	Non-Cohesive Bed Porosity	0.25	0.50	-
P ₆	Parameter For Deviation	0.20	2.20	-
P ₇	Beta	0.85	4.00	-
P ₈	Secondary Currents Alpha Coefficient	0.75	1.00	-
P ₉	Shield's Parameter	0.030	0.055	-

Measurement Error, Sample Size and number of Iterations: The measurement error, in this case, was selected as 0.08. The reference Bayesian Model Evidence (BME) value for each model was determined by MC integration (Equation 3.13) over ensembles of 150,000 realizations per model. Moreover, the iteration via Bayesian updating was performed for *ten* times.

Stochastic Calibration and Validation Scenarios: The conventional approach to calibration and validation is to calibrate a model for a time period and validate it for another period. For the simplicity, however, we calibrated the numerical model of the Bend Channel for the measurement locations at 90 degrees, and then validation was performed for the observation points located at 180 degrees. Within this approach, we created the response surface using the measurements at the calibration locations and used them for the validation scenario without any alterations.

4.2 Bayesian Model Ranking

The results of the BMS for the numerical model of Channel Bend for all five selected hydro-morphodynamic models are provided in the following section. The Bayesian model ranking is presented at the end of this section under the title of *BME Comparison*. Moreover, some figures and diagrams of competing models are incorporated into Appendix I.

Meyer-Peter-Müller Model: The plots in Figure 4.1 illustrate the simulation output of the hydro-morphodynamic model including the Meyer-Peter-Müller equation for the bed-load transport rate at the 90 degrees and 180 degrees of the channel bend, respectively against the output of the surrogate model considering the parameter set with the highest likelihood in the calibration stage. The blue line represents the response surface and the simulated bed evolution is shown with the red curve. The horizontal axis shows the distance from the inner side of the flume, and the vertical axis presents the bed evolution after 300 minutes.

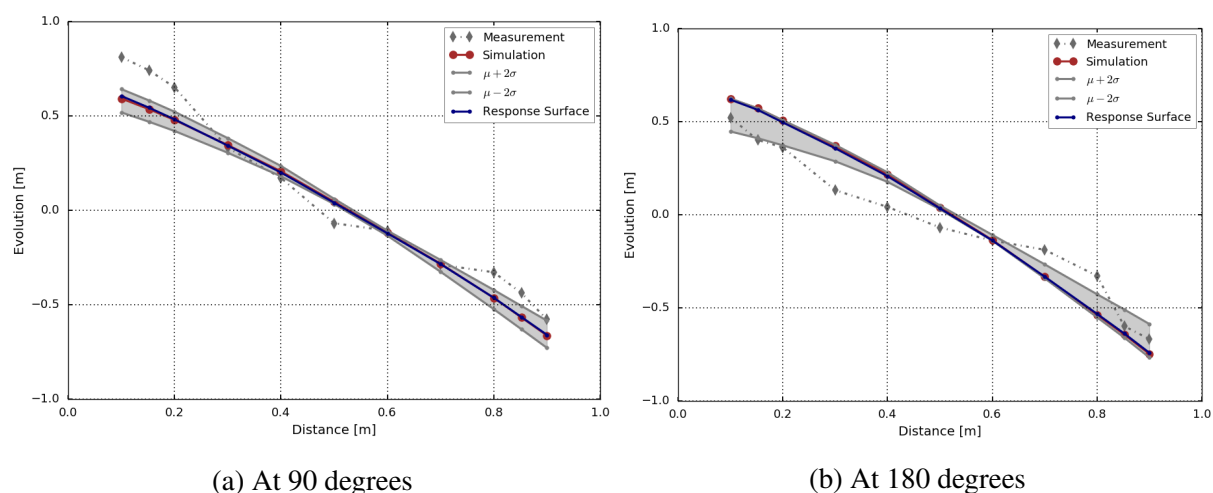


Figure 4.1: Simulation output vs. response surface (calibration-Meyer-Peter-Müller model)

Additionally, the gray area exhibits the performance range (confidence interval) of the response

surface considering the posterior parameter sets. The lower bounds of this zone are shown by the mean value of response surface outputs of the posterior parameter set minus two times of their standard deviation, and the upper bounds mean plus two times the standard deviation. As it is noticeable from Figure 4.1a and Figure 4.1b, the improved response surface after iterations acceptably represented the original numerical model in Telemac-2d-Sisyphé.

The likelihood of the prior realizations before and after improvement of the response surface are presented in Appendix I. Figure 4.2 shows the probability density function (PDF) of the posterior distribution of uncertain parameters along with their statistical characteristics. Kernel Density Estimation (KDE) approach was employed to approximate the probability density function of a variable. KDE is a fundamental data smoothing problem that allows us to make inferences about the population, based on a finite data sample and are closely linked to histograms.

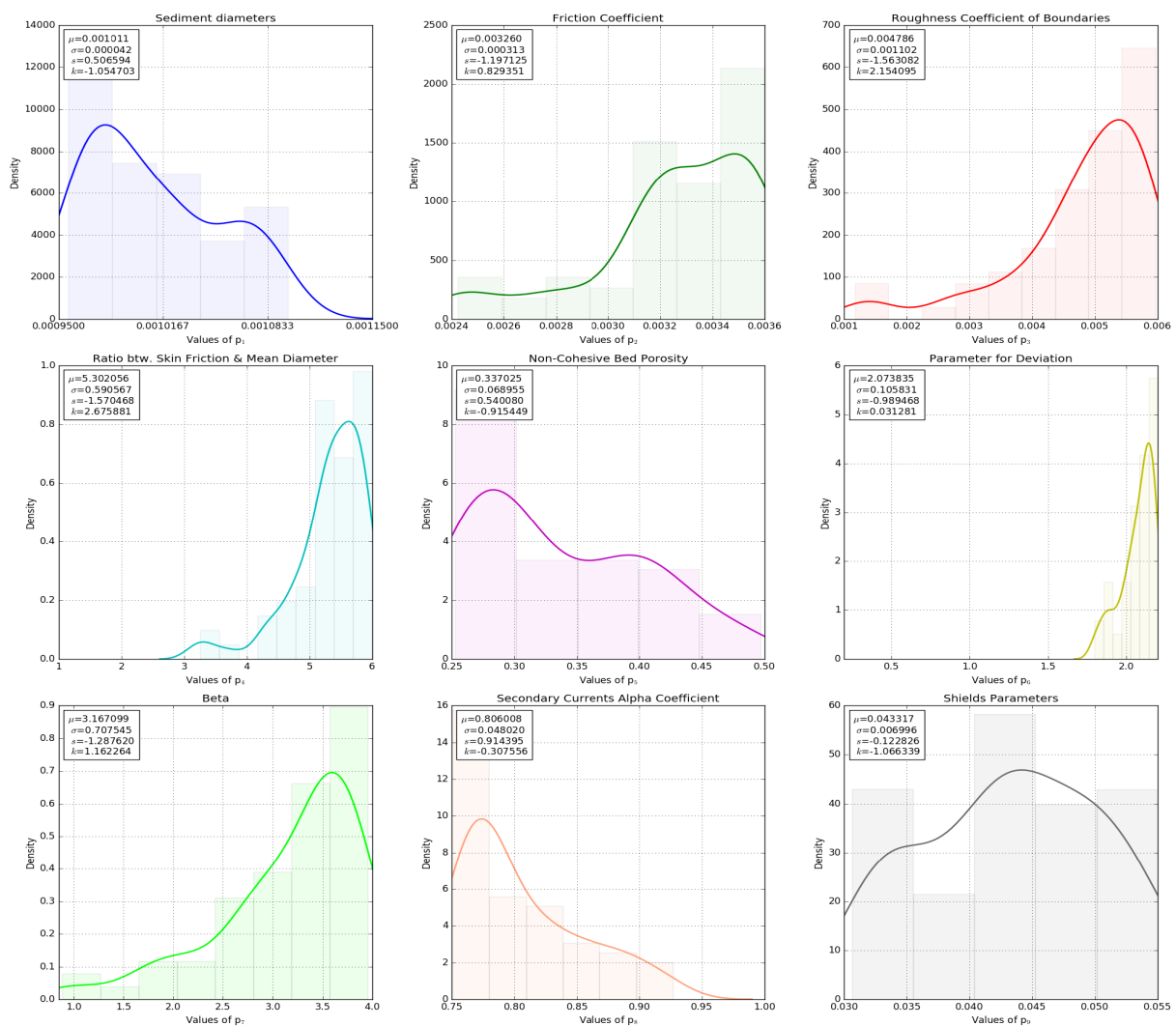


Figure 4.2: The posterior PDF of parameters (calibration-Meyer-Peter-Müller model)

The likelihood weights of the prior realization for the validation stage were assigned based on the validation measurements (measurement locations at 180 degrees). Figure 4.3 demonstrates the simulation output and the performance range of the response surface for the parameter set with the highest likelihood.

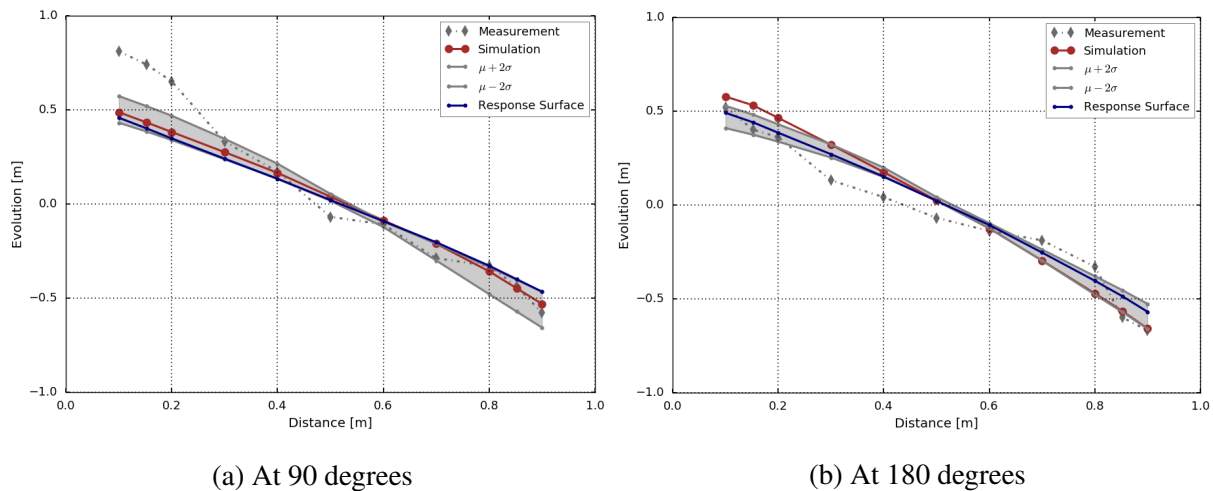


Figure 4.3: Simulation output vs. response surface (validation-Meyer-Peter-Müller model)

In Figure 4.3, the visible misfit of the simulation production and the reduced model (response surface) at location 180 degree can be attributed to the fact that the response surface, constructed in calibration stage, has not been adapted to the validation positions. In other words, no iteration on the improvement of the surrogate model was taken into account in the validation step.

The validation's prior likelihood weights (shown in Appendix I) was improved significantly, and it suggests that the posterior realizations after the validation show better performance for the validation locations within their pre-defined ranges. Figure 4.4 shows the probability density function (PDF) of the posterior distribution of uncertain parameters after validation step.

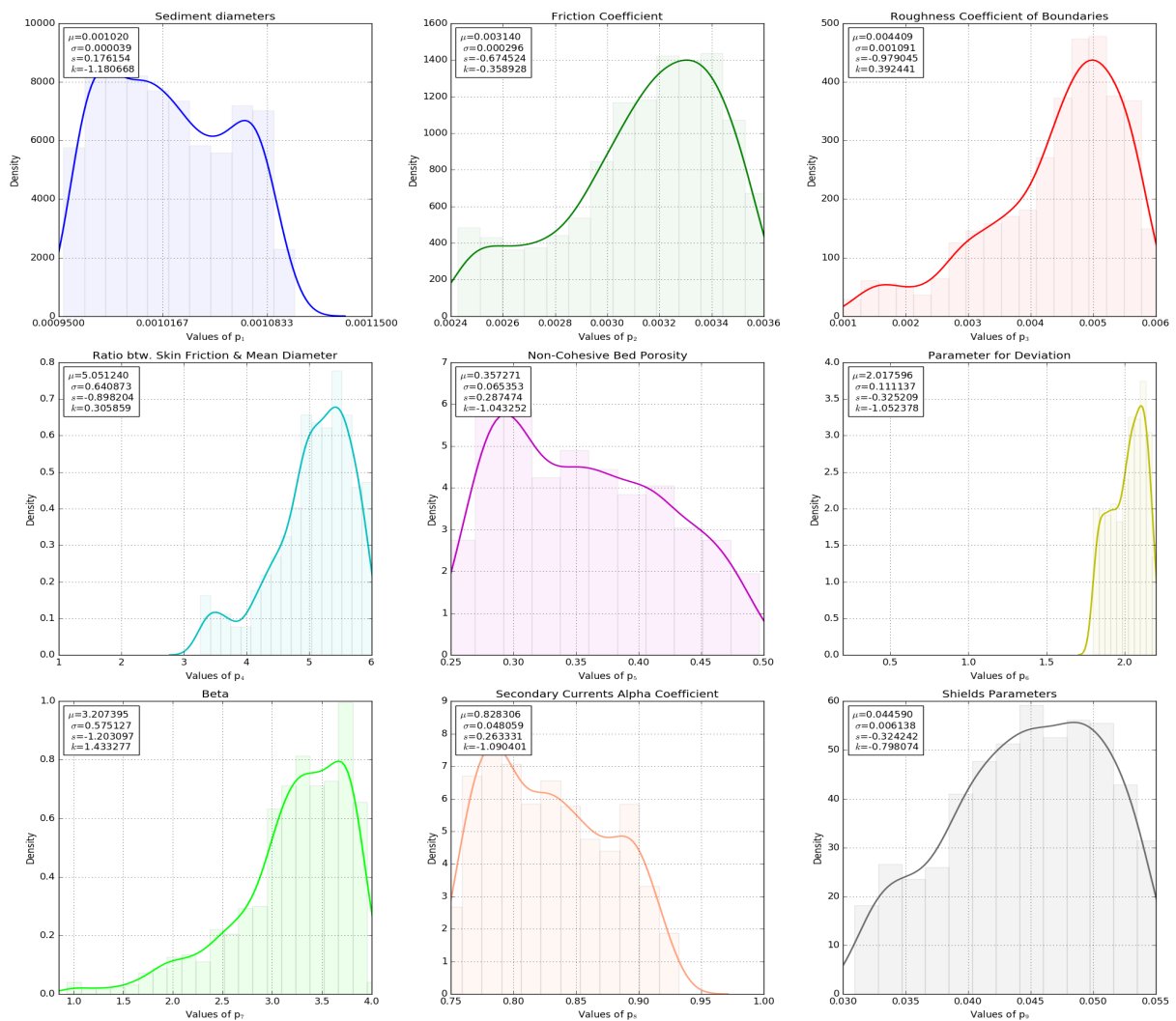


Figure 4.4: The Posterior PDF of parameters (Validation-Meyer-Peter-Müller Model)

Einstein-Brown Model: The results of the hydro-morphodynamic model comprising of the bed-load transport rate of Einstein-Brown (1950) are presented in the following section. The plots in Figure 4.5 show the model's simulation output against the response surface in calibration step (using measurements at the location of 90 degrees).

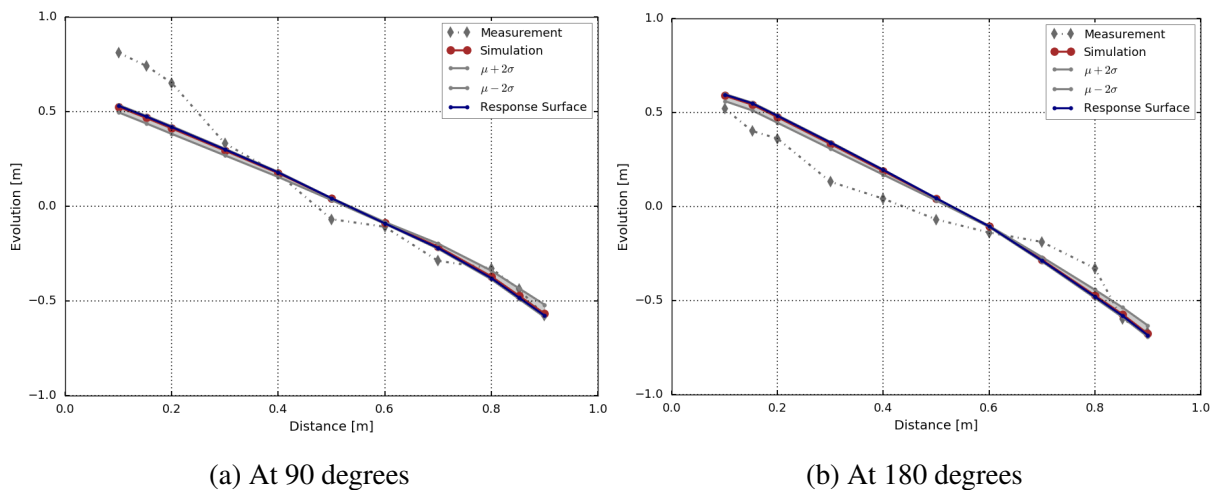


Figure 4.5: Simulation output vs. response surface (calibration-Einstein-Brown model)

Similar to the previous model, the likelihood of the prior realizations before and after improvement of the response surface are presented in Appendix I. For the Einstein-Brown model, many realizations (parameter sets) received lower likelihood weights in comparison with the Meyer-Peter-Müller model.

Figure 4.6 displays the probability density function (PDF) of the posterior distributions of uncertain parameters with their corresponding statistical characteristics. Due to the poor likelihood weight, fewer realizations remained after the bootstrap-filtering step, and this is reflected in the posterior PDF of parameters for the Einstein-Brown model in comparison with that of Meyer-Peter-Müller model (Figure 4.2).

Figure 4.7 demonstrates the simulation output and the performance range of the response surface for the parameter set with the highest likelihood in the validation step (using observations at 180 degrees of the channel bend).

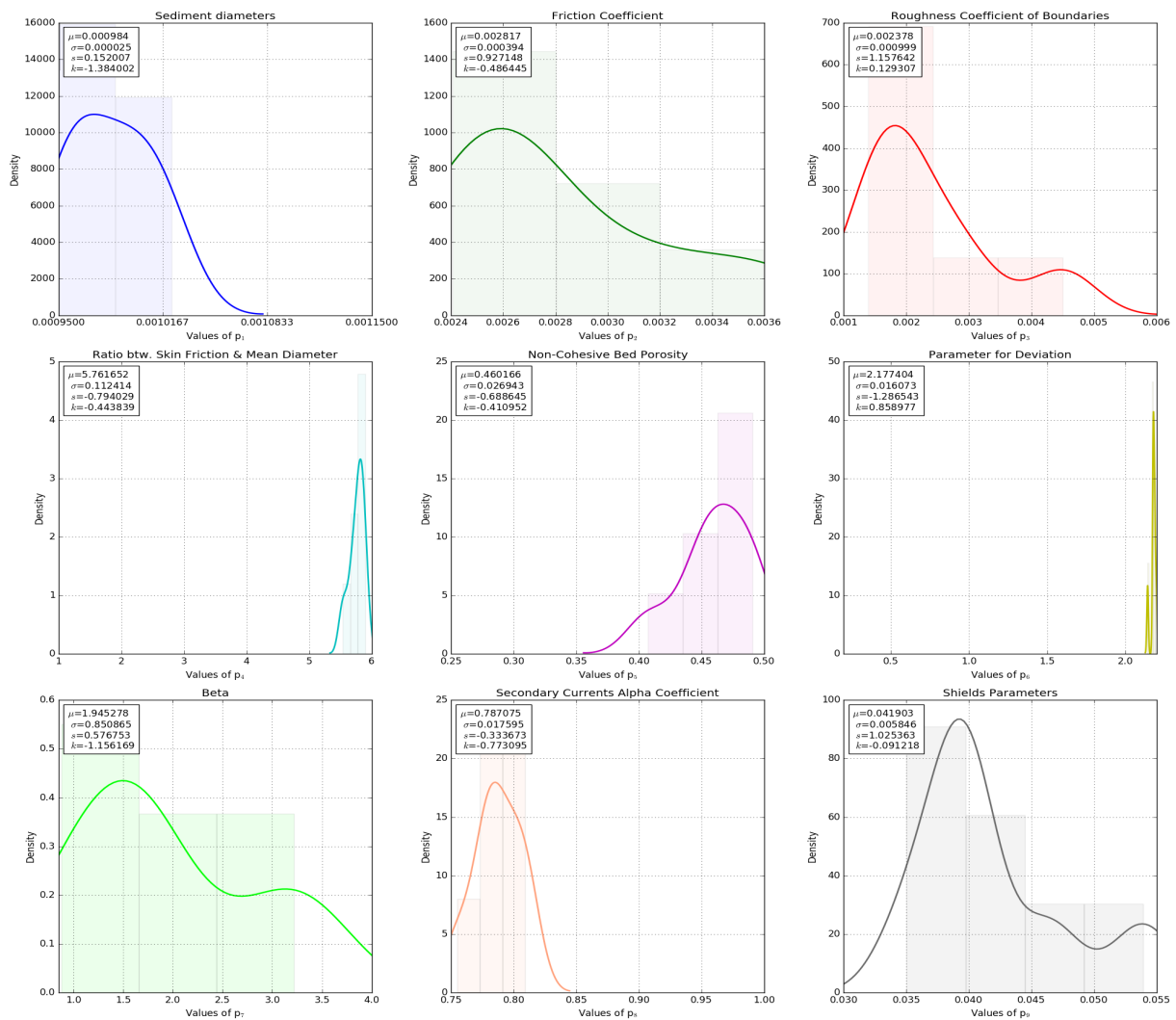
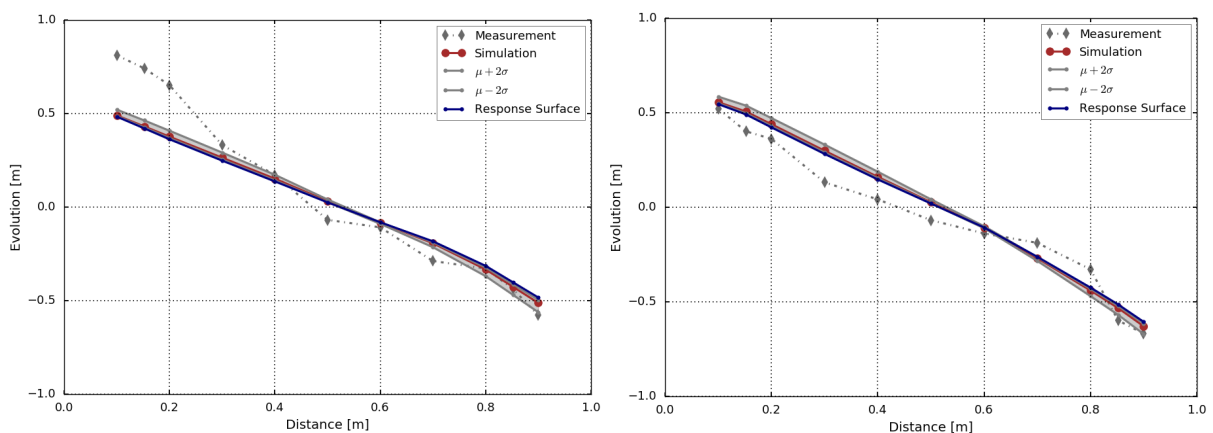


Figure 4.6: The posterior PDF of parameters (calibration-Einstein-Brown model)



(a) At 90 degrees

(b) At 180 degrees

Figure 4.7: Simulation output vs. response surface (validation-Einstein-Brown model)

Figure 4.8 exhibits the probability density function (PDF) of the posterior distribution of uncertain parameters after validation step. Many distributions formed more concentrated shape that are informative for the further task of the optimization.

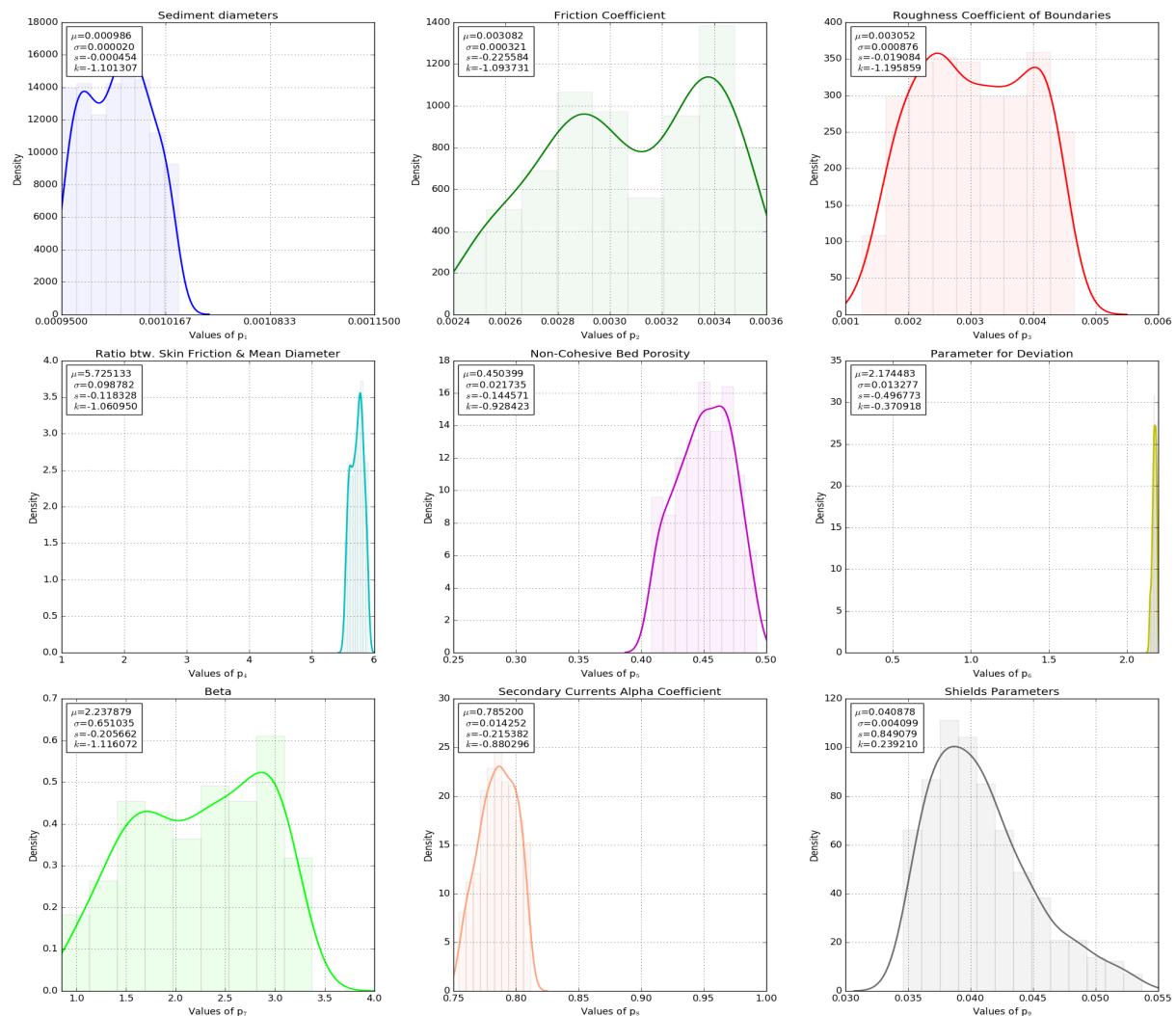


Figure 4.8: The posterior PDF of parameters (validation-Einstein-Brown model)

Modified Engleund-Hansen Model: The plots in Figure 4.9 illustrate the model's simulation output against the response surface in calibration step (using measurements at the location of 90 degrees). The confidence interval of the response surface (the gray area) was considerably narrow due to few remaining parameter sets passed the bootstrap-filtering stage in the calibration stage. This fact also mirrored in the posterior probability density function in Figure 4.10.

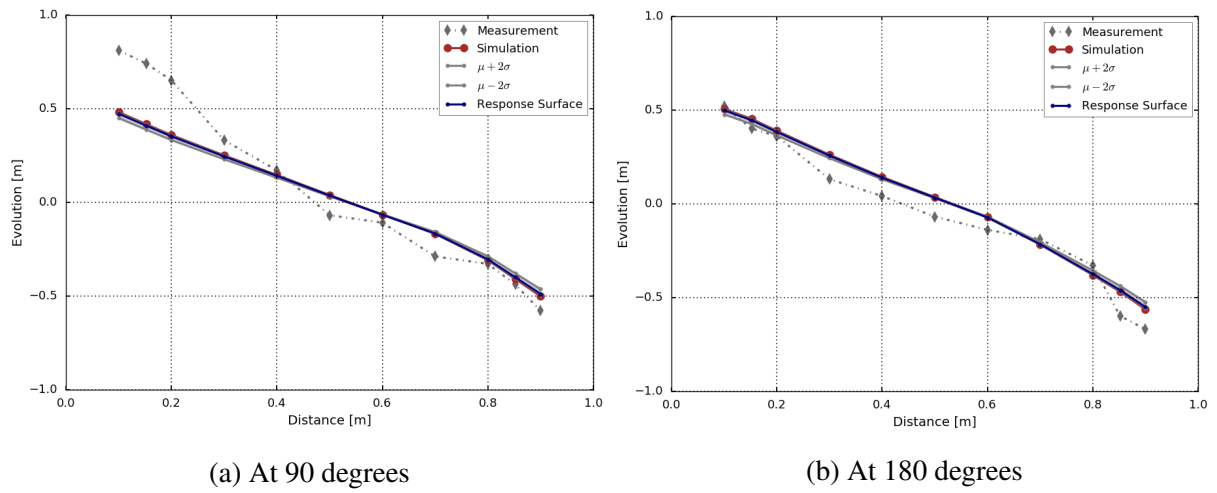


Figure 4.9: Simulation output vs. response surface (calibration-Mod. Engleund-Hansen model)

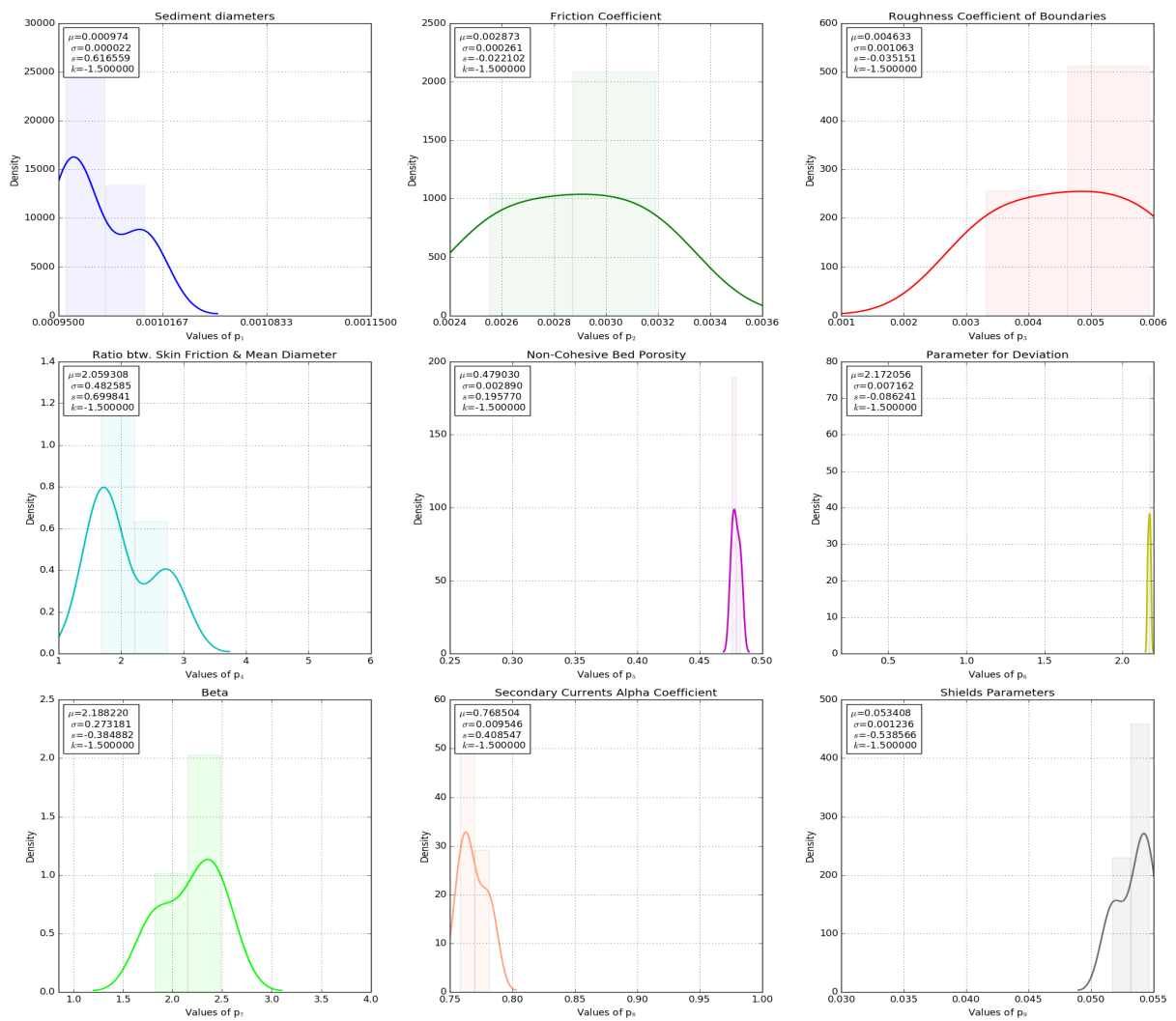


Figure 4.10: The posterior PDF of parameters (calibration-Mod. Engleund-Hansen model)

The posterior information on best parameter sets in the calibration stage was considered as the prior knowledge on the distribution of the parameters for the validation step. Additionally, the enlargement of the prior was conducted. Figure 4.11 shows the simulation output and the performance range of the response surface for the parameter set with the highest likelihood in the validation step.

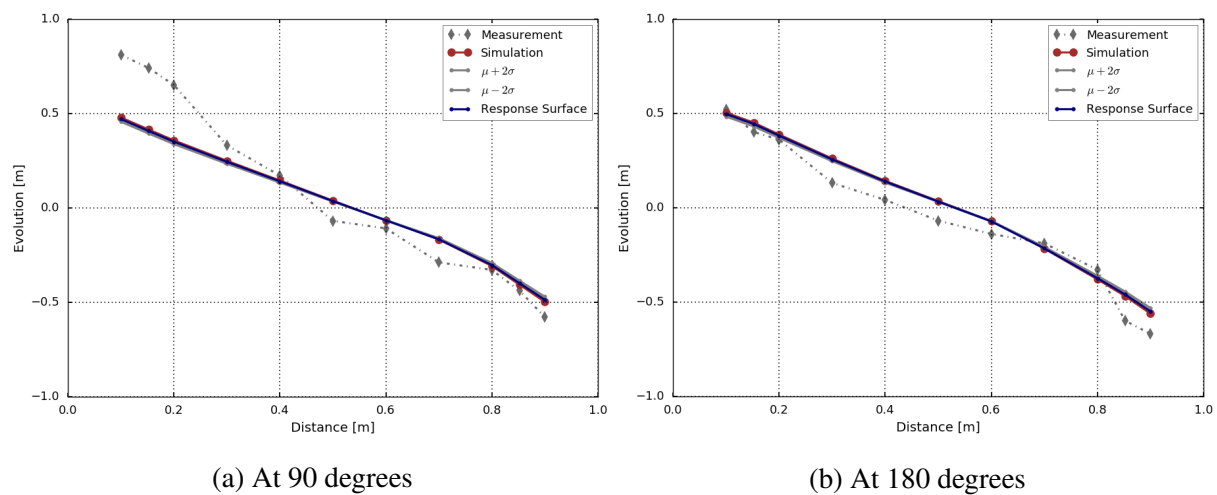


Figure 4.11: Simulation output vs. response surface (validation-Mod. Engleund-Hansen Model)

Similar to Figure 4.9, the validation step also generated thin performance domain of the response surface. In contrast, more realizations remained after the bootstrap-filtering and the probability distribution of the parameters are more concentrated.

Van Rijn Model: The plots in Figure 4.13 illustrate the model's simulation output against the response surface in the calibration step for the Van Rijn model. Although the simulated bed evolution fell within the performance range of the response surface (the gray area), the constructed response surface after ten times improvement, unlike other models, failed to adequately represent the original model.

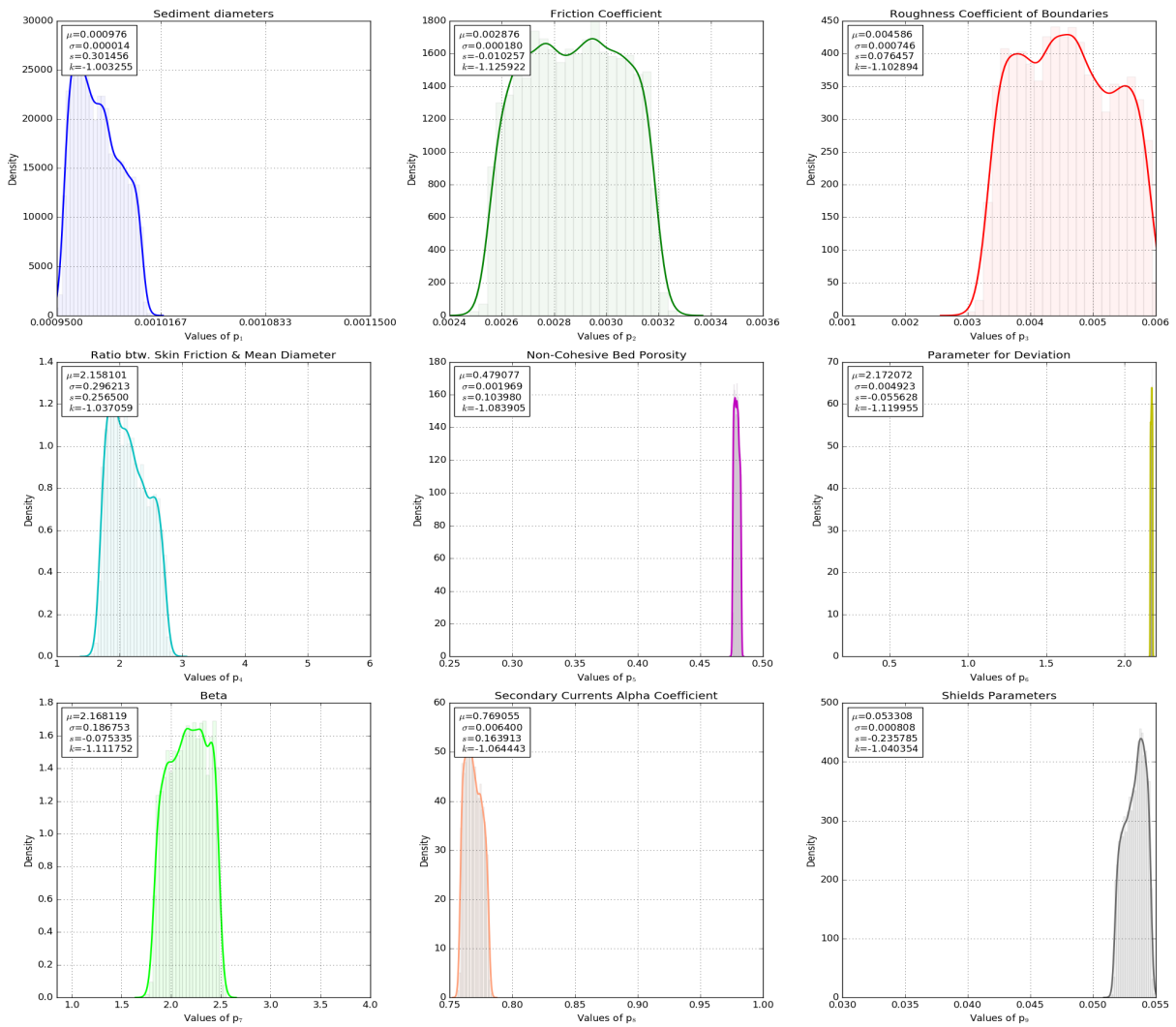
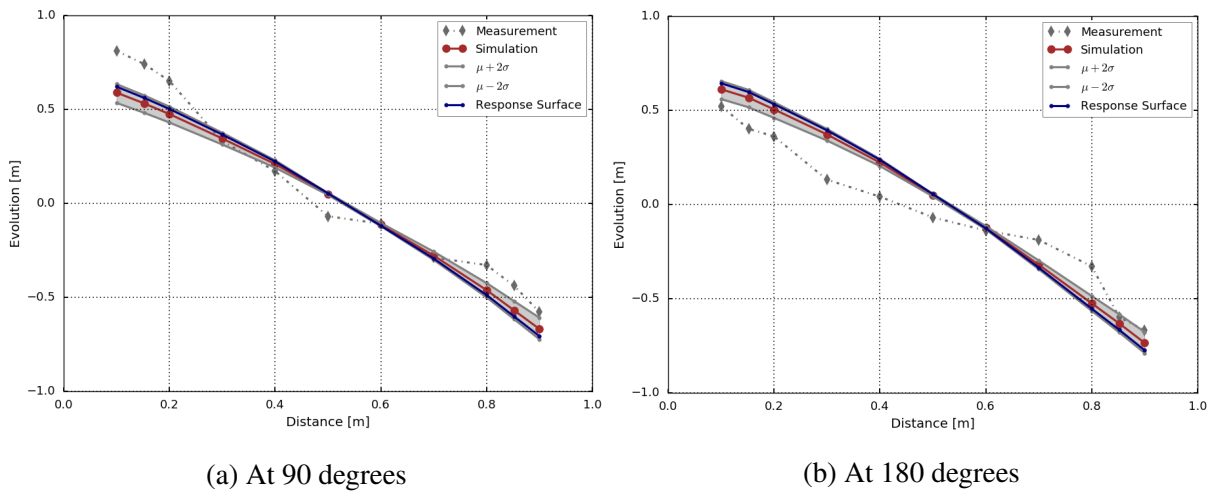


Figure 4.12: The posterior PDF of parameters (validation-Mod. Engleund-Hansen model)



(a) At 90 degrees

(b) At 180 degrees

Figure 4.13: Simulation output vs. response surface (calibration-Van Rijn model)

The likelihood weights after the improvement of the response surface, shown in Appendix I, show a significant reduction. The posterior probability distributions of the parameters, the simulation bed evolution versus the response surface, and the posterior probability distributions of the parameters in the validation step follow.

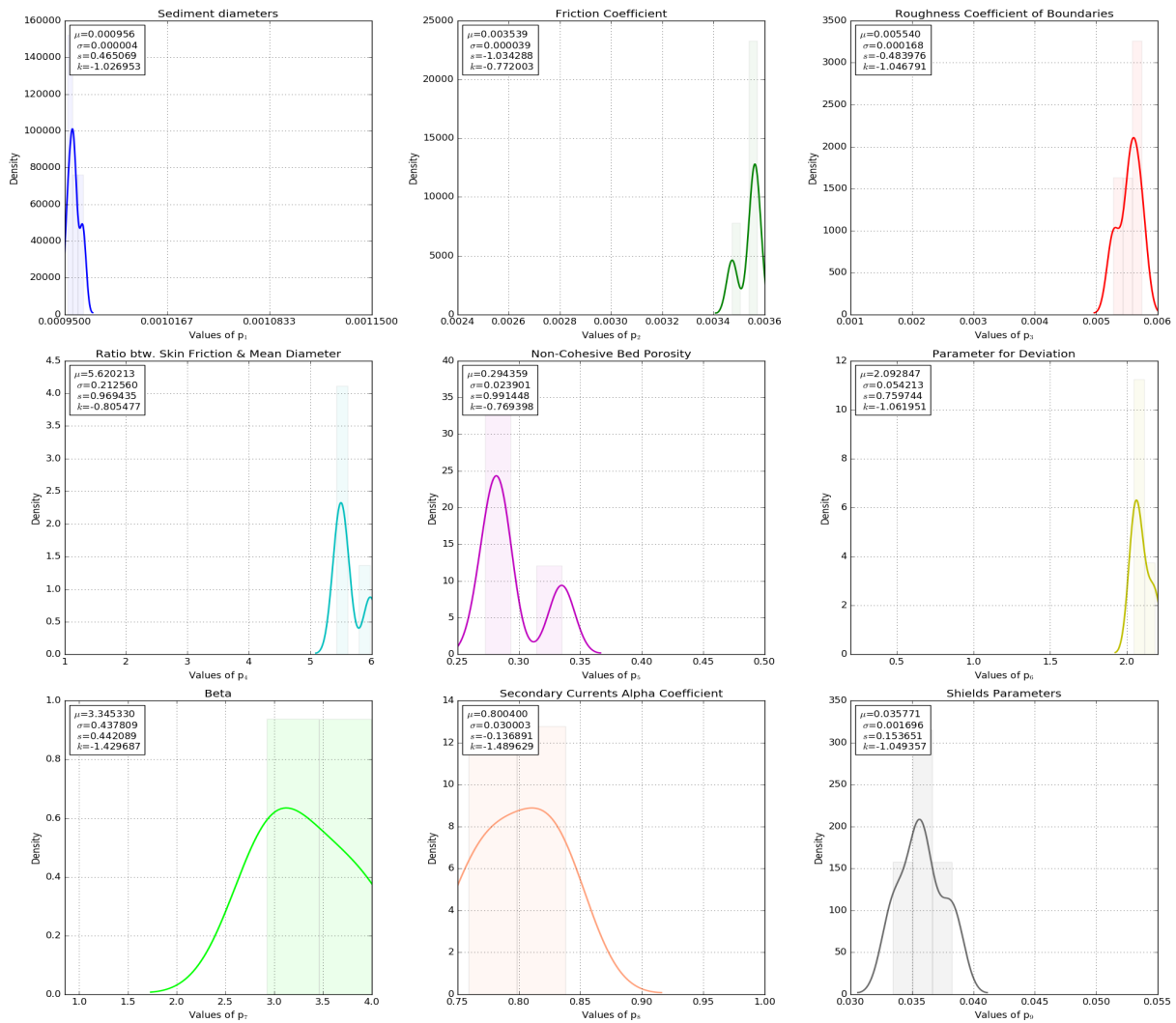


Figure 4.14: The posterior PDF of parameters (calibration-Van Rijn model)

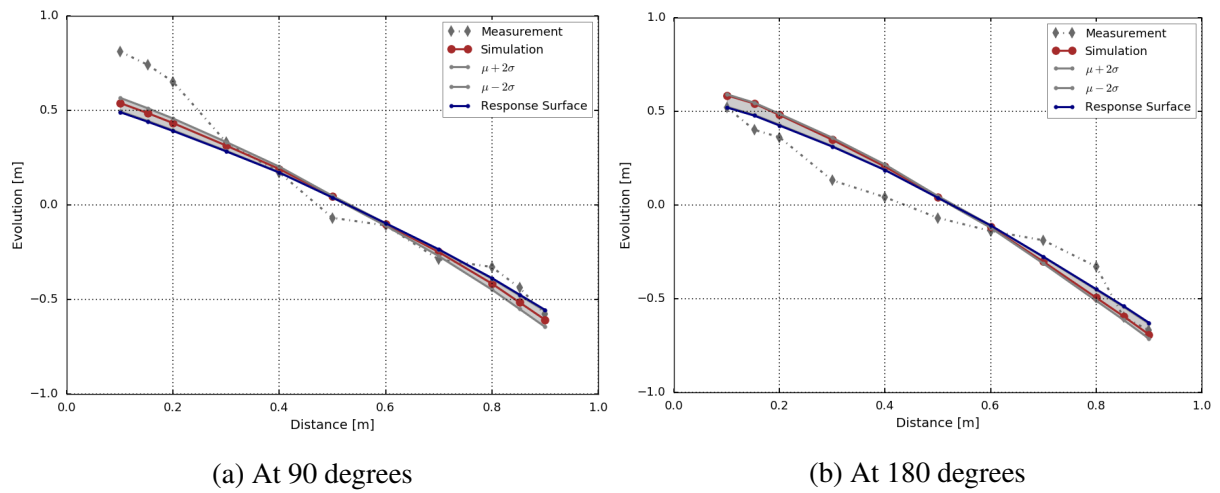


Figure 4.15: Simulation output vs. response surface (Validation-Van Rijn model)

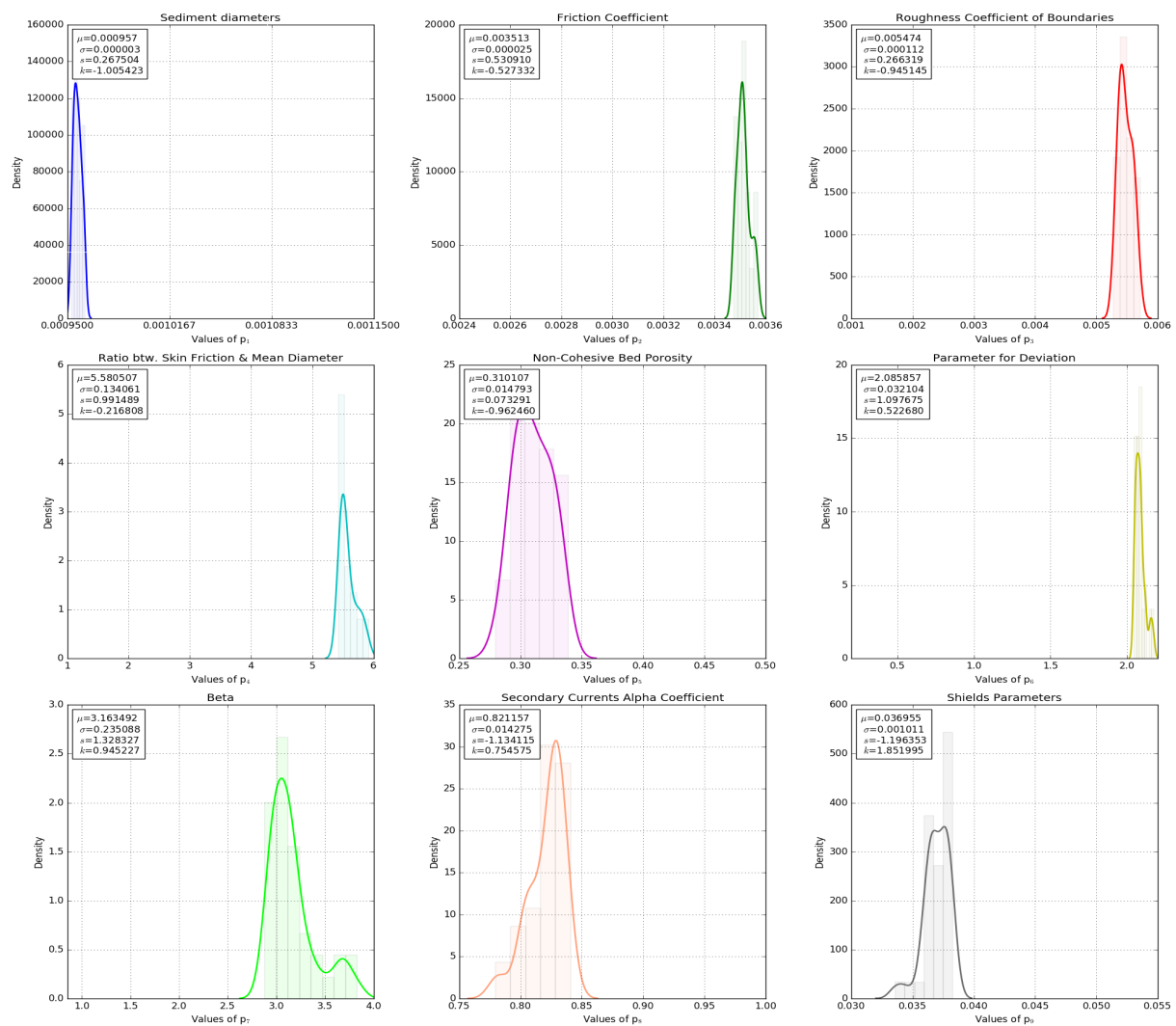


Figure 4.16: The posterior PDF of parameters (validation-Van Rijn model)

From the diagrams above, it is evident that the surrogate model was not fruitful to be a replacement for the original model in Telemac-2d-Sisyphé.

Wu Model: The last tested hydro-morphodynamic model included the bed-load transport rate equation suggested by Wu et al. (2000). This variant was manually introduced to morphodynamic module Sisyphé. The response surface built in the Bayesian framework could capture the behavior of the original model in Telemac-2d-Sisyphé as shown in Figure 4.17.

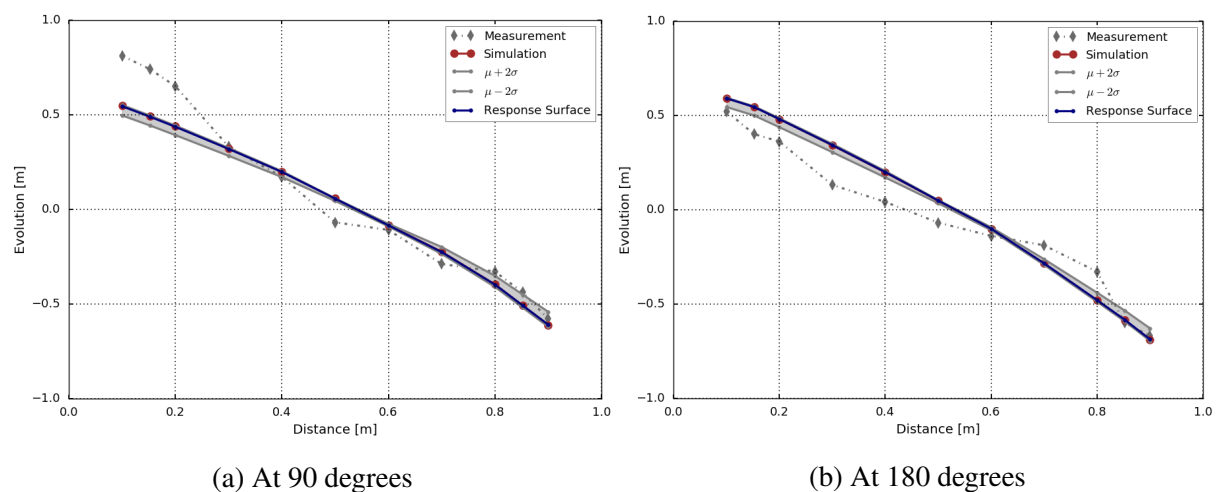


Figure 4.17: Simulation output vs. response surface (calibration-Wu model)

The probability distribution of parameters are presented in Figure 4.17. The distribution shapes suggest fairly wide ranges, which are less informative for any inferences for any further task of optimization.

The posterior realizations resulting from the calibration was used as the prior information in the validation stage. Also, the response surface established in the calibration was implemented in the validation phase without any modifications. The realization with the highest likelihood, was inserted in the original numerical model in Telemac-2d-Sisyphé and the surrogate model. Figure 4.19 illustrates the resulting bed evolution curves.

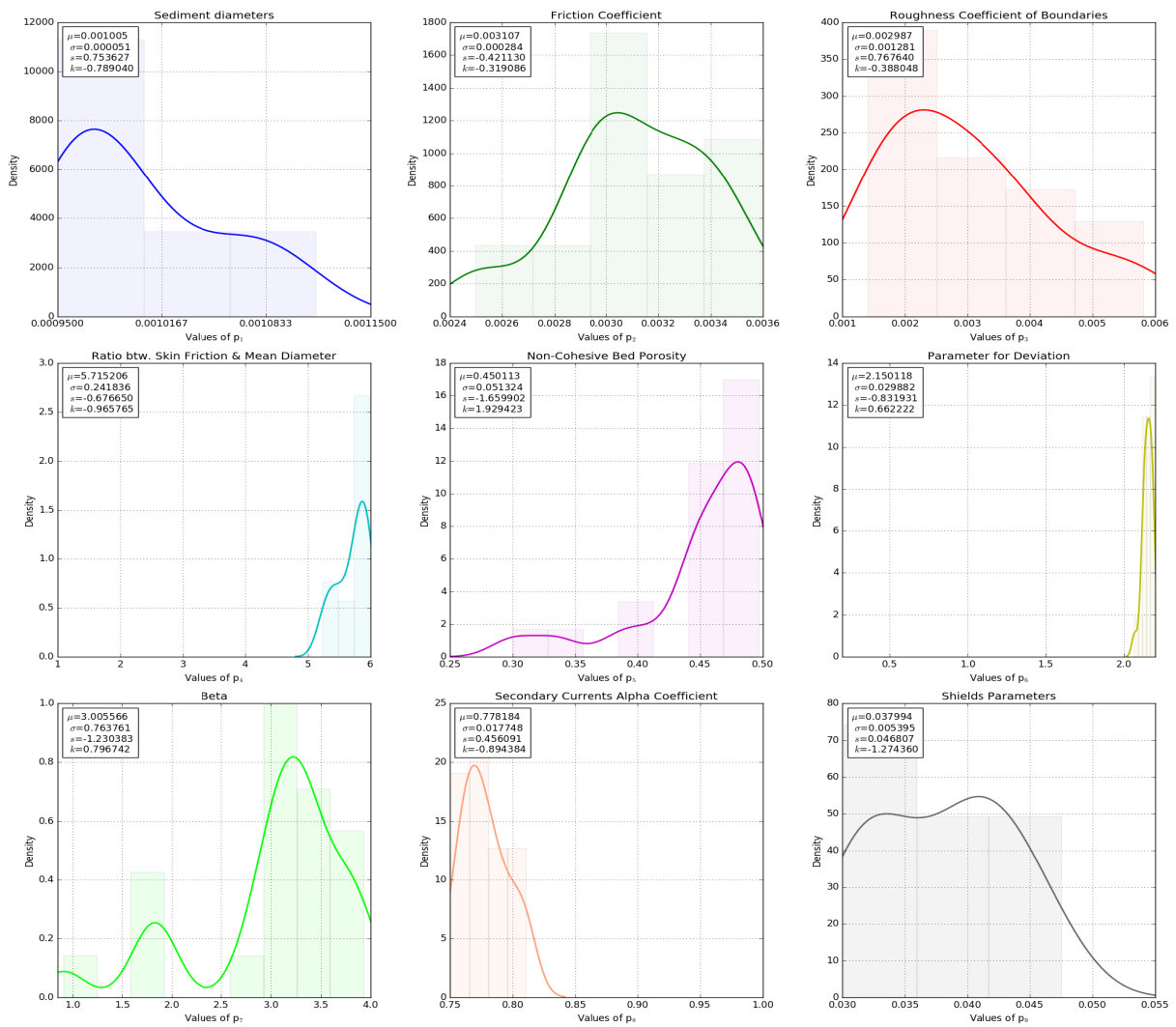


Figure 4.18: The posterior PDF of parameters (calibration-Wu model)

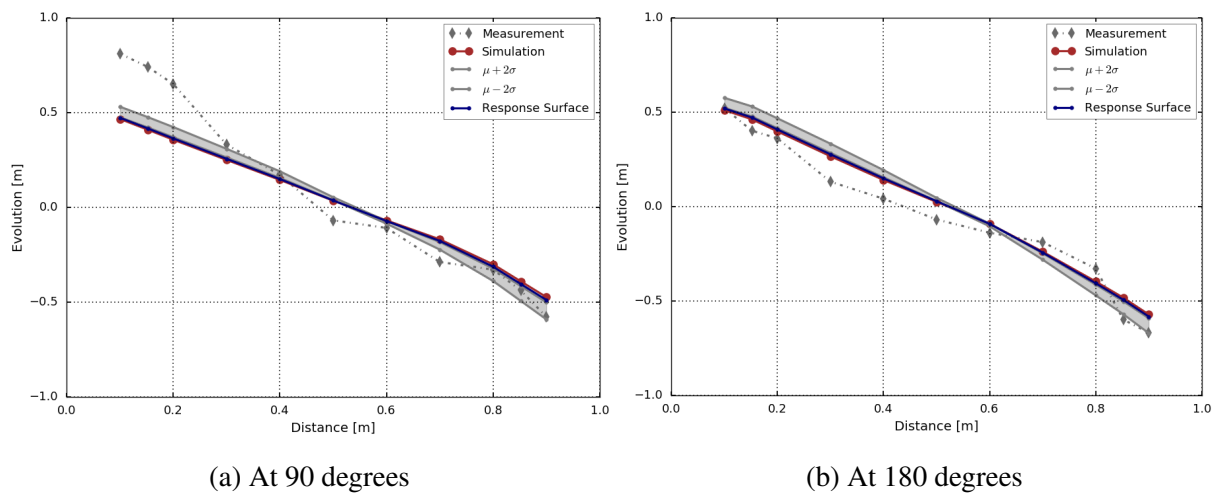


Figure 4.19: Simulation output vs. response surface (validation-Wu model)

The probability distributions, shown in Figure 4.20, demonstrate adequately focused distribution shapes, which can effectively assist the user in identifying the best calibration parameter set.

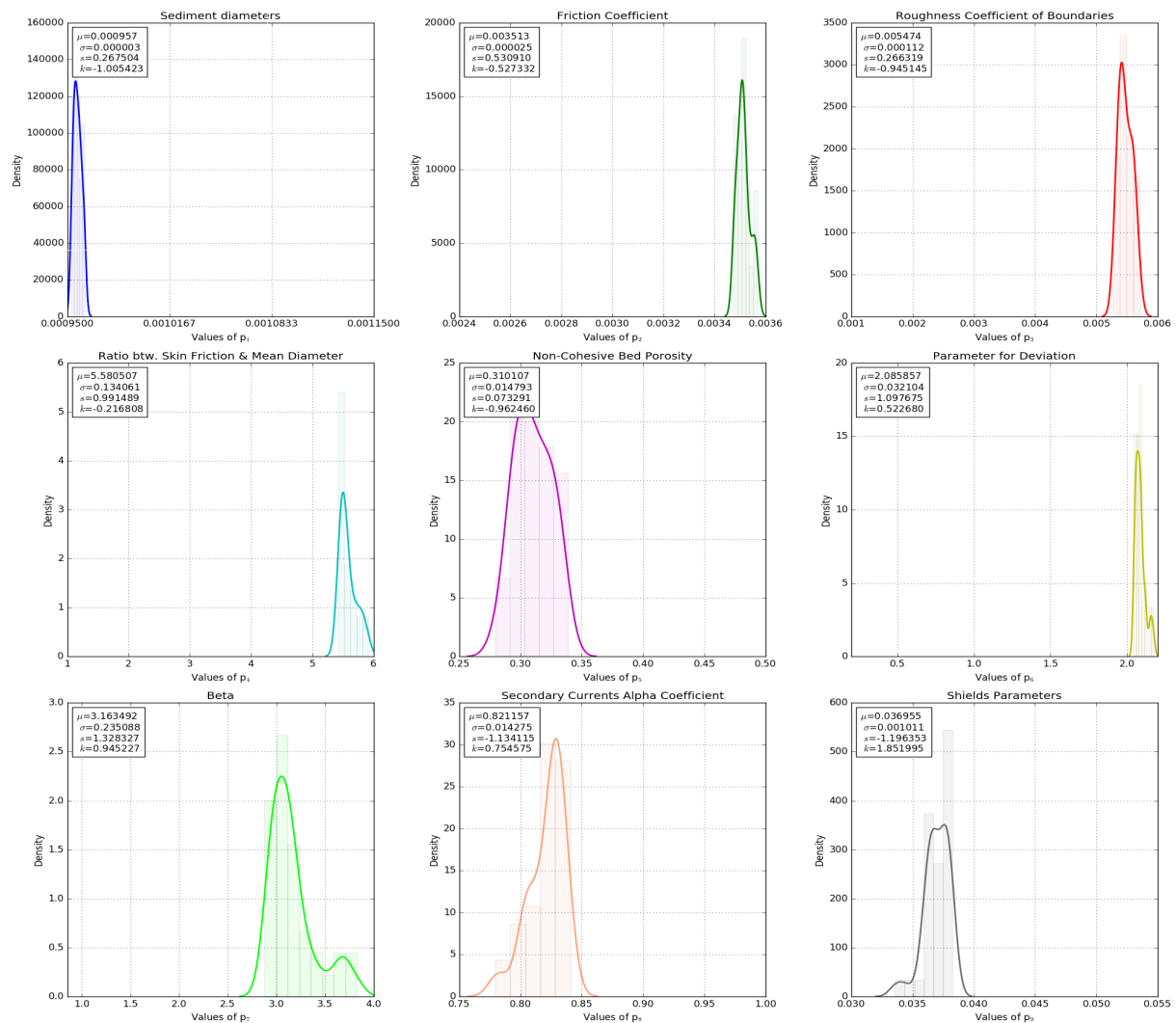


Figure 4.20: The posterior PDF of parameters (validation-Wu model)

BME Comparison: Bayesian model selection is performed based on Bayesian Model Evidence (BME), which is a product of Bayesian Model Averaging (see Section 3.3.1). BME term also referred to as marginal likelihood or prior predictive of the observed data based on the prior distribution of the parameters (Equation 3.12) is calculated by implementing Simple Monte Carlo integration method. The development of BME values of the competing models over the iterations on the improvement of the response surface (surrogate model) is depicted in Figure 4.21.

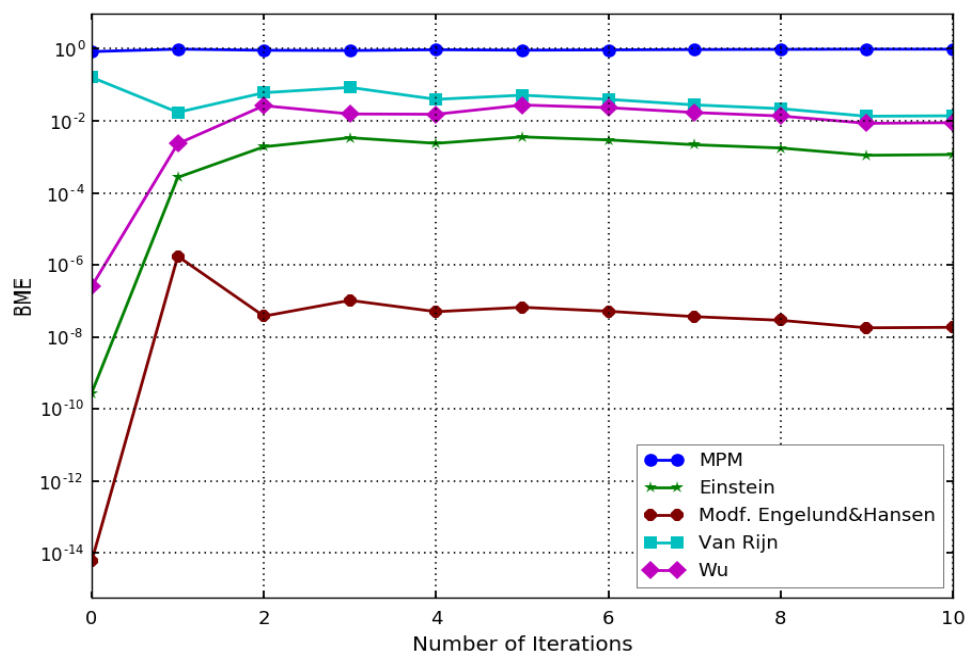


Figure 4.21: Bayesian model evidence vs. iterations for channel bend model in calibration step (Log-scale)

According to the graph above, the hydro-morphodynamic model of Meyer-Peter-Müller demonstrated the best performance among the competing models after the calibration step. However, model selection must be made based on the BME values after the validation. Table 4.3 summarizes the BME values of the competing models calculated according to Equation 3.10 after the validation step.

Table 4.3: The BME comparison after the validation (channel bend)

Hydro-Morphodynamic Model	BME of Validation	Rank
Meyer-Peter-Müller	0.191	2
Einstein-Brown	0.042	4
Modified Engelund-Hansen	0.71	1
Van Rijn	0.0014	5
Wu	0.058	3

Table 4.3 reveals that the hydro-morphodynamic model containing the modified Engelund-Hansen bed-load transport rate equation was the best model after validation step. However, this model had been the least favorable model in the calibration step. Even though the likelihood weights were substantially small after the calibration step, the response surface of the model was also best representation of the original numerical model at the validation locations.

On the contrary, the morphodynamic model containing the Van Rijn bed load equation was placed in the last rank among other competing models in the validation step, though it was ranked as the second in the calibration phase.

In the calibration stage, only few parameter sets survived for the model of modified Engelund-Hansen, indicating that many of the prior parameter sets performed poorly, which explains why its average likelihood (BME) was the lowest and the model was placed in the last rank. In the validation step, however, this model scored the best, because little uncertainty remained after the calibration. None of the other models showed a significantly better fit, and along with a small uncertainty, this model gained the highest rank.

4.3 Uncertainty Analysis of BMS for Channel Bend

Uncertainty analysis, in general, attempts to determine probabilities of individual outcomes when some aspects of the system are not exactly known. The aim here is to characterize the reduction of uncertainties of BME calculation in the BMS algorithm quantitatively. Therefore, the impact of various prior information (different mean values and variances of parameters) on the outcome of BME was investigated, and the prediction confidence intervals after calibration step for the competing hydro-morphodynamic models were determined.

The BMS was repeated for the channel bend model for 100 times (i.e. slightly dissimilar prior distributions) with the measurement error of 0.1, and 30,000 samples. Figure 4.23 presents the BME value ranges for all model. The thickness of the lines indicate that the standard deviation was remarkably negligible.

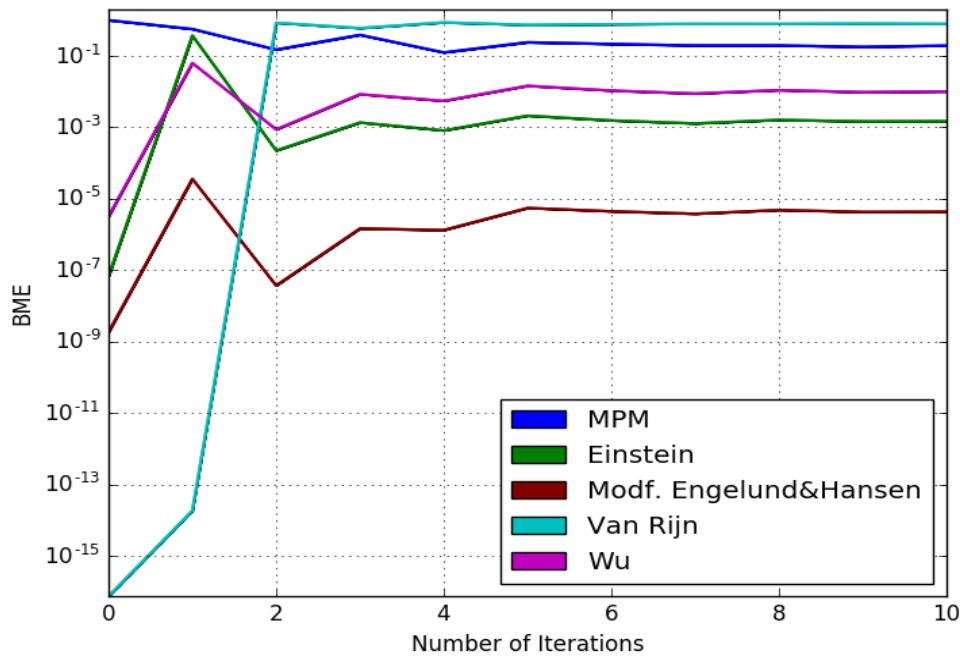


Figure 4.22: Performance range of the BME values after calibration

The uncertainty of the BME rates after the stochastic validation step for all morphodynamic models is provided as a box plot diagram in Figure 4.23. It presents in quartiles as the statistical data, separating the extreme values. The spacing between the different parts of the box specify the degree of dispersion (kurtosis) and skewness in the BME rates.

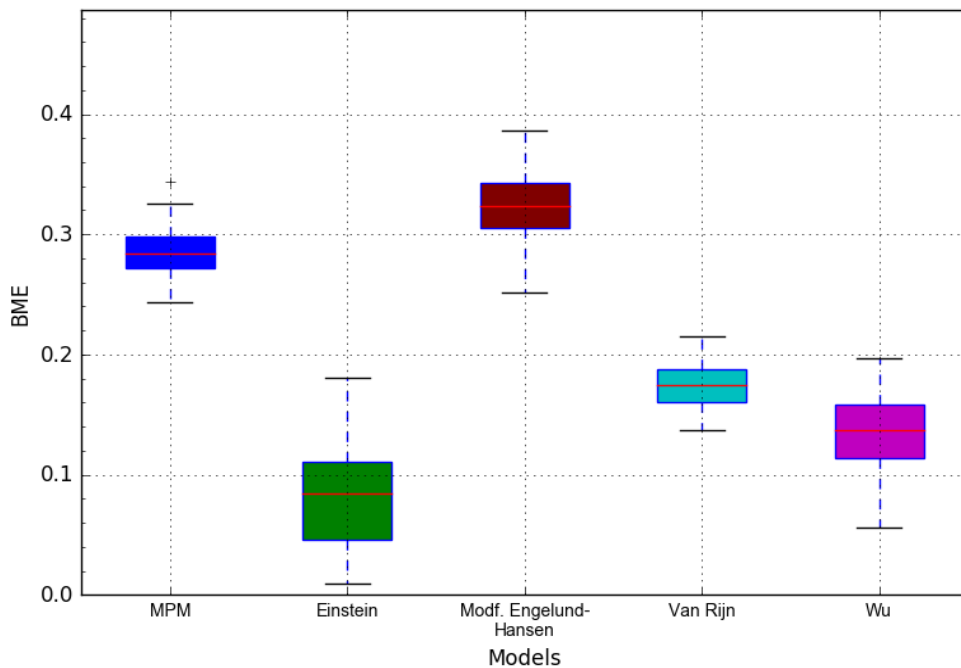


Figure 4.23: Box plot for the BME values after validation

Similar to the results of BME comparison in Section 4.2, the hydro-morphodynamic model including Modified equation of Engleund-Hansen was the least favorable model after the calibration step. However, this model was ranked mostly as the best model after the validation step, as shown in Figure 4.23. Some important statistical features of the BME values, such as mean, median, standard deviation, skewness and kurtosis values are summarized in Table 4.4.

Table 4.4: The statistical characteristics of the BME values after validation (Channel Bend)

Model	Mean	Standard Deviation	Skewness	Kurtosis
Meyer-Peter-Müller	0.285	0.019	0.180	0.110
Einstein-Brown	0.082	0.044	0.084	-0.828
Modified Engelund-Hansen	0.324	0.027	0.003	-0.171
Van Rijn	0.175	0.018	0.067	-0.696
Wu	0.135	0.032	-0.369	-0.444

The results of uncertainty analysis of channel bend model indicates that morphodynamic models of Van Rijn and modified Engelund-Hansen were ranked as the best and the worst models after the calibration step, respectively. Similar to the previous case (Section 4.2), the morphodynamic model with the modified bed-load transport equation of Engelund-Hansen was performed better than its rival after the validation.

4.4 Summary

This chapter entailed the results of the implementation of the BMS framework proposed by the current thesis for the first test case. This scenario included the model selection of the numerical model of Bend Channel inspired by the experiment of Yen and Lee (1995), provided by BAW in Karlsruhe.

The top morphodynamic model in the ranking was the morphodynamic model containing *Modified Engleund-Hansen* bed-load equation. The concentrated posterior parameters' distributions navigated us to a more credible area for the uncertain parameters for the task of history matching. Moreover, a section was devoted to the uncertainty analysis of the Bayesian model selection for channel bend, shedding light on the variation of the Bayesian Model Evidence (BME) rates under various prior information on the uncertain parameters.

5 Bayesian Model Selection for the Lower Rhine Model

Meandering channel sections present a particularly difficult challenge for hydro-morphodynamic modeling. Significant sedimentation on inner bends and erosion on outer curves characterize these regions. As a result, the shape of the banks and riverbed is constantly changing, producing dynamic conditions in curved channels, thus affecting the flow features. This alteration may disturb particularly the inland navigation, as well as flood events.

In addition to the test case of Channel Bend (Chapter 4), the algorithm was implemented in model selection for the hydro-morphodynamic numerical model of the 10-km stretch of the lower Rhine (see Section 4.3). The following chapter starts with the Bayesian Model Selection (BMS) of the twin experiment of the lower Rhine model in Section 5.1, followed by the BMS of the real case (Section 5.2). Each section includes the setup and implementation of the BMS framework for each item, in which all the considered components of the framework are presented. Then, the results of the implementation of the BMS framework in the test case of the hydro-morphodynamic model of the river Rhine are provided.

5.1 BMS for Twin Experiment of the Lower Rhine Model

The second hydro-morphodynamic numerical model introduced to the framework was the model of 10-km of the Lower Rhine River. The algorithm was initially benchmarked with a synthetic test case (Twin Experiment) to evaluate its ability in the identification of the best model for a numerical hydro-morphodynamic model of a natural river with an artificial measurement. Section 2.2 provided a detailed introduction to the location and characteristics of the area, as well as the model geometry, numerical model, initial and boundary conditions, and the synthetic measurements.

5.1.1 Setup and Implementation

The synthetic bed evolution was the simulation outputs of the hydro-morphodynamic model including *Wu formula* as displayed in Figure 2.15 and Figure 2.16. In this test, the framework must navigate us to the morphodynamic model of Wu equation. All the considered morphodynamic models, BMS framework's inputs, as well as calibration and validation scenarios, are summarized in the following sections.

Examined Hydro-Morphodynamic Models: Table 5.1 lists the selected sediment transport formulae for the morphodynamic models in the twin test of the numerical model of the lower Rhine.

Table 5.1: The morphodynamic models used in the twin experiment of lower Rhine model

Name of the bed load Equation	Year	Mode of Transport
Meyer-Peter-Müller	1948	Bed-load
Einstein-Brown	1950	Bed-load
Modified Engelund-Hansen	1980	Total-load
Van Rijn	1984	Bed-load
Hunziker	1995	Bed-load
Wu	2000	Bed-load

Chosen Uncertain Parameters and their Bounds: The uniform distribution of the uncertain parameters have been selected for all parameters. The selected hydro-morphodynamic parameters and the corresponding ranges are illustrated in Table 5.2.

Table 5.2: The selected uncertain parameters and their ranges (twin experiment)

ID	Uncertain Parameter's Name	Lower Bound	Upper Bound	Unit
P ₁	Sediment diameter	0.0156	0.02345	m
P ₂	Friction Coefficient of the main channel	0.475	0.525	m
P ₃	Friction Coefficient of the flood plain	0.095	0.105	m
P ₄	Beta	0.85	4.00	-
P ₅	Secondary Currents Alpha Coefficient	0.75	1.00	-

Measurement Error, Sample Size, and number of Iterations: Although the synthetic measurement were used here, the measurement error was assumed to be 0.03. This error was designed to account for inherent observation inaccuracy in the system as explained in Section 3.5.

The determination of the reference BME value for each model was performed by MC integration over ensembles of 20,000 realizations per model. Also, ten iterations of Bayesian updating were set for each model.

Stochastic Calibration and Validation Scenarios: The common approach to calibration and validation was implemented here, i.e. the models were validated within another period than that of the calibration stage. Note that the response surface, which was established using the measurements in the calibration stage, has been implemented in the validation stage without any modifications. However, the calibrated parameter set may vary in the validation step (stochastic validation).

5.1.2 Bayesian Model Ranking for the Twin Experiment

The outputs of the BMS for the numerical model of the lower Rhine for the competing hydro-morphodynamic models are presented in the following section. The likelihood weights before and after the surrogate model's improvements in the calibration phase and after the validation phase for all variants can be found in Appendix II.

Meyer-Peter-Müller Model: Figure 5.1 illustrates the simulated output of Telemac-2d-Sisyphé for the morphodynamic model including the Meyer-Peter-Müller formula versus the synthetic bed evolution after 35 days. Additionally, it entails the response surface (surrogate model). Note that the parameter set with the highest likelihood was selected to generate these outputs in Figure 5.1. Further, the horizontal axis shows the distance from the inlet boundary (738.5-km of the lower Rhine), whereas the vertical axis represents the bed evolution.

This plot indicates that the surrogate model after the calibration stage was a suitable representation of the original numerical model.

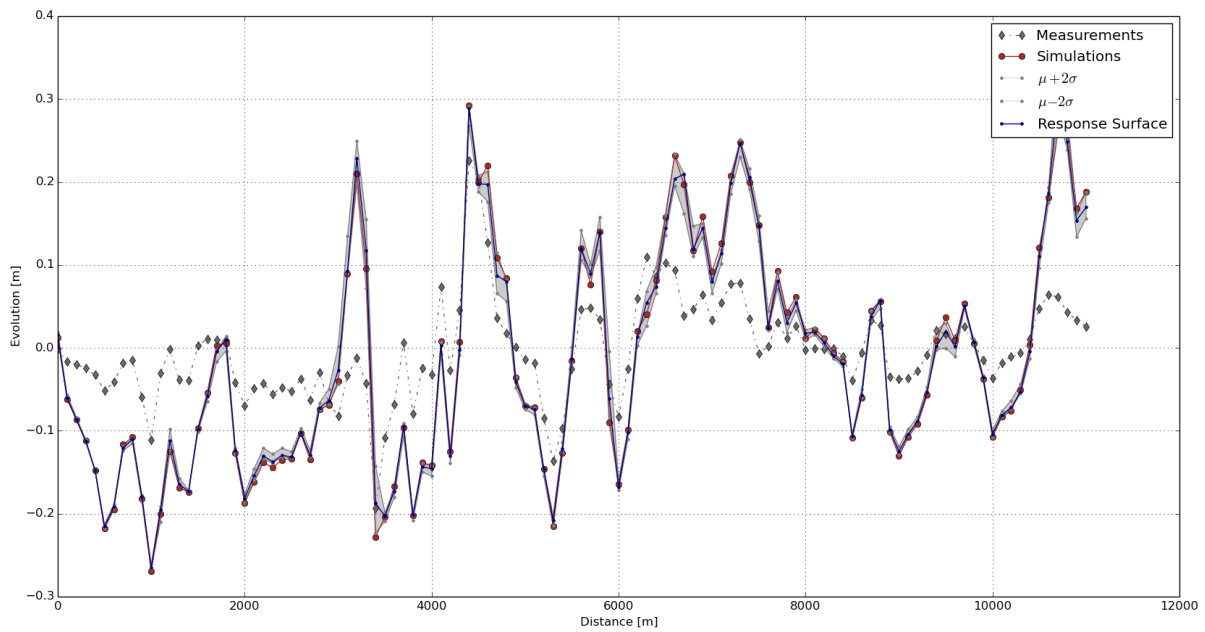


Figure 5.1: Simulation output vs. response surface (calibration-Meyer-Peter-Müller model)

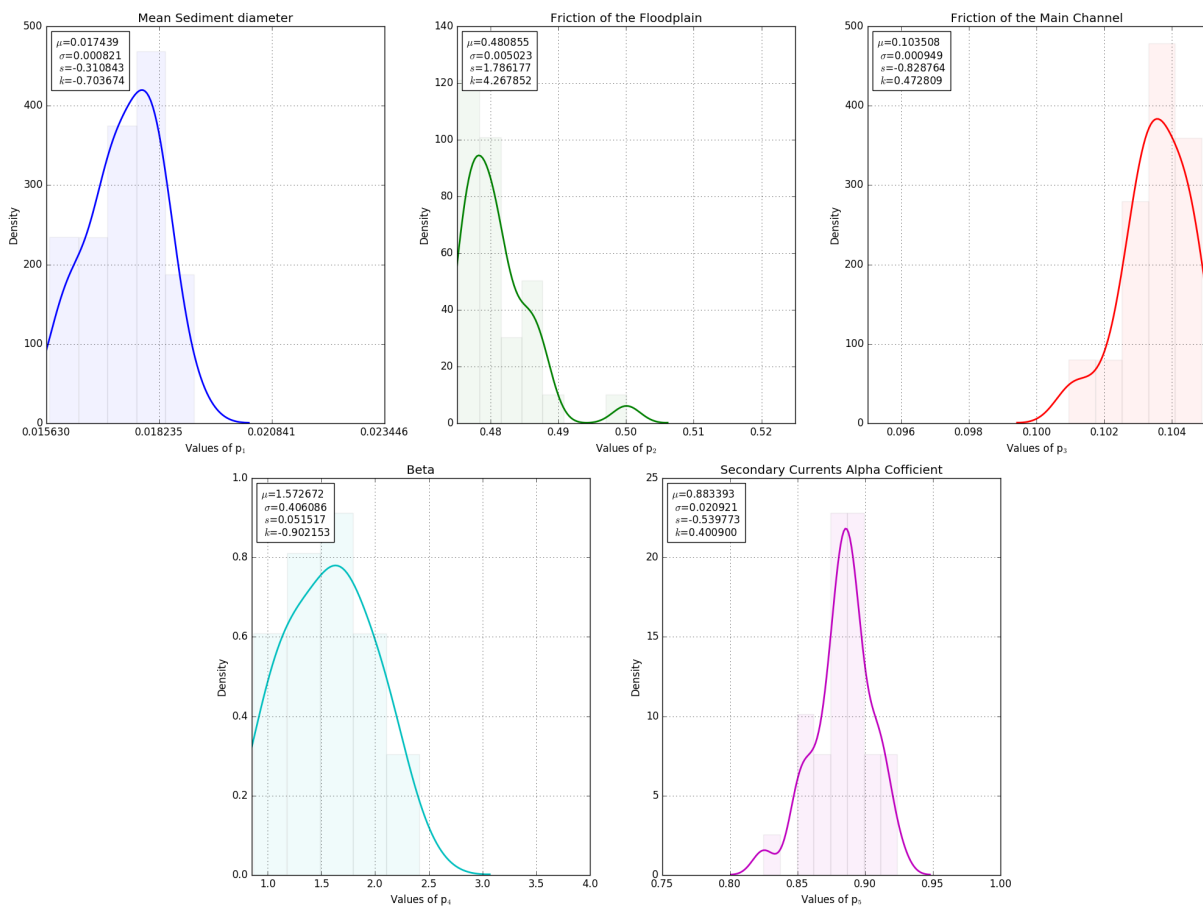


Figure 5.2: The posterior PDF of parameters (calibration-Meyer-Peter-Müller model)

Figure 5.2 demonstrates the PDFs of parameters, whose realizations (parameter sets) received comparatively higher likelihoods along with their corresponding statistical characteristics. As mentioned in Section 3.3, the remaining realizations after the calibration phase were used as the prior knowledge for the validation step, in which the procedure was repeated with the constructed response surface in the calibration step and a different bed evolution data set. The output of the surrogate model and the original numerical model for the realization with the highest likelihood after the validation stage is illustrated in Figure 5.3.

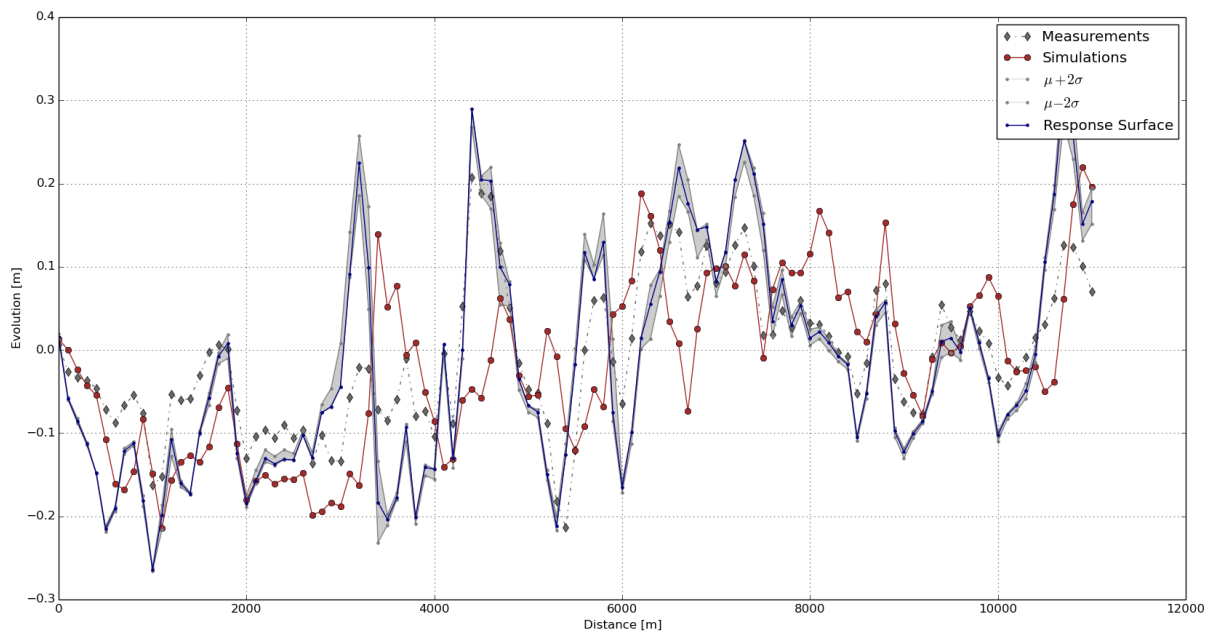


Figure 5.3: Simulation output vs. response surface (validation-Meyer-Peter-Müller model)

The misfit between the original numerical model and its reduction (response surface) implies that the reduced model in calibration was not a sufficient approximation of the original numerical model. The parameter distributions of the survived realizations after the bootstrap filtering (Section 3.2.2) using the validation dataset are shown in Figure 5.4.

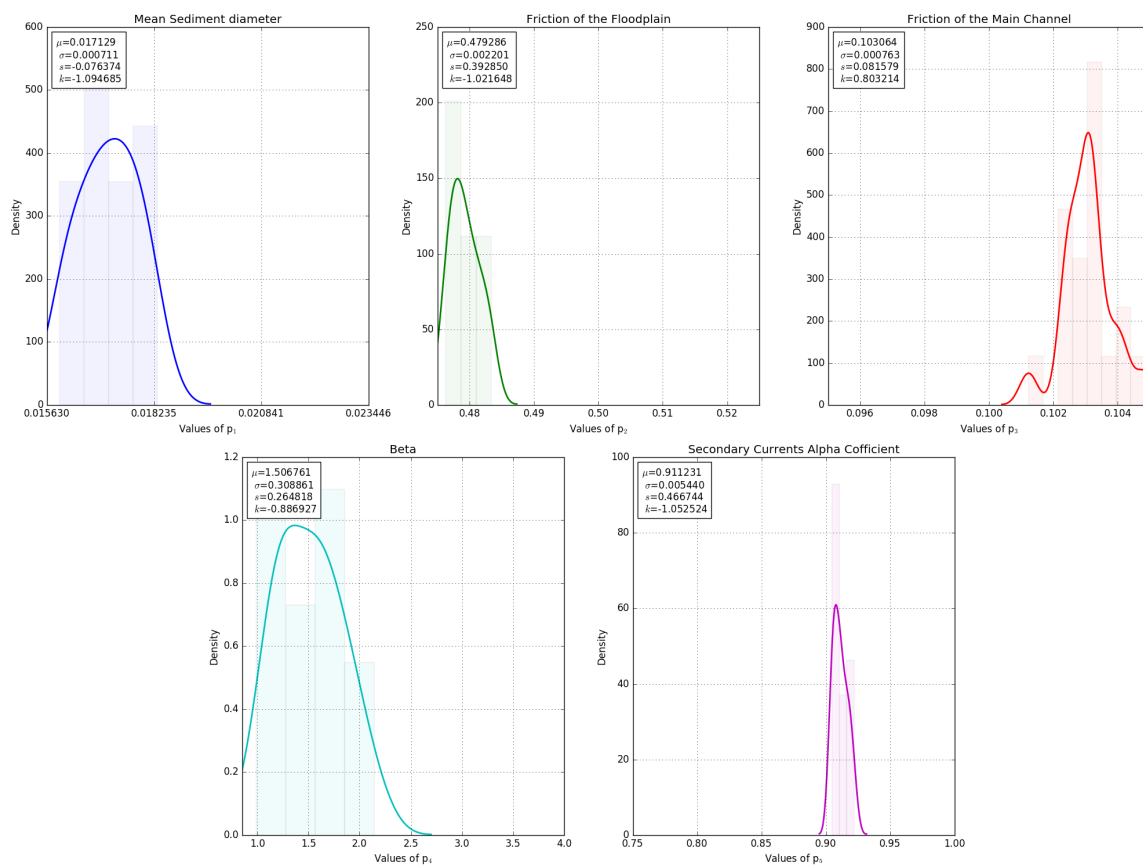


Figure 5.4: The posterior PDF of parameters (validation-Meyer-Peter-Müller model)

The yielded distributions of the parameters, which were initially assumed to be uniform approximately resemble the Gaussian (Normal) distribution.

Einstein-Brown Model: In the following, the diagrams for the hydro-morphodynamic numerical model embedding Einstein-Brown formula for calculation of the bed-load transport are presented. Figure 5.5 indicates that the surrogate model did not adequately represent the original numerical model at some locations. This fact could be associated with the presence of some degree of nonlinearity in the real model at these positions.

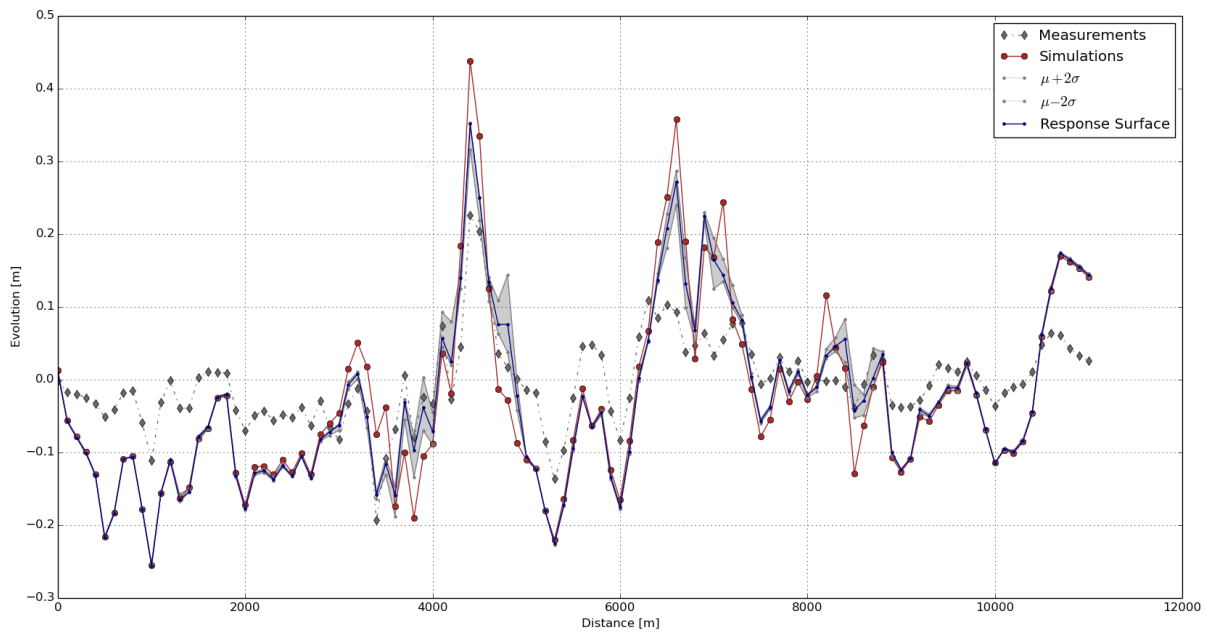


Figure 5.5: Simulation output vs. response surface (calibration-Einstein-Brown model)

The probability density functions of the posterior parameter sets after the calibration step, shown in Figure 5.6, reveals that all the parameters except the floodplain's friction followed the rather normal distribution. The reason can be associated to whether the floodplain was not inundated often enough during the simulation period, so that there is no statistical significance for the friction floodplain parameter.

The posterior parameter sets and the surrogate model were used in the validation step. The simulation output of the original models against the response surface for the most probable parameter set is depicted in Figure 5.7. The response surface approximated the synthetic bed evolutions more acceptably in comparison with the original model.

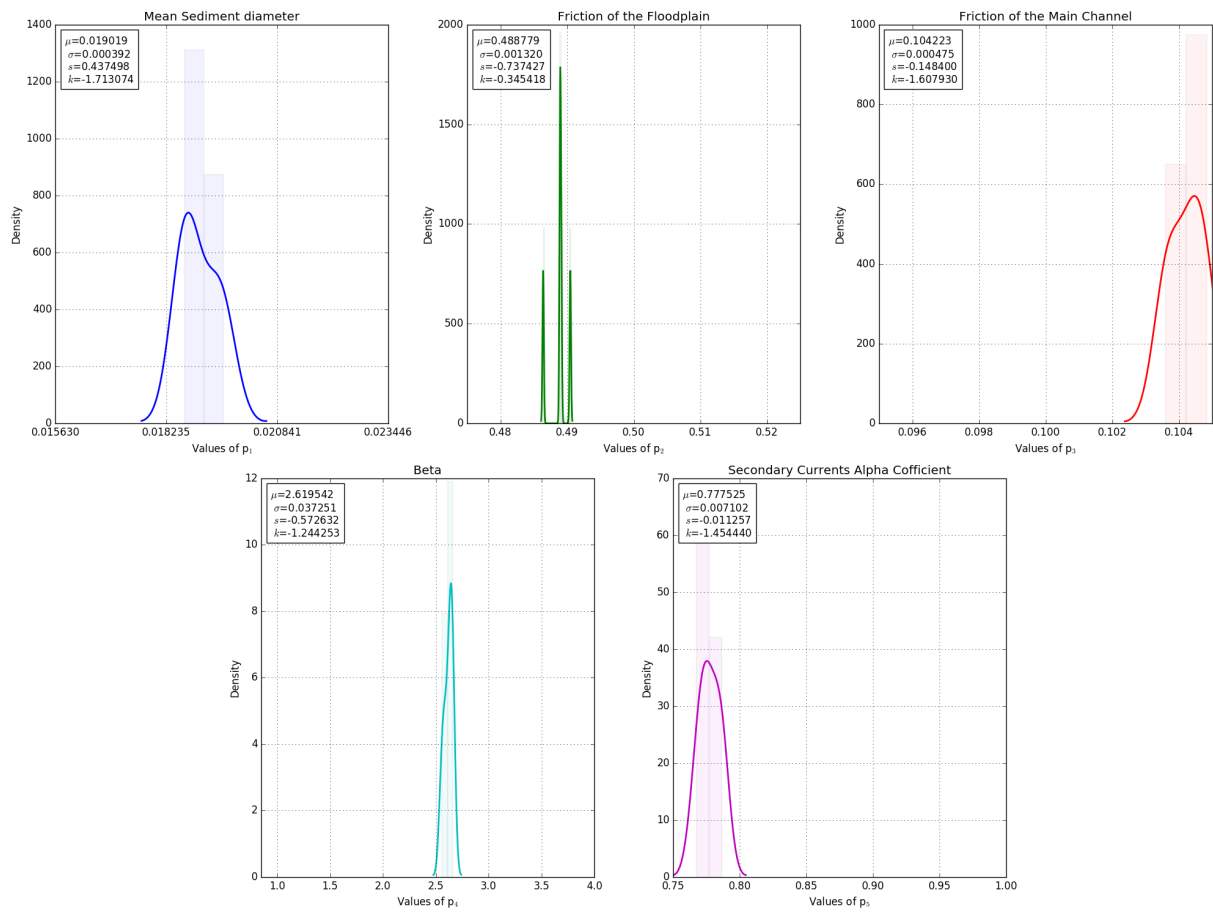


Figure 5.6: The posterior PDF of parameters (calibration-Einstein-Brown model)

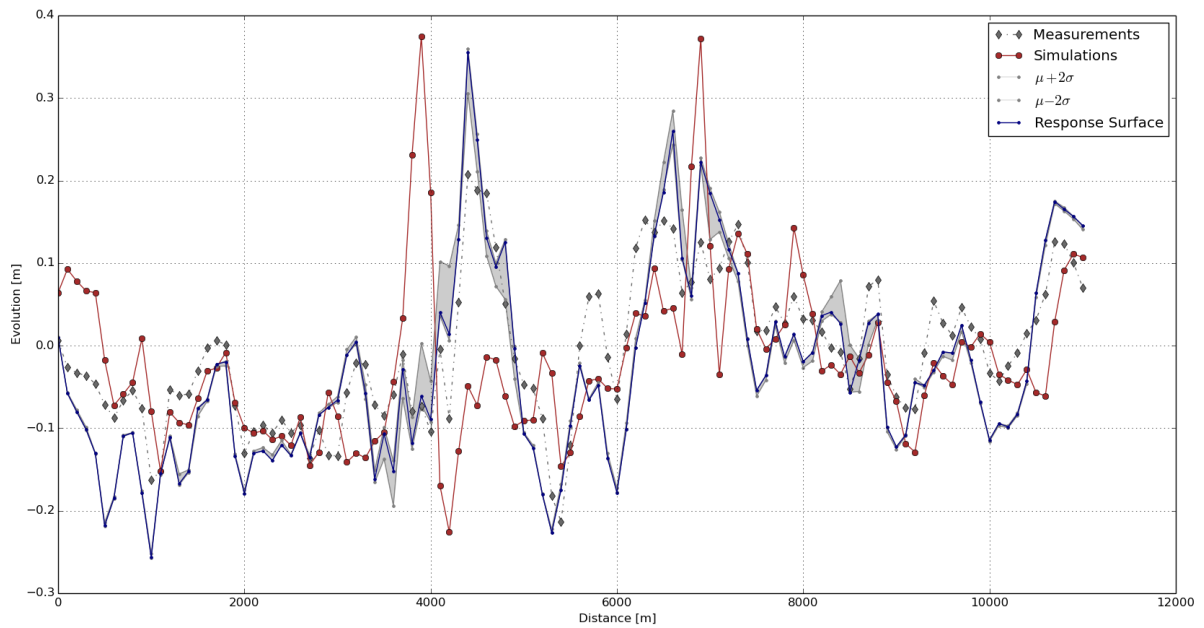


Figure 5.7: Simulation output vs. response surface (validation-Einstein-Brown model)

Comparing the posterior distribution of parameters after the calibration (Figure 5.6) and the validation steps (Figure 5.7), one can conclude that more realizations passed the bootstrap filtering stage successfully after validation than calibration phase. This fact does not necessarily signify that the realizations after the validation possessed higher likelihood weights than after the calibration. Further, the shapes of the PDFs are more concentrated and resemble that of normal distributions.

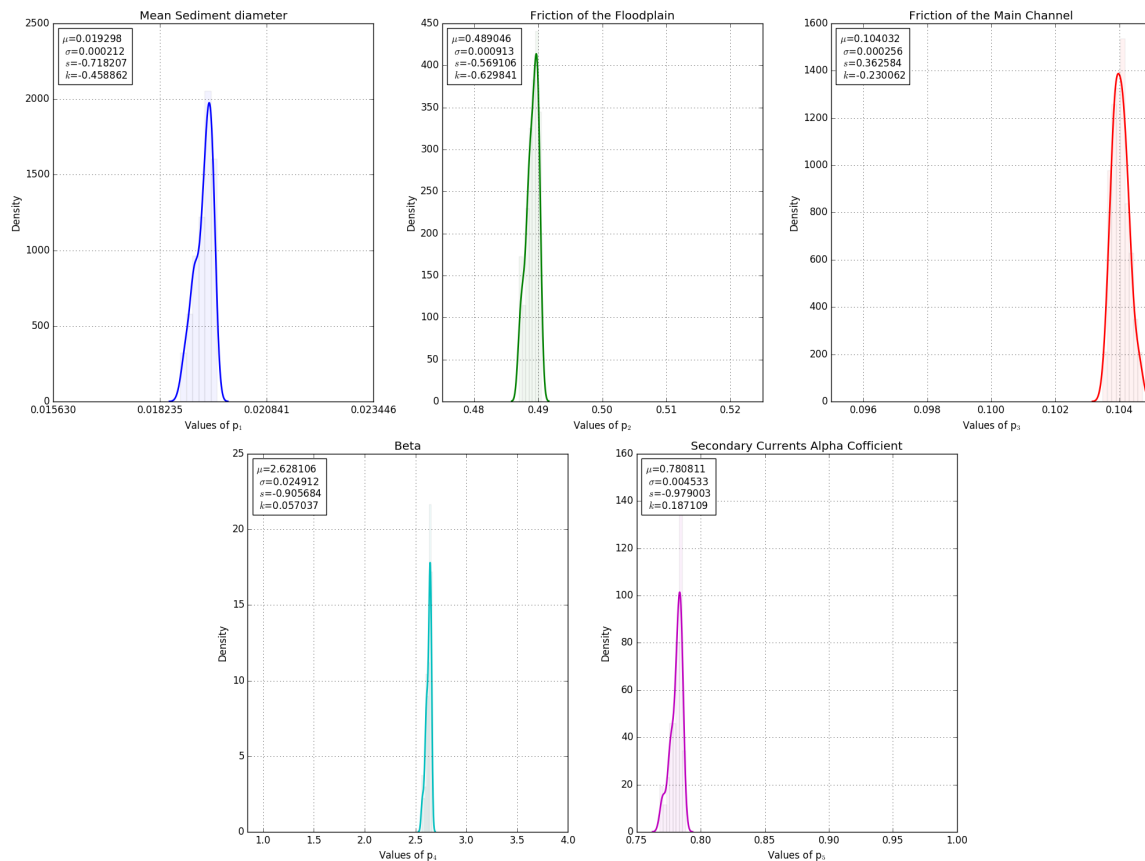


Figure 5.8: The posterior PDF of parameters (validation-Einstein-Brown model)

Modified Engelund-Hansen Model: Similar to other models, the surrogate model correctly represented the original numerical model (Figure 5.9). However, the original hydro-morphodynamic model containing the modified Engelund-Hansen equation in Telemac-2d-Sisyph only exhibited better match between 3-km and 6-km after the inlet boundary.

Figure 5.10 illustrates the parameter distributions after the calibration. The initial uniform shapes of parameters resulted in the less informative distributions with several peaks, i.e. the realizations with relatively better likelihoods were concentrated around various values oppose to the previous models.

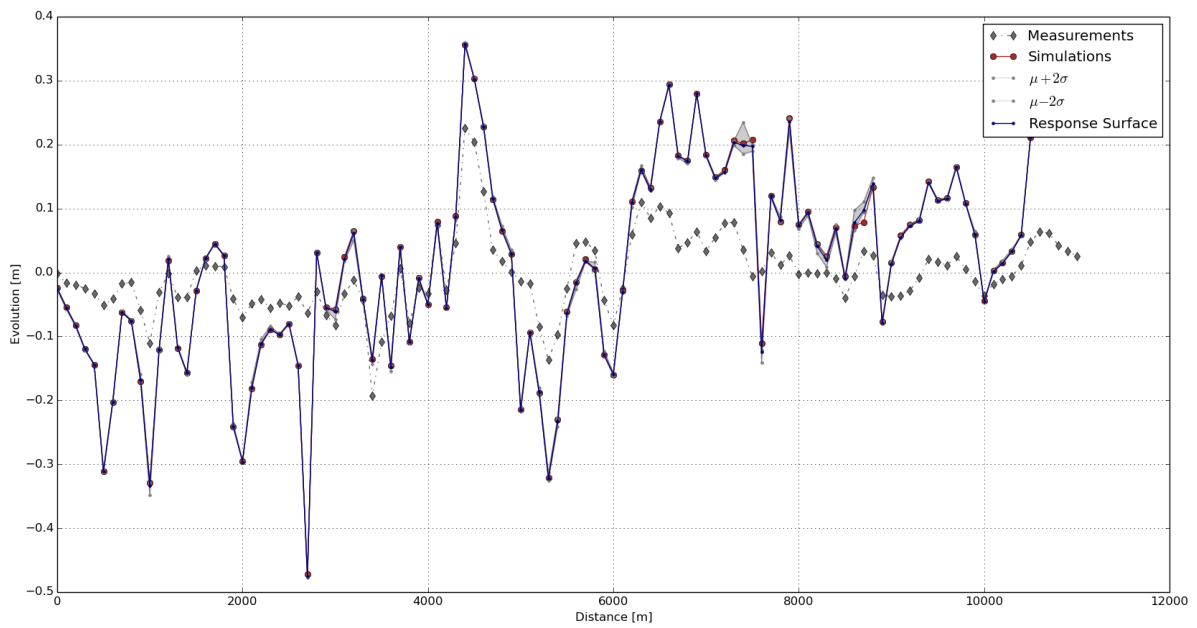


Figure 5.9: Simulation output vs. response surface (calibration-Mod. Engelund-Hansen model)

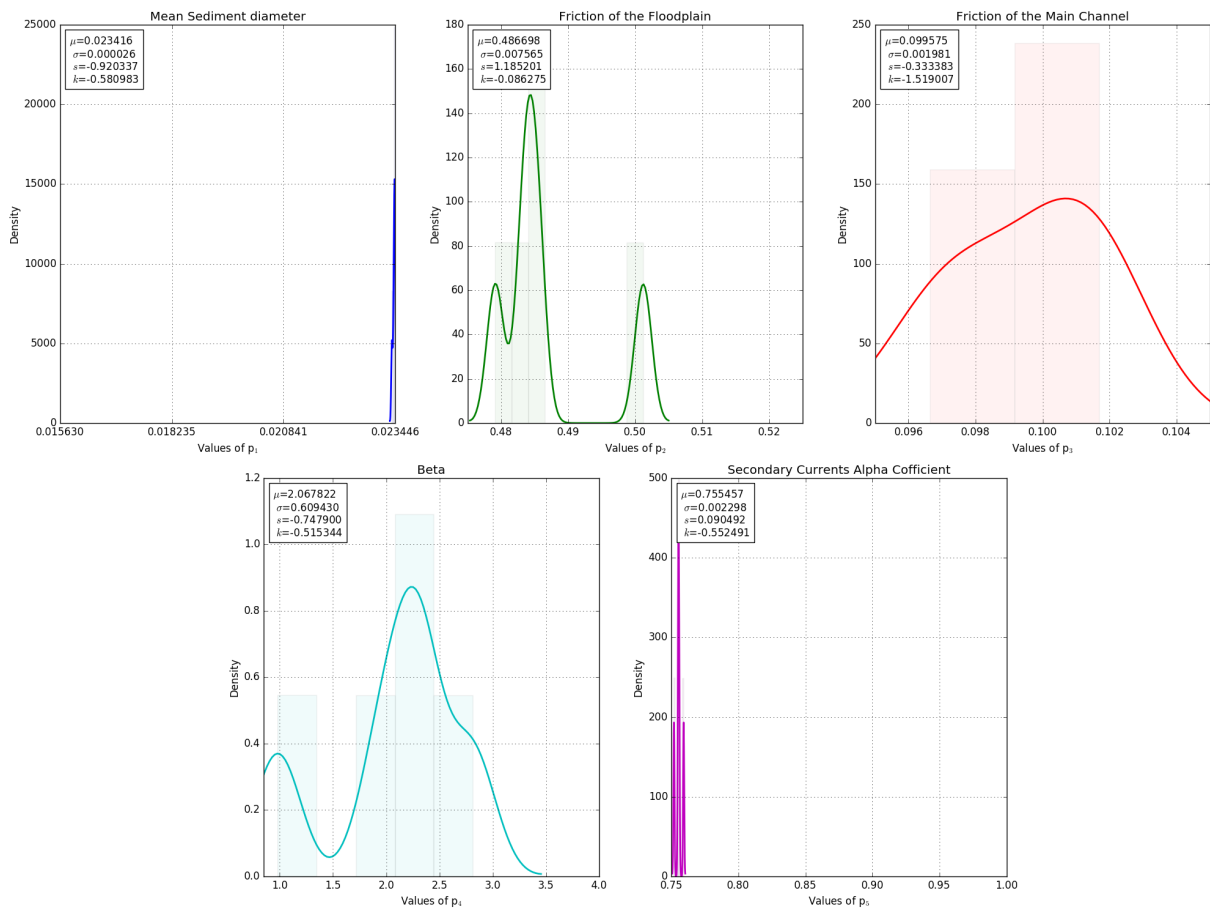


Figure 5.10: The posterior PDF of parameters (calibration-Mod. Engelund-Hansen model)

The surrogate model, which was built using the calibration data set, was verified with another synthetic bed evolution. The performance of this model against the original model via their most probable parameter set is shown in Figure 5.11.

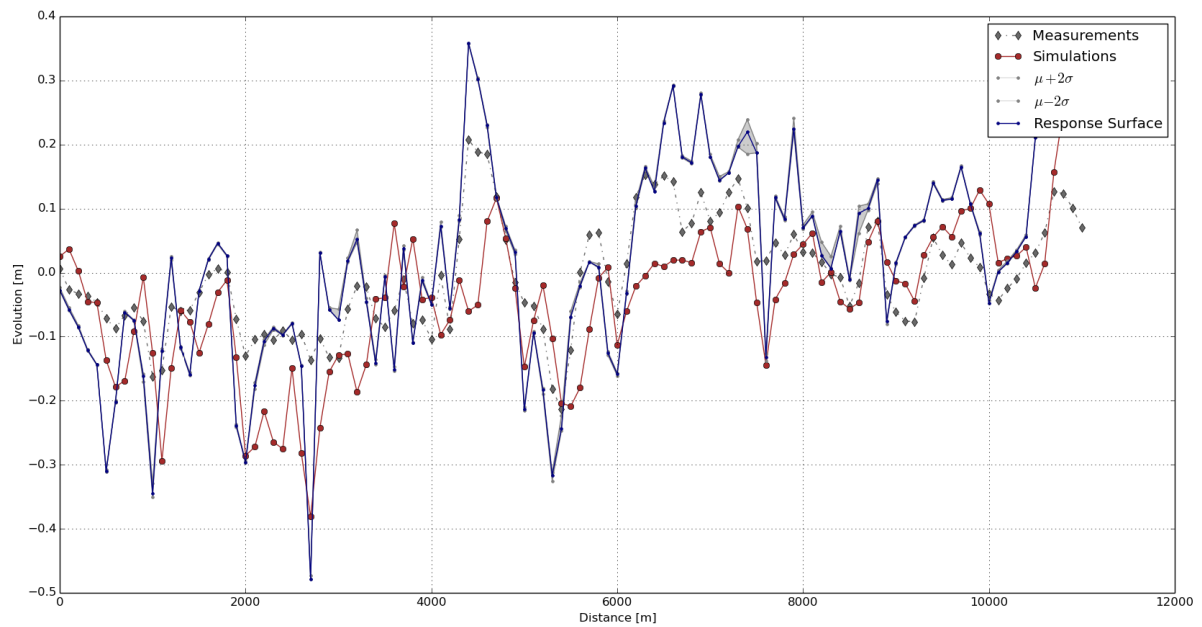


Figure 5.11: Simulation output vs. response surface (validation-Mod. Engelund-Hansen model)

The probability distribution functions of the parameters after the validation step (Figure 5.12) display more concentrated peaks, providing additional instructive information about the most probable region of parameters for the task of the optimization.

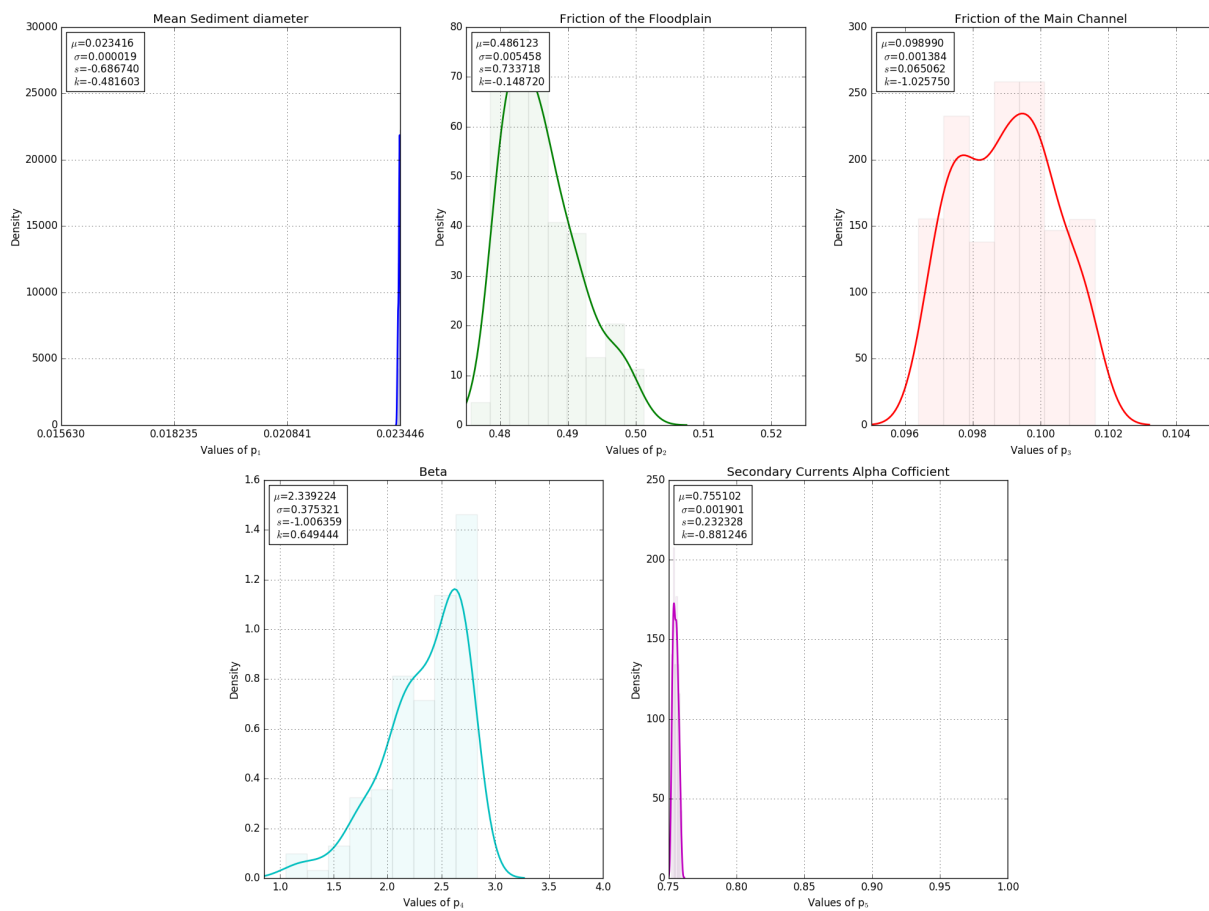


Figure 5.12: The posterior PDF of parameters (validation-Mod. Engelund-Hansen model)

Van Rijn Model: The morphodynamic variant of the Van Rijn transport equation in Sisyphe coupled with the hydrodynamic module (Telemac) could approximate the synthetic bed evolution of the lower Rhine satisfactorily, according to Figure 5.13. Moreover, the response surface, constructed in the calibration phase, matched the output of the original numerical model similar to all competing models.

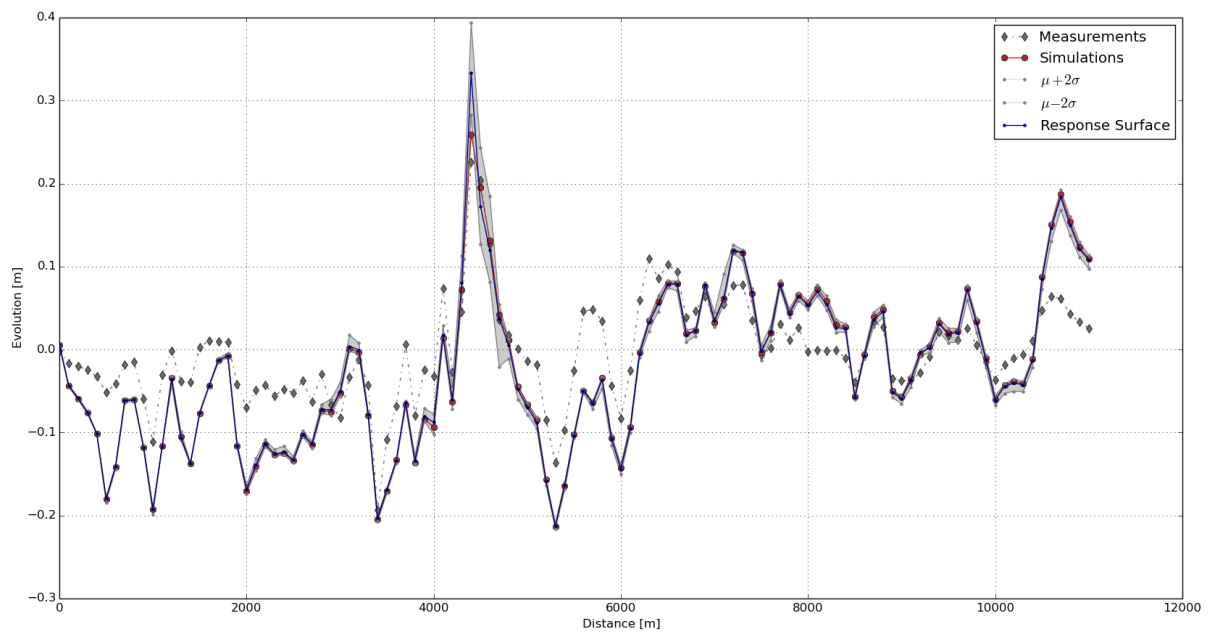


Figure 5.13: Simulation output vs. response surface (calibration-Van Rijn model)

The probability density functions of posterior parameter sets are illustrated in Figure 5.14. Contrary to the previously presented models, the distributions covered relatively larger regions of the prescribed parameter ranges, suggesting that a large number of realizations received high likelihood weights. This fact indicates that the simulated averaged bed evolution for many parameter sets within the defined parameter space were closer to the measurements.

Figure 5.15 displays the outputs of the original and reduced model for the parameter set with the maximum likelihood weight. Even though the surrogate model from calibration step has not been adapted to the new data set (validation data set), it presented a proper fit with the synthetic measurements.

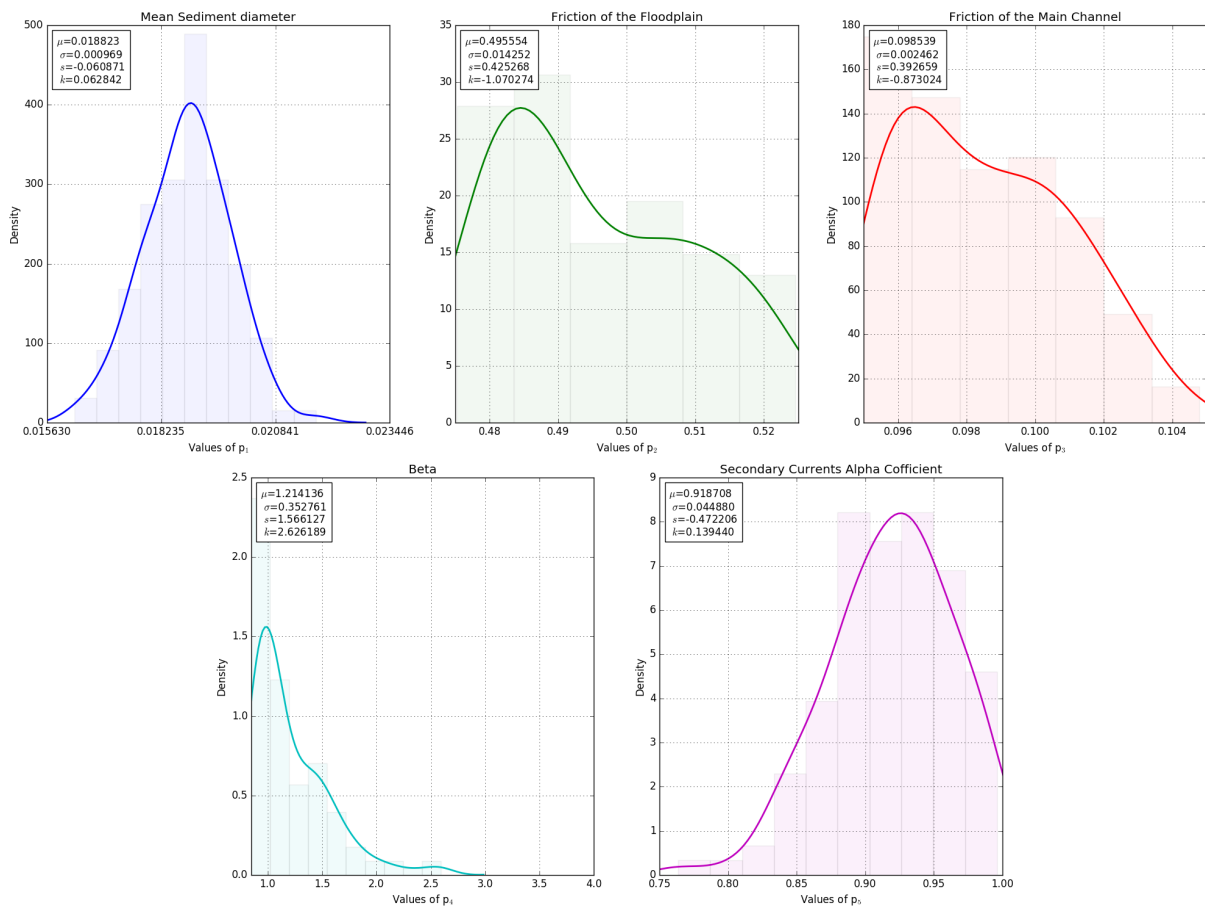


Figure 5.14: The posterior PDF of parameters (calibration-Van Rijn model)

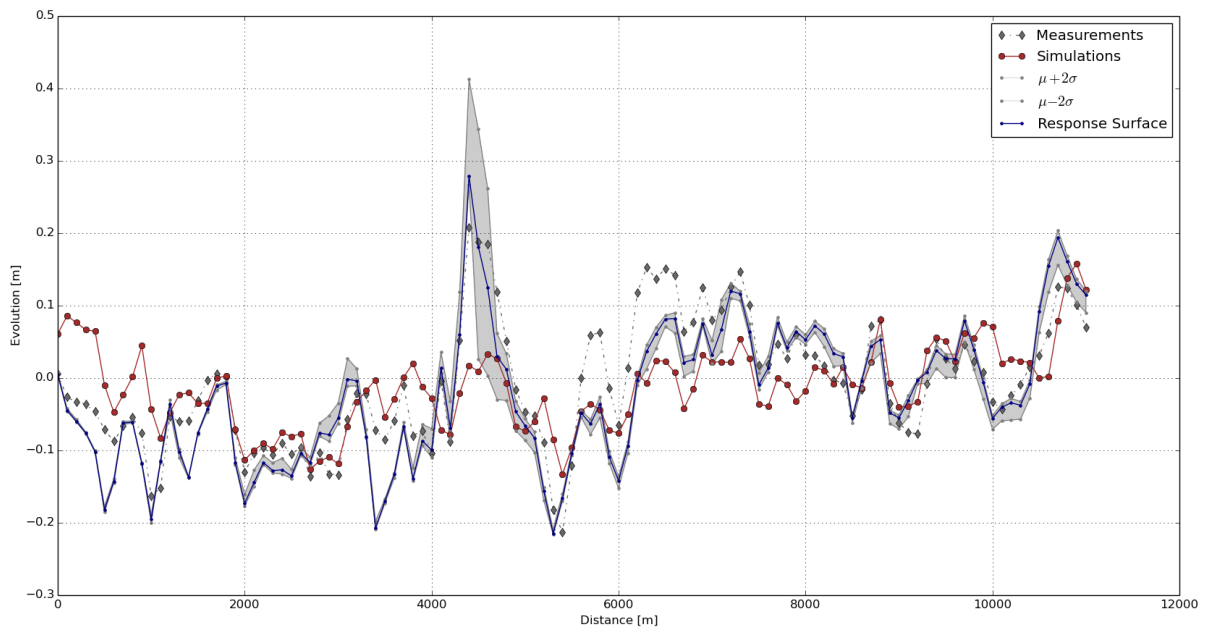


Figure 5.15: Simulation output vs. response surface (validation-Van Rijn model)

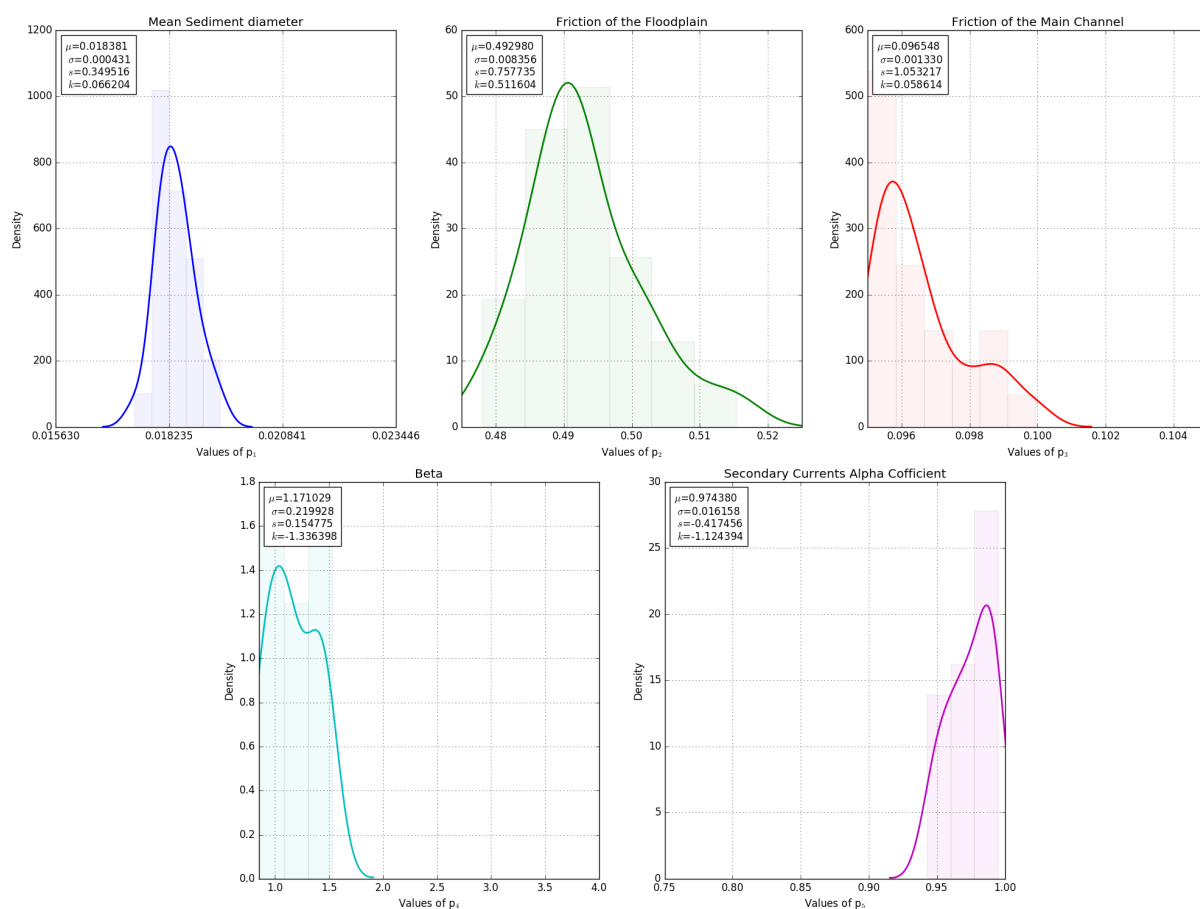


Figure 5.16: The posterior PDF of parameters (validation-Van Rijn model)

The parameter distributions after the validation step were more concentrated in comparison to that of calibration phase (Figure 5.14).

Hunziker Model: The simulation output of the Hunziker model against the corresponding response surface, which is shown in Figure 5.17 indicates a close fit between this model and its reduced version (response surface) and the artificial measurement after the calibration stage. Further, the probability distributions of the posterior parameters, presented in Figure 5.18, signify relatively focused formations.

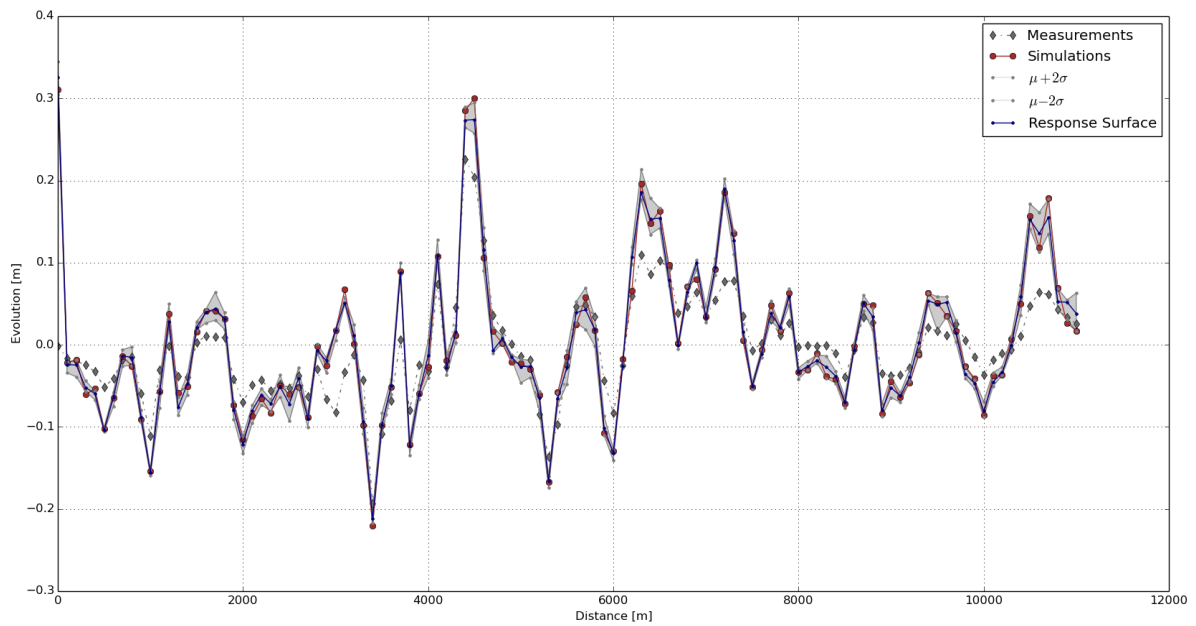


Figure 5.17: Simulation output vs. response surface (calibration-Hunziker model)

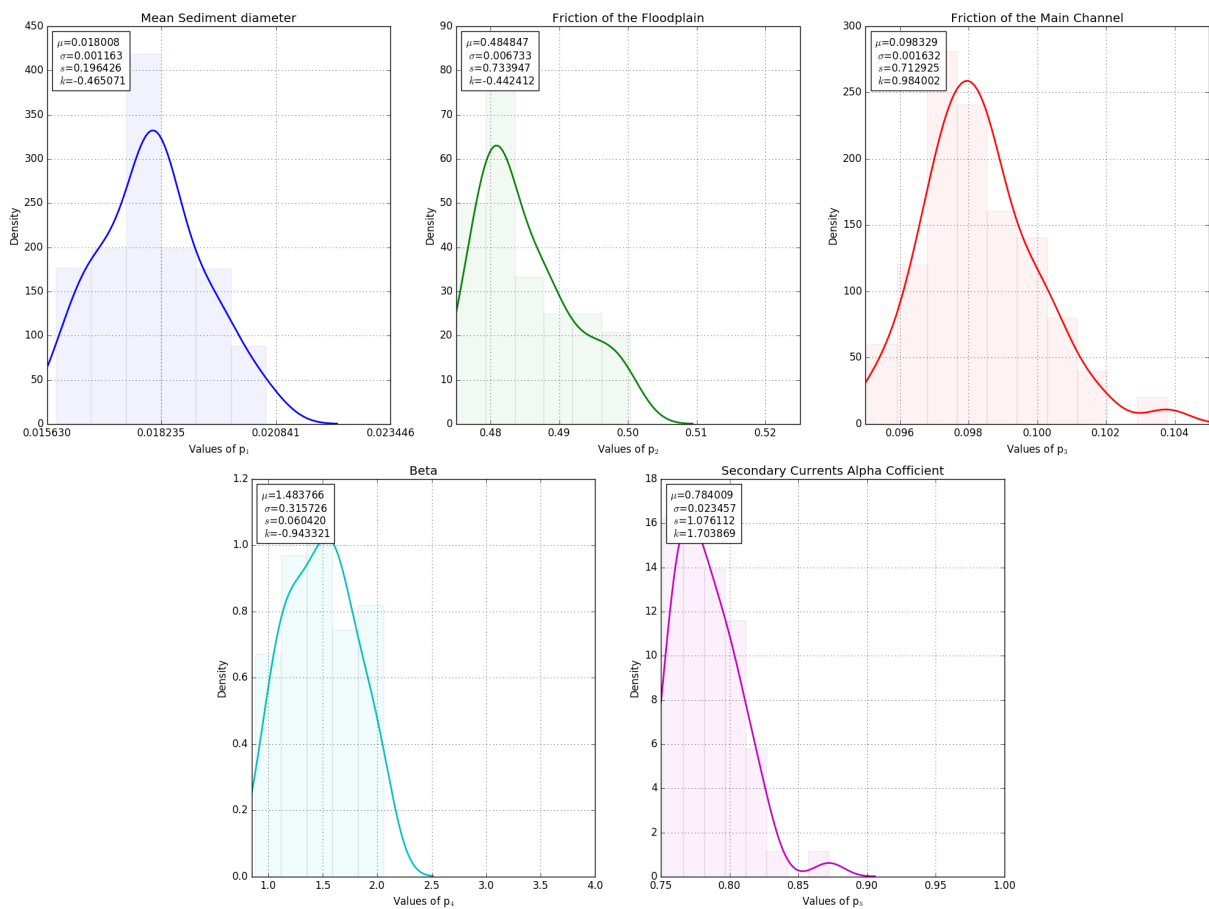


Figure 5.18: The posterior PDF of parameters (calibration-Hunziker model)

As illustrated in Figure 5.19, the simulated bed evolution of the original numerical model succeeded in approximating the artificial bed evolution. The constructed response surface, however, in the calibration step was generally in good agreement with the validation bed development.

The posterior probability distributions after the validation, shown in Figure Figure 5.20 , provides better guidance in locating the best parameter set identification for the task of optimization.

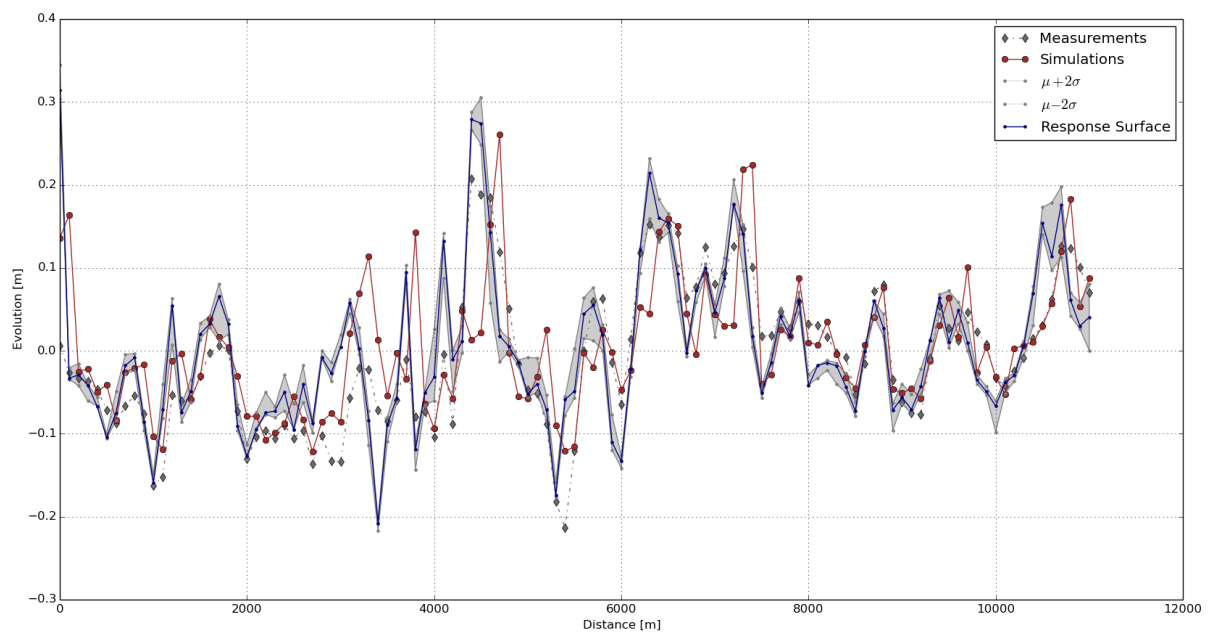


Figure 5.19: Simulation output vs. response surface (validation-Hunziker model)

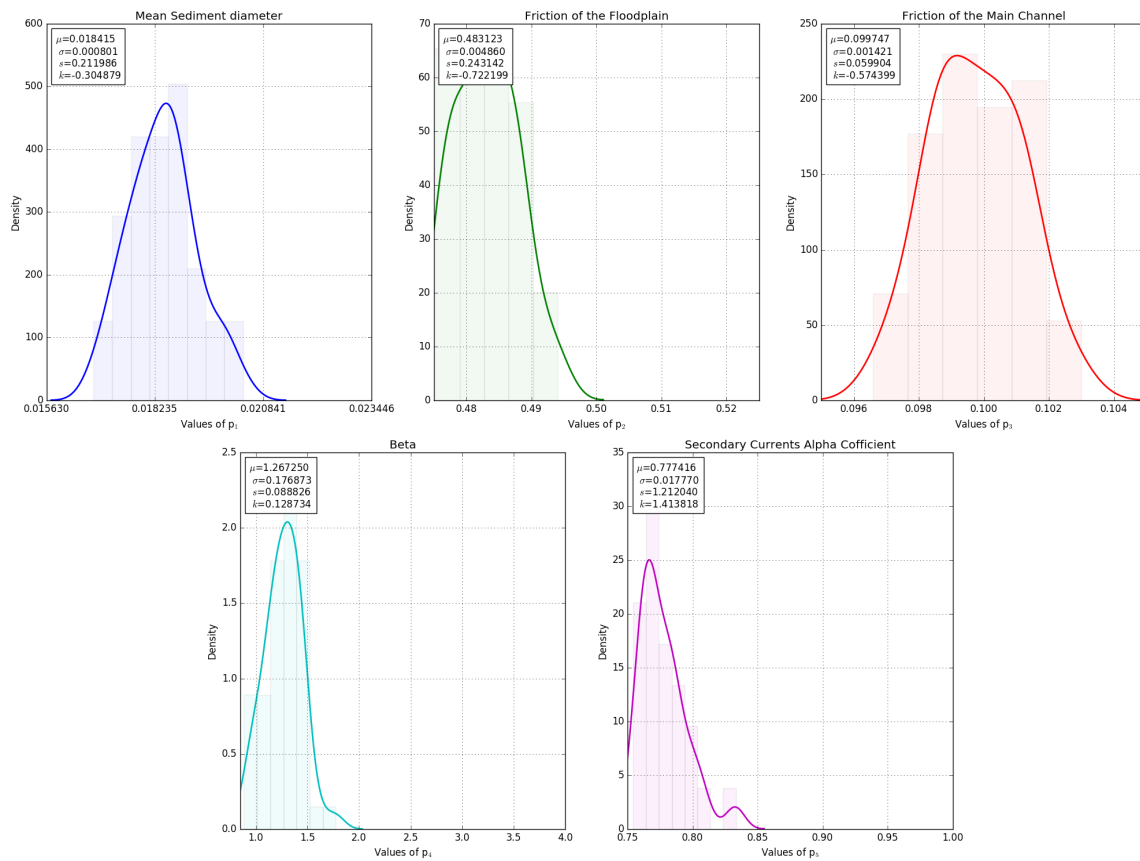


Figure 5.20: The posterior PDF of parameters (validation-Hunziker model)

Wu Model: The hydro-morphodynamic model including the sediment transport of Wu et al. (2000) was used to generate the artificial bed load evolution. As it is visible in Figure 5.21, the synthetic measurement, the simulated bed evolution of the original model and the response surface entirely overlapped, this indicates that the reduction model technique embedded in the BMS framework was utterly successful in approximating the original model.

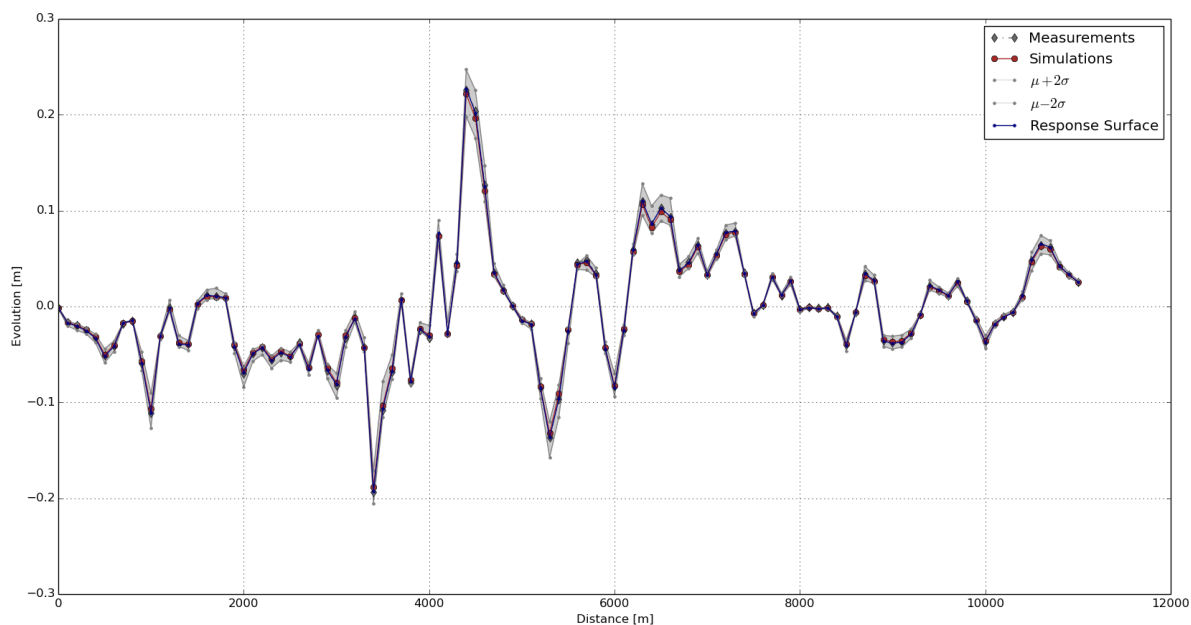


Figure 5.21: Simulation output vs. response surface (calibration-Wu model)

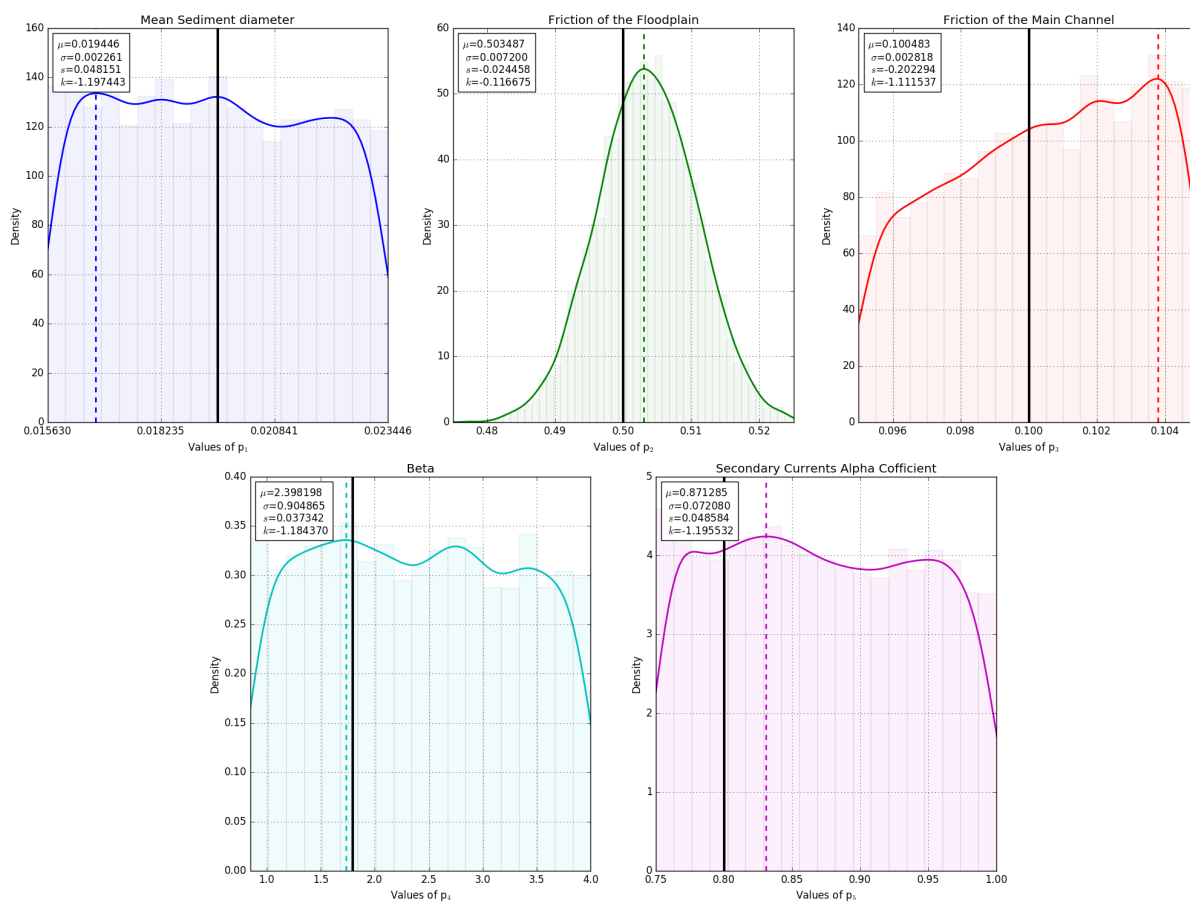


Figure 5.22: The posterior PDF of parameters (calibration-Wu model)

Figure 5.22 presents the probability density distributions of the parameters after the calibration step. The dashed lines represent the values with the highest likelihood weights, whereas the black lines show the parameter values used for generating the synthetic bed evolution for calibration data set. The non-distinguishable distribution shapes indicate that several parameters received approximately similar likelihoods.

The simulated bed evolution of the original model and the surrogate model for the realization with the highest likelihood after the validation step is presented in Figure 5.23.

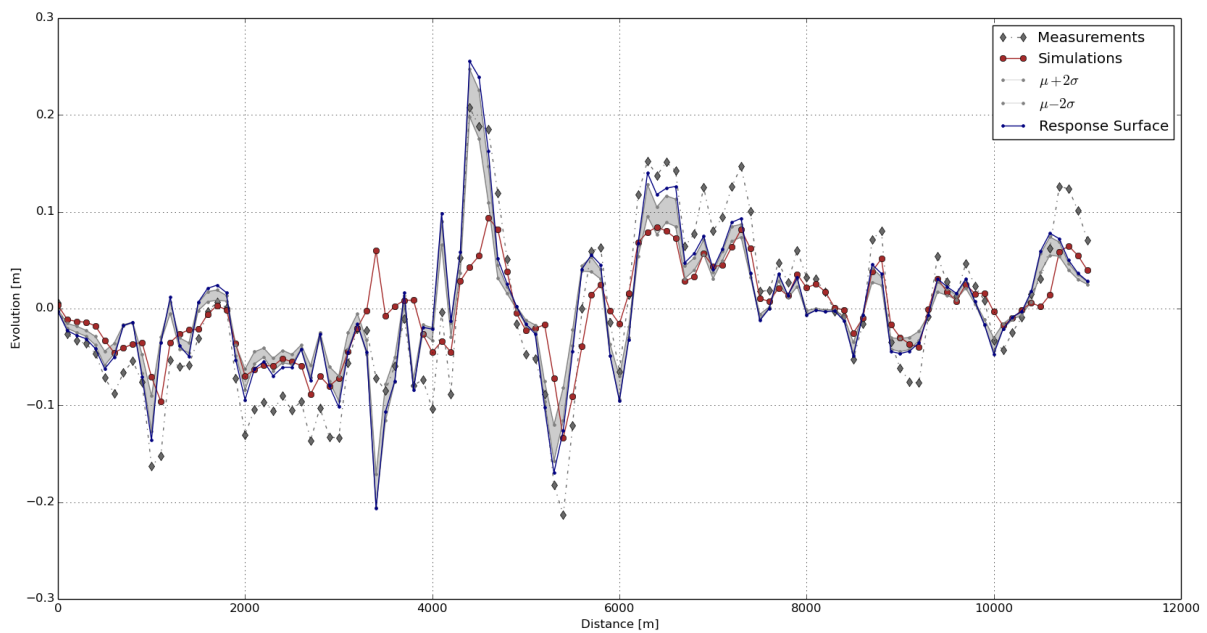


Figure 5.23: Simulation output vs. response surface (validation-Wu model)

The posterior distribution of parameters after the validation stage is shown in Figure 5.24.

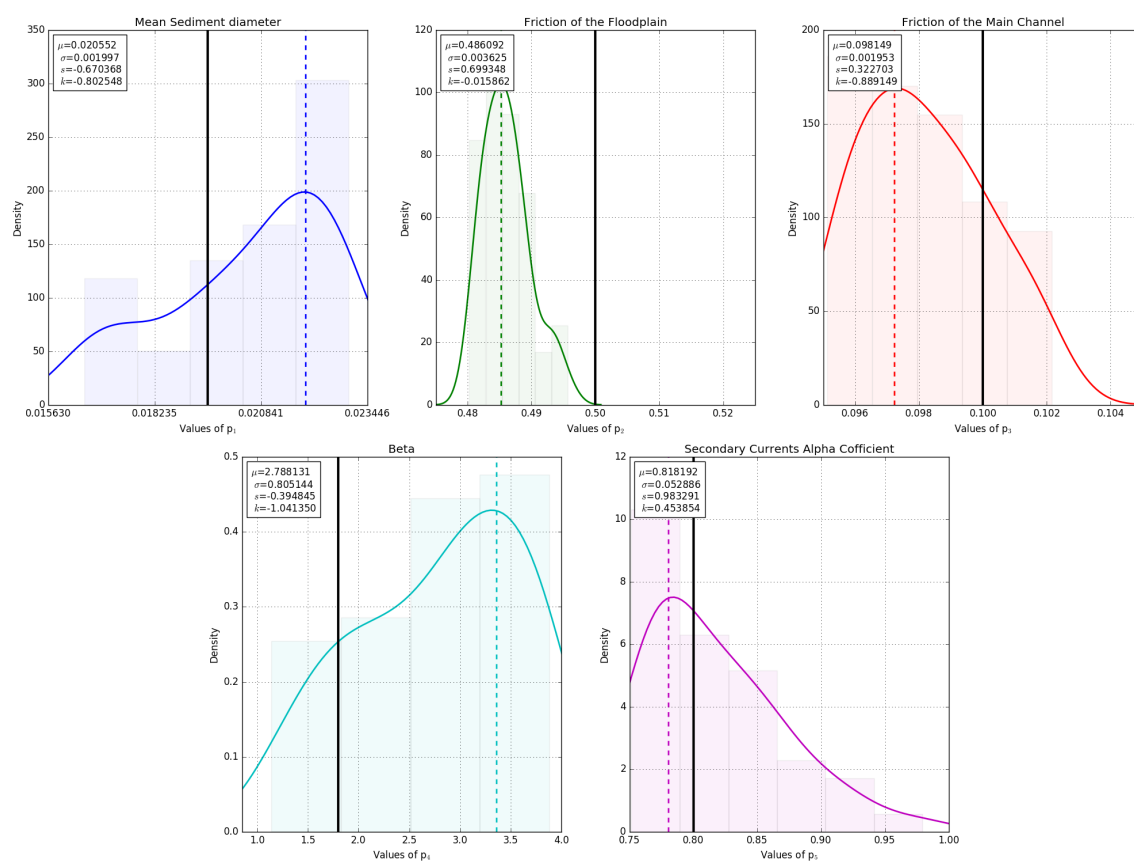


Figure 5.24: The posterior PDF of parameters (validation-Wu model)

The difference between the known parameter values (black lines) and the values of parameters with highest density (dashed lines) for the calibration and validation steps are summarized in Table 5.3.

Table 5.3: The accuracy of parameter inferences after calibration and validation step

Parameters	after calibration (%)	after validation (%)
Mean sediment diameter	-14.32	+12.19
Friction coefficient of the main channel	+3.79	-2.78
Friction coefficient of the floodplain	+0.60	-2.95
Beta	-3.61	+86.53
Secondary currents alpha coefficient	+3.83	-2.48

The absolute value of discrepancy reduced for the mean sediment diameter, the friction coefficient of main channel, and secondary currents alpha coefficient. In contrast, the variance of the friction coefficient of floodplain increased slightly. The biggest change of the discrepancy belonged to the variable *beta*. This variation is not unexpected because the surrogate

model that also influences the likelihood assignment step was not adapted to the new synthetic measurement data set. Moreover, several solutions might exist for one problem, i.e. different parameter set might produce the same results; this is known as ill-posed problems. According to Hadamard (1902), well-posed mathematical models of physical phenomena must possess the properties that a unique solution exists, and its behavior varies continuously with the initial condition, whereas the problems that are not well-posed are labeled *ill-posed*.

The validation step with smaller measurement error (0.025) was repeated to investigate the effect of the measurement error on the discussed discrepancies. The posterior probability density distributions are presented in Figure 5.25, and the associated differences in parameters for the initial measurement error and new error are presented in Table 5.4.

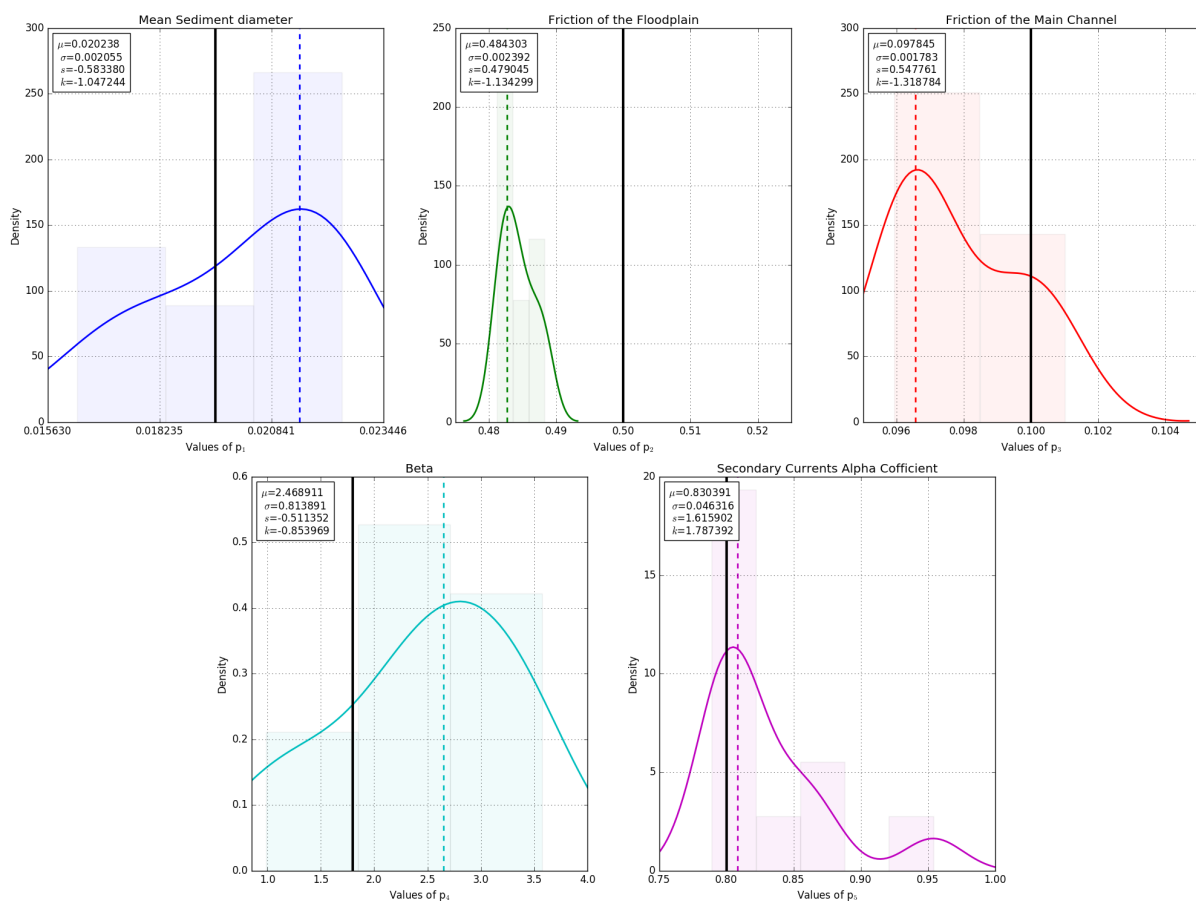


Figure 5.25: The posterior PDF of parameters with measurement error of 0.025 (validation- Wu model)

Table 5.4: The impact of measurement error on parameter inferences after validation step

Parameters	Meas. Error 0.03 (%)	Meas. Error 0.025 (%)
Mean sediment diameter	+12.19	+9.99
Friction coefficient of the main channel	-2.78	-3.464
Friction coefficient of the floodplain	-2.95	-3.45
Beta	+86.53	+36.67
Secondary currents alpha coefficient	-2.48	+1.05

From the table above, it can be inferred that the smaller measurement error relatively improved the accuracy of the identifying the most likely regions of variables for the task of optimization.

BME Comparison: As discussed in Section 3.3.1, Bayesian Model Evidence (BME) is a product of Bayesian Model Averaging, also referred to as marginal likelihood or prior predictive of the observed data based on the prior distribution of the parameters (Equation 3.12). The development of BME values of the competing models against the iterations on the improvement of their surrogate models (response surface) in calibration step is presented in Figure 5.26.

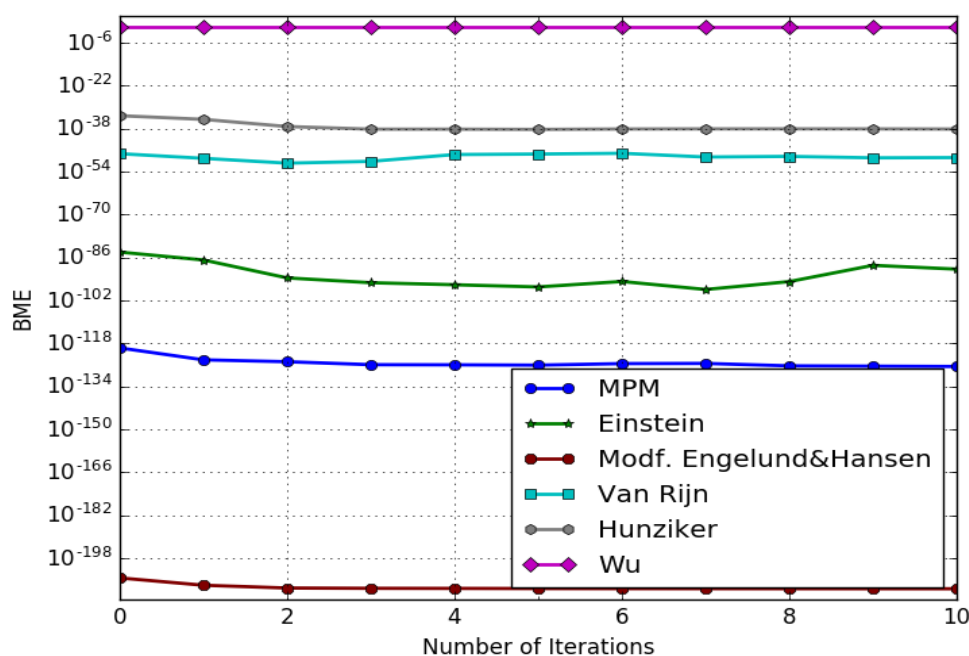


Figure 5.26: Bayesian model evidence vs. iterations for twin experiment of lower Rhine model in calibration step (Log-scale)

According to the graph above, the hydro-morphodynamic model including Wu equation obtained noticeably higher BME values (approx. 1) and the model including modified Engelund

and Hansen acquired considerably small BME values. However, the final model ranking is based on the BME values after the validation. Table 5.5 summarizes the BME values of the variants after the validation step.

Table 5.5: The BME comparison after the validation for the twin experiment of the lower Rhine model

Hydro-Morphodynamic Model	BME of Validation	Rank
Meyer-Peter-Müller	3.20E-57	5
Einstein-Brown	3.63E-37	4
Modified Engelund-Hansen	3.40E-120	6
Van Rijn	1.30E-13	2
Hunziker	1.42E-32	3
Wu	0.99	1

As it is evident from the table above, the model variant of Wu equation is the clear winner. This fact is also in accordance with our finding for the model ranking after the calibration step. Additionally, the Van Rijn model surpassed the Hunziker model in the validation step.

5.2 BMS of the Real Lower Rhine Model

The real bed evolution observation of the lower Rhine between 738.5 and 749.0 from 2002 to 2004 and from 2004 to 2006 shown in Figure 2.13 and Figure 2.14 were introduced to the framework as the calibration and validation measurements, respectively. In this case, four competing hydro-morphodynamic models were considered.

5.2.1 Setup and Implementation

All the considered morphodynamic models, BMS framework's inputs, as well as calibration and validation scenarios are summarized in the following sections.

Examined Hydro-Morphodynamic Models: The selected sediment transport formulae for the morphodynamic models in the real test of the numerical model of the lower Rhine is summarized in Table 5.6.

Table 5.6: The morphodynamic models used in the real model of the lower Rhine

Name of the bed load Equation	Year	Mode of Transport
Meyer-Peter-Müller	1948	Bed-load
Van Rijn	1984	Bed-load
Hunziker	1995	Bed-load
Wu	2000	Bed-load

Chosen Uncertain Parameters and their Bounds: The uniform distribution of the parameters were selected for all parameters. The similar selected hydro-morphological parameters in the twin experiment, but with different lower and upper bounds are used in this investigation as illustrated in Table 5.7.

Table 5.7: The selected uncertain parameters and their ranges (real lower Rhine model)

ID	Uncertain Parameter's Name	Lower Bound	Upper Bound	Unit
P ₁	Sediment diameter	0.01856	0.02051	m
P ₂	Friction Coefficient of the main channel	0.49	0.51	m
P ₃	Friction Coefficient of the flood plain	0.098	0.102	m
P ₄	Beta	0.85	4.00	-
P ₅	Secondary Currents Alpha Coefficient	0.75	1.00	-

Measurement Error, Sample Size and number of Iterations: Similar to the twin experiment, the measurement error of 0.05 and ensembles of 20,000 realizations per model were defined. Contrary to the twin experiment, five iterations of Bayesian updating were prescribed for each model.

Stochastic Calibration and Validation Scenarios: The models were stochastically calibrated, and validated within two different periods of two years. Section 2.4 presented the measured bed evolution plots, the derivation method, and all other specifications.

5.2.2 Bayesian Model Ranking for the Real lower Rhine Model

The following section includes the output of the BMS for the numerical model of the lower Rhine with real bed evolution for all four rival hydro-morphodynamic models. The remaining results are presented in a separate section in Appendix II.

Meyer-Peter-Müller Model: The plot in Figure 5.27 illustrates the simulation output of the hydro-morphodynamic model including the Meyer-Peter-Müller equation for the bed-load transport rate and the bed evolution measurement from 2002 to 2004. Furthermore, the blue curve signifies the constructed response surface considering the parameter set with the highest likelihood after the calibration phase.

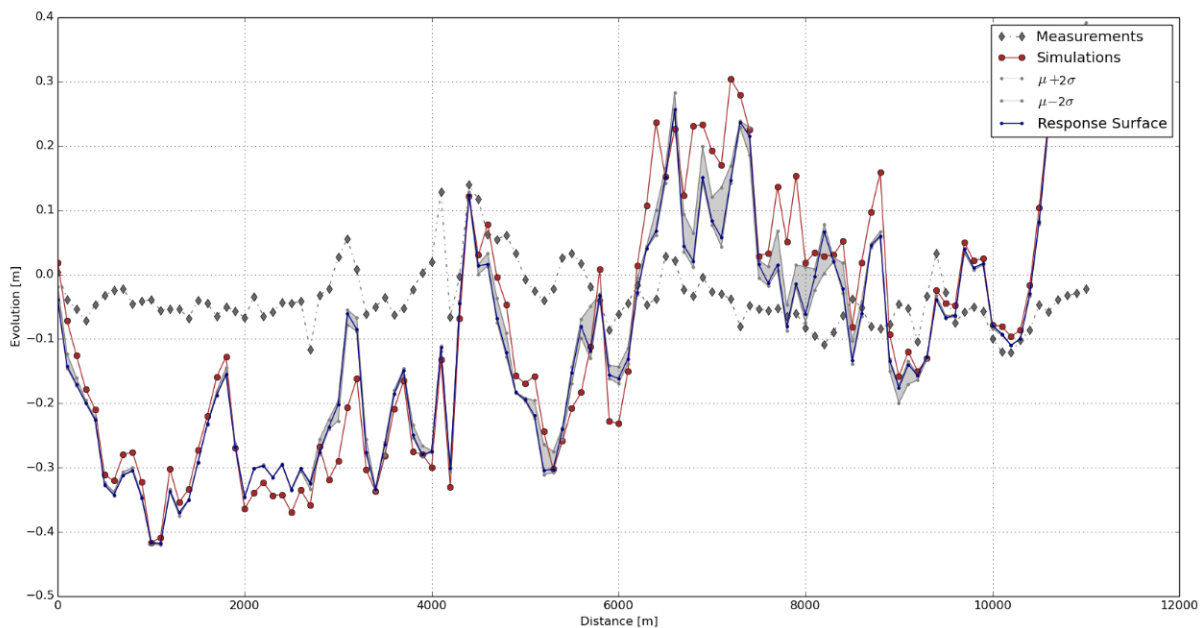


Figure 5.27: Simulation output vs. response surface (calibration-Meyer-Peter-Müller model)

As it is visible from Figure 5.27, the updated response surface after five iterations could reasonably capture the pattern of the original hydro-morphodynamic model in Telemac-2d-Sisyphe but was not utterly successful in representing its magnitude.

Figure 5.28 displays the probability density function (PDF) of the posterior distribution of uncertain parameters along with their statistical moments.

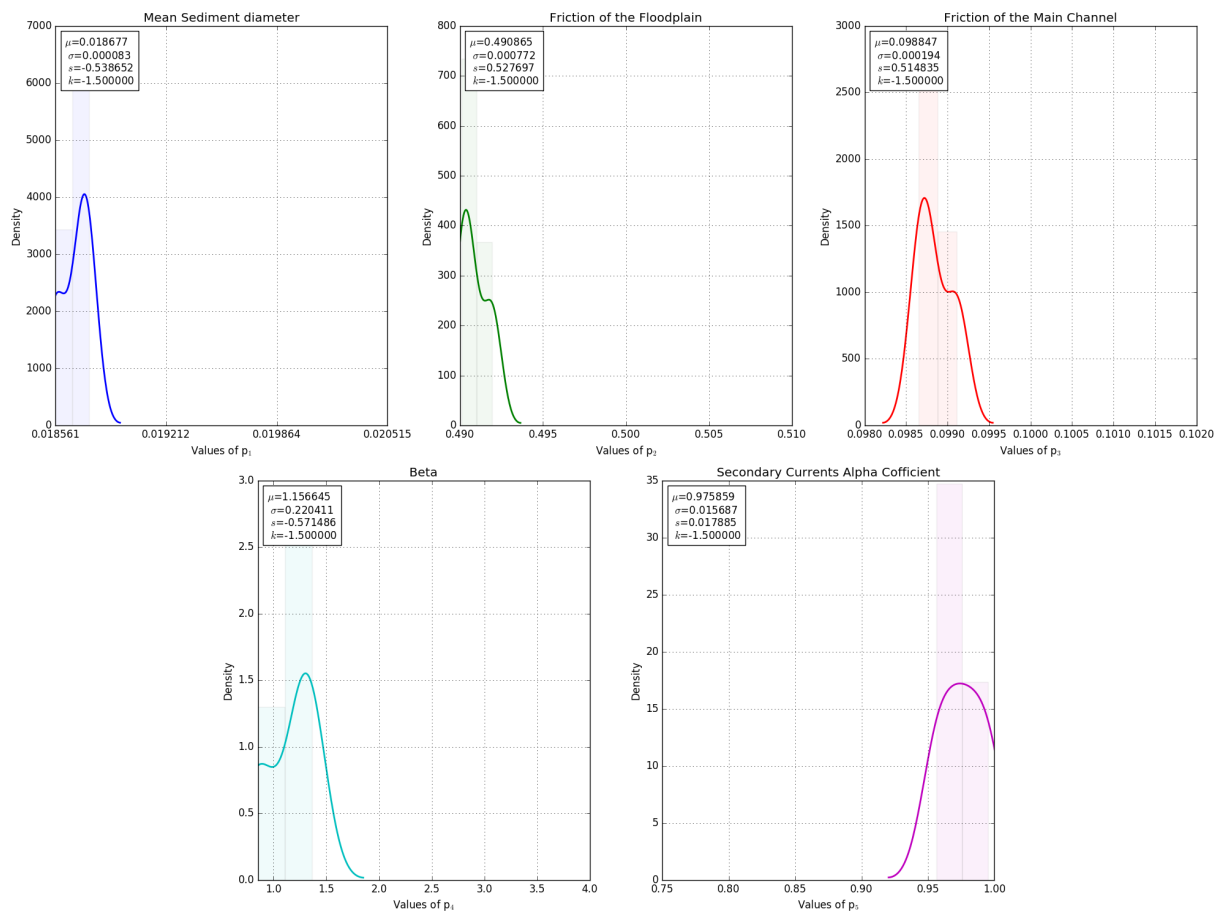


Figure 5.28: The posterior PDF of parameters (calibration-Meyer-Peter-Müller model)

As mentioned previously, the likelihood weights of the prior realization for the validation stage were assigned based on the validation measurements (the measurement period of 2004 to 2006).

Figure 5.29 illustrate the simulation output and the performance range of the response surface for the parameter set with the highest likelihood after the validation step. Figure 5.30 shows the probability density function (PDF) of the posterior distribution of uncertain parameters after validation step.

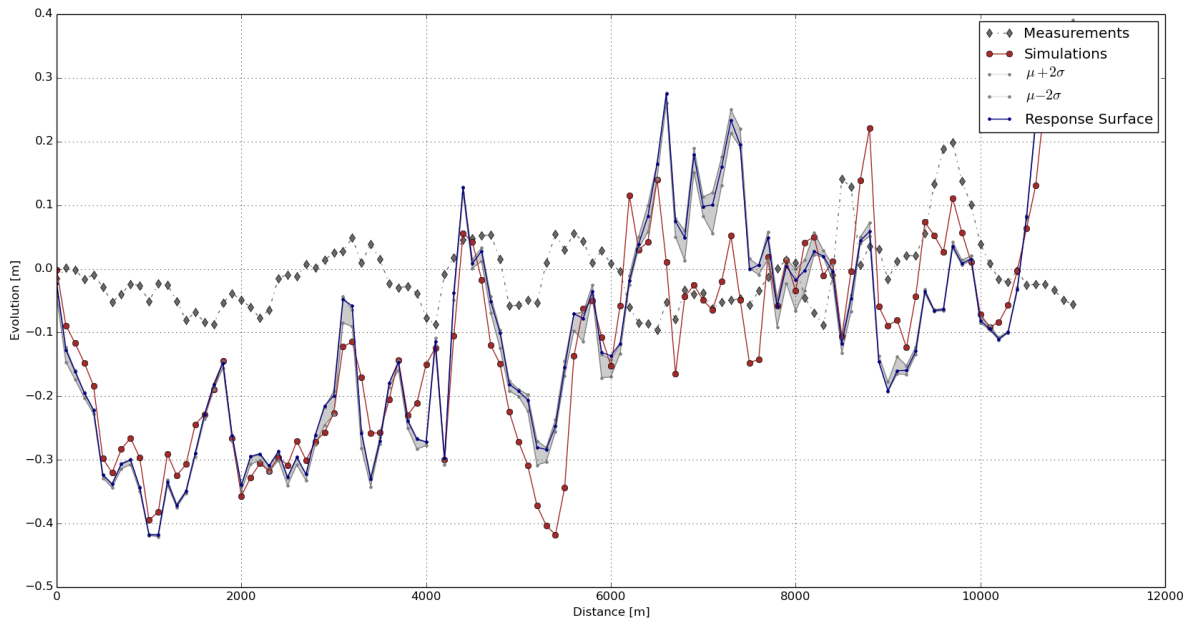


Figure 5.29: Simulation output vs. response surface (validation-Meyer-Peter-Müller model)

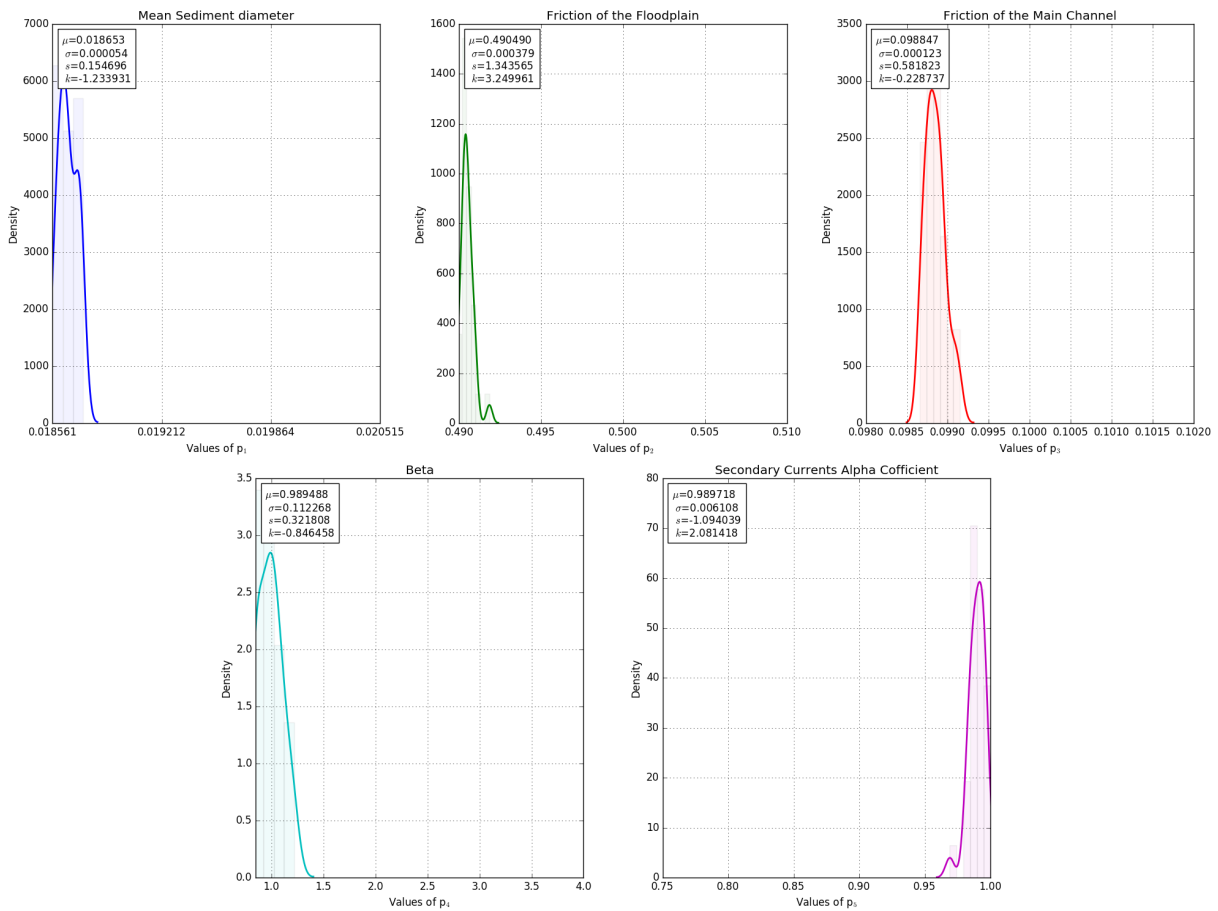


Figure 5.30: The posterior PDF of parameters (validation-Meyer-Peter-Müller model)

Van Rijn Model: Figure 5.31 illustrates the measured bed evolution versus the original model's simulation output and the response surface using the most probable parameter set in the calibration step. According to this graph, the response surface could not approximate the original model before the fifth kilometer from the inlet boundary correctly, particularly the peak values. However, this misfit changed significantly towards the outlet edge.

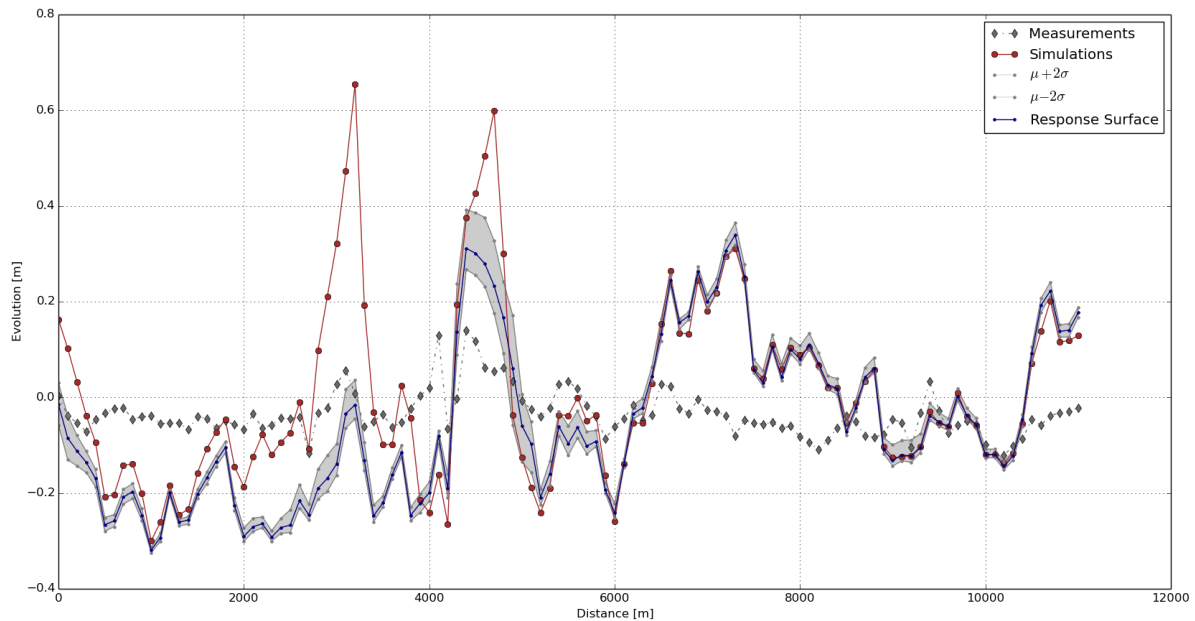


Figure 5.31: Simulation output vs. response surface (calibration-Van Rijn model)

The posterior information on best parameter sets in the calibration stage was utilized as the prior knowledge on the distribution of the parameters for the validation step. Additionally, the enlargement of the prior ensembles was conducted. Figure 5.32 shows the simulation output and the performance range of the response surface for the parameter set with the highest likelihood in the validation step.

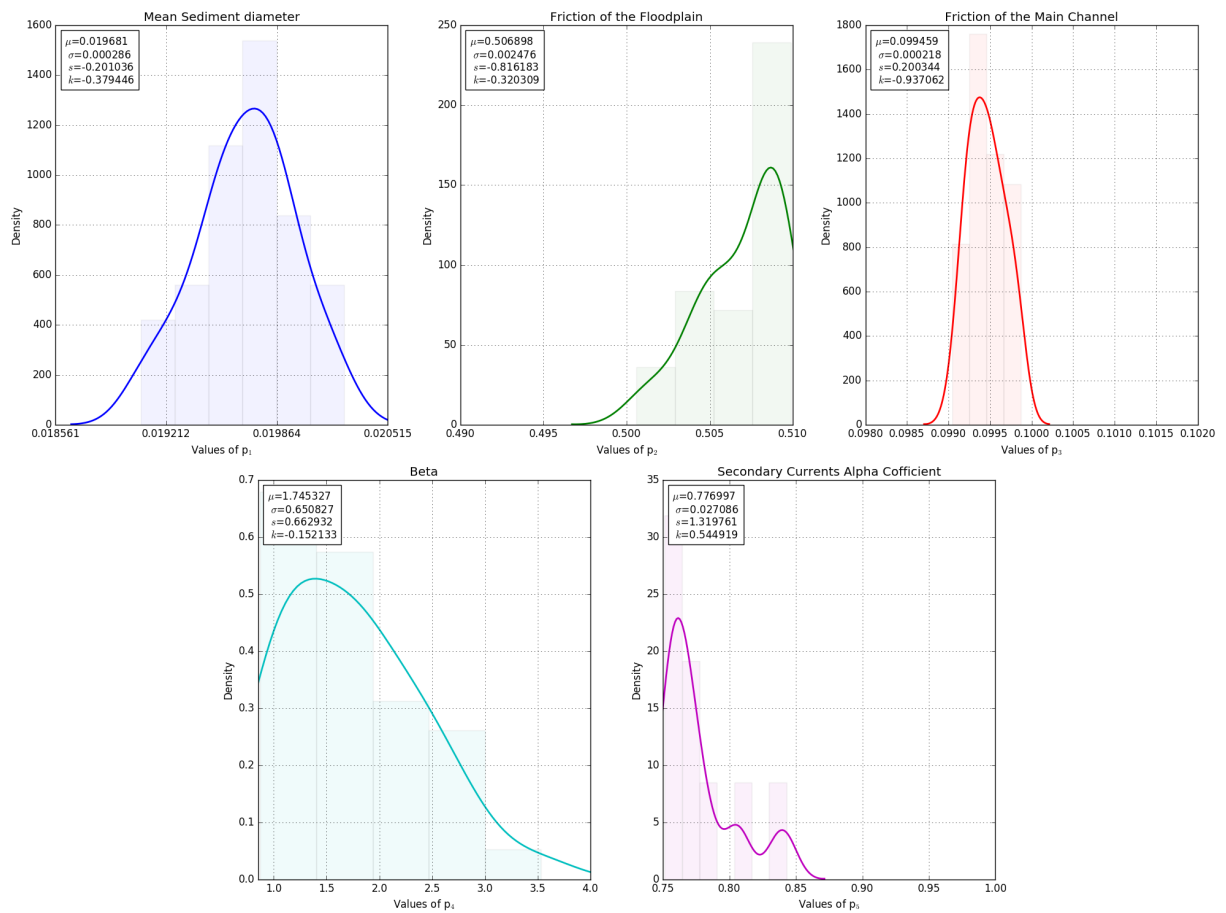


Figure 5.32: The posterior PDF of parameters (calibration-Van Rijn model)

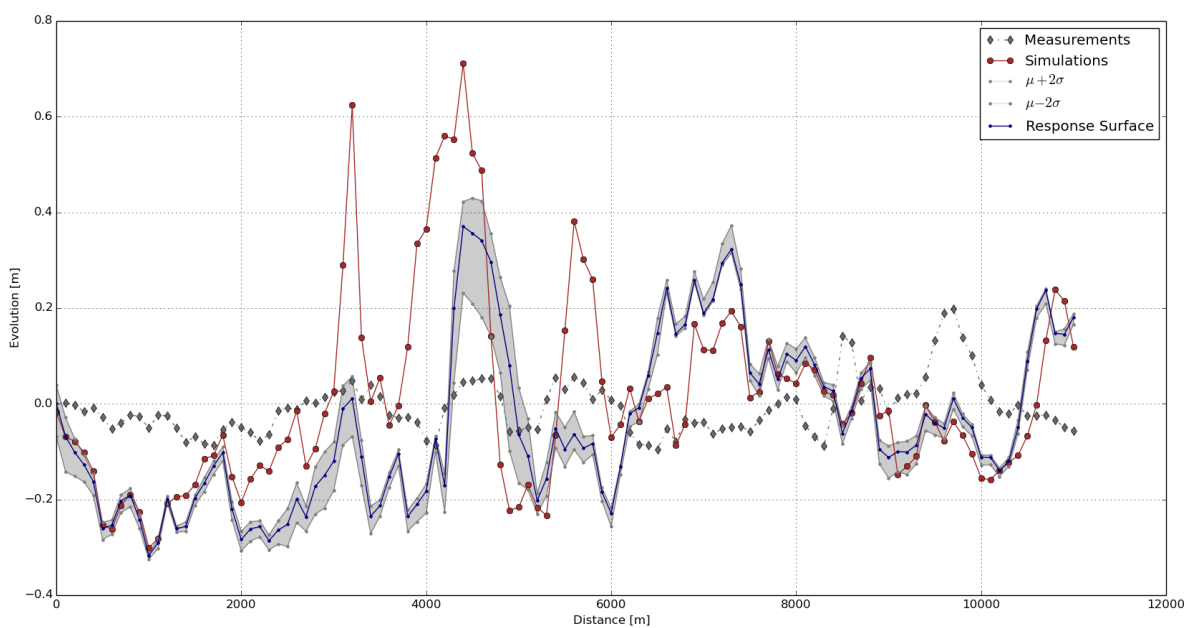


Figure 5.33: Simulation output vs. response surface (validation-Van Rijn model)

Similar to the calibration phase (Figure 5.31), the constructed surrogate model did not embrace the peaks. Note that the algorithm has not modified the response surface in the validation step.

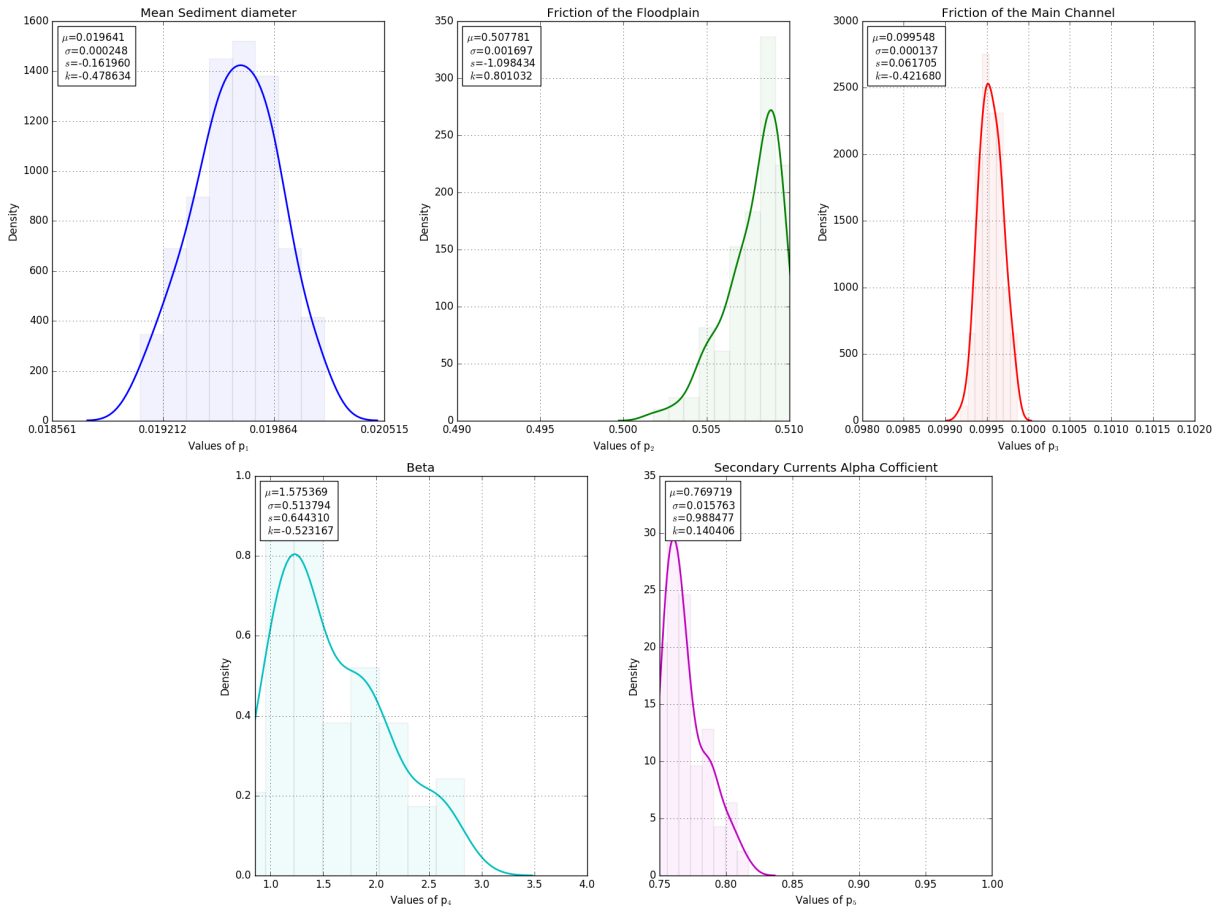


Figure 5.34: The posterior PDF of Parameters (validation-Van Rijn model)

Hunziker Model: The outcomes of the hydro-morphodynamic model involving the bed-load transport rate of Hunziker (1995) are presented in the following section. Figure 5.35 shows the model's simulation output against the response surface after calibration step using the parameter set with the highest likelihood. According to this graph, the performance range (the gray area) of the final response surface after five iterations contained the simulated bed evolution at numerous measurement locations.

Figure 5.36 demonstrate the PDFs of the posterior distribution of uncertain parameters after the calibration step.

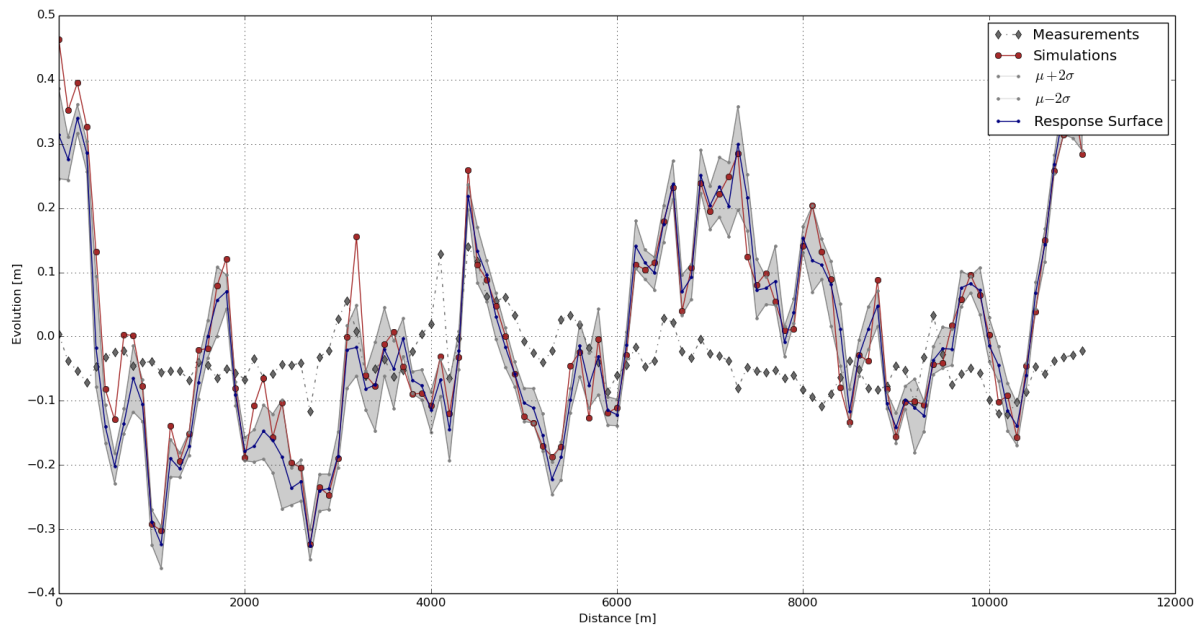


Figure 5.35: Simulation output vs. response surface (calibration-Hunziker model)

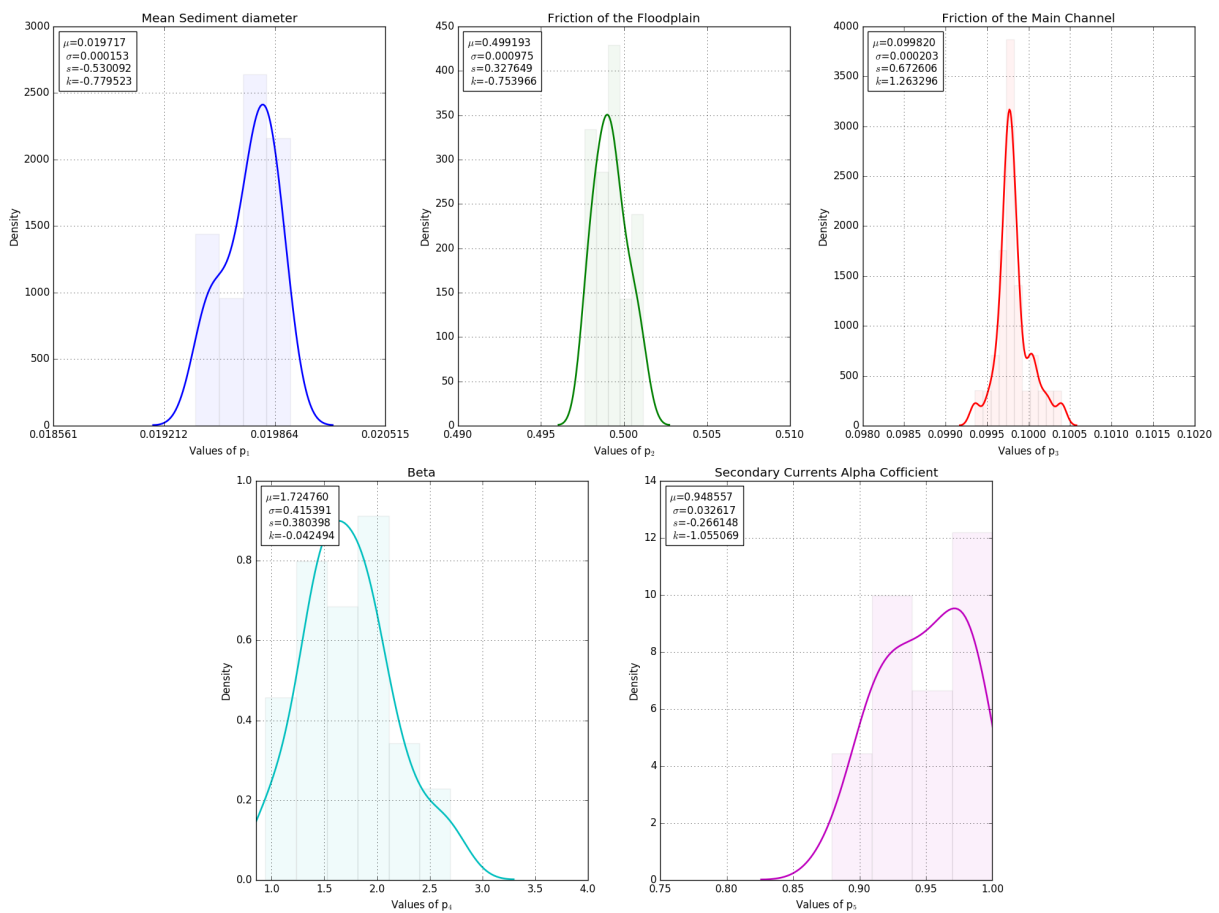


Figure 5.36: The posterior PDF of parameters (calibration-Hunziker model)

Figure 5.37 exhibits the simulation output and the response surface for the parameter set with the highest likelihood and its performance range in the validation step. This plot indicates that the constructed response surface in the calibration stage could also perform well for another measurement period.

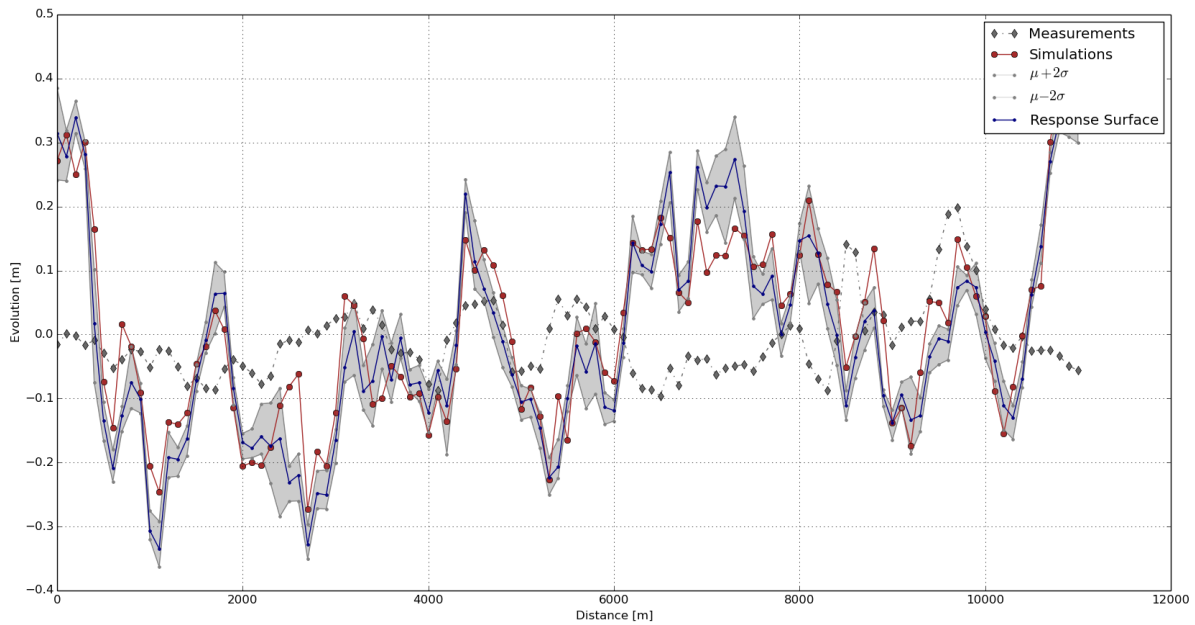


Figure 5.37: Simulation output vs. response surface (validation-Hunziker model)

The posterior probability density distributions of uncertain parameters after validation step in Figure 5.38 shows more informative distributions with unique peaks that are helpful for inferring the plausible region of parameters to be used in further optimization task.

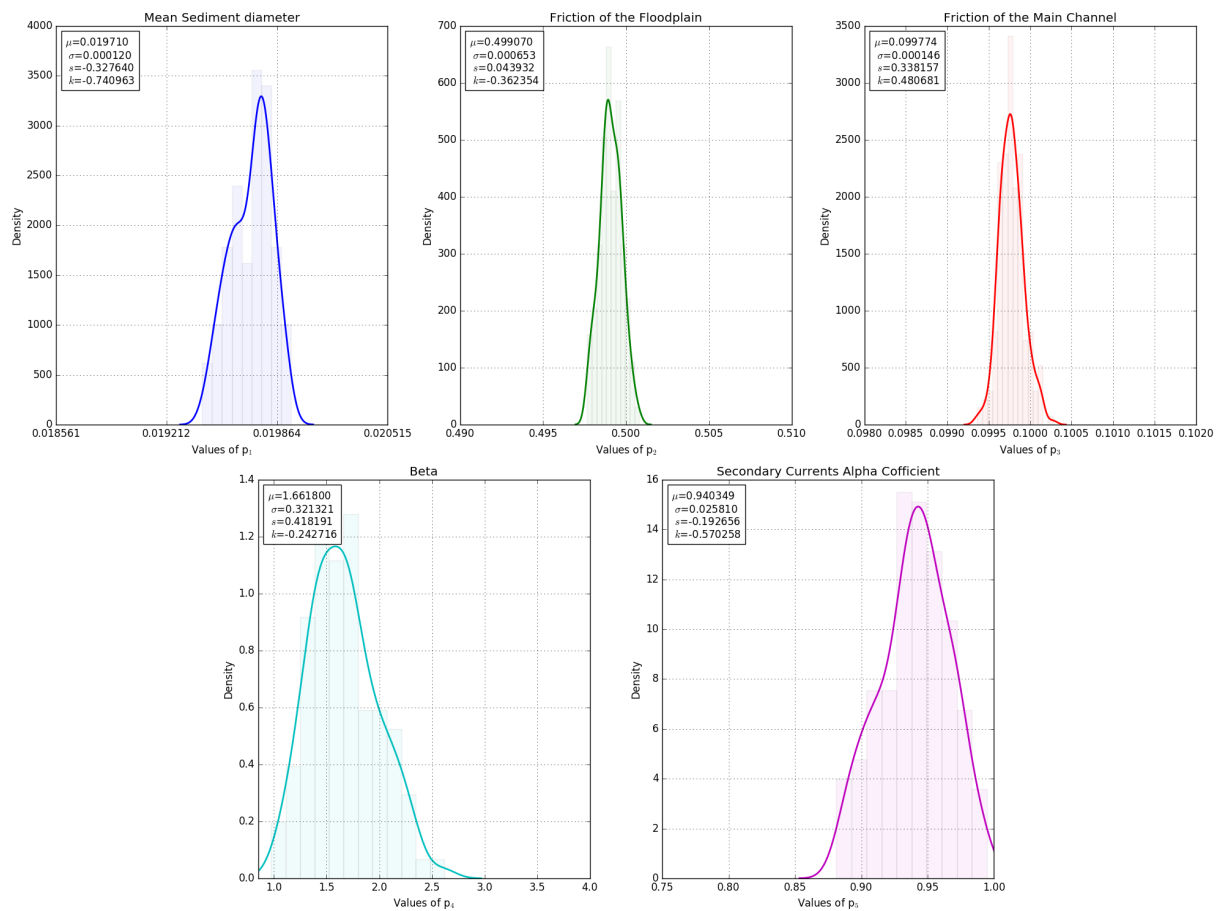


Figure 5.38: The posterior PDF of parameters (validation-Hunziker model)

Wu Model: As shown in Figure 5.39, the response surface built in the Bayesian framework could capture the overall pattern, but it slightly failed in disclosing the magnitude of the original model in Telemac-2d-Sisyphe. The performance range of the response surface (the gray area in Figure 5.39) was considerably small due to few remaining parameter sets passed the rejection sampling stage in the calibration stage. This fact also expressed in the posterior probability density function in Figure 5.40.

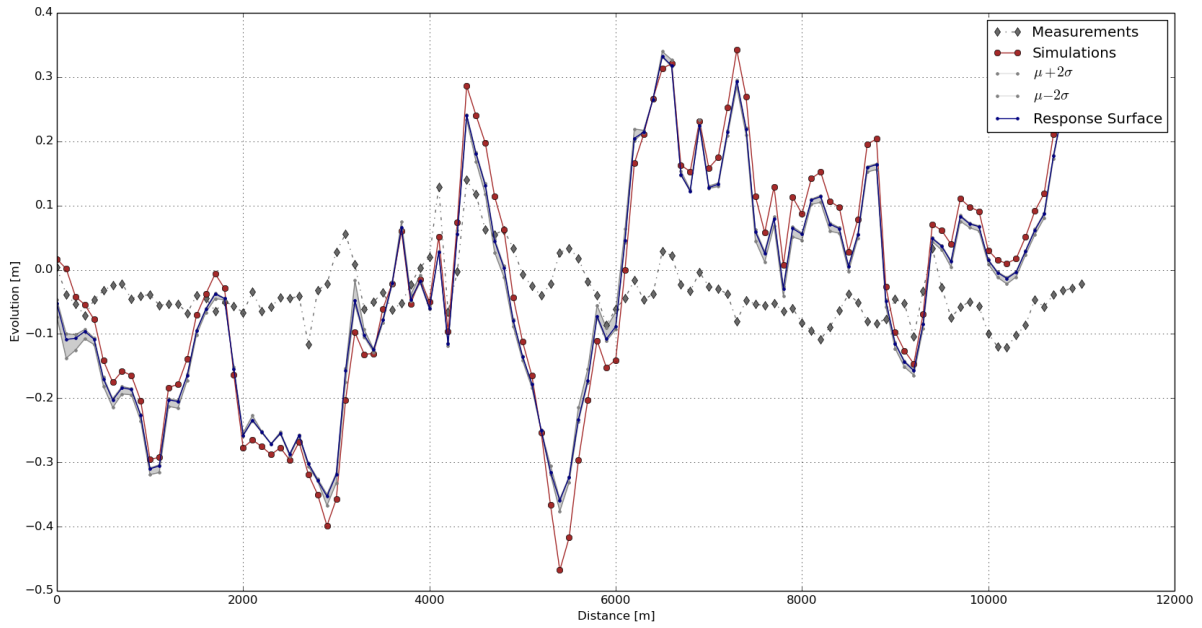


Figure 5.39: Simulation output vs. response surface (calibration-Wu model)

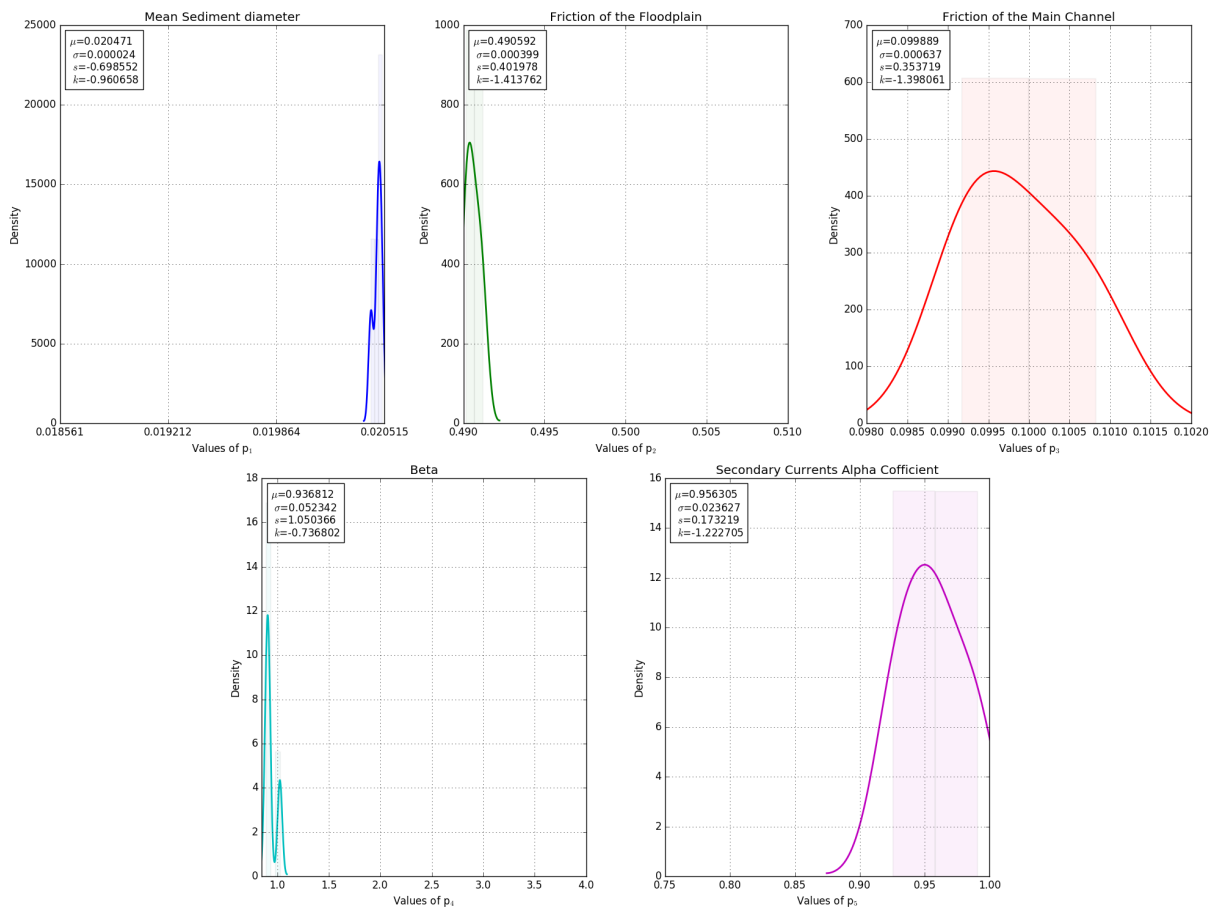


Figure 5.40: The posterior PDF of parameters (calibration-Wu model)

Figure 5.41 demonstrates the simulation output and the performance of the response surface for the parameter set with the highest likelihood in the validation step. Similar to the calibration case, the performance range is narrow, suggesting that the output of response surface for all the parameter sets after validation had a small variance.

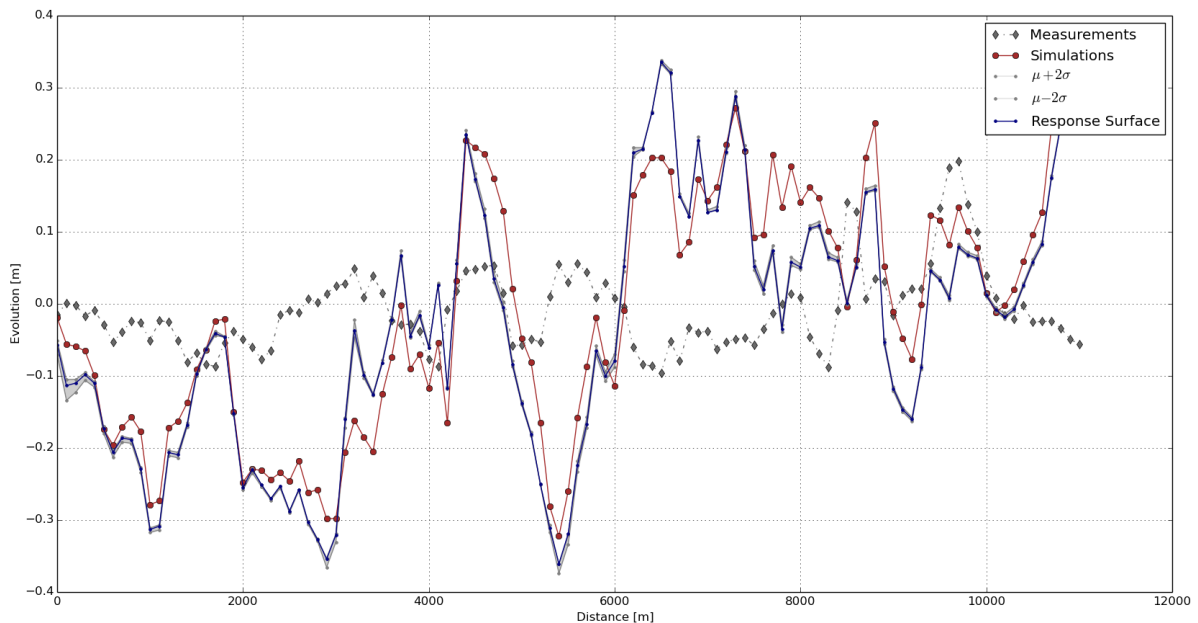


Figure 5.41: Simulation output vs. response surface (validation-Wu model)

Considering the performance range of the surrogate model (Figure 5.41) and the posterior PDF of the parameters in Figure 5.42, the response surface behaved similarly for a relatively wide range of the values for the friction coefficient of the main channel and the secondary current alpha coefficient.

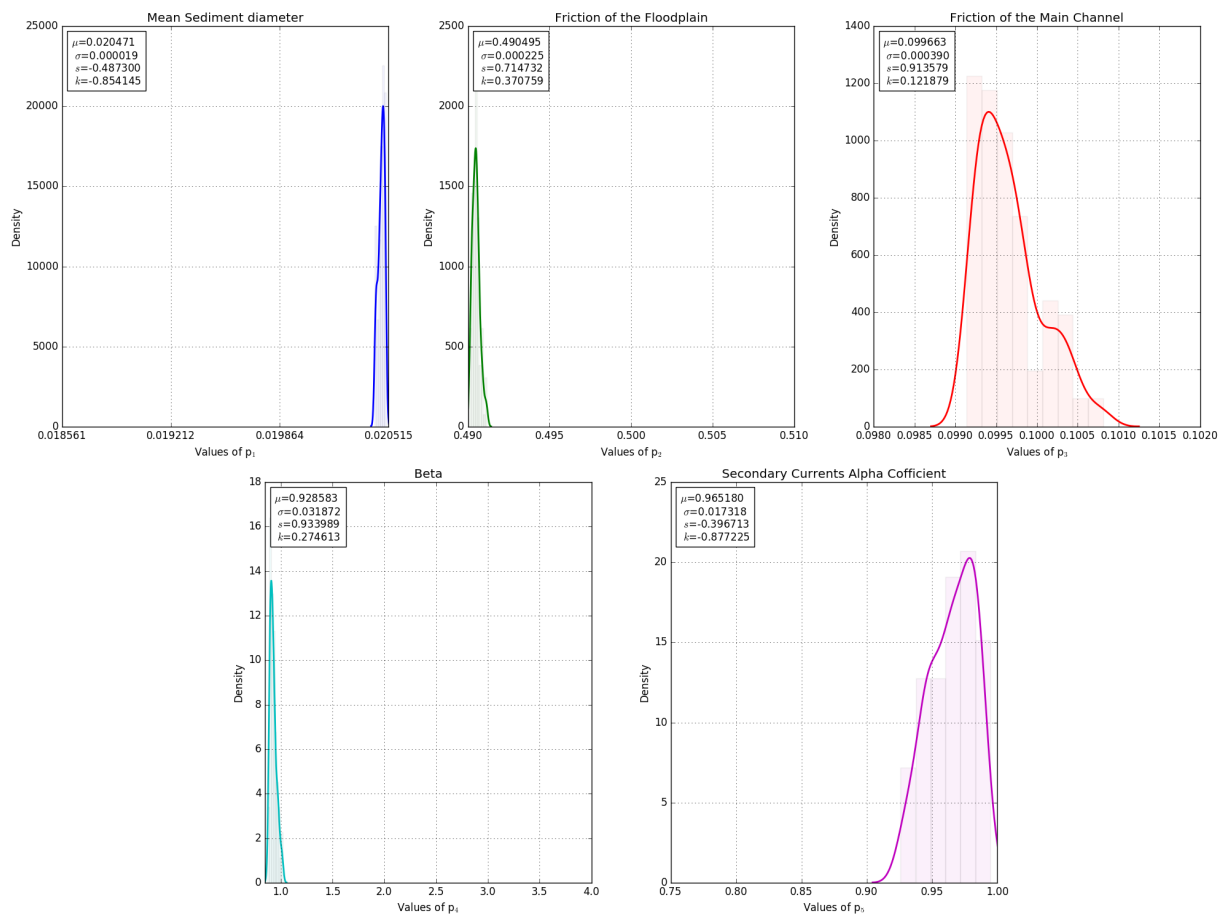


Figure 5.42: The posterior PDF of parameters (validation-Wu model)

BME Comparison: The development of BME values of the competing models over the iterations on the improvement of the response surface (surrogate model) is depicted in Figure 5.43.

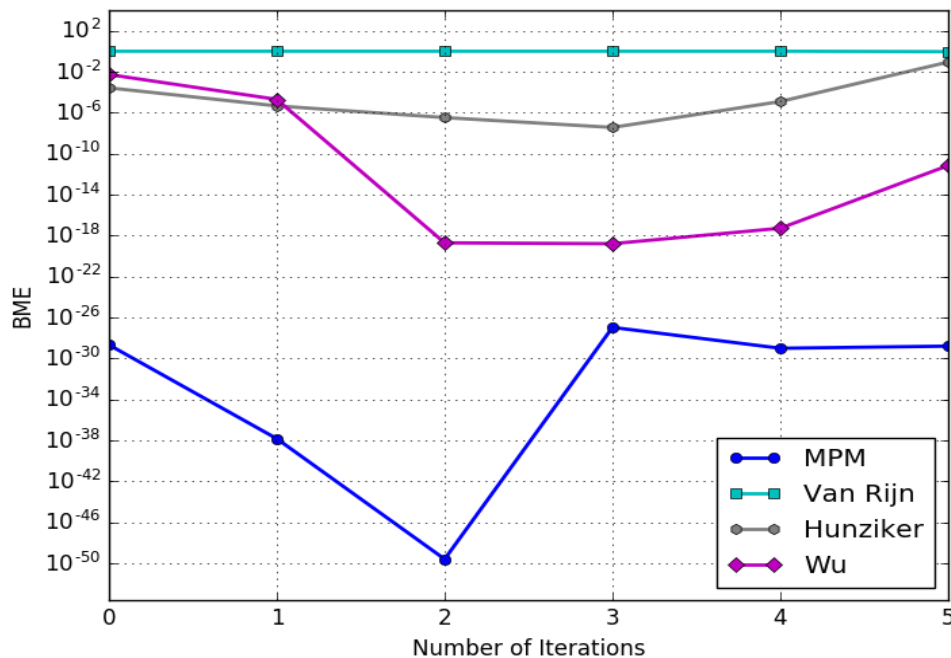


Figure 5.43: Bayesian model evidence vs. iterations for real lower Rhine model in calibration step (Log-scale)

The diagram in Figure 5.43 indicates that the likelihoods have undergone a rapid decline after the first iteration on the improvement of the response surface, but enhanced gradually afterward. This incident could be associated with the nonlinear nature of the original model or the response surface was updated with incorrect information from the original model's output. Additionally, the BME rates (Equation 3.13) after the validation stage is listed in Table 5.8.

Table 5.8: The BME comparison after the validation for the real lower Rhine model

Hydro-Morphodynamic Model	BME of Validation	Rank
Meyer-Peter & Müller	2.22E-33	4
Van Rijn	2.27E-7	2
Hunziker	0.99	1
Wu	1.43E-11	3

The hydro-morphodynamic model containing the Hunziker bed-load transport rate displayed more acceptable performance in comparison to its competing model after the validation (Fig-

ure 5.38). This model, however, was ranked as the second favorable model in the calibration stage. Given the fact that the curve representing two best-performed models are close, it is likely that if more iterations on the improvement of response surface were taken into accounts, the performance of the Hunziker model could overpass that of the Van Rijn model. Figure 5.44 demonstrate the simulated bed evolution using the Hunziker bed-load equation. The red areas stand for the deposition spots, and the erosion occurred in the blue sections. Comparing this simulation result with Figure 2.12, it is evident that the numerical overestimated the bed evolution.

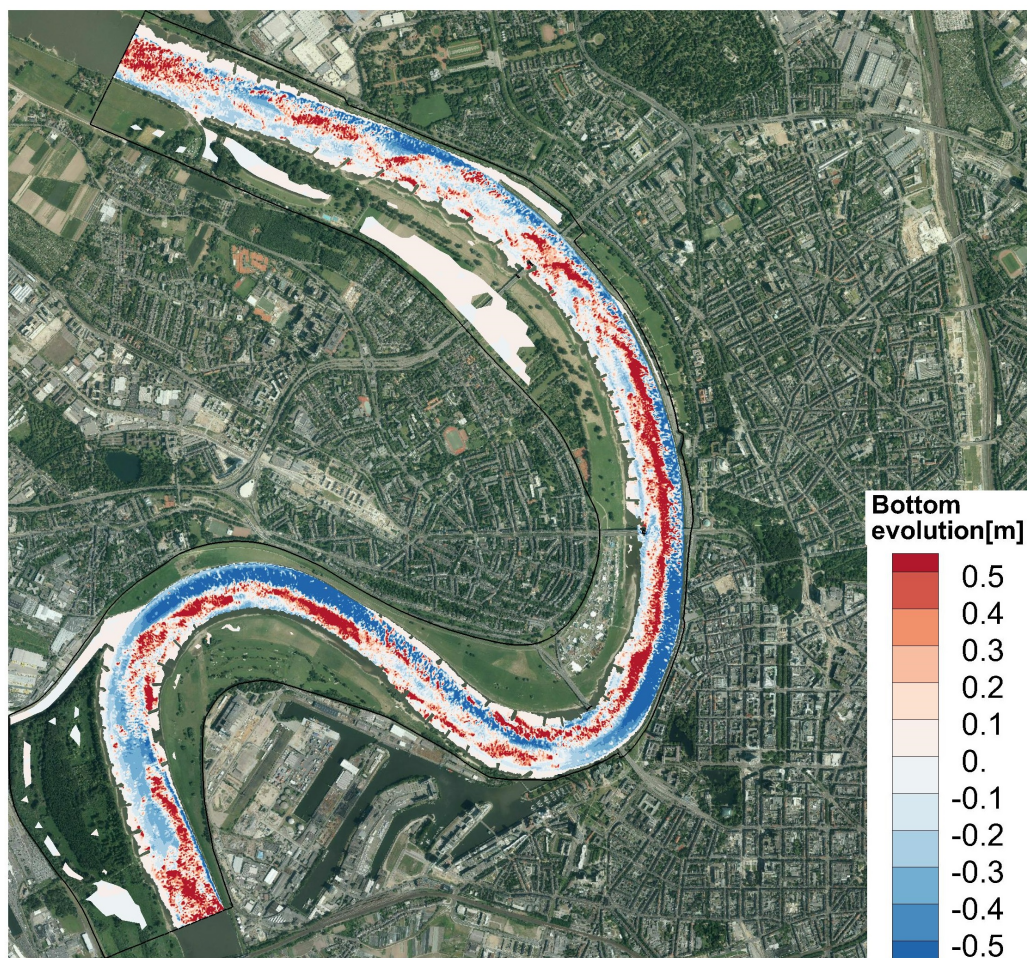


Figure 5.44: Simulated bed evolution with Hunziker model with bed evolution from 2002 to 2004

By comparing the presented graphs of the other rival model variants, the following conclusions can be drawn:

- It is evident that the constructed response surface failed, to some extent, in capturing the original model's behavior.
- The adequate local representation of the original model via response surfaces for all models at the inlet and outlet of the study area and their distances from the measurements indi-

cates that the real numerical model failed in matching the historical data at the boundaries. This situation could stem from the uncertainty in boundary conditions.

- The fact that the simulation output from the original numerical model in Telemac-2d-Sisyphé fell in the performance range of the surrogate model of the morphodynamic including Hunziker equation as shown in Figure 5.38 and they were in a more fair distance to the measurement reveal that this model was more favorable comparing to its other competitors.
- For some models in the real case of lower Rhine model, the surrogate model is at significant distance from the original simulations than for others. In that case, if the surrogate is closer to the measurements than its original model it will be ranked higher than it should and BMS is "unfair".

5.3 Summary

The presented chapter included the results of the model selection for the numerical model of the 10-km river reach of the lower Rhine in Telemac-2d-Sisyphé software, provided by BAW in Karlsruhe. The Bayesian Model Selection (BMS) for this river model was implemented considering two different scenarios. First, the BMS was conducted by benchmarking with a synthetic test case, in which measurement for a short period was taken into consideration. Then, real bed evolution of a two-year term was inserted in the BMS framework.

The framework successfully ranked the model used for the generation of the synthetic measurement. Additionally, the comparison of the probability density distributions of parameters for the first rated model with the known parameter values could direct us to the most probable region of the most variables with an acceptable precision. The accuracy of the calibration parameter set inference of the proposed approach needs to be investigated in detail by employing scenarios of twin experiment with varying measurement errors.

In model selection for the case with the real measurement of the lower Rhine, the hydro-morphodynamic including Hunziker equation was ranked in the first place among four different models. As shown in Figure 5.37, the simulation output from the original numerical model in Telemac-2d-Sisyphé and the surrogate model of the selected morphodynamic model were in a more acceptable range of the measurement comparing to its other opponents.

6 Summary and Conclusions

In the field of river engineering, hydro-morphodynamic history matching, in which the model simulations are adjusted to reproduce the past measurements, demands a remarkably sound expertise of the processes under investigation. The difficulty includes the selection of the best model among the available variants. Moreover, the non-trivial task of identifying the matched parameters within the model can expressively complicate the history matching process. Addressing these issues, this master's thesis established a Bayesian Model Selection (BMS) framework that assists even less experienced modeler to rank different available hydro-morphodynamic models according to their predictive abilities.

This chapter presents all the findings and the conclusions of the current research, as well as some recommendations. Section 6.1 provides a summary of this report, in which the statement of the problem, the framework's concepts and properties, and the verification tests are described. Afterward, the conclusions that are drawn from the results presented in the previous chapters are listed in Section 6.2. Finally, Section 6.3 entails some recommendations for further investigations.

6.1 Thesis Summary

Problem Statement: Water currents in natural rivers cause riverbed scour, particles (heavier than water) movement and material depositions, creating the bed topography changes. This phenomenon is called fluvial hydro-morphodynamics, in which sediment transport plays the major role, as shown in Section 2.1. According to Apsley (2014), the reasons that sediment transport phenomenon is of great importance in river engineering include but are not limited to risk assessment of scouring of bridges, weirs and channel banks; estimation of the siltation in an upstream reservoir of a dam; prediction of possible bed topographical changes of rivers and estuaries.

Considering the definitions of Einstein (1950) and Vanoni (2006), there are two distinct transport modes of sediments in a river, namely Bed-load transport and Suspended-load transport.

In the former, the sediment particles relocate via a rolling, sliding or leaping movement with a distance of a few grain sizes, also known as saltation, and are in continual contact with the channel bed. In the latter case, however, turbulent forces in the water uphold the particles, allowing them to be transmitted over considerable distances without touching the riverbed. Many fluvial research and management applications focus more on the estimation of bed-load because it governs the morphology of streams' bed.

Bed-load transport formulations correspond flow discharge to bed load transport. They demonstrate a vastly spatially and temporally variable phenomenon. These equations are copious and used extensively in both applied and theoretical studies. Gomez and Church (1989), who conducted the most comprehensive assessment of bed load formulae to date, state that there are more bed load equations in existence than there are reliable data to test them. Consequently, none or even few equations have been recognized as being particularly appropriate for designated application in many hydro-morphodynamic investigations. Hence, the challenge is the determination of the best model that describes the morphodynamic condition of a river in any modeling exercise.

Not only does the model selection for the hydro-morphodynamic modeling requires lots of expertise, but the determination of calibration model parameters also makes it even more complicated. To address these issues, the current study offered a framework that assists less experienced modeler to rank different available models according to their capability of future predictions and simultaneously leads the user to the most probable region of parameters for calibration of the corresponding models.

Description of offered Solution: This study suggested a Bayesian Model Selection (BMS) framework to direct the modeler towards the most robust and sensible representation of the hydro-morphodynamic conditions of the river under investigation. The proposed framework considers Bayesian Model Evidence (BME) as a model evaluation yardstick for ranking competing models. BMS performs a compromise between bias and variance, i.e. it blends a measure for goodness of fit with a penalty for unacceptable model complexity. Derived in a Bayesian context, BME not only accounts for measurement errors in the calibration data but it also takes parameters' uncertainty into consideration. Ergo, BME is superbly appropriate in the assessment of model's quality under uncertainty.

BME is closely connected with model weights in the context of Bayesian model selection. Computing the BMEs, the biased free numerical method of "Simple Monte Carlo Integration" (Schöniger et al., 2014) was used. The prior definition of the parameter space is a criterion for a reliable, accurate approximation of BME. To tackle this issue, an advanced model reduction technique, surrogate model (response surface), has been employed, attained via the arbitrary

polynomial chaos expansion (aPC). This aPC-based approach does not have any restrictions on the shapes of distributions and can process even less informative distributions. With this response surface framework, usually high computational costs of proper filtering of the prior distributions of parameters became viable for quantification of the model uncertainty.

To adapt the surrogate model to the original numerical model and avoid misleading inferences of parameter ranges, the toolkit encompasses an iterative approach to improvement of the response surface. A flowchart summary of the procedure in the BMS toolkit was presented in Figure 3.1.

Implementation in Case Studies: To evaluate the functionality of proposed framework, two case studies were conducted; namely a test case channel bend model, based on an experiment done by Yen and Lee (1995) and a river model of the lower Rhine, provided by the Federal Waterways Research Institute (BAW) in Karlsruhe. The channel bend model has been constructed based on a laboratory experiment in an 180-degree channel bend to investigate bed topography and crosswise sediment sorting in a channel bend under unsteady flow conditions. The second case study was performed on a river model of the Lower Rhine at Düsseldorf/Neuss (Rhine-km 739.0 to Rhine-km 749.0), which has an intense meandering with two close meandering curves and active bed-load transport.

The hydro-morphodynamic models of the two case studies have been constructed in the TELEMAC-MASCARET (www.telemac.org) simulation software, which is an open-source integrated suite of solvers for simulation in the field of free surface flow (Hervouet (2000)). Firstly, the hydrodynamic module, TELEMAC-2D derives the hydrodynamic conditions via solving the shallow water equations and then the morphodynamic modeling by the morphodynamic module, SISYPHE takes place, whose output is the bed evolution, calculated by Exner equation (Equation 2.4). The coupling between the hydrodynamic (Telemac-2d) and morphodynamic (Sisyphe) modules is also regarded. Additionally, bed slope effect and secondary current effect modify the bed evolution.

6.2 Conclusions

The results of BMS for the first test case; i.e. Channel bend, was presented in Chapter 4. As mentioned in Section 2.3, the models were calibrated using measurements in one cross section and validated with the observation locations at another cross section, due to lack of enough data time series.

In the calibration stage, only few parameter sets survived for the model including the modified bed-load equation of Engelund-Hansen, suggesting that large number of the prior parameter

sets performed poorly. This explains why its average likelihood (BME) was the lowest and the model was placed in the last rank after the calibration. However, this model scored best in the validation step, because little uncertainty remained after the calibration. Further, none of the other models yielded a better fit, and along with a small uncertainty, this model obtained the highest rank. On the contrary, the morphodynamic model containing the Van Rijn bed load equation was placed in the last rank among other competing models in the validation step, though it was ranked as the second in the calibration phase.

To investigate the impact of various prior information of sensitive parameters, i.e. different mean values and variances, on the outcome of BME with limited calibration and validation datasets for the channel bend model, BMS was repeated for 100 times; i.e. slightly dissimilar prior distributions. The standard deviation of BME values in calibration were remarkably lower than in validation step. This fact indicates that the Bayesian model selection using the measurements at the 90 degrees of the bend is less sensitive to the prior distributions of parameters than at 180 degrees of channel.

The results of uncertainty analysis also revealed that morphodynamic models of Van Rijn and modified Engelund-Hansen were ranked as the best and the worst models after the calibration step, respectively. Whereas, the morphodynamic model with the modified bed-load transport equation of Engelund-Hansen was performed better than its rival after the validation. Therefore, one can conclude that less representative surrogate model of the original morphodynamic model of Van Rijn in the calibration stage led to unreal BMEs, and the posterior model weight of this model after validation with another data set decreased.

The main contribution of this thesis was the BMS for the real-world river model for the lower Rhine. First, the BMS of the benchmarking test case with a synthetic bed evolution measurement was performed, where an exact solution was known. The BMS toolkit successfully led us to the known solution, which was the model used to generate the artificial bed evolution observations. Additionally, the posterior distributions of parameters navigated us to the most probable regions of the parameters for deterministic calibration, which were roughly near the unique parameter set used for the artificial bed evolution. Investigating the impact of the measurement error specified that lower measurement error values results in more precise parameter inferences.

Secondly, the BMS was performed for the river model with real measured bed developments for two data sets from 2002 to 2004 and 2004 to 2006. The hydro-morphodynamic embedding the Hunziker bed load equation was labeled as the superior model obtaining a posterior model weight of nearly 100% (BME = 1).

Overall, the findings and conclusions of this study can be summarized as following:

- The suggested BMS toolkit can provide a reasonable guidance in the task of model selection for hydro-morphodynamic models by providing a ranking of competing models considering a global measure of model quality.
- This framework can roughly direct the user to the most probable parameter regions for the further task of optimization via probability density distributions of uncertain variables. The nature of problem in hydro-morphodynamic modeling can be identified as ill-posed. In these problems, a unique solution might not exist, i.e. more parameter sets produce the same output.
- The reduced model derived from response surface framework can adequately represent the original numerical model and can be considered in the task of history matching to reduce the computational costs of optimization with the try-and-error approach.
- Better surrogate models allow a more authentic BMS ranking. Here, the model selection toolkit was limited to linear surrogate models, and this could be improved in future studies.
- Model ranking based on BMS becomes more reliable, when surrogate models are closer to the actual models. On the other hand, if the original model is to be used but it is computationally expensive, it leads to undesirable statistics and the estimated BME value again is not representative. Therefore, a compromise must be taken into account between the reliability of the model ranking and the computational costs of total required simulations of original model.
- BMS performs a trade-off between model performance and complexity. Before calibration, some models might have larger parameter uncertainty than others. Consequently, they are penalized much harder. This effect might diminish after calibration. Hence, getting different model ranking in calibration and validation is not "bad" per se.
- Using more calibration and validation data sets eliminates the discrepancy in the selection of the best-performed model after the calibration and validation steps.
- Instability of some models hindered the model selection process. Therefore, the preference of the user for working with a particular model needs to be taken into accounts in the BME approximation.

6.3 Recommendations for Further Investigations

The following recommendations for further studies can be suggested to improve the proposed BMS toolkit of this study.

- In the present study, a linear surrogate model was used to approximate the original mathematical model. Introducing additional terms to the linear model can account for any degree of possible nonlinearity in the original system.
- The Simple Monte Carlo integration approach was used in this study for BME calculation. However, other available numerical BME approximation methods can also be compared in a separate study.
- The impact of measurement error on model ranking and parameter inference ability of framework can be explored using benchmarking with different scenarios on test cases (twin experiment).
- The impact of enough measurement data was addressed briefly in this thesis. This effect can be studied further with implementing different scenarios in a benchmarking test.
- The toolkit features a possibility of assigning different measurement errors to some observation locations. Since there are uncertainties in inlet and outlet boundaries of numerical models of natural rivers, the impact of allocating higher weights to these regions to account for the uncertainties in BME approximation.

A Appendix I: BMS for the Channel Bend Model

In the following sections, the likelihood weights of parameters before and after improvement of response surface, the posterior of parameters versus their weights and the likelihood weights of prior parameter sets in validation step are presented for all models.

Meyer-Peter-Müller Model:

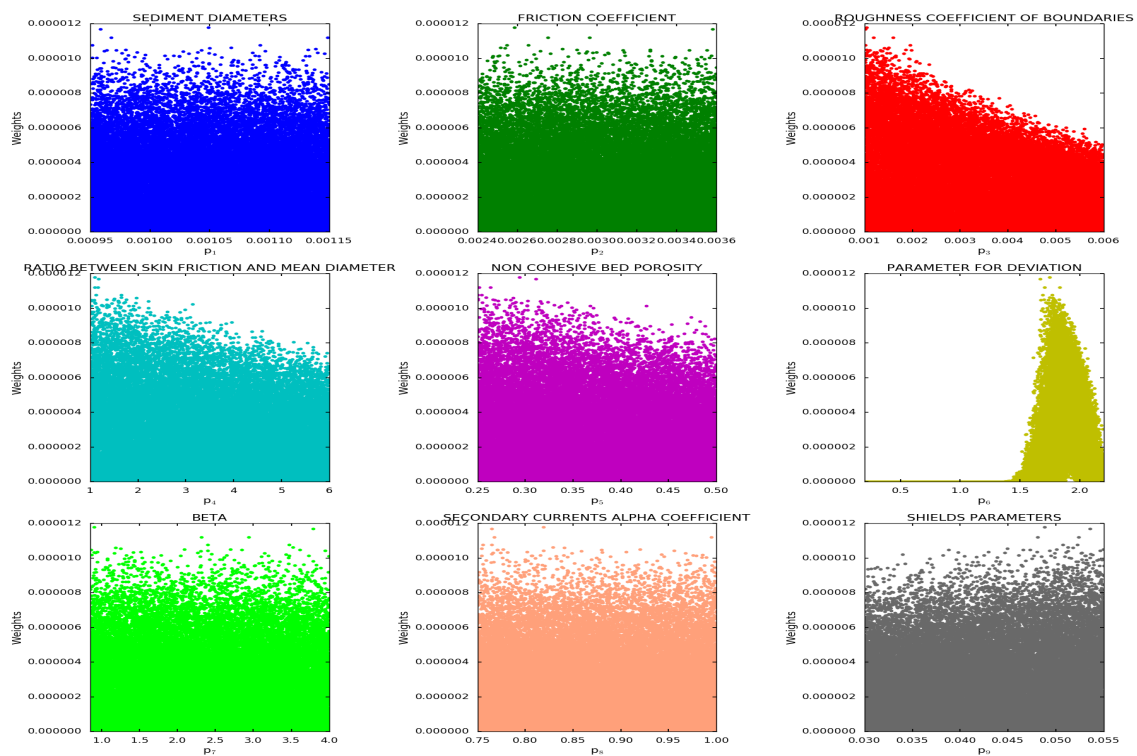


Figure A.1: Prior likelihood weights before iterations (calibration-Meyer-Peter-Müller model)

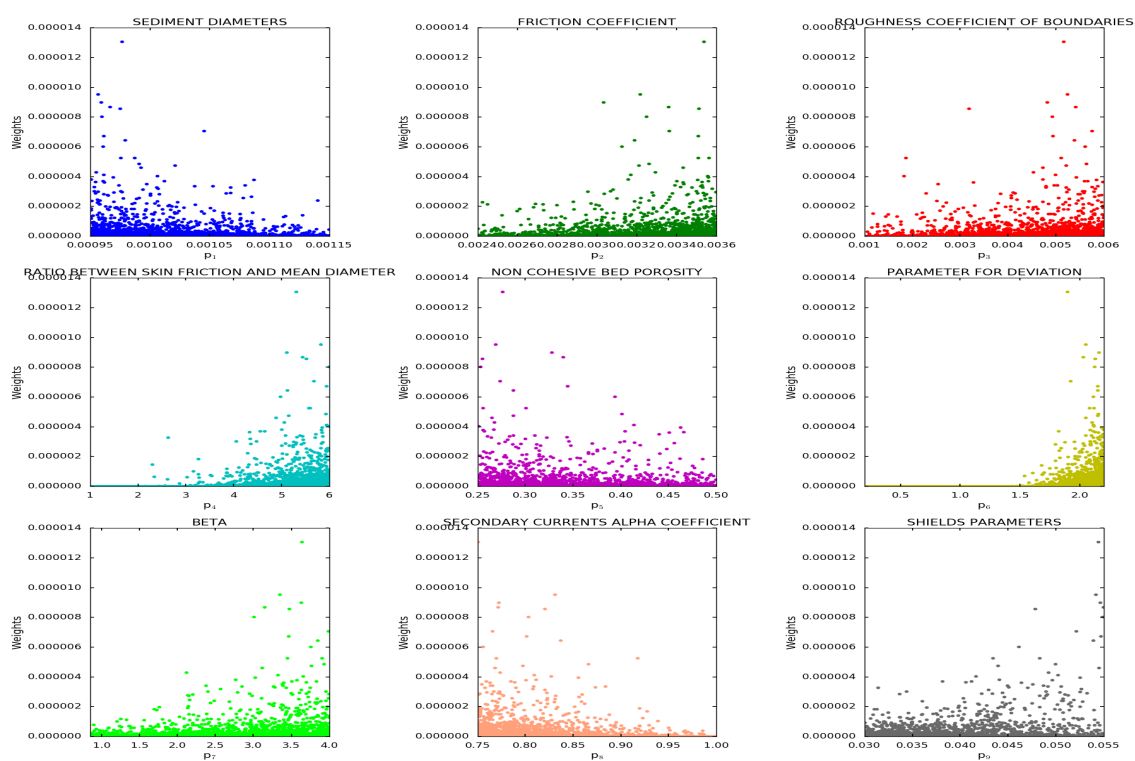


Figure A.2: Prior likelihood weights after iterations (calibration-Meyer-Peter-Müller model)

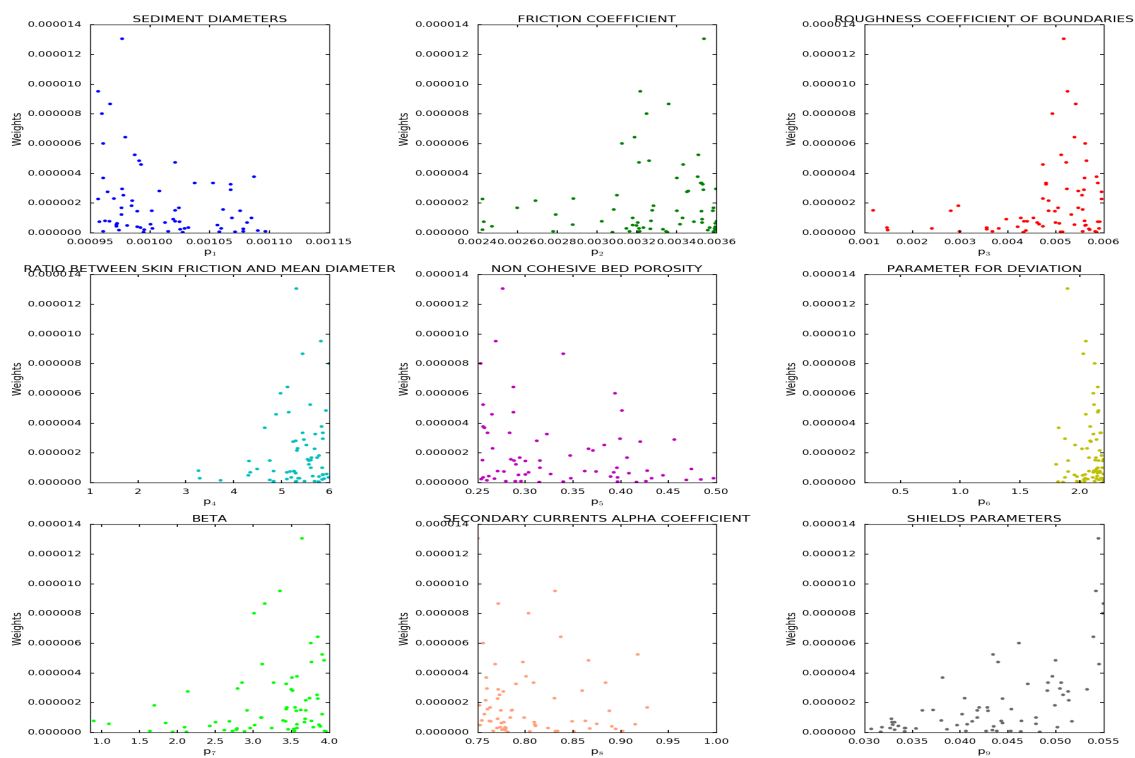


Figure A.3: Posterior likelihood weights after rejection sampling (calibration-Meyer-Peter-Müller model)

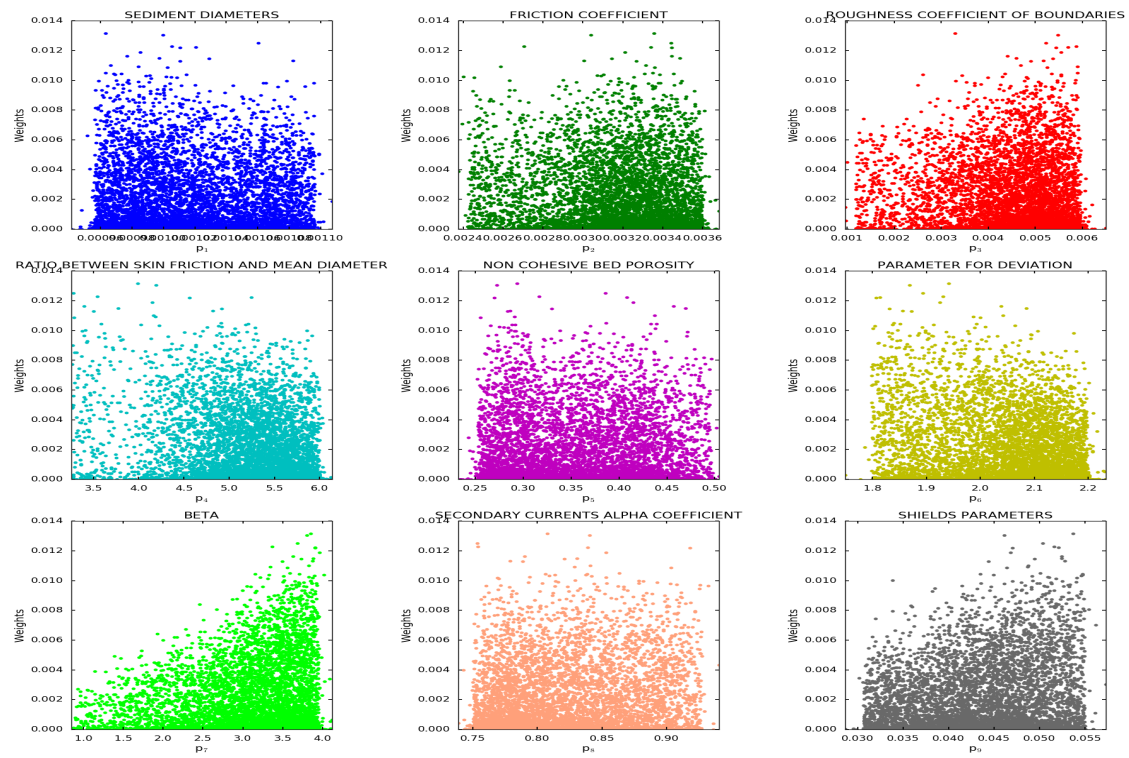


Figure A.4: Prior likelihood weights (validation-Meyer-Peter-Müller model)

Einstein-Brown Model:

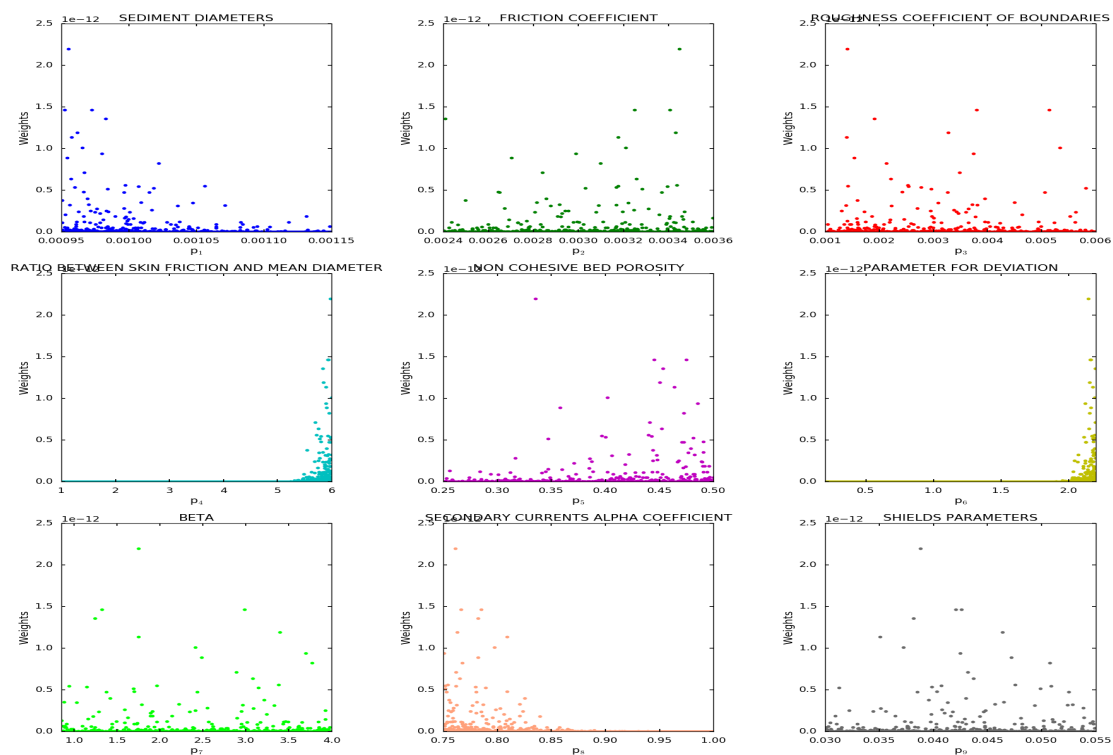


Figure A.5: Prior likelihood weights before iterations (calibration-Einstein-Brown model)

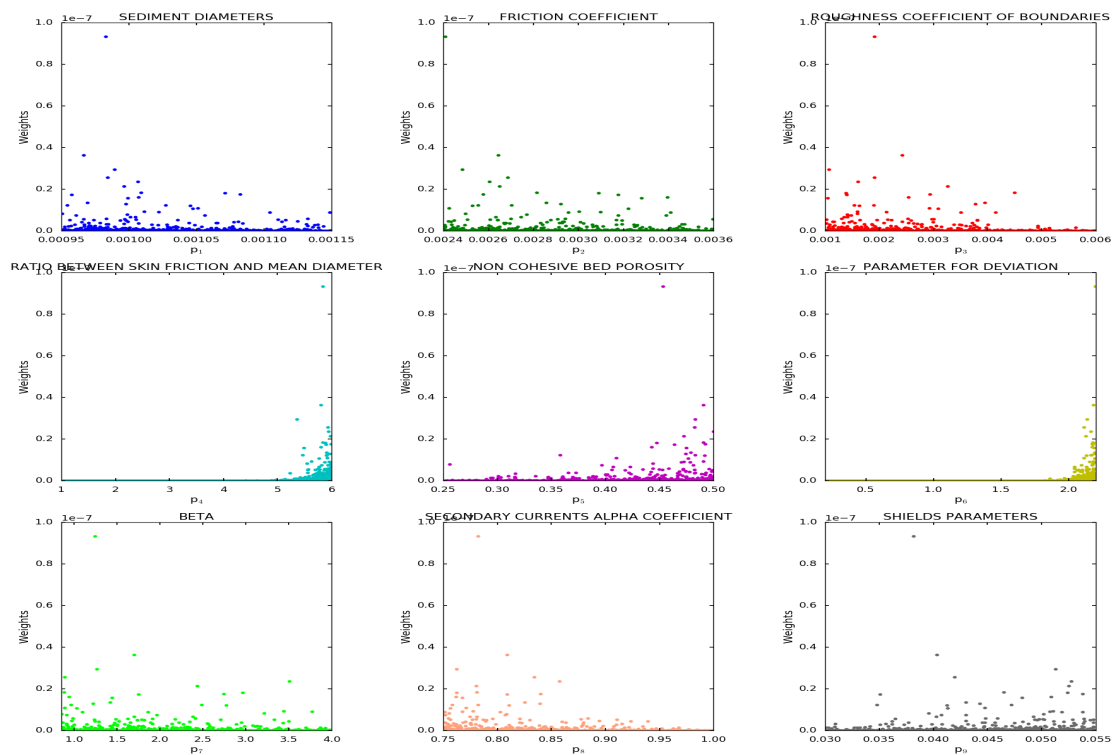


Figure A.6: Prior likelihood weights after iterations (calibration-Einstein-Brown model)

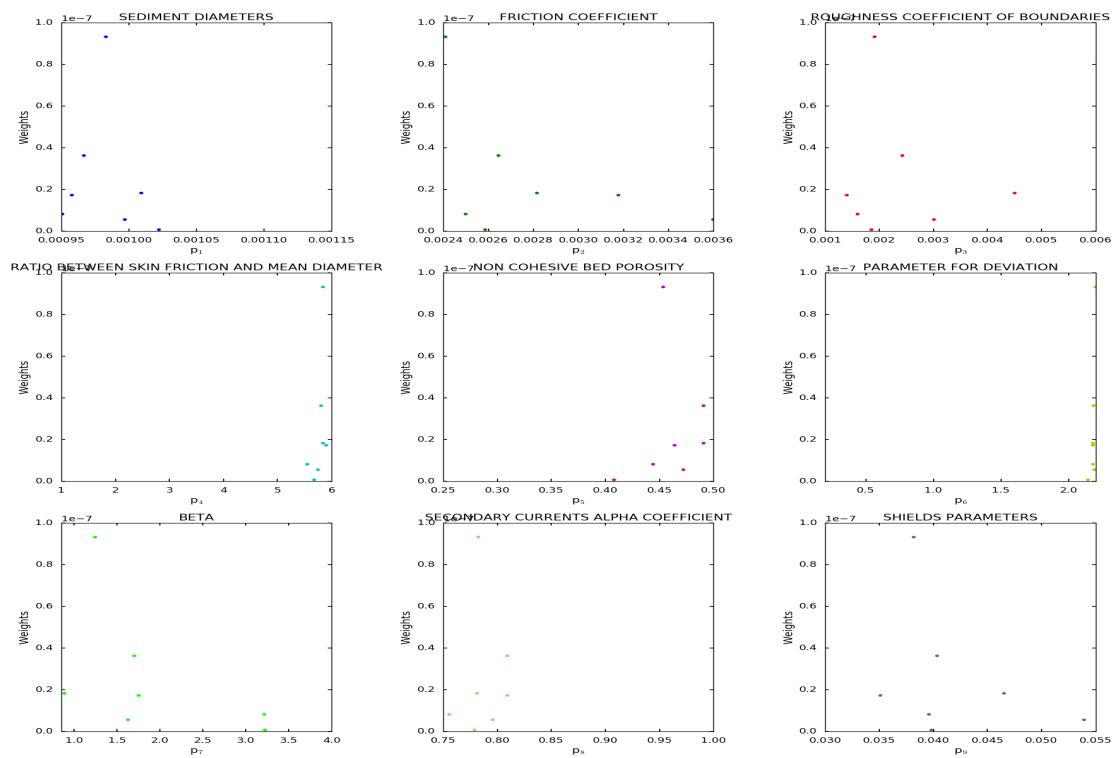


Figure A.7: Posterior likelihood weights after rejection sampling (calibration-Einstein-Brown Model)

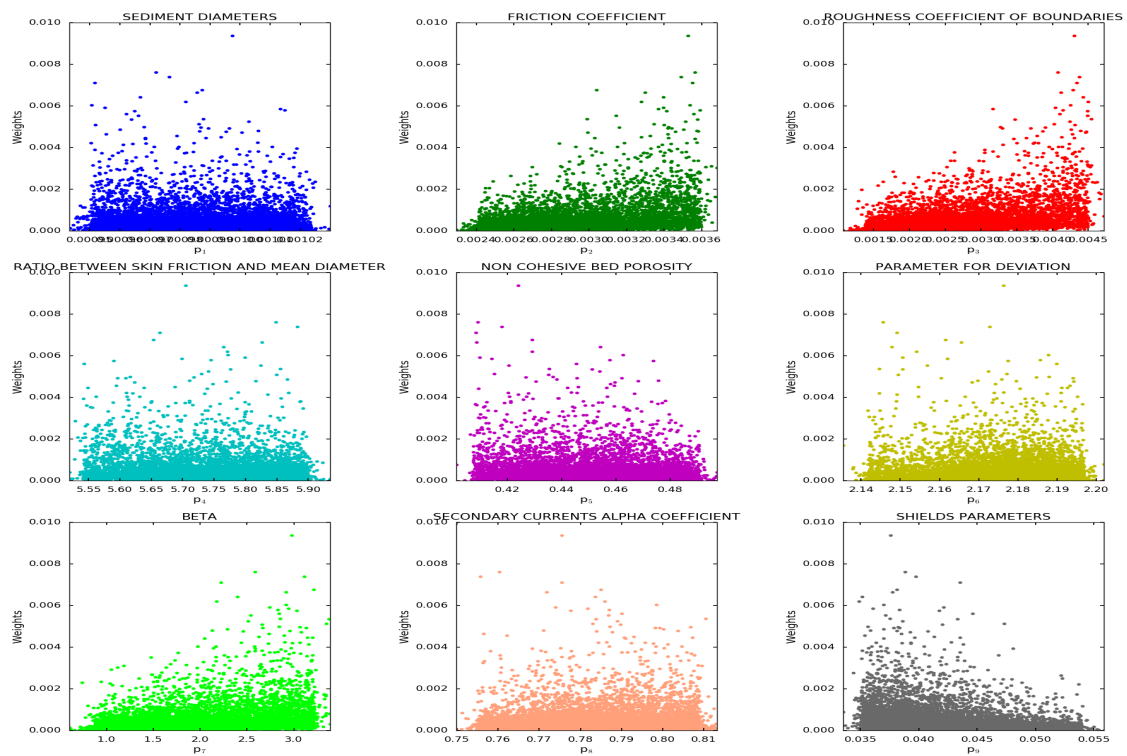


Figure A.8: Prior likelihood weights (validation-Einstein-Brown model)

Modified Engelund-Hansen Model:

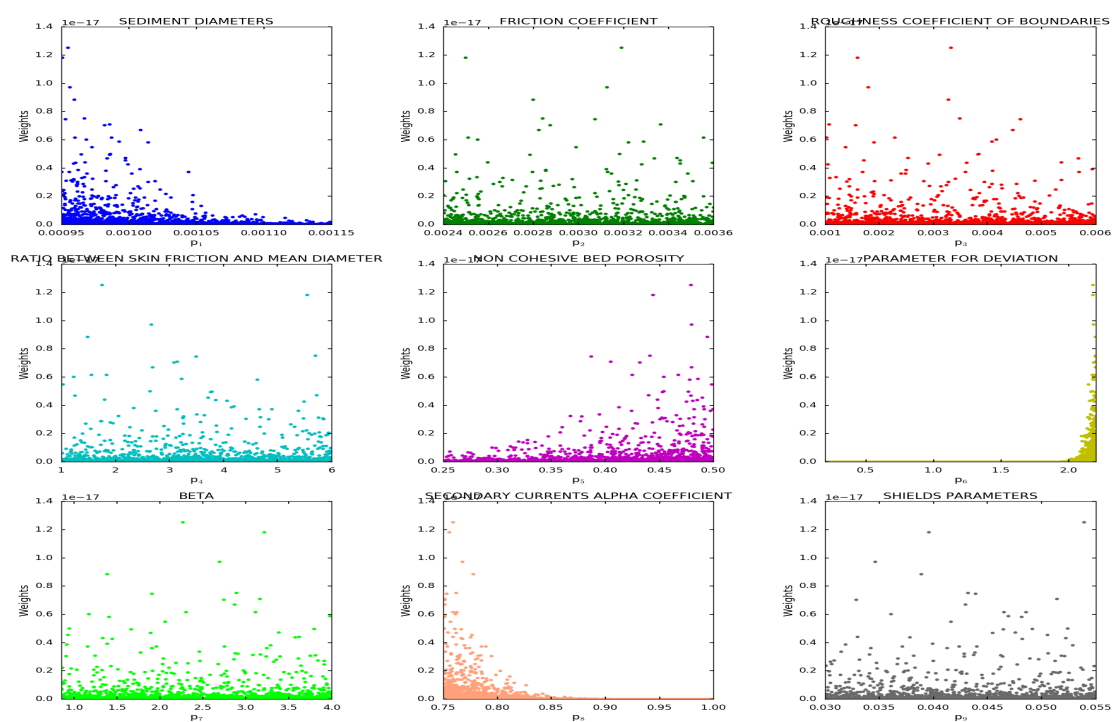


Figure A.9: Prior likelihood weights before iterations (calibration-mod. Engelund- Hansen model)

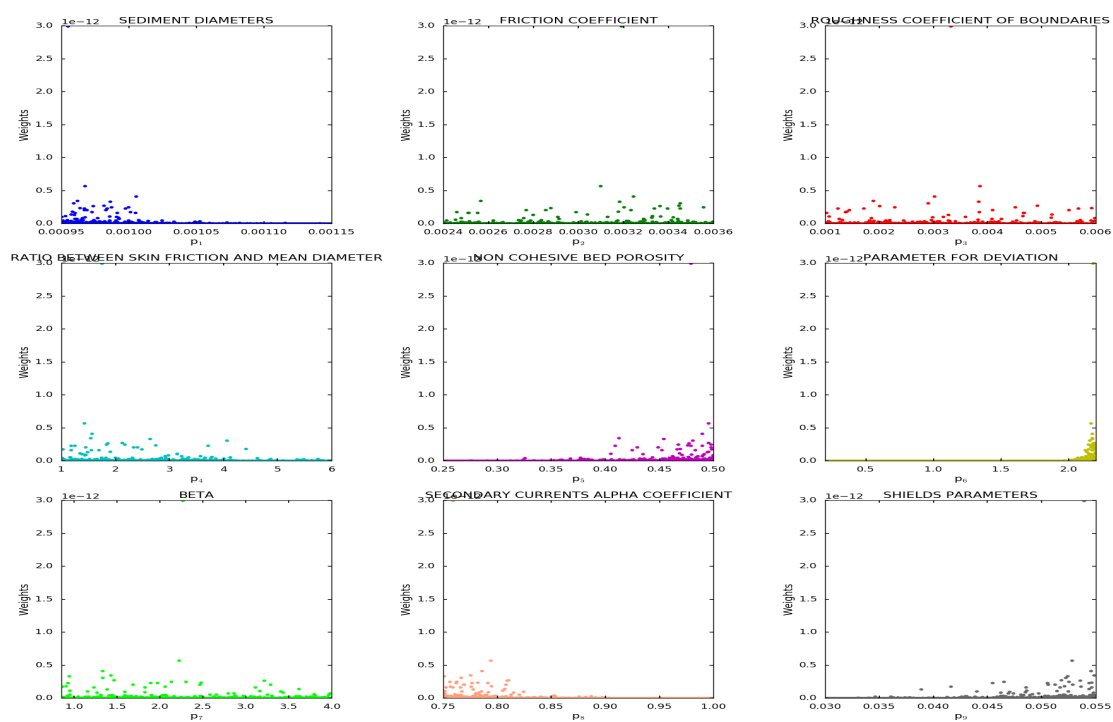


Figure A.10: Prior likelihood weights after iterations (calibration-mod. Engelund- Hansen model)

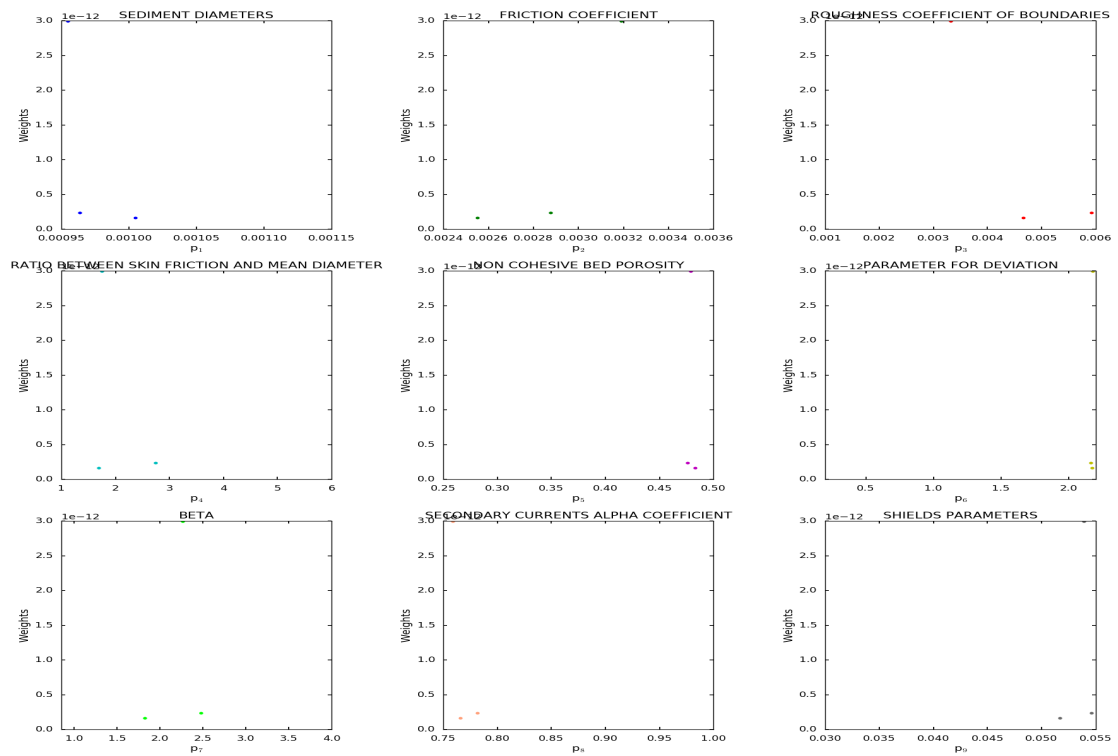


Figure A.11: Posterior likelihood weights after rejection sampling (calibration-mod. Engelund-Hansen model)

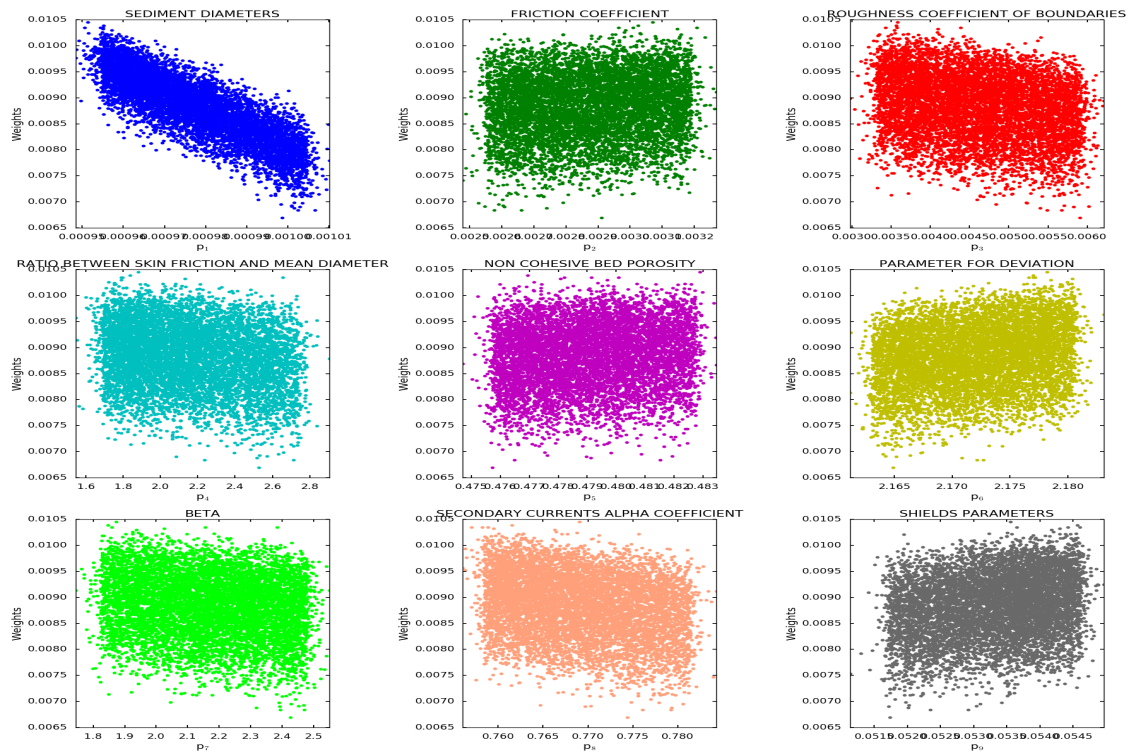


Figure A.12: Prior likelihood weights (validation-mod. Engelund-Hansen model)

Van Rijn Model:

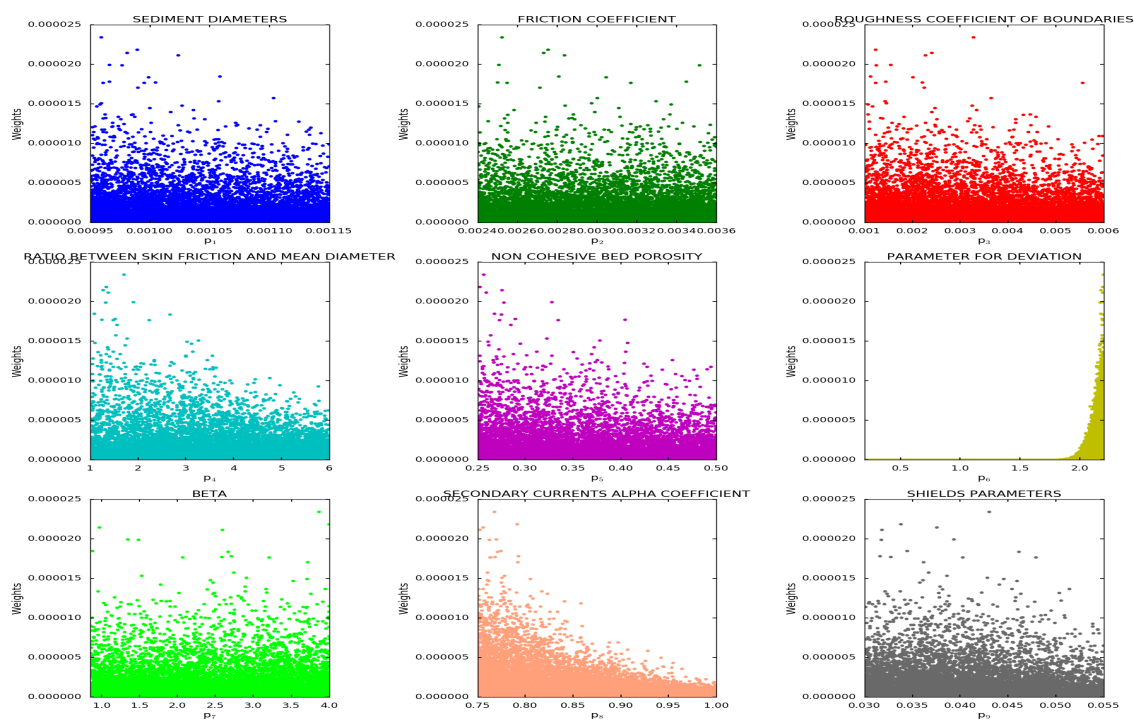


Figure A.13: Prior likelihood weights before iterations (calibration-Van Rijn model)

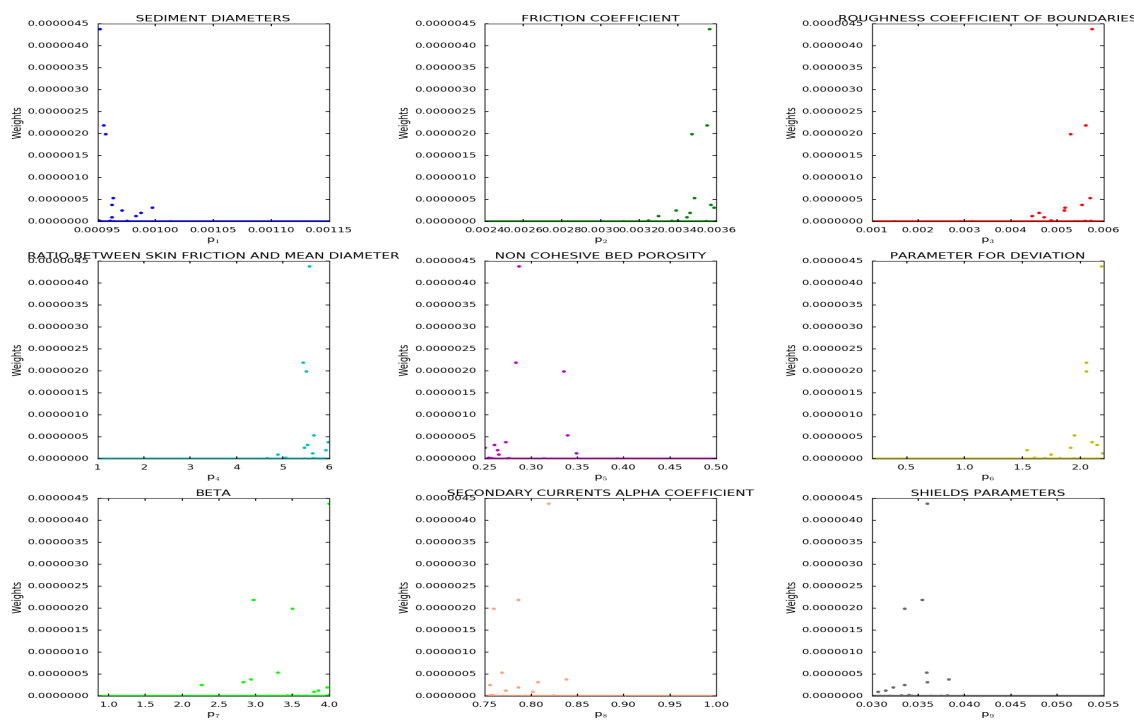


Figure A.14: Prior likelihood weights after iterations (calibration-Van Rijn model)

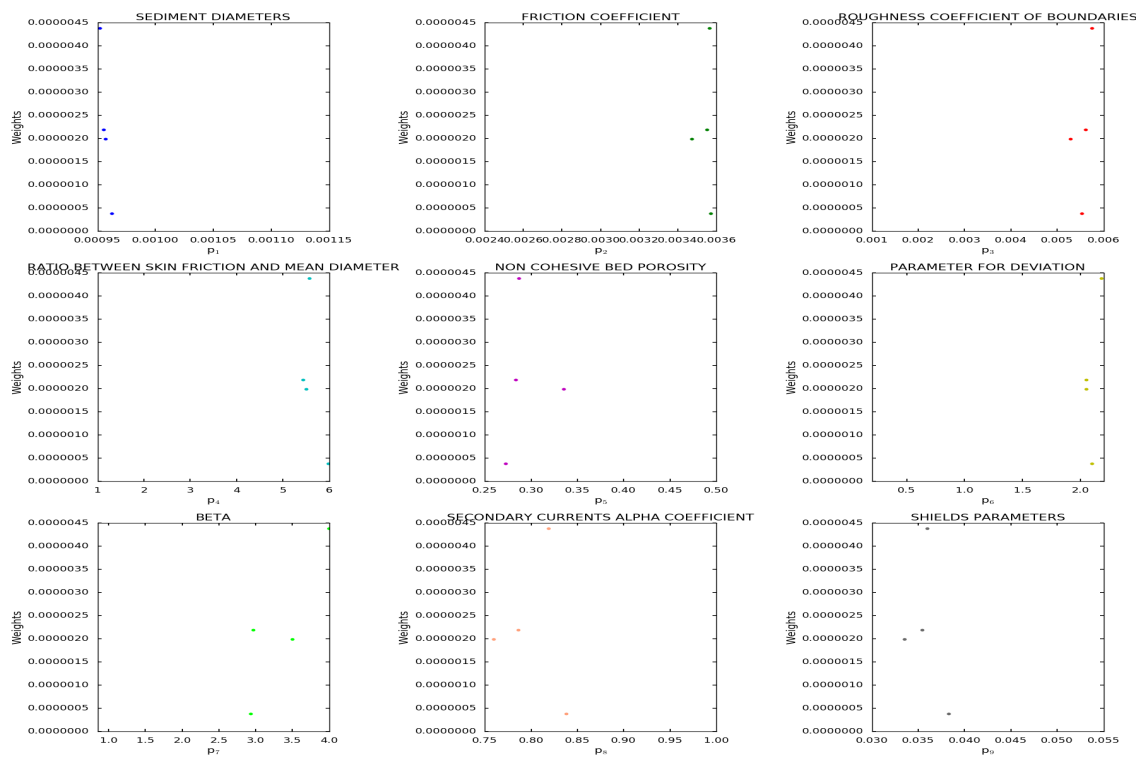


Figure A.15: Posterior likelihood weights after rejection sampling (calibration-Van Rijn model)

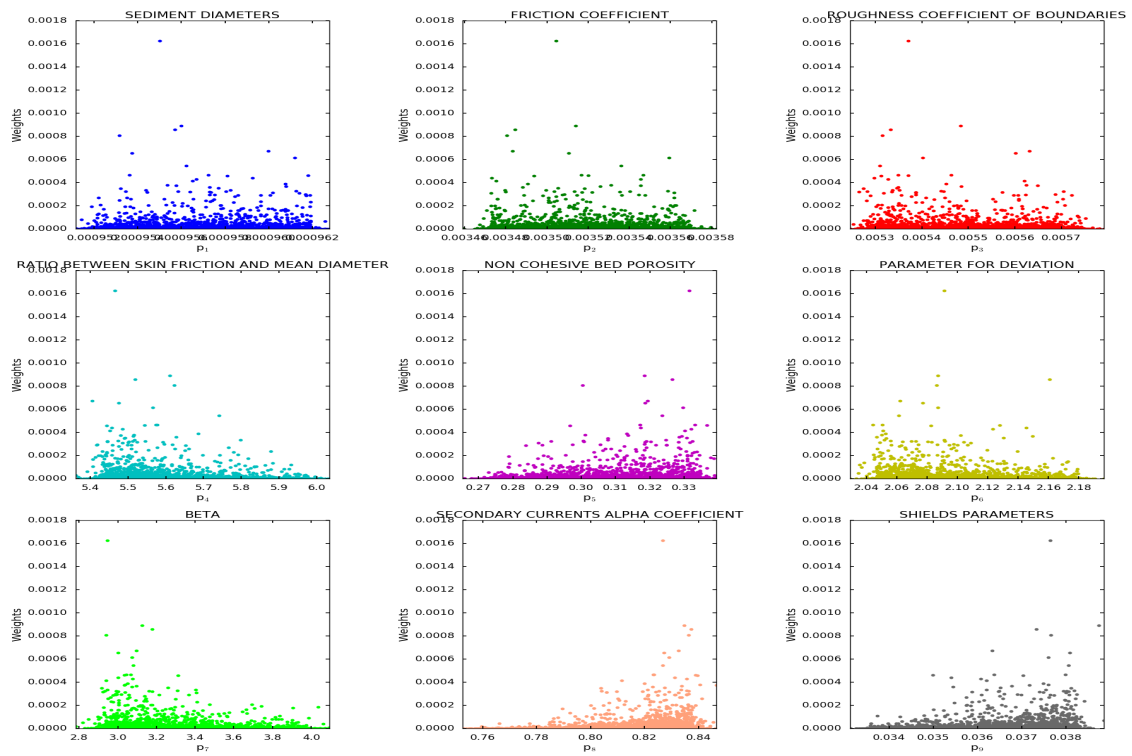


Figure A.16: Prior likelihood weights (validation-Van Rijn model)

Wu Model:

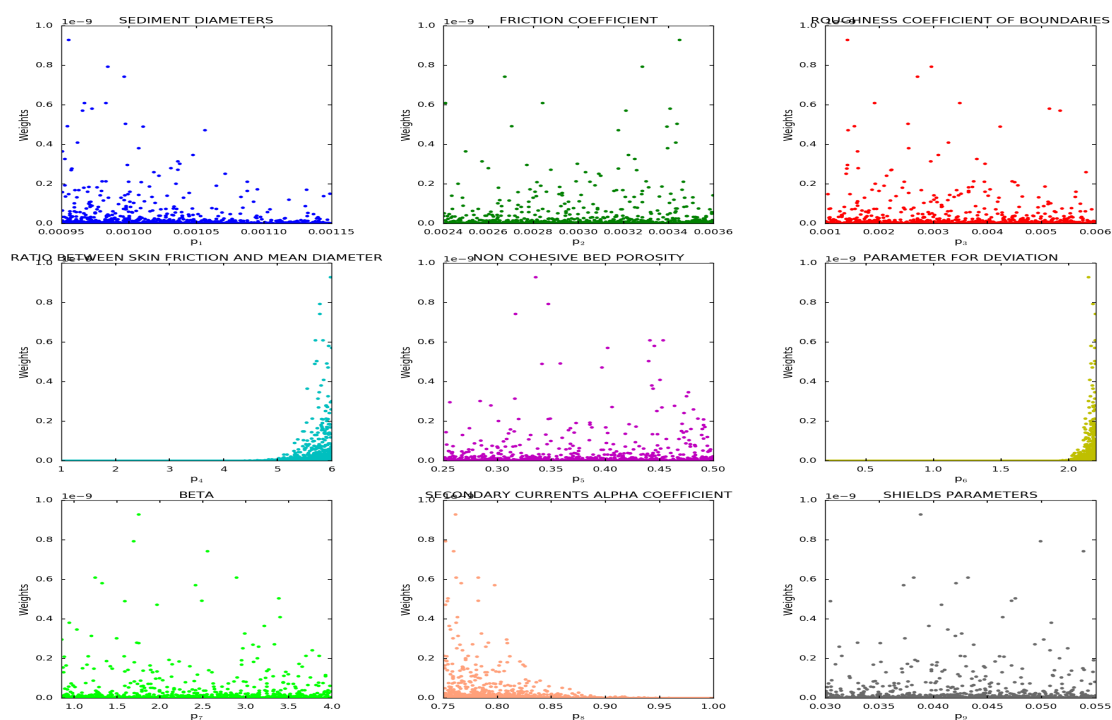


Figure A.17: Prior likelihood weights before iterations (calibration-Wu model)

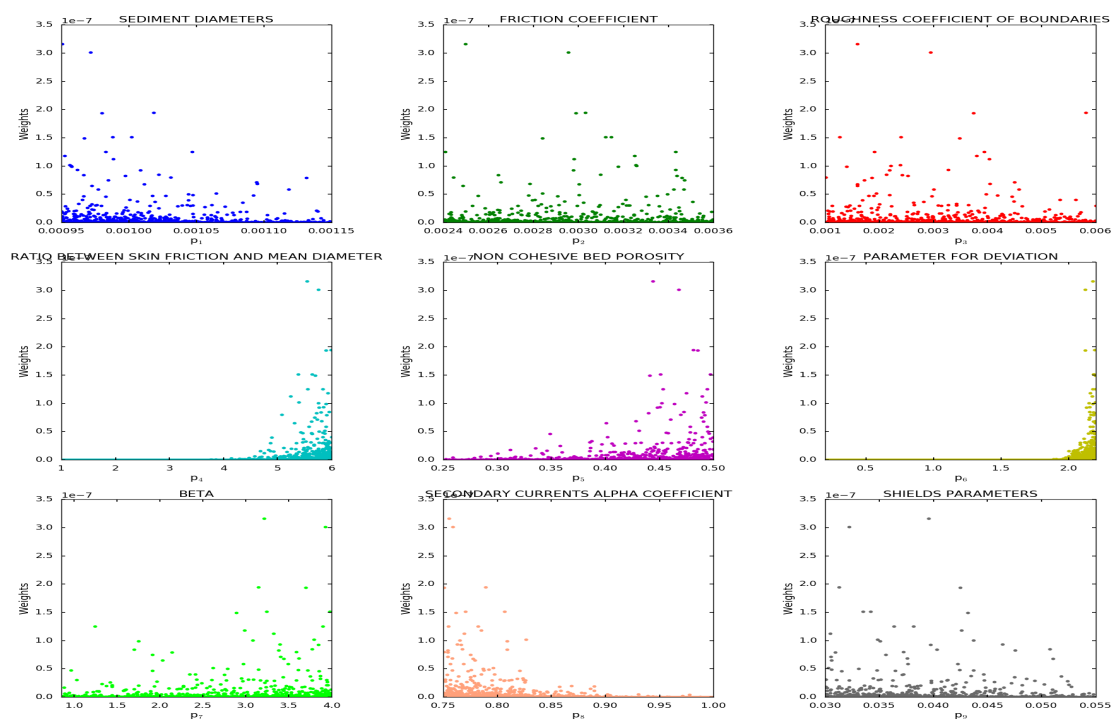


Figure A.18: Prior likelihood weights after iterations (calibration-Wu model)

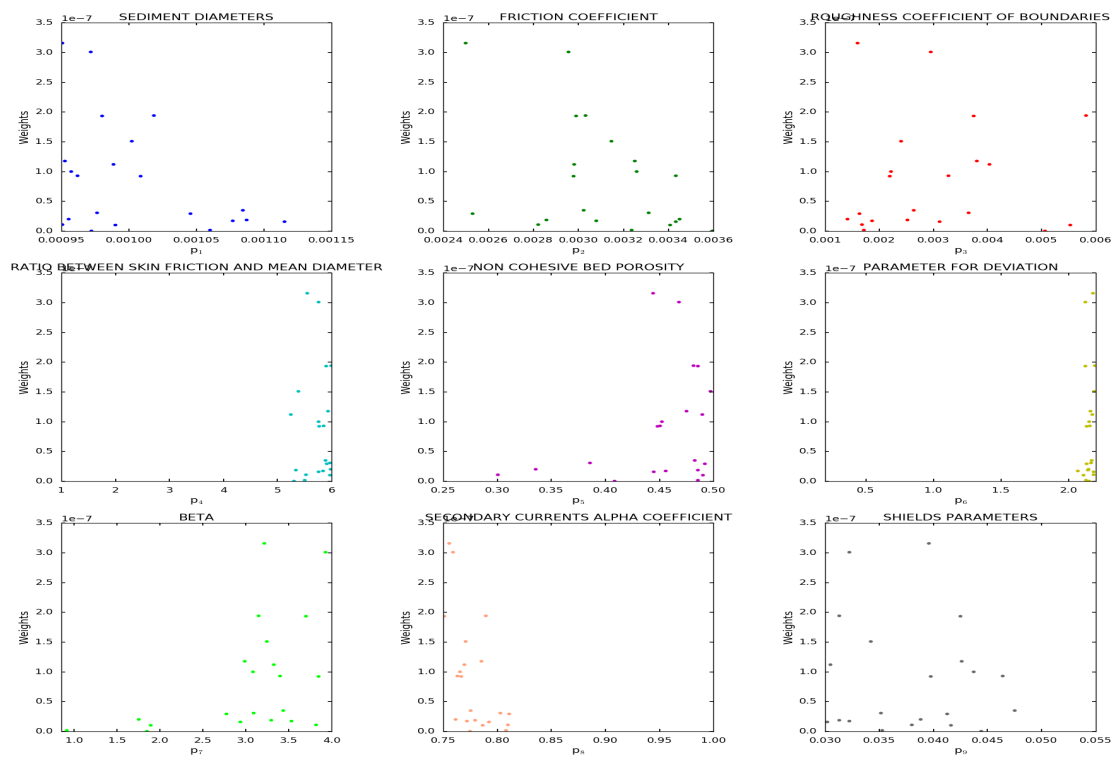


Figure A.19: Posterior likelihood weights after rejection sampling (calibration-Wu model)

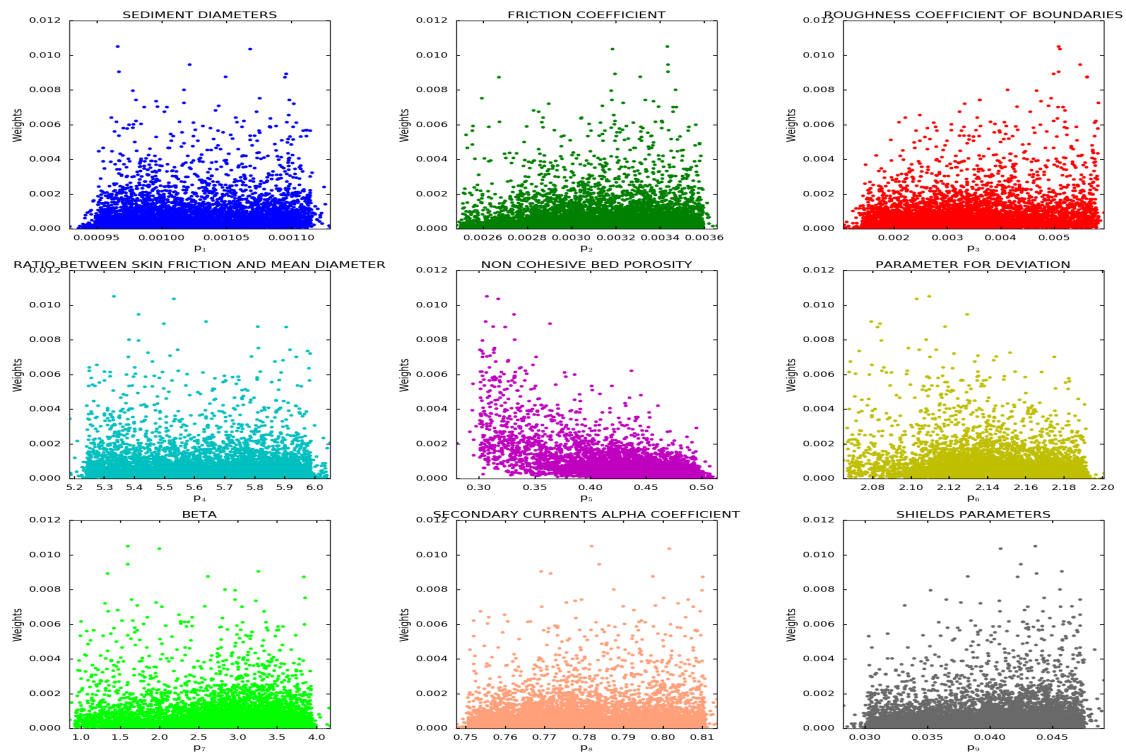


Figure A.20: Prior likelihood weights (validation-Wu model)

B Appendix II: BMS for the Lower Rhine Model

This appendix is composed of two sections, namely BMS for Twin Experiment of the Lower Rhine River Model in Section B.1, and BMS of the the Lower Rhine River Model with Real Measurement in Section B.2. Each section entails the likelihood weights of parameters before and after improvement of response surface, the posterior of parameters versus their weights and the likelihood weights of prior parameter sets in validation step are presented for all models.

B.1 BMS for Twin Experiment

Meyer-Peter-Müller Model:

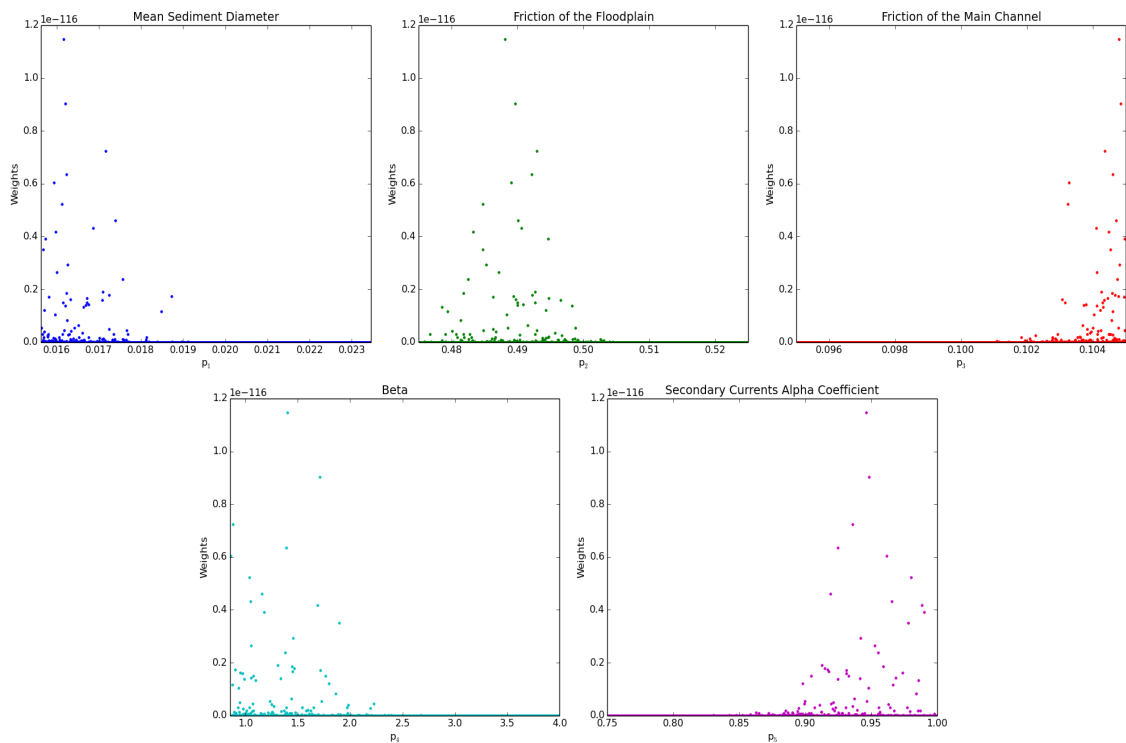


Figure B.1: Prior likelihood weights before iterations (calibration-Meyer-Peter-Müller model)

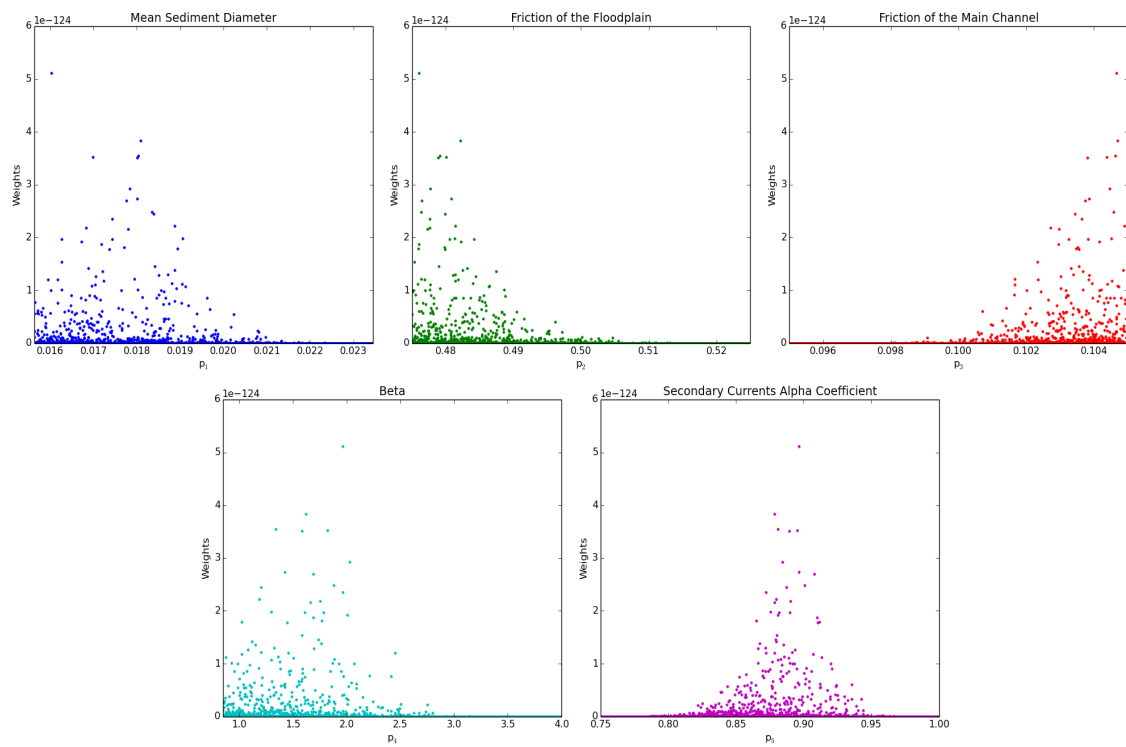


Figure B.2: Prior likelihood weights after iterations (calibration-Meyer-Peter-Müller model)

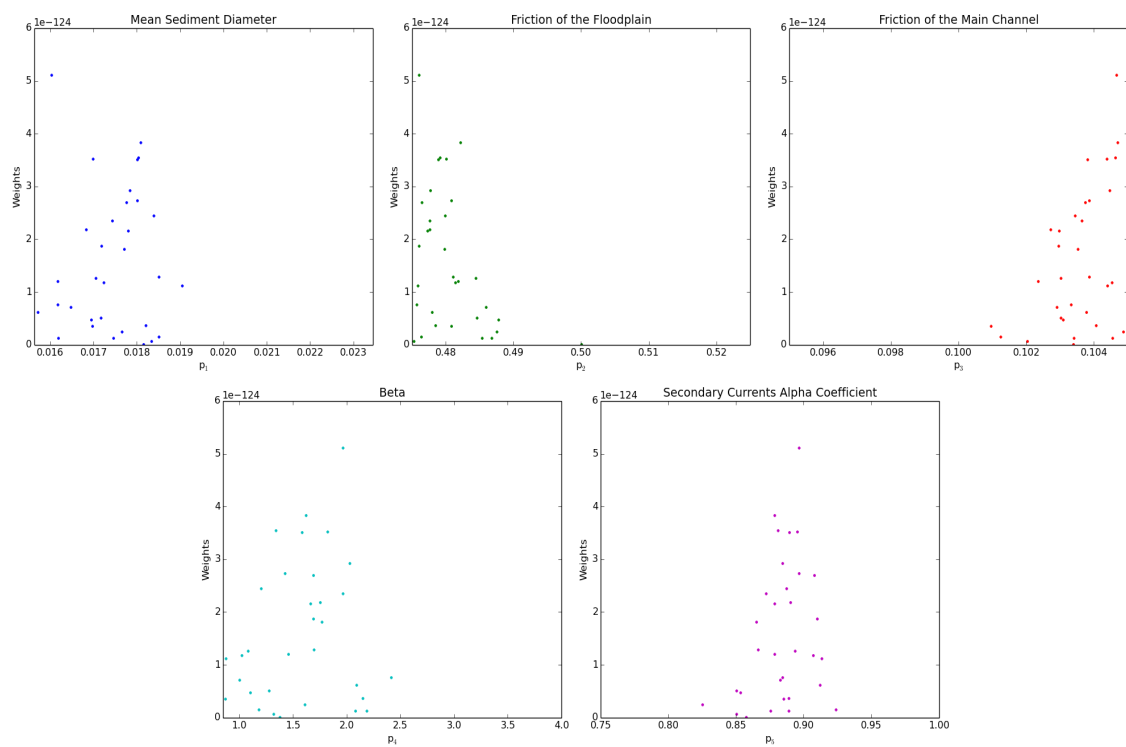


Figure B.3: Posterior likelihood weights after bootstrap-filtering (calibration-Meyer-Peter-Müller model)

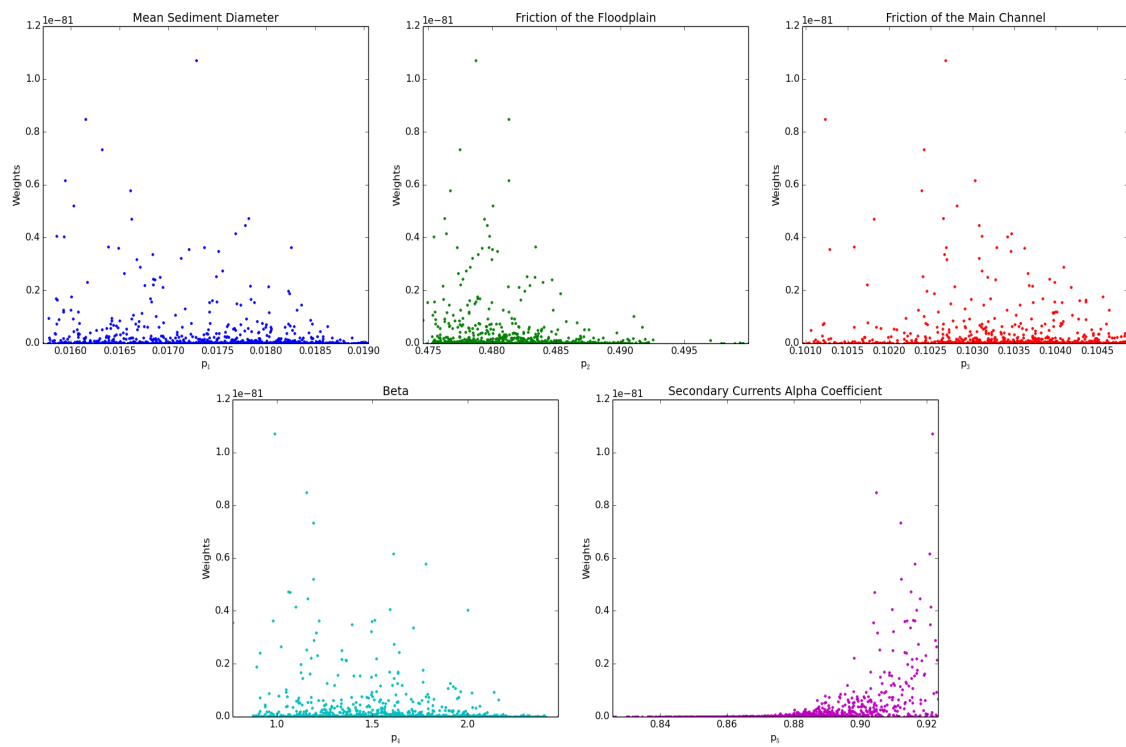


Figure B.4: Prior likelihood weights (validation-Meyer-Peter-Müller model)

Einstein-Brown Model:

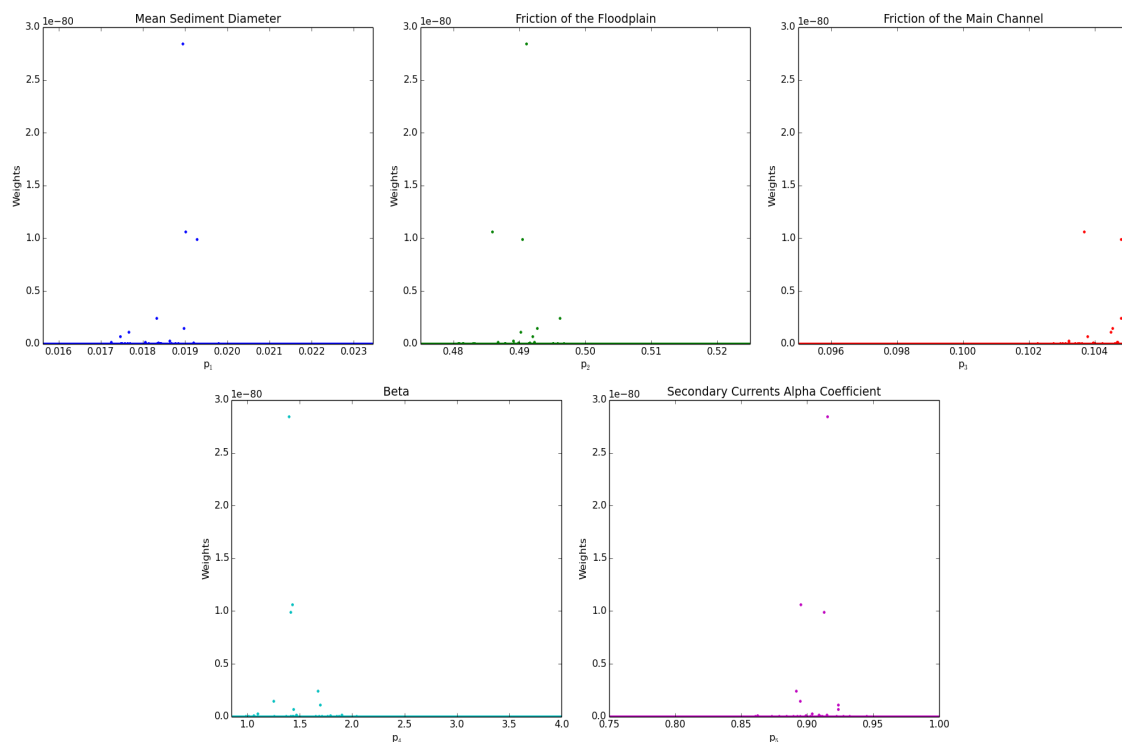


Figure B.5: Prior likelihood weights before iterations (calibration-Einstein-Brown model)

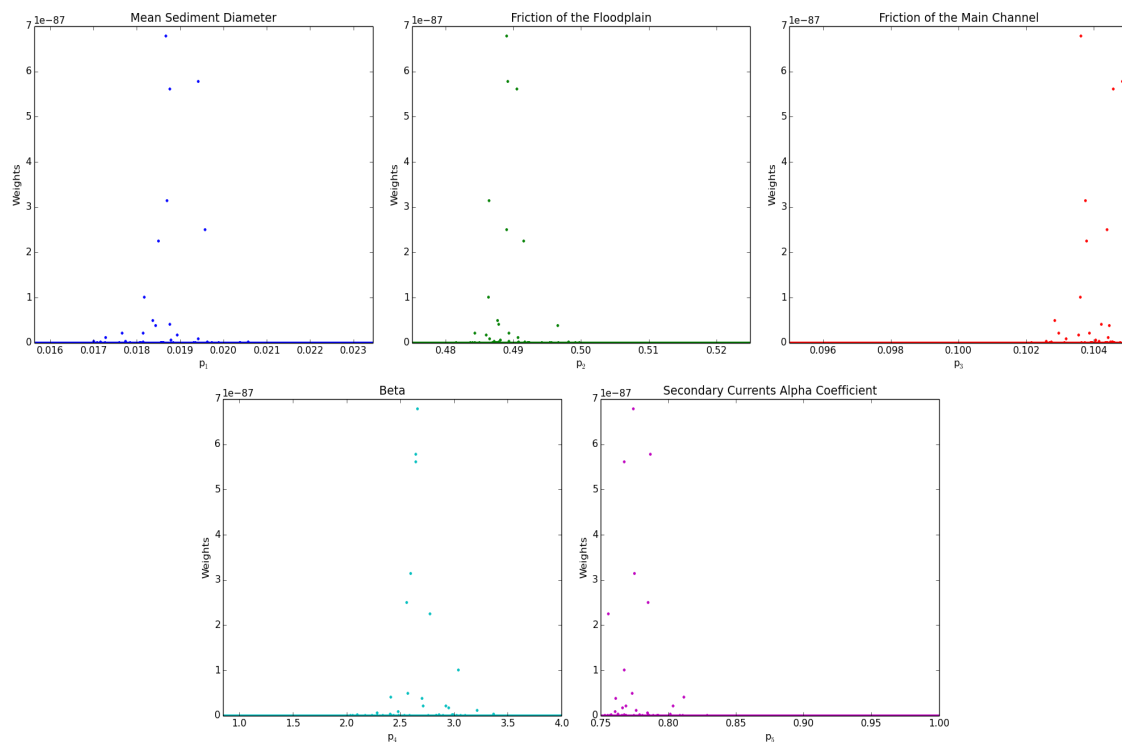


Figure B.6: Prior likelihood weights after iterations (calibration-Einstein-Brown model)

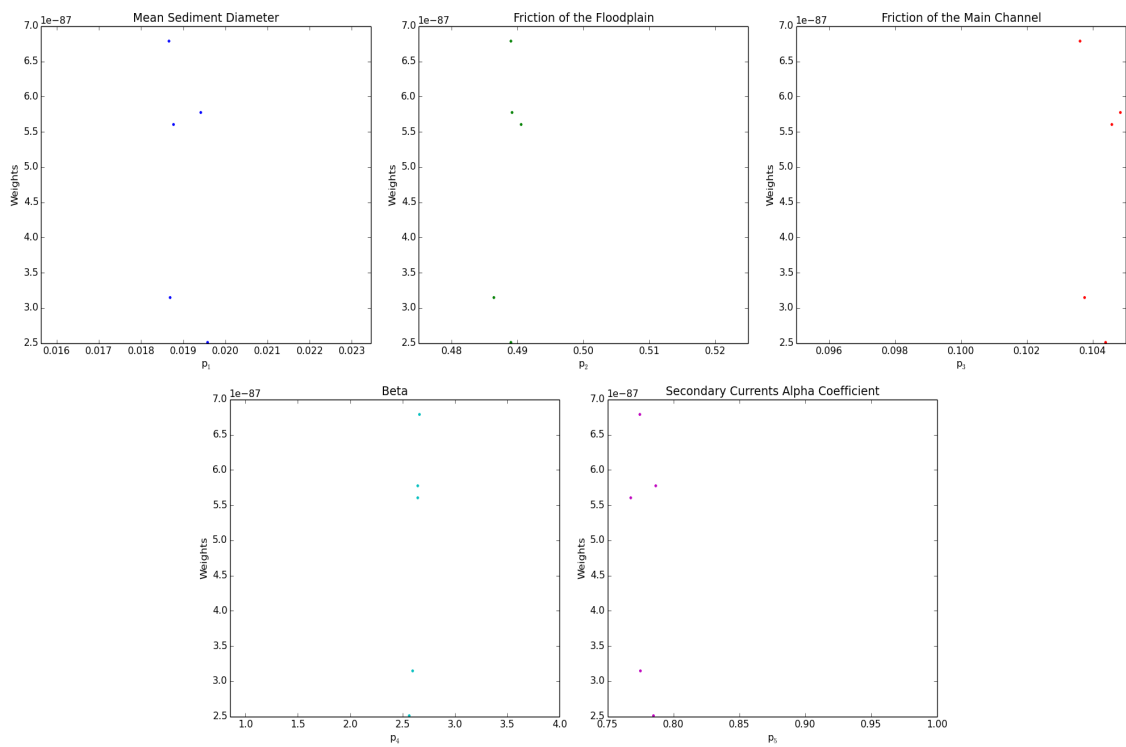


Figure B.7: Posterior likelihood weights after bootstrap-filtering (calibration-Einstein-Brown model)

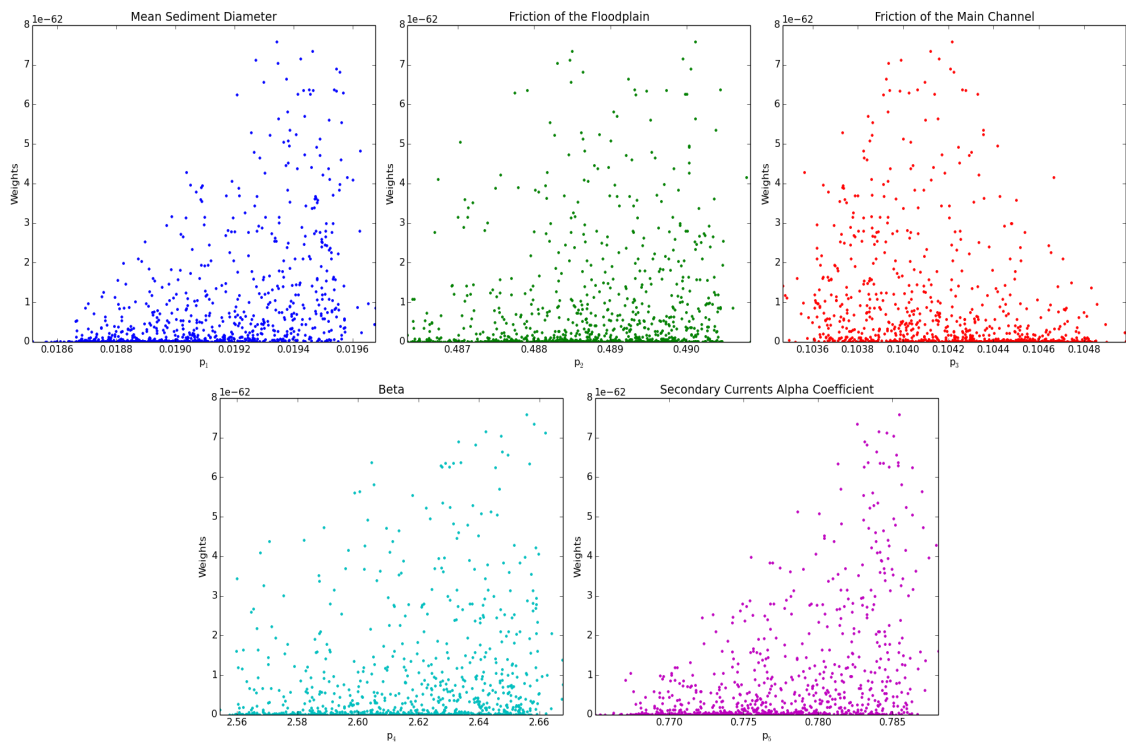


Figure B.8: Prior likelihood weights (validation-Einstein-Brown model)

Modified Engelund-Hansen Model:

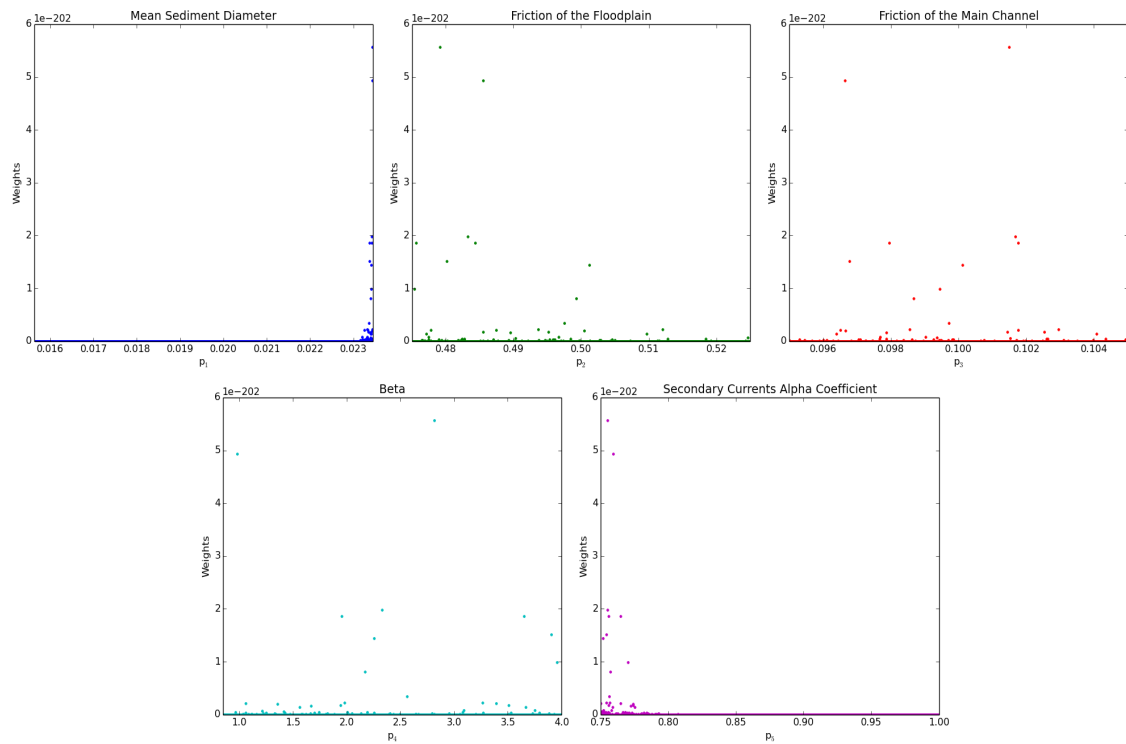


Figure B.9: Prior likelihood Weights before iterations (calibration-Mod. Engelund-Hansen model)

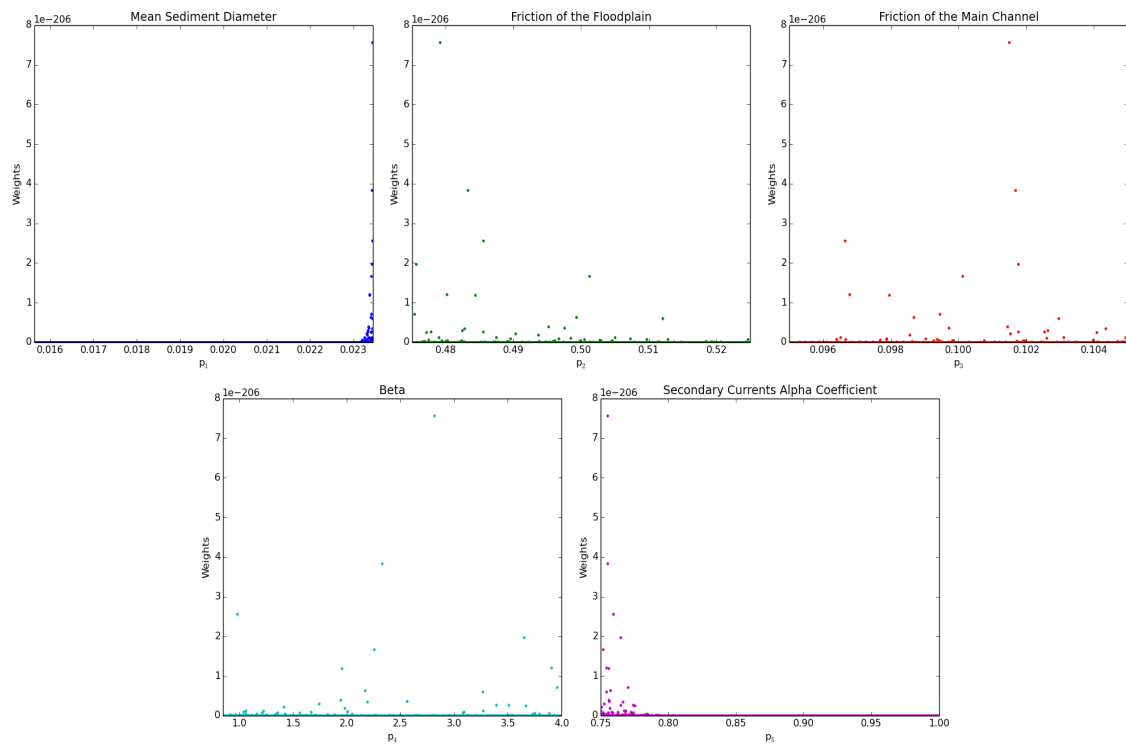


Figure B.10: Prior likelihood weights after iterations (calibration-Mod. Engelund-Hansen model)

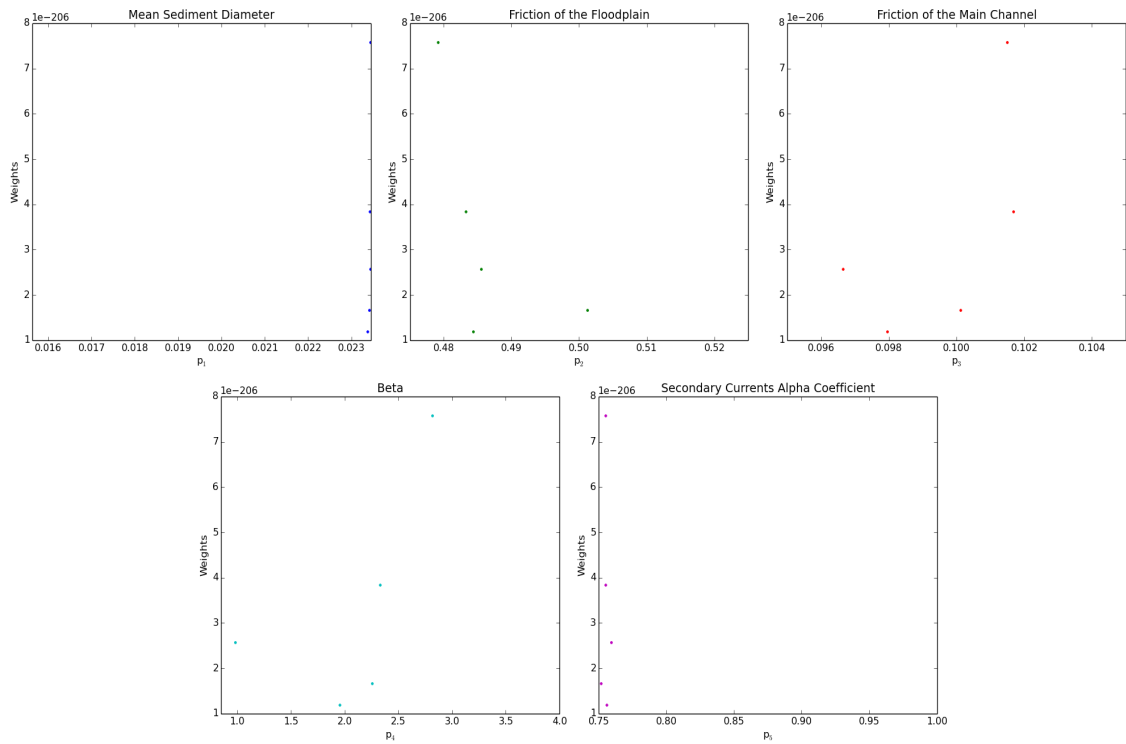


Figure B.11: Posterior likelihood weights after bootstrap-filtering (calibration-Mod. Engelund-Hansen model)

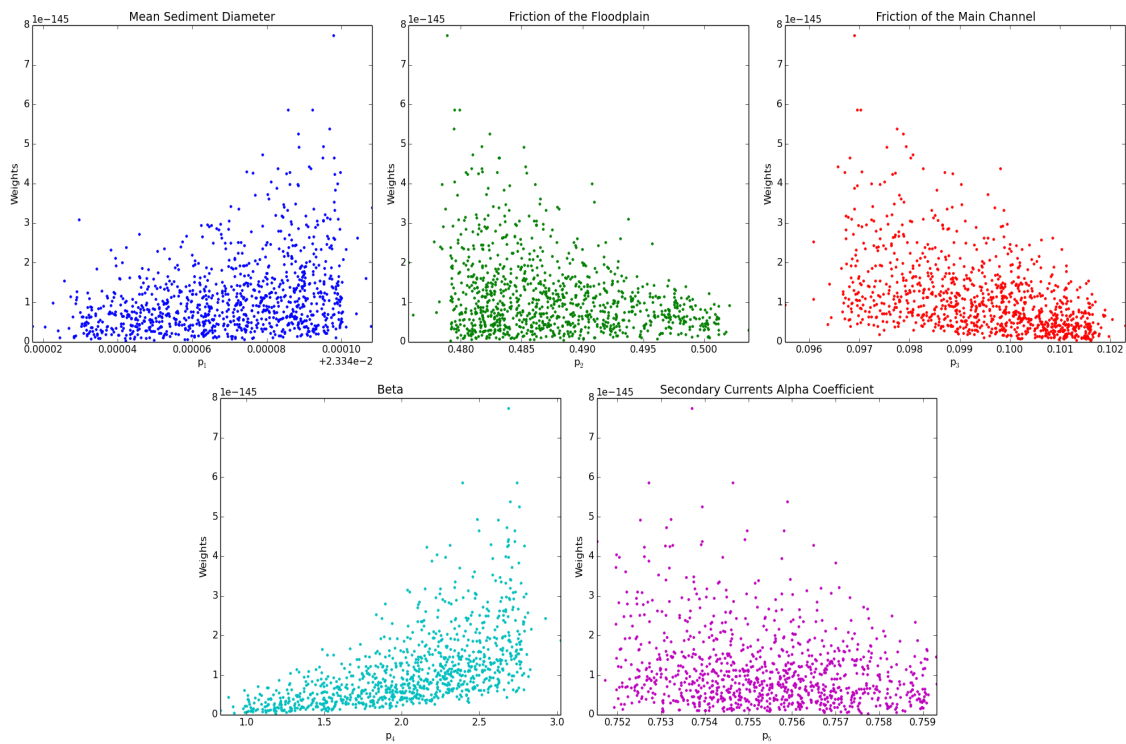


Figure B.12: Prior likelihood weights (validation-Mod. Engelund-Hansen model)

Van Rijn Model:

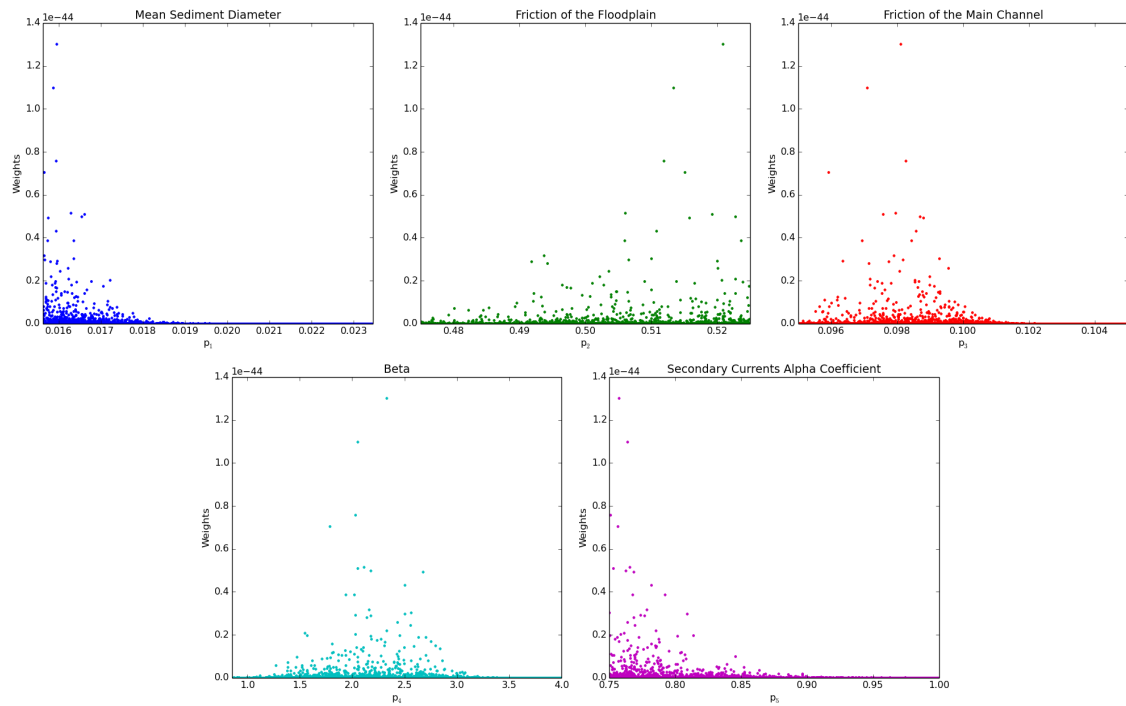


Figure B.13: Prior likelihood weights before iterations (calibration-Van Rijn model)

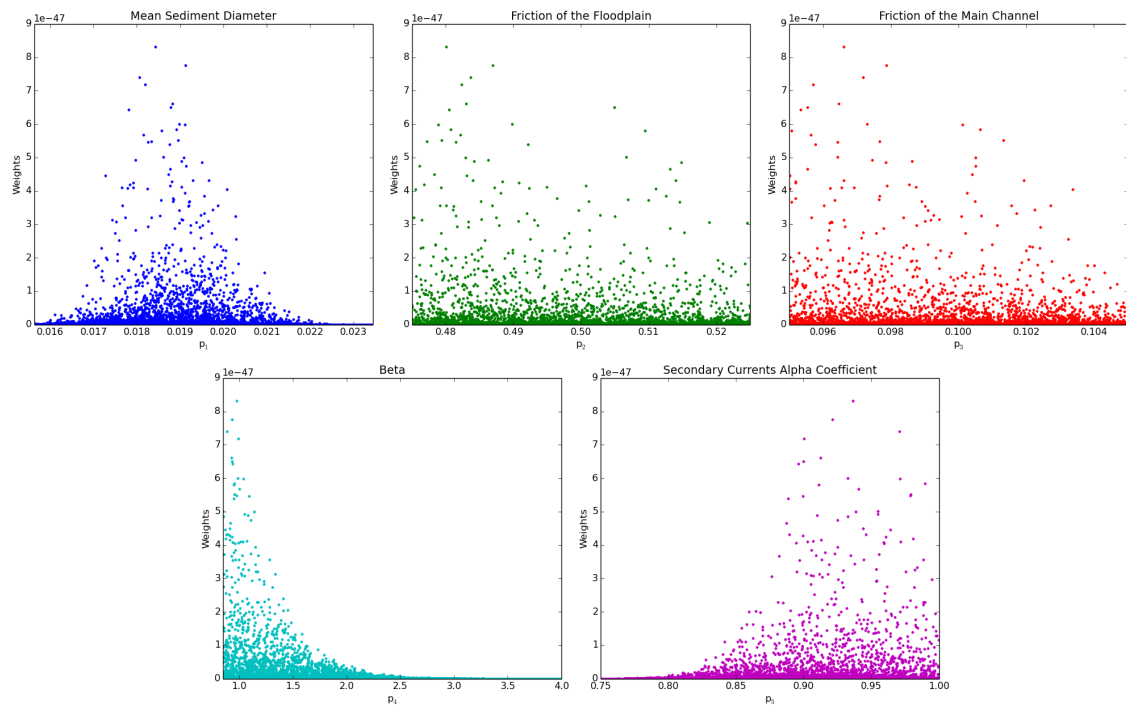


Figure B.14: Prior likelihood weights after iterations (calibration-Van Rijn model)

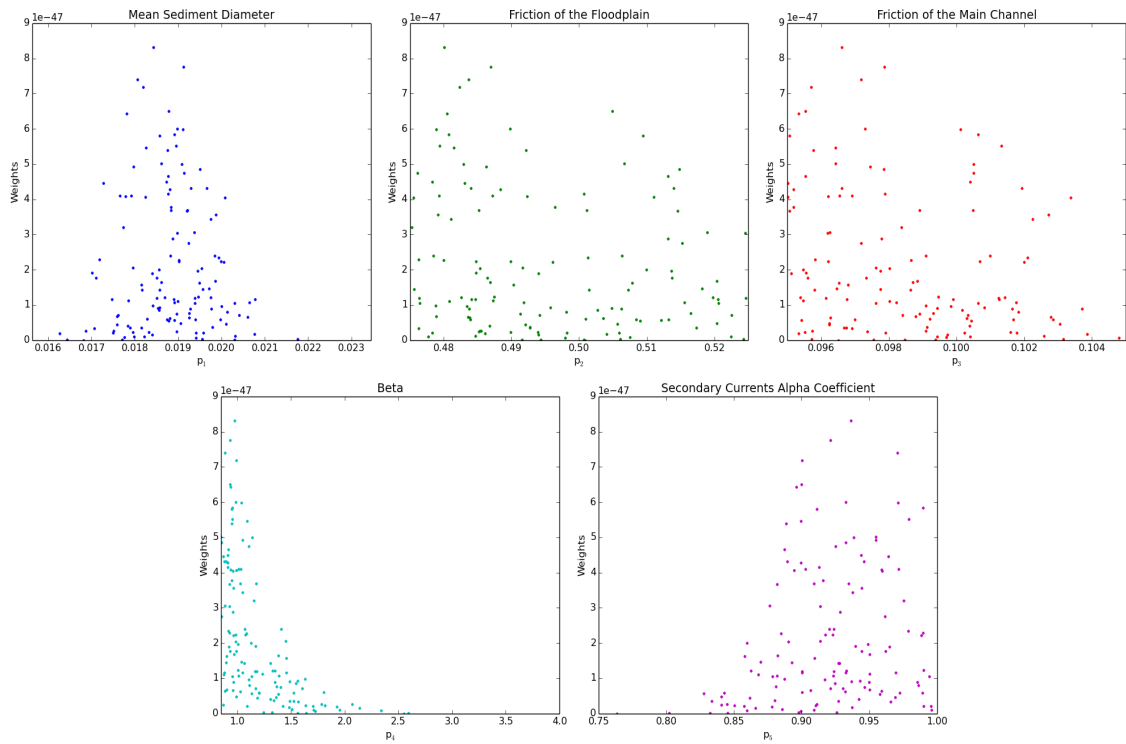


Figure B.15: Posterior likelihood weights after bootstrap-filtering (calibration-Van Rijn model)

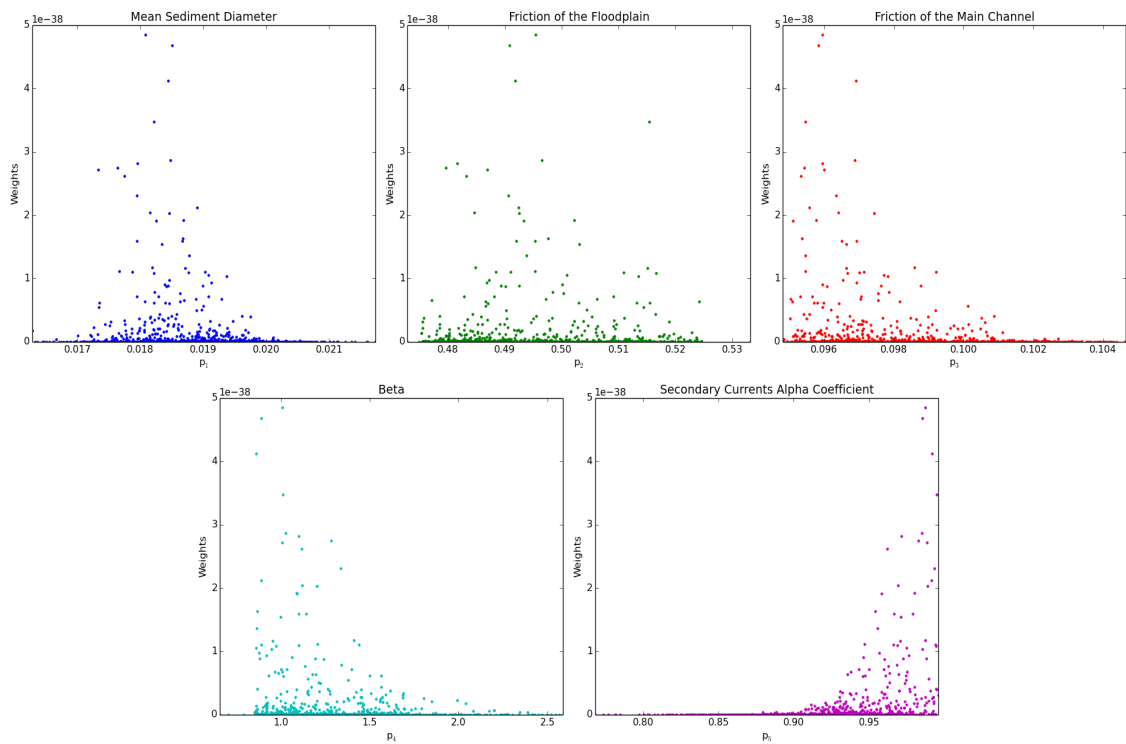


Figure B.16: Prior likelihood weights (validation-Van Rijn model)

Hunziker Model:

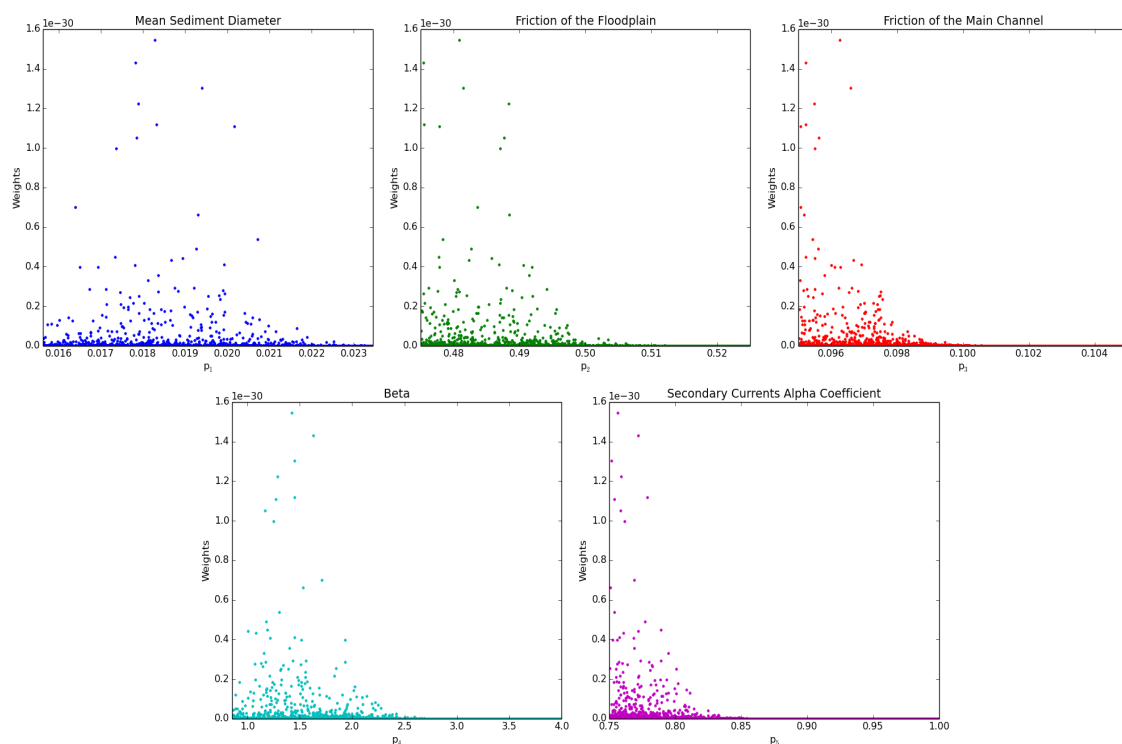


Figure B.17: Prior likelihood weights before iterations (calibration-Hunziker model)

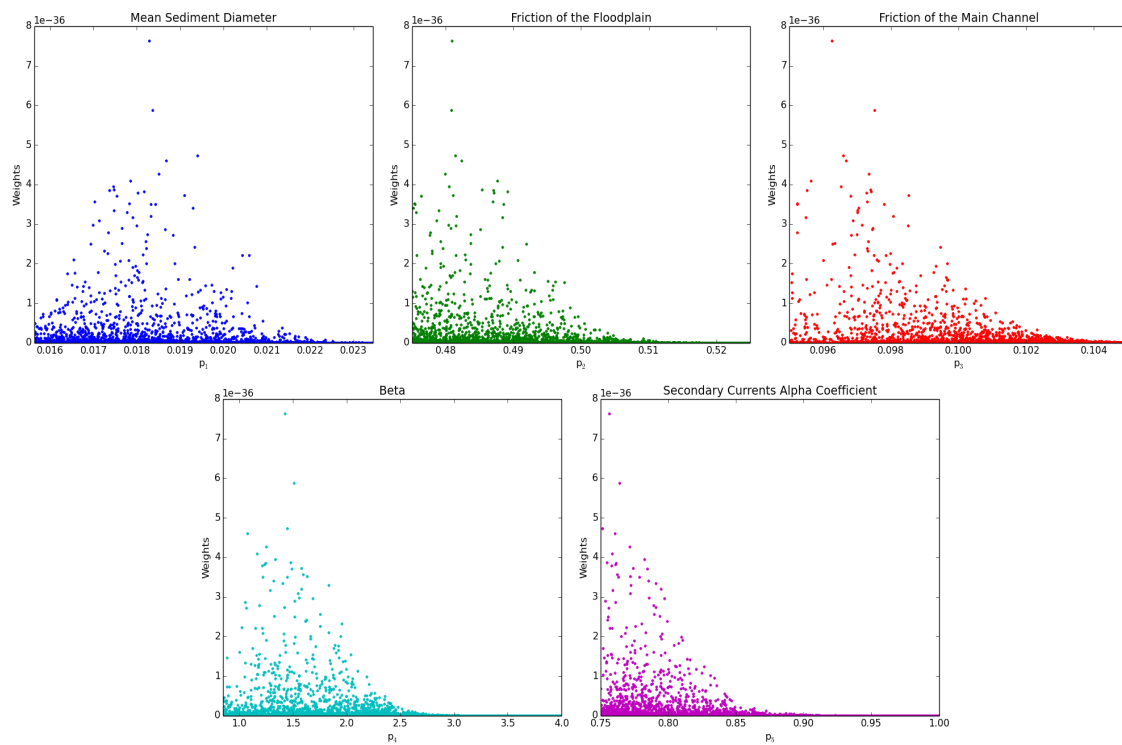


Figure B.18: Prior likelihood weights after iterations (calibration-Hunziker model)

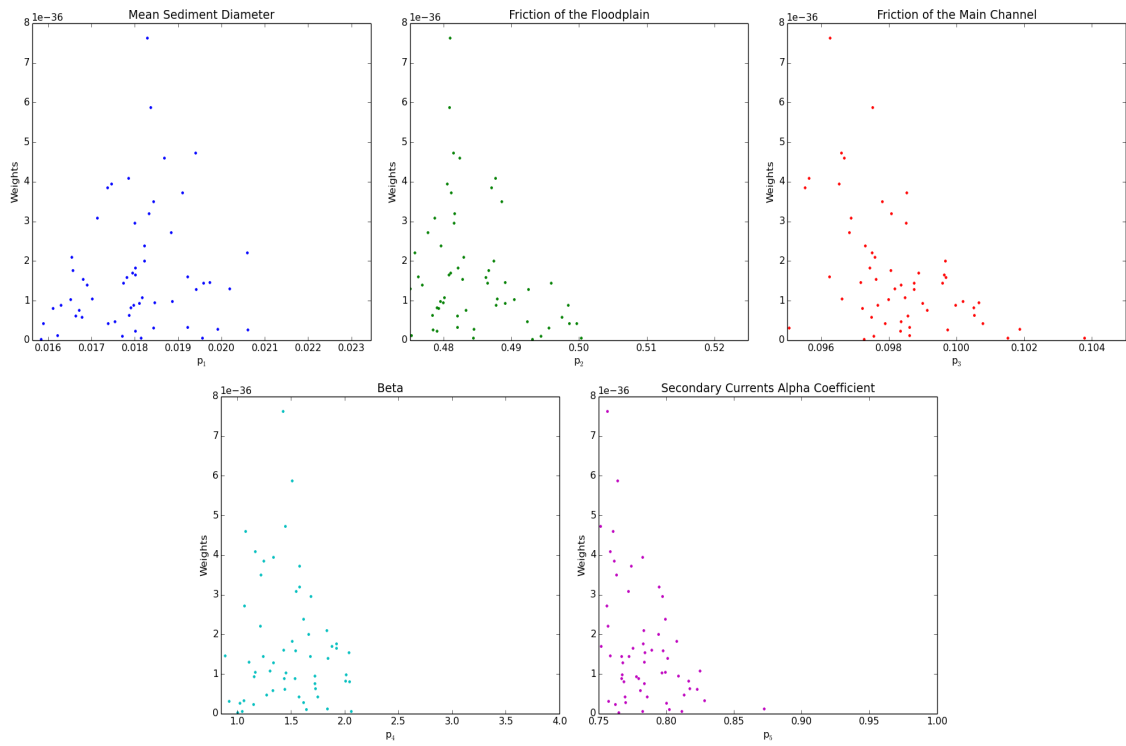


Figure B.19: Posterior likelihood weights after bootstrap-filtering (calibration-Hunziker model)

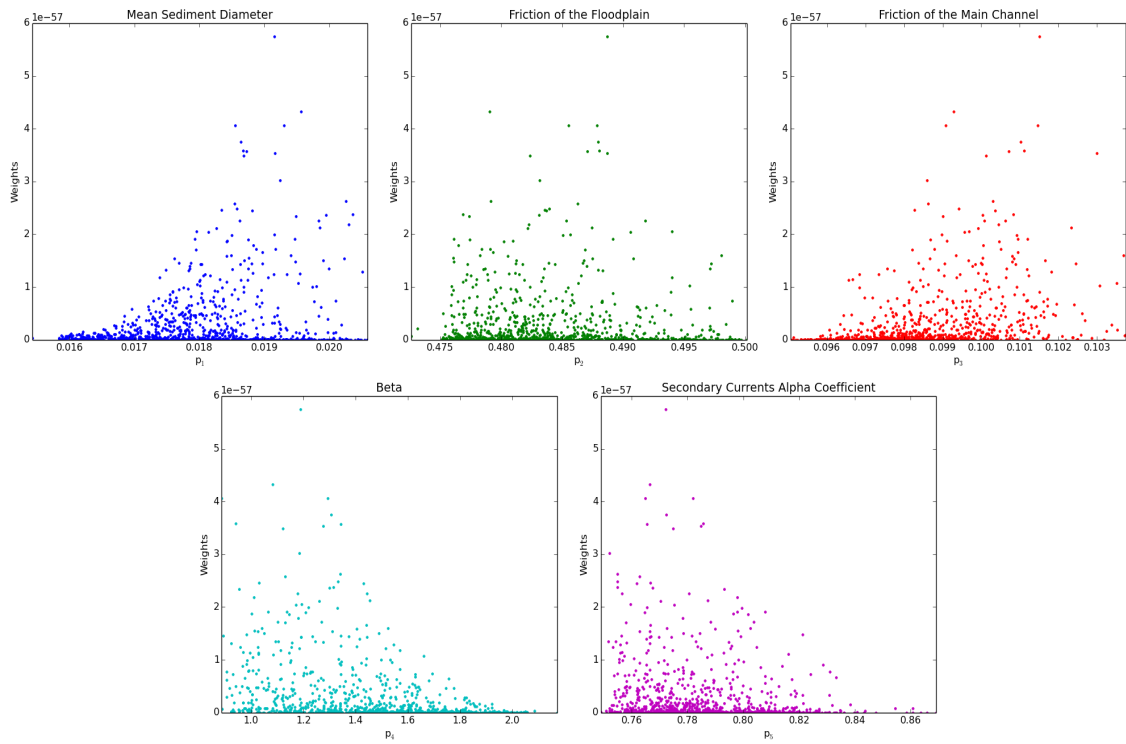


Figure B.20: Prior likelihood weights (validation-Hunziker model)

Wu Model:

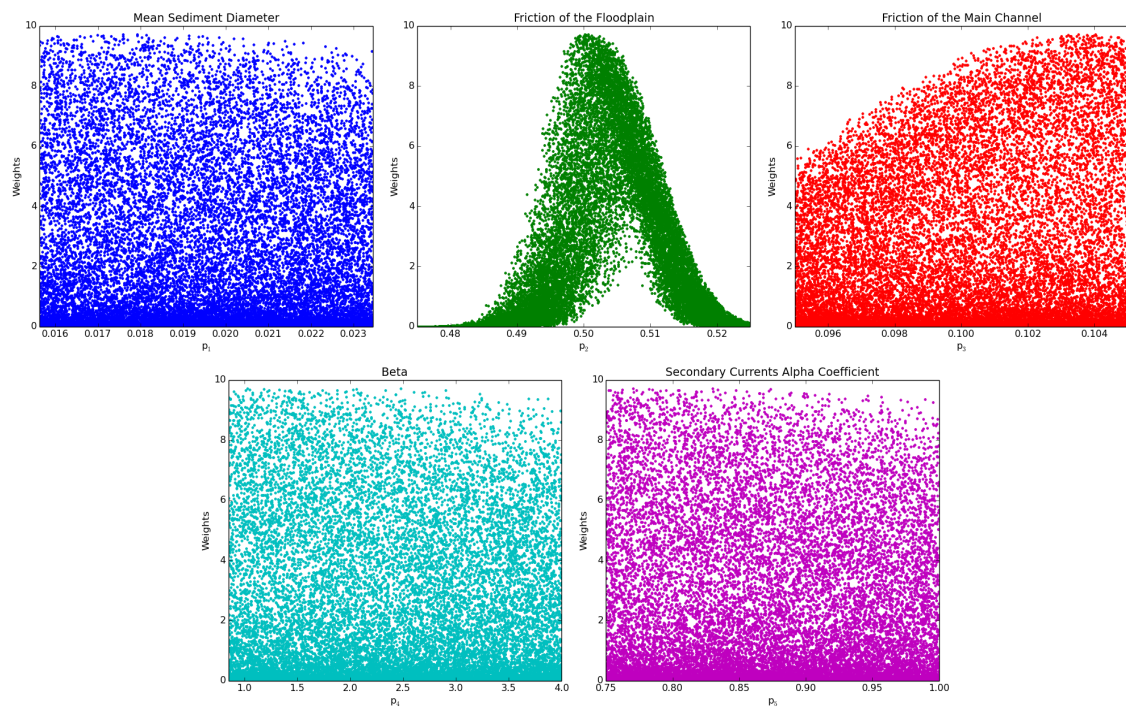


Figure B.21: Prior likelihood weights before iterations (calibration-Wu model)

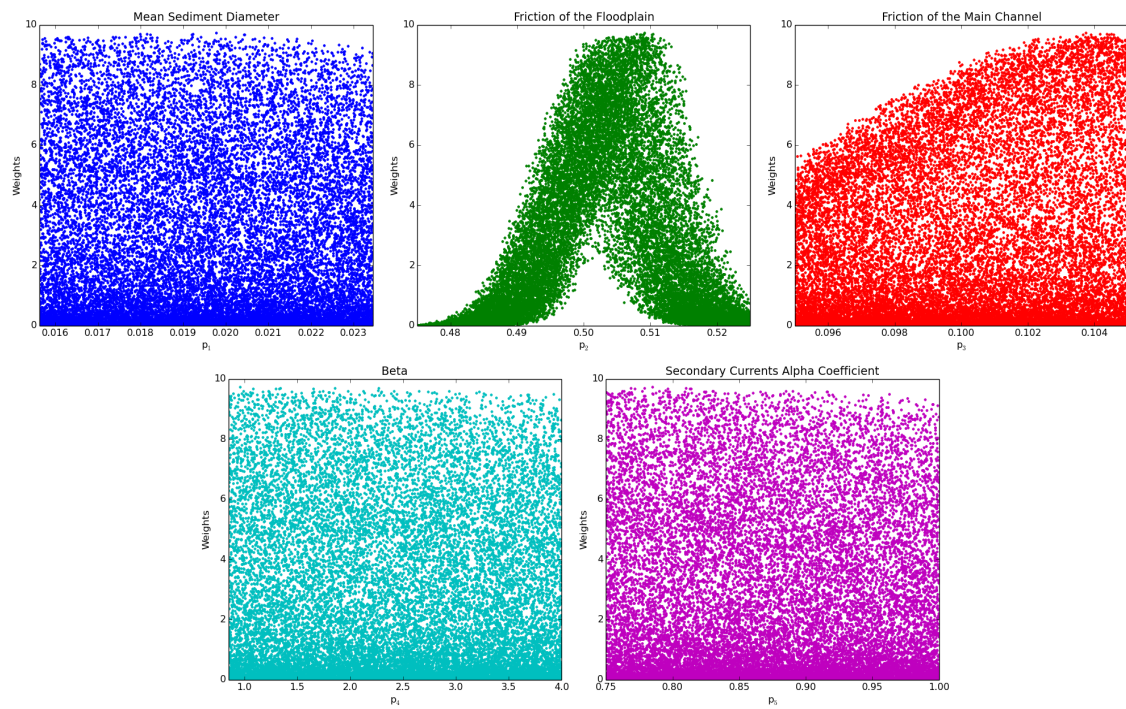


Figure B.22: Prior likelihood weights after iterations (calibration-Wu model)

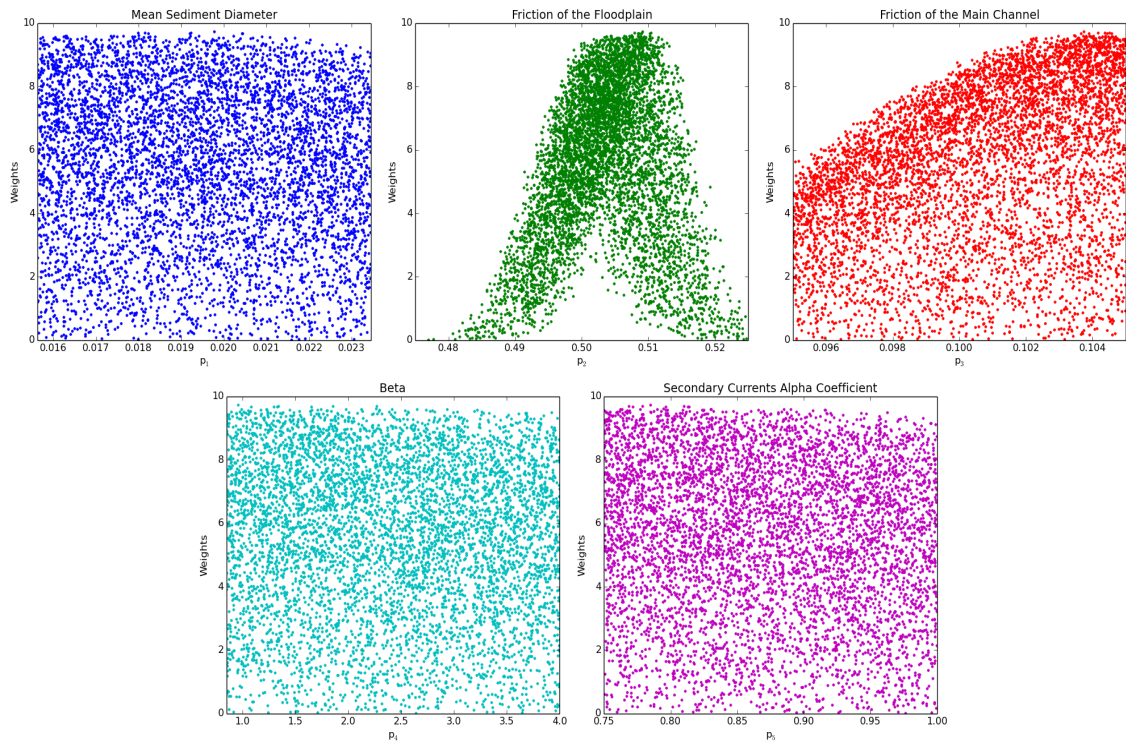


Figure B.23: Posterior likelihood weights after bootstrap-filtering (calibration-Wu model)

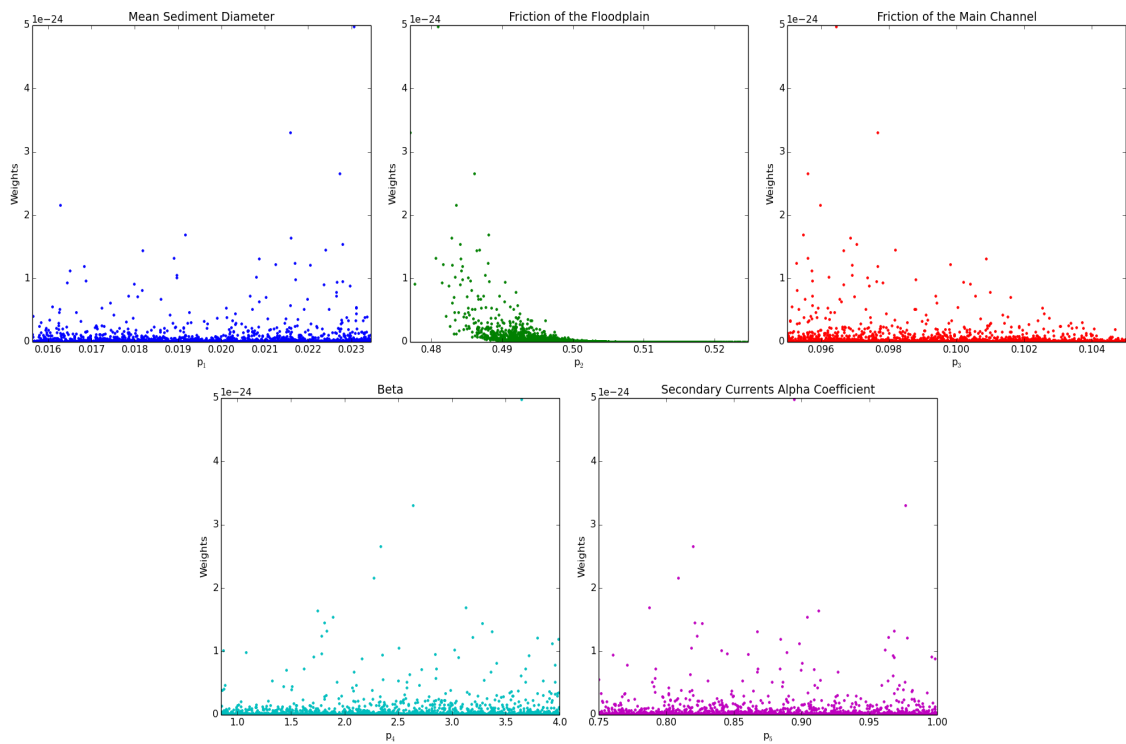


Figure B.24: Prior likelihood weights (validation-Wu model)

B.2 BMS of the the Real Lower Rhine Model

Meyer-Peter-Müller Model:

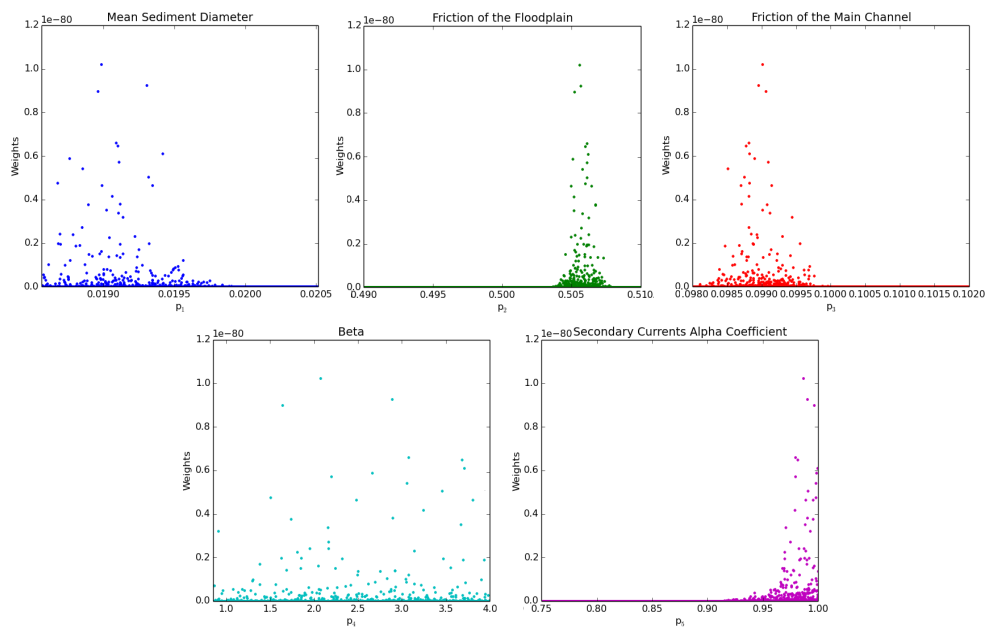


Figure B.25: Prior likelihood weights before iterations (calibration-Meyer-Peter-Müller model)

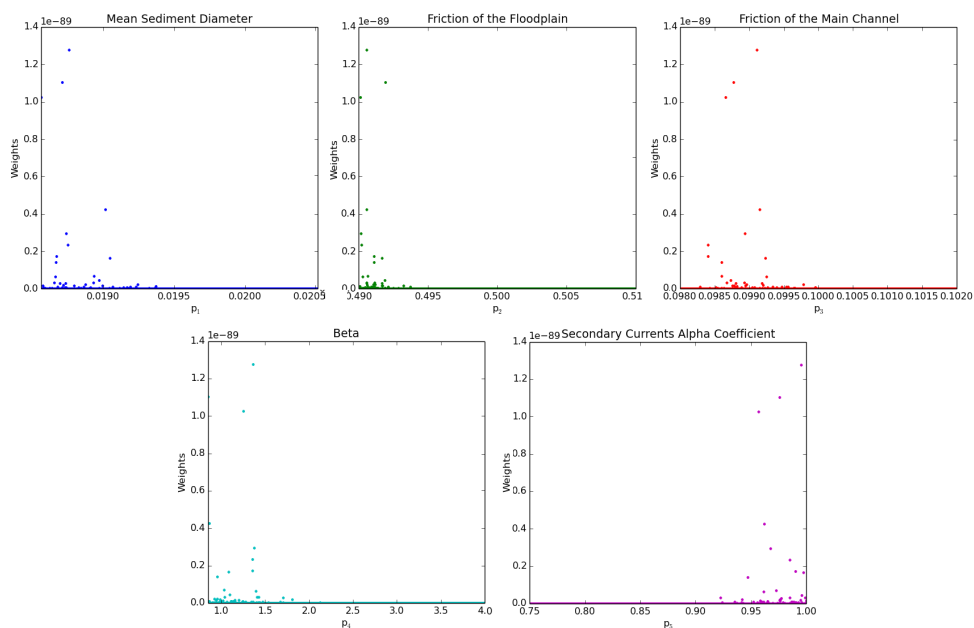


Figure B.26: Prior Likelihood Weights after Iterations (calibration-Meyer-Peter-Müller model)

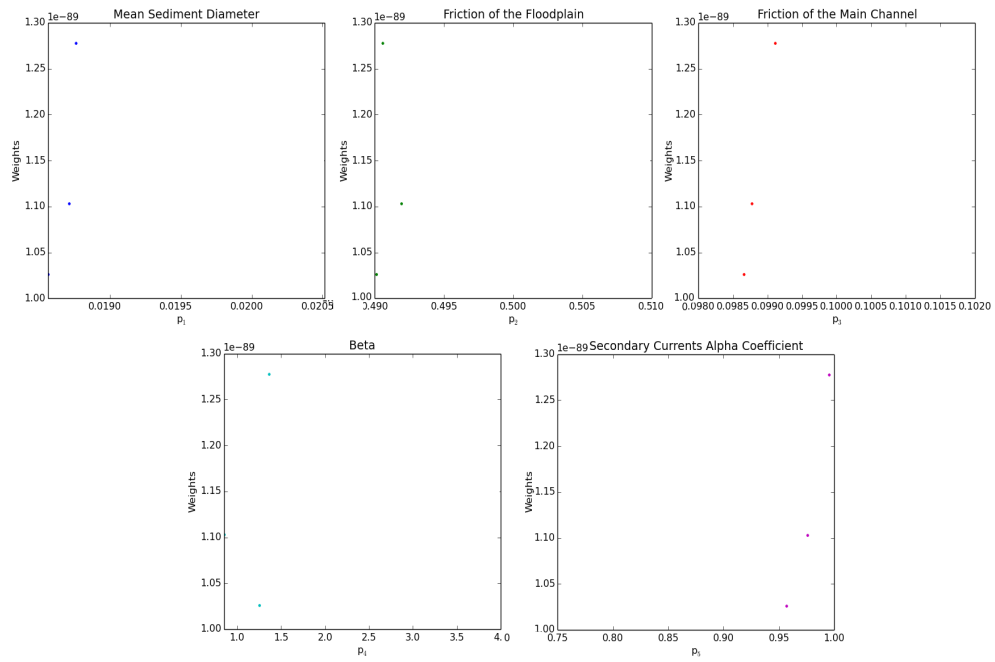


Figure B.27: Posterior likelihood weights after bootstrap-filtering (calibration-Meyer-Peter-Müller model)

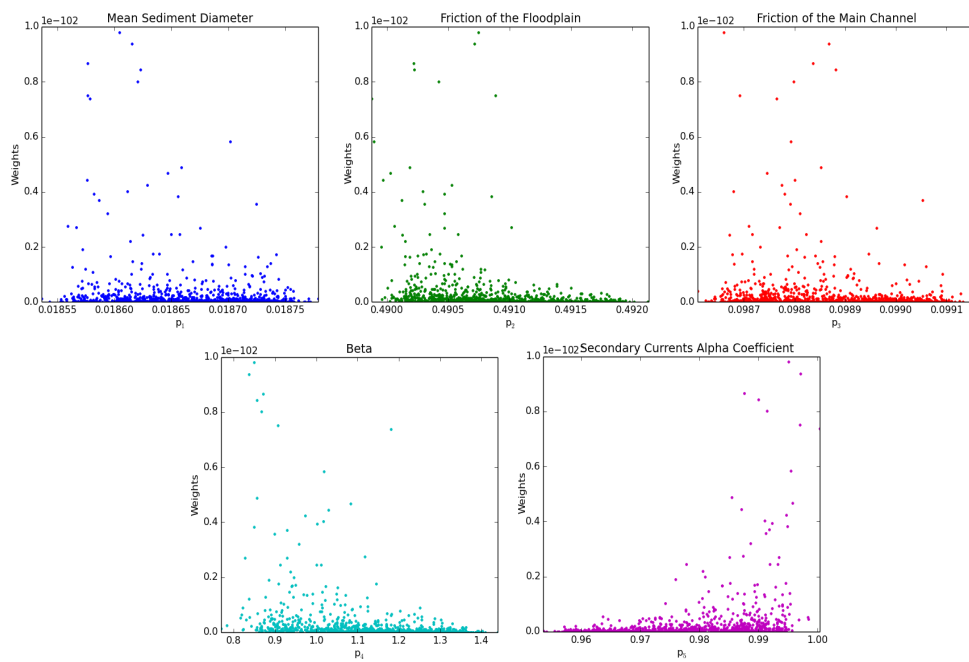


Figure B.28: Prior likelihood weights (validation-Meyer-Peter-Müller model)

Van Rijn Model:

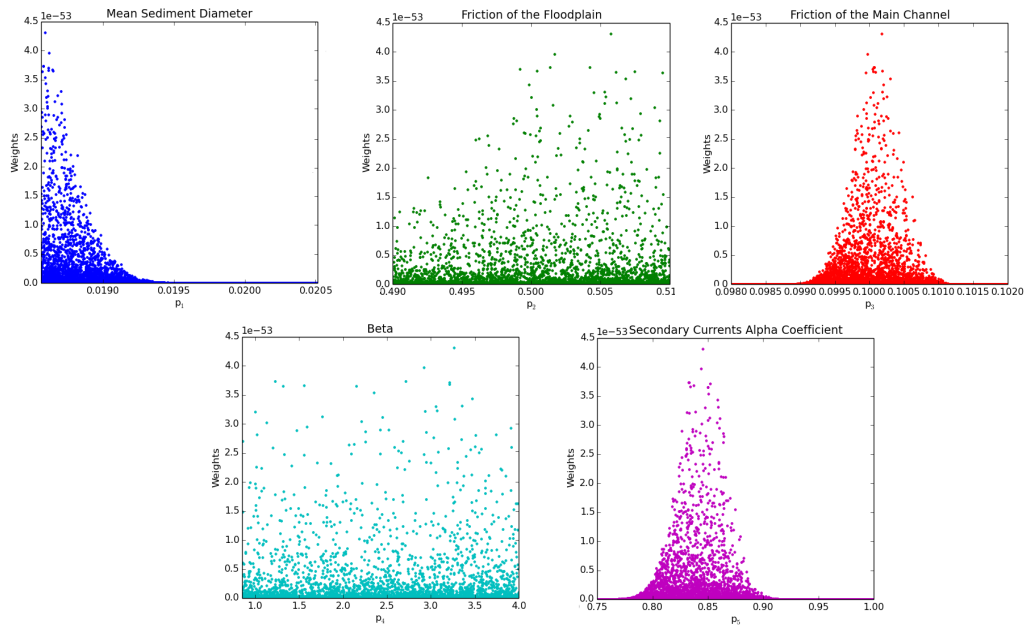


Figure B.29: Prior likelihood weights before iterations (calibration-Van Rijn model)

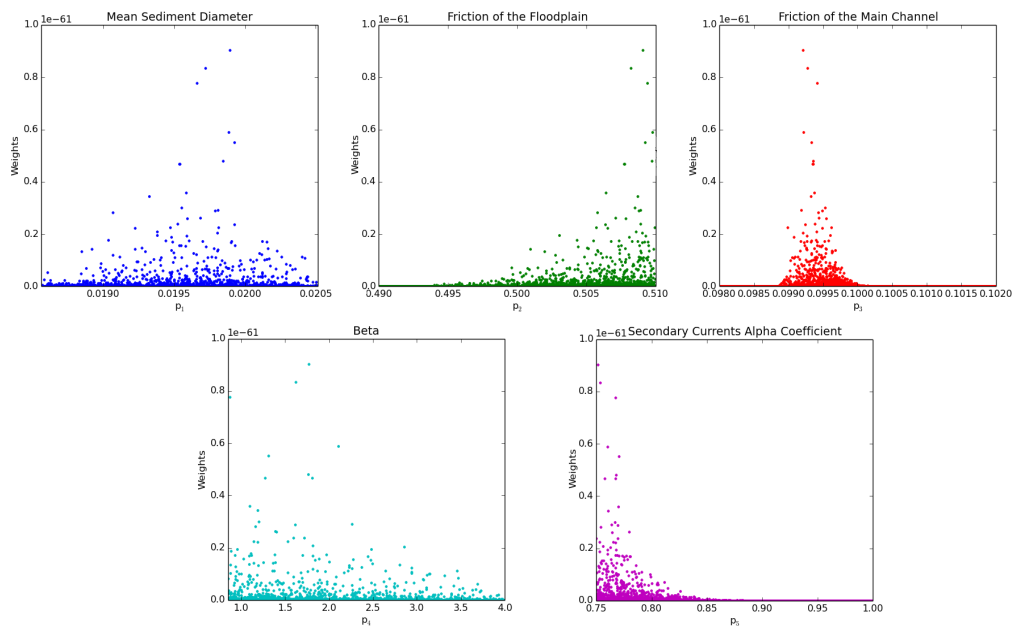


Figure B.30: Prior likelihood weights after iterations (calibration-Van Rijn model)

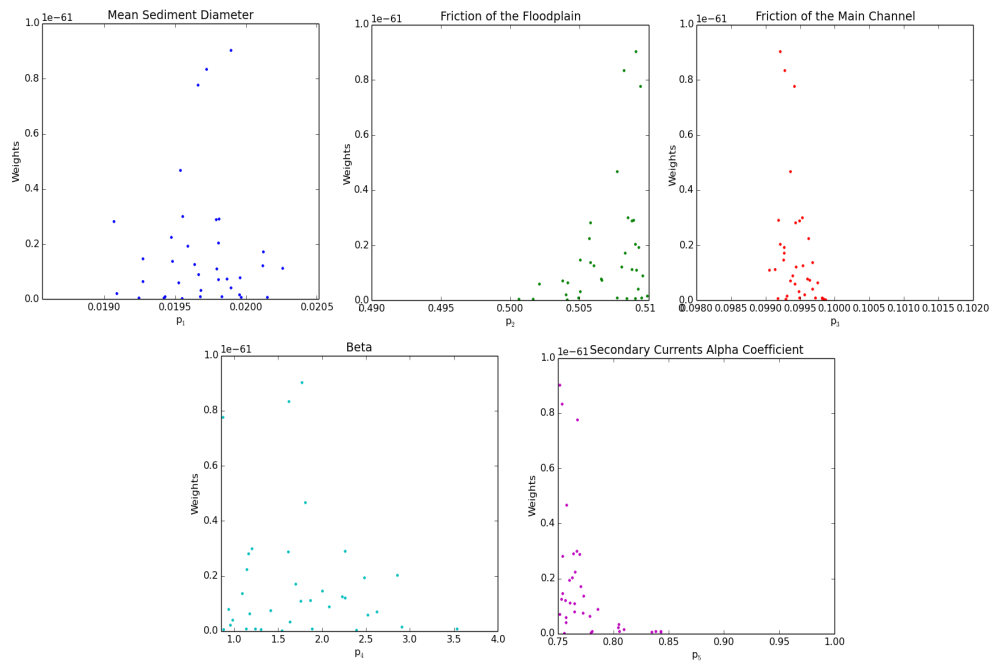


Figure B.31: Posterior likelihood weights after bootstrap-filtering (calibration-Van Rijn model)

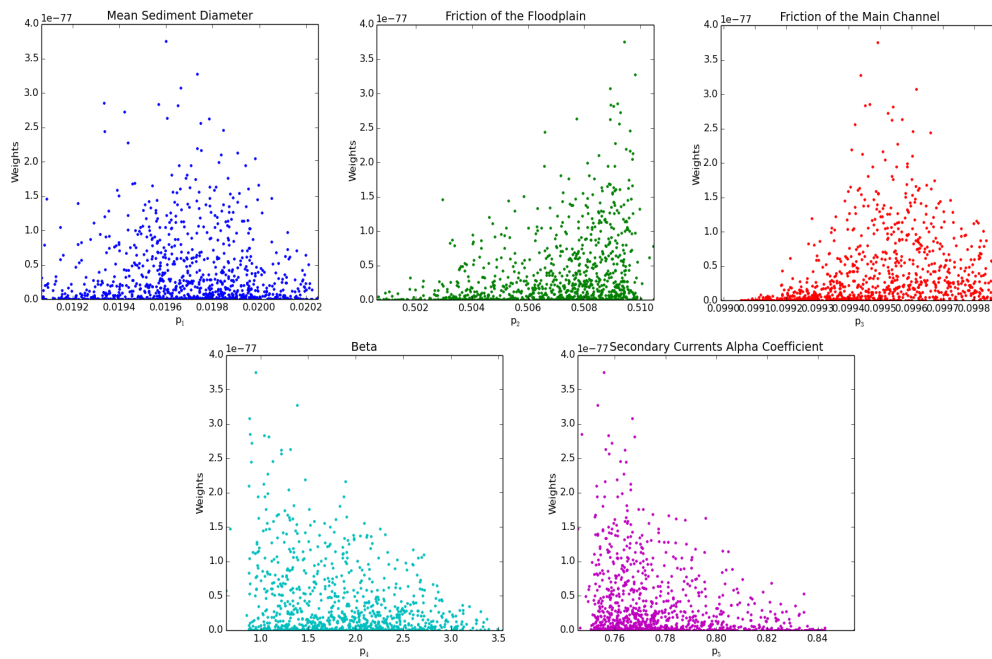


Figure B.32: Prior likelihood weights (validation-Van Rijn model)

Hunziker Model:

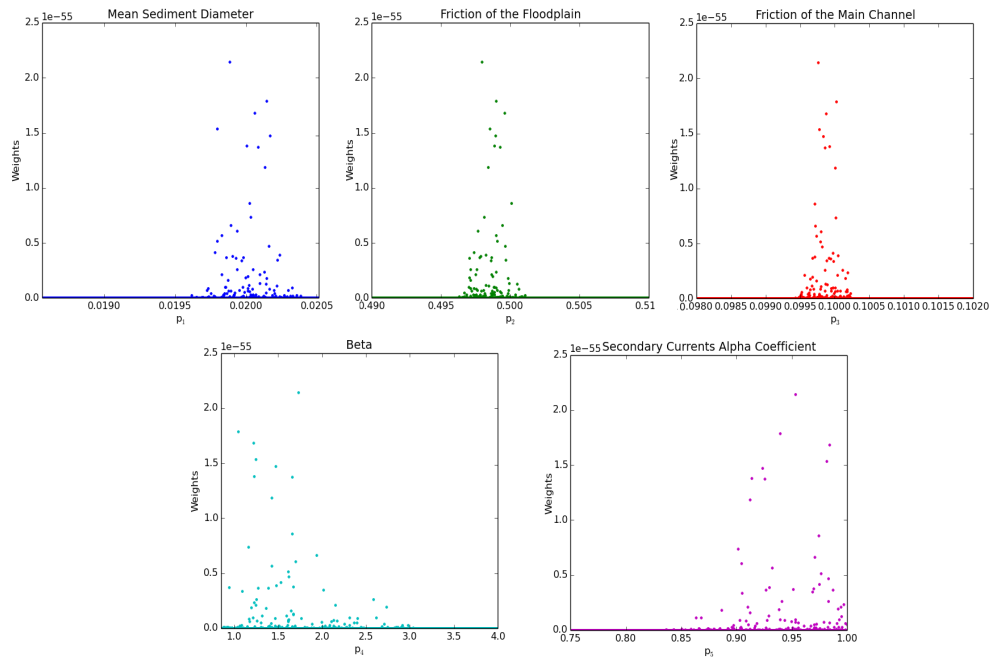


Figure B.33: Prior likelihood weights before iterations (calibration-Hunziker model)

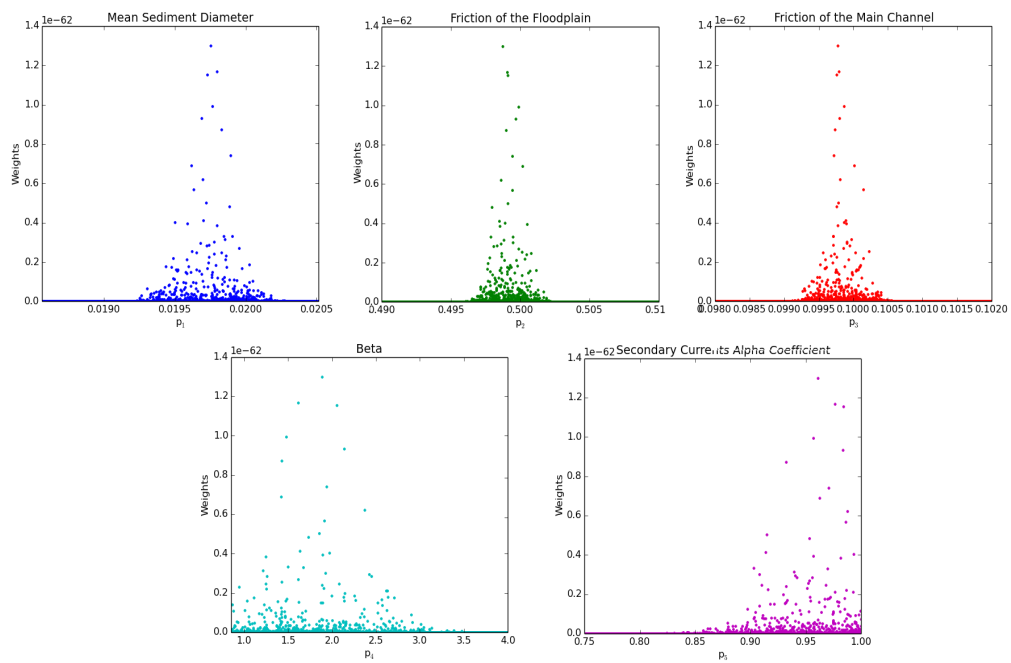


Figure B.34: Prior likelihood weights after iterations (calibration-Hunziker model)

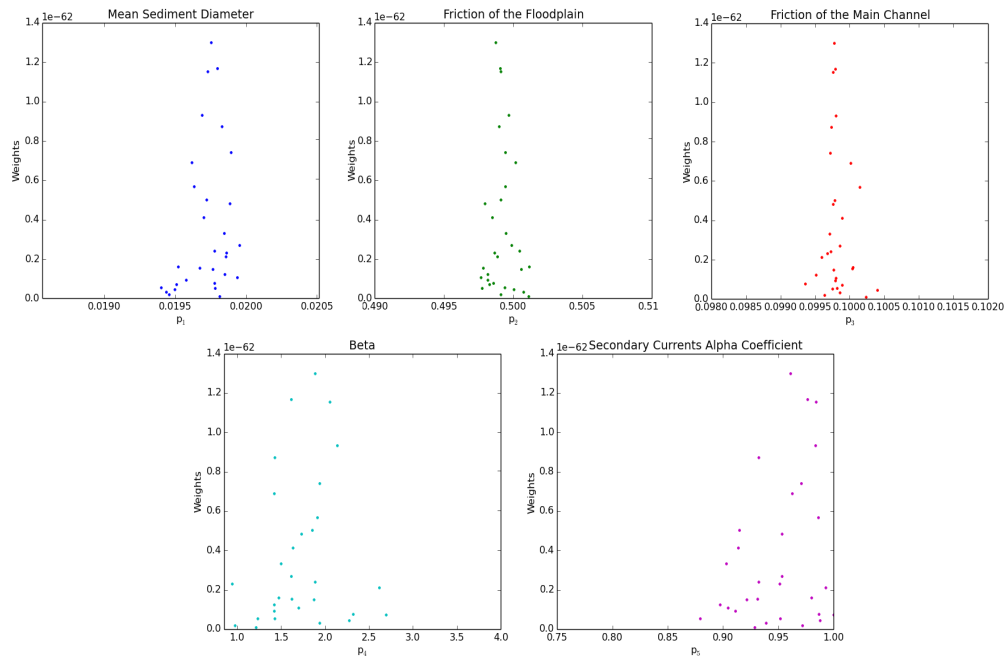


Figure B.35: Posterior likelihood weights after bootstrap-filtering (calibration-Hunziker model)

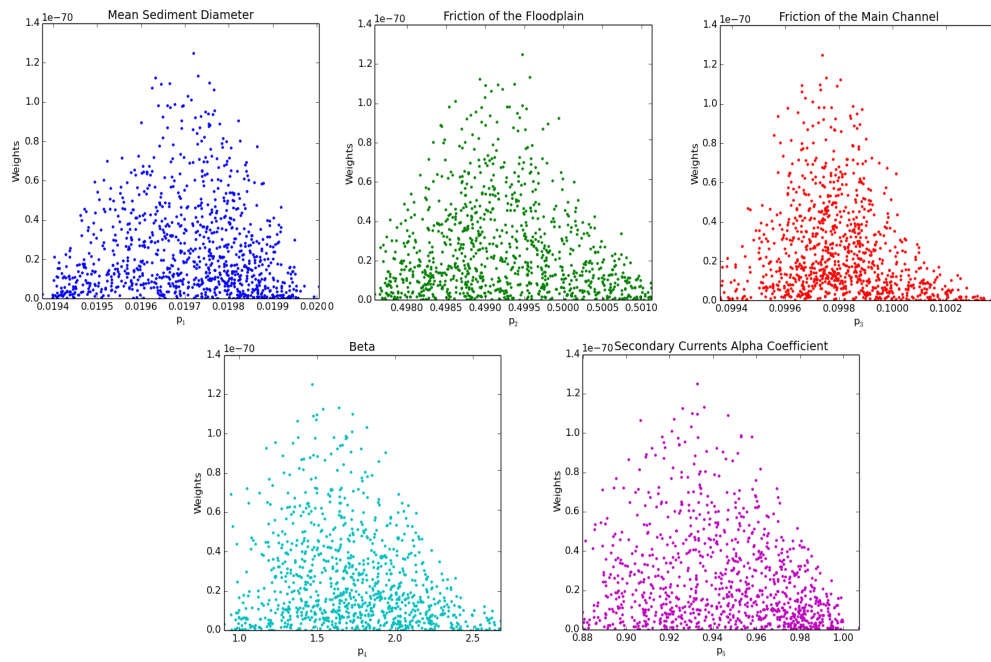


Figure B.36: Prior likelihood weights (validation-Hunziker model)

Wu Model:

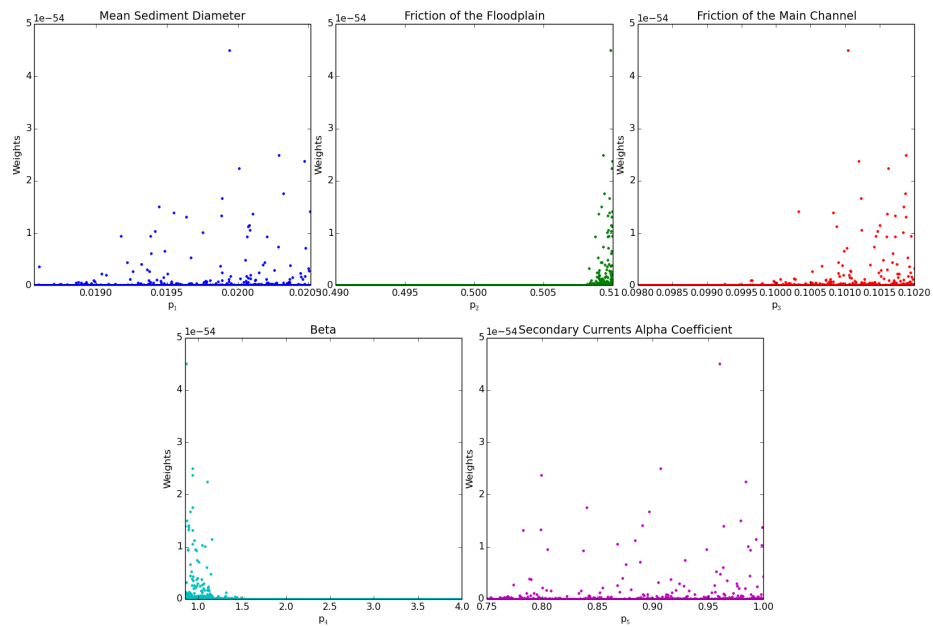


Figure B.37: Prior likelihood weights before iterations (calibration-Wu model)

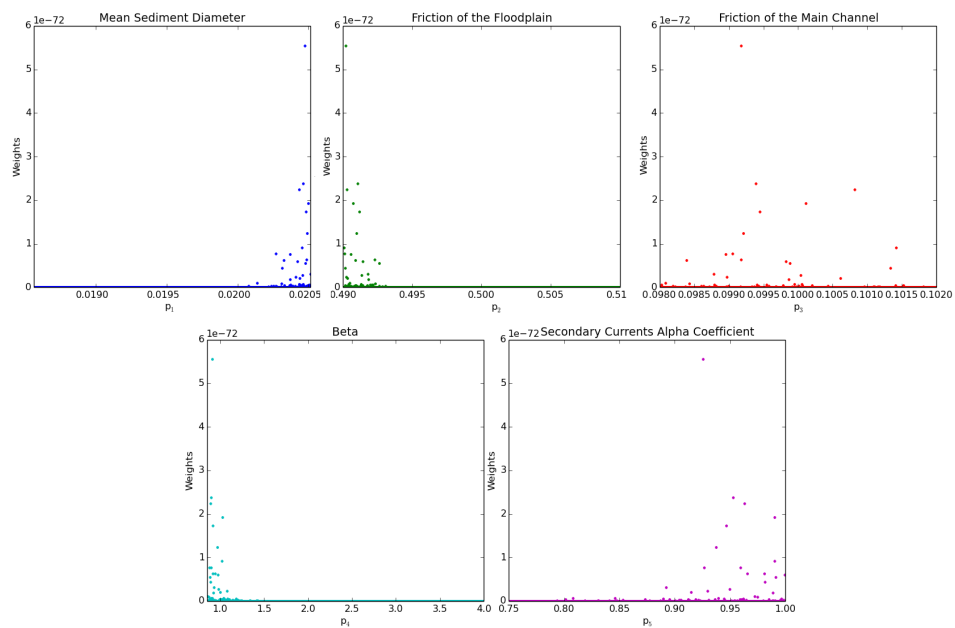


Figure B.38: Prior likelihood weights after iterations (calibration-Wu model)

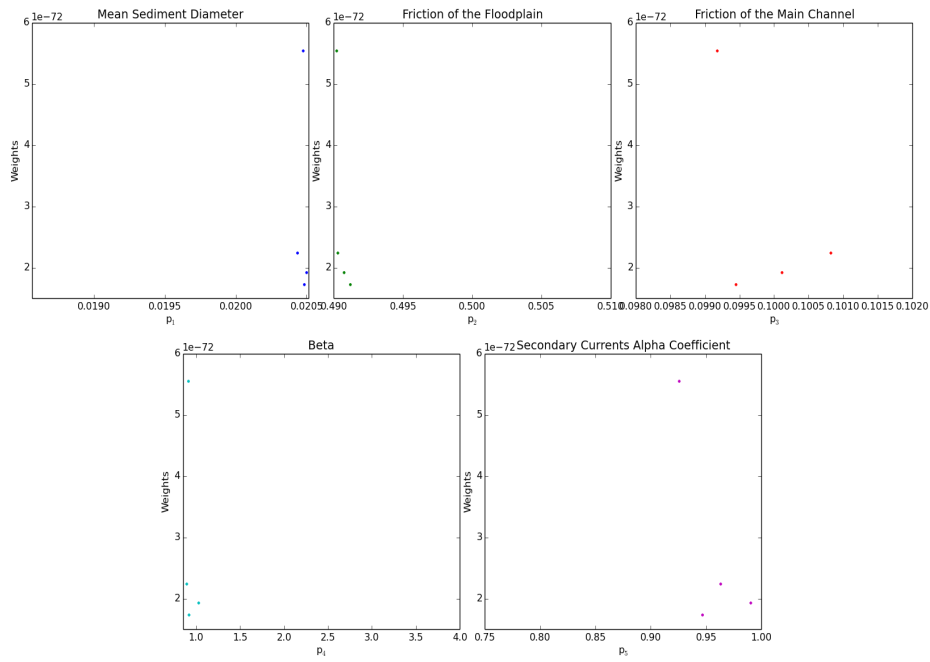


Figure B.39: Posterior likelihood weights after bootstrap-filtering (calibration-Wu model)

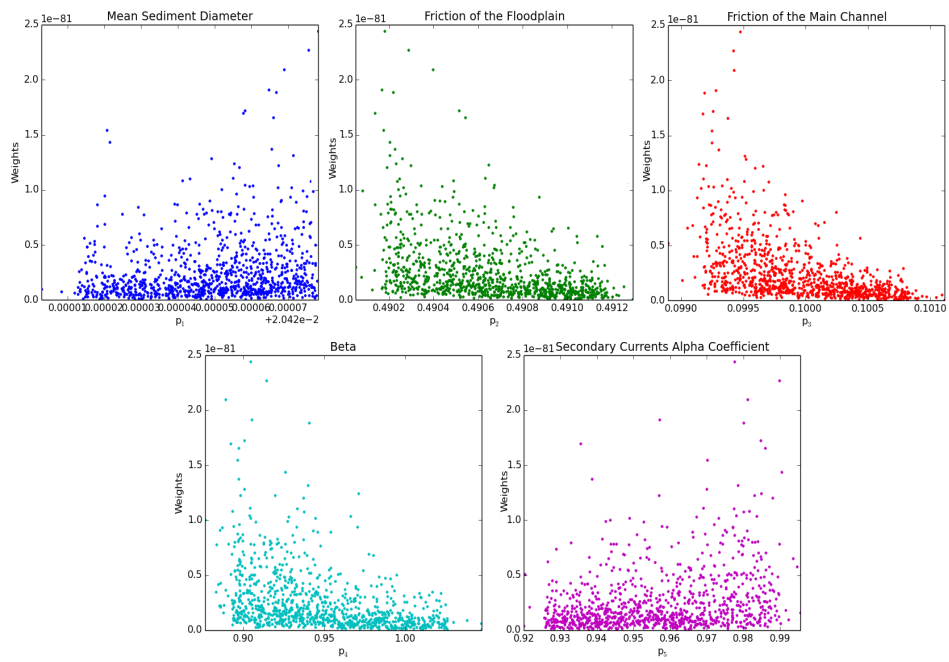


Figure B.40: Prior likelihood weights (validation-Wu model)

References

- Ackers, P. and Rodney White, W. Sediment Transport: New Approach and Analysis. *J. Hydraul. Div.*, 99(11):2041–2060, 1973.
- Almedeij, J. and Diplas, P. Bed load sediment transport in ephemeral and perennial gravel bed streams. *Eos, Trans. Am. Geophys. Union*, 86(44):429, 2005. 10.1029/2005EO440002.
- Apsley, D. Introduction to sediment transport. (September 1993):1–16, 2014. 10.1016/B978-0-7506-5978-9.50012-X.
- Backhaus, L. *Vergleich morphodynamischer Prognosen des Feststofftransportmodells "Neuss-Düsseldorf" in Abhängigkeit von 2D- und 3D-Strömungsansätzen mit dem Verfahren Telemac/Sisyphé*. PhD thesis, Karlsruher Institut für Technologie, 2013.
- Bagnold, R. A. An Approach to the Sediment Transport Problem from General Physics. *USGS Prof. Pap.*, page 42, 1966. ISSN 0016-7568. 10.1017/S0016756800049074.
- Batalla, R. J. Evaluating Bed-material Transport Equations using Field Measurements in a Sandy Gravel-bed Stream, Arbúcies River, NE Spain. *Earth Surf. Process. Landforms Landforms*, 22(2):121–130, 1997.
- Bathurst, J. C. Effect of Coarse Surface Layer on Bed-Load Transport. *J. Hydraul. Eng.*, 133(11):1192–1205, 2007. 10.1061/(ASCE)0733-9429(2007)133:11(1192).
- Bayes, M. and Price, M. An Essay towards Solving a Problem in the Doctrine of Chances. *Philos. Trans. R. Soc. London*, 53(4):370–418, jan 1763. 10.1098/rstl.1763.0053.
- Brown, C. *Sediment transportation*. John Wiley & Sons, New York, 1950.
- Carson, M. a. and Griffiths, G. a. Bedload transport in gravel channels. *J. Hydrol. New Zeal.*, 26(1):1–151, 1987.
- Celik, I. and Rodi, W. Suspended sediment-transport capacity for open channel flow. *J. Hydraul. Eng.*, 117(2):191–204, 1991.

- Chang, H. H. Selection of gravel-transport stream modeling formula. *J. Hydraul. Eng.*, 120(5): 646–651, 1994.
- Chollet, J. and Cunge, J. New interpretation of some head loss flow velocity relationship for deformable bed. *J. Hydraul. Eng.*, 17(1):1–13, 1980.
- Cole, C. V., Tarapore, Z. S., Kanhere, V. N., and Dixit, J. G. Sediment discharge formulae- a comparative analysis. *SedimentTransportation*, 1, 1973.
- Di Cristo, C., Iervolino, M., and Vacca, A. Linear stability analysis of a 1-D model with dynamical description of bed-load transport. *J. Hydraul. Res.*, 44(4):480–487, 2006. 10.1080/00221686.2006.9521699.
- Draper, D. Assessment and Propagation of Model Uncertainty, 1995.
- du Boys, M. P. Etudes du régime et l'action exercé par les eaux sur un lit à fond de graviers indéfiniment affouiable. *Ann. Ponts Chaussees*, 5(18):141–195, 1879.
- Einstein, H. A. The Bed-Load Function for Sediment Transportation in Open Channel Flows. *Soil Conserv. Serv.*, (1026):1–31, 1950.
- Engelund, F. Flow and bed topography in channel bends. *J. Hydraul. Div.*, 100(11):1631–1648, 1974.
- Engelund, F. and Hansen, E. A monograph on sediment transport in alluvial streams. *Tek. Forl.*, page 65, 1967. 10.1007/s13398-014-0173-7.2.
- Evans, M. and Swartz, T. Methods for Approximating Integrals in Statistics with Special Emphasis on Bayesian Integration Problems. *Stat. Sci.*, 10(3):254–272, aug 1995. 10.1214/ss/1177009938.
- Evensen, G. *Data Assimilation*. Springer Berlin Heidelberg, Berlin, Heidelberg, 2009. 10.1007/978-3-642-03711-5.
- Garde, R. J. and Ranga Raju, K. G. *Mechanics of sediment transportation and alluvial stream problems*. New Delhi : Wiley Eastern Ltd, reprinted edition, 1977.
- Gilbert, G. K. The transport of debris by running water. *U.S. Geol. Surv. Prof. Pap. 86*, pages 1–263, 1914.
- Gomez, B. and Church, M. An Assessment of Bedload Sediment transport Formulae for Gravel Bed Rivers. *Water Resour. Res.*, 25(6):1161–1186, 1989.

- Graf, W. H. *Hydraulics of Sediment Transport*. McGraw Hill, New York, 1971.
- Greco, M., Iervolino, M., Leopardi, A., and Vacca, A. A two-phase model for fast geomorphic shallow flows. *Int. J. Sediment Res.*, 27(4):409–425, 2012. 10.1016/S1001-6279(13)60001-3.
- Gunter, A. Die kritische mittlere Sohlenschubspannung bei Geschiebemischungen unter Berücksichtigung der Deckschichtbildung und der turbulenzbedingten Sohlenschubspannungsschwankungen. (4649):1–70, 1971.
- Habersack, H. M. and Laronne, J. B. Evaluation and improvement of bed load discharge formulas based on Helley-Smith sampling in an alpine gravel bed river. *J. Hydraul. Eng.*, 128(5):484–499, 2002. 10.1061/(ASCE)0733-9429(2002)128:5(484).
- Habibi, M. *Sediment transport estimation methods in river systems*. PhD thesis, 1994.
- Hadamard, J. Sur les problèmes aux dérivées partielles et leur signification physique. *Princet. Univ. Bull.*, pages 49–52, 1902.
- Hammersley, J. M. MONTE CARLO METHODS FOR SOLVING MULTIVARIABLE PROBLEMS. *Ann. N. Y. Acad. Sci.*, 86(3):844–874, dec 1960. 10.1111/j.1749-6632.1960.tb42846.x.
- Hervouet, J.-M. TELEMAC modelling system: an overview. *Hydrol. Process.*, 14(13):2209–2210, 2000.
- Hervouet, J.-M. *Hydrodynamics of free surface flows: modelling with the finite element method*. John Wiley & Sons, 2007.
- Hirano, M. River bed degradation with armoring. *Trans. Japanese Soc. Civ. Eng.*, 3(2), 1971.
- Hoeting, J. a., Madigan, D., Raftery, A. E., and Volinsky, C. T. Bayesian Model Averaging: A Tutorial. *Stat. Sci.*, 14(4):382–417, 1999. 10.2307/2676803.
- Hubbell, D. and Matejka, D. Investigations of Sediment Transportation Middle Loup River At Dunning , Nebraska. page 122, 1959.
- Hunziker, R. P. Fraktionsweiser Geschiebetransport. (11037):5–209, 1995.
- Jaeggi, M. Abflussberechnung in kiesführenden flüssen. *Wasserwirtschaft*, 24(5):263–267, 1984.
- Johnson, J. W. *Laboratory investigations on bedload transportation and bed roughness*. SCS-TP. U.S. Dept. of Agriculture, Soil Conservation Service, 1943.

- Jordan, B. P. R. Fluvial Sediment of the Mississippi River at St . Louis , Missouri. pages 1–98, 1965.
- Kass, R. E. and Raftery, A. E. Bayes Factors. *J. Am. Stat. Assoc.*, 90(430):773–795, jun 1995. 10.1080/01621459.1995.10476572.
- Lang, P. TELEMAC-2D Software Release 7.0 USER MANUAL. (October):1 – 6, 2010.
- Li, H. and Zhang, D. Probabilistic collocation method for flow in porous media: Comparisons with other stochastic methods. *Water Resour. Res.*, 43(9):1–13, 2007. 10.1029/2006WR005673.
- López, R., Vericat, D., and Batalla, R. J. Evaluation of bed load transport formulae in a large regulated gravel bed river: The lower Ebro (NE Iberian Peninsula). *J. Hydrol.*, 510:164–181, 2014. 10.1016/j.jhydrol.2013.12.014.
- Martin, Y. Evaluation of bed load transport formulae using field evidence from the Vedder River, British Columbia. *Geomorphology*, 53(1-2):75–95, 2003. 10.1016/S0169-555X(02)00348-3.
- Martin, Y. and Ham, D. Testing bedload transport formulae using morphologic transport estimates and field data: lower Fraser River, British Columbia. *Earth Surf. Process. Landforms*, 30(10):1265–1282, 2005.
- Messing, S. Geschiebezugabe unterer Niederrhein, 2008.
- Meyer-Peter, E. and Müller, R. Formulas for Bed-Load Transport. *Proc. 2nd Meet. Int. Assoc. Hydraul. Res.*, pages 39–64, 1948.
- Meyer-Peter, E., Favre, H., and Einstein, H. A. Neuere Versuchsergebnisse über den Geschiebetrieb. *Veranstaltungen des Bundesanstalt für Gewässerkd.*, 103(13):1–4, 1934.
- Misri, R. L., Garde, R. J., and Ranga Raju, K. G. Bed Load Transport of Coarse Nonuniform Sediment. *J. Hydraul. Eng.*, 110(3):312–328, 1984. ISSN 0733-9429. 10.1061/(ASCE)0733-9429(1984)110:3(312).
- Müller, R. Ueberprüfung des geschiebegesetzes und der berechnungsmethode der Versuchsanstalt für Wasserbau an der ETH mit hilfe der direkten geschiebemessungen am Rhein. *Schweiz. Bauztg.*, 110:180–184, 1937.
- Oladyshkin, S. and Nowak, W. Polynomial Response Surfaces for Probabilistic Risk Assessment and Risk Control via Robust Design. *InTech*, 2012a.

- Oladyshkin, S. and Nowak, W. Data-driven uncertainty quantification using the arbitrary polynomial chaos expansion. *Reliab. Eng. Syst. Saf.*, 106(2010):179–190, 2012b. 10.1016/j.ress.2012.05.002.
- Oladyshkin, S., Class, H., Helmig, R., and Nowak, W. An integrative approach to robust design and probabilistic risk assessment for CO₂ storage in geological formations. *Comput. Geosci.*, 15(3):565–577, 2011a. 10.1007/s10596-011-9224-8.
- Oladyshkin, S., Class, H., Helmig, R., and Nowak, W. A concept for data-driven uncertainty quantification and its application to carbon dioxide storage in geological formations. *Adv. Water Resour.*, 34(11):1508–1518, 2011b. 10.1016/j.advwatres.2011.08.005.
- Oladyshkin, S., Class, H., and Nowak, W. Bayesian updating via bootstrap filtering combined with data-driven polynomial chaos expansions: Methodology and application to history matching for carbon dioxide storage in geological formations. *Comput. Geosci.*, 17(4): 671–687, 2013. 10.1007/s10596-013-9350-6.
- Oliver, D., Reynolds, A. C., Bi, Z., and Abacioglu, Y. Integration of production data into reservoir models. *Pet. Geosci.*, 7:65–73, 2001.
- Oliver, D. S., Reynolds, A. C., and Liu, N. *Inverse theory for petroleum reservoir characterization and history matching*. Cambridge University Press, 2008.
- Papanicolaou, A. N. T., Krallis, G., and Edinger, J. Sediment Transport Modeling Review: Current and Future Development. 134(1):1–14, 2008.
- Parker, G. Some random notes on grain sorting. In *Grain Sorting Semin.*, pages 19–76, Ascona, Switzerland, 1992.
- Parker, G. and Klingeman, P. C. On why gravel bed streams are paved. *Water Resour. Res.*, 18(5):1409–1423, 1982. 10.1029/WR018i005p01409.
- Parker, G., Klingeman, P. C., and McLean, D. G. Bedload and size distribution in paved gravel-bed streams. *J. Hydraul. Eng.*, 109(5):793–794, 1983. 10.1061/(ASCE)0733-9429(1983)109:5(793).
- Raudkivi, A. J. *Loose Boundary Hydraulics*. Balkema, Rotterdam, The Netherlands, 4th edition, 1998.
- Red-Horse, J. R. and Benjamin, A. S. A probabilistic approach to uncertainty quantification with limited information. *Reliab. Eng. Syst. Saf.*, 85(1-3):183–190, 2004. 10.1016/j.ress.2004.03.011.

- Reid, I., Powell, D. M., and Laronne, J. B. Prediction of Bed-Load Transport by Desert Flash Floods. *J. Hydraul. Eng.*, 122(3):170–173, 1996.
- Robert, A. *River Processes:: An Introduction to Fluvial Dynamics*. Oxford University Press, London, 2003. ISBN 9780340763391.
- Rottner, J. A Formula for Bed Load Transportation. *Houille Blanche*, 4(3):301–307, 1959.
- Schoklitsch, A. Der geschiebetrieb und die geschiebefracht. *Wasserkraft Wasserwirtschaft*, 4: 1–7, 1934.
- Schöniger, A., Wöhling, T., Samaniego, L., and Nowak, W. Model selection on solid ground: Rigorous comparison of nine ways to evaluate Bayesian model evidence. *Water Resour. Res.*, 50(12):9484–9513, 2014. 10.1002/2014WR016062.
- Shields, A. Application of similarity principles and turbulence research to bed-load movement (in German). *Mitt. Preuss. Versuchsanst. Wasserbau Schiffbau*, 26:5–24, 1936.
- Shulits, S. and Hill, R. D. Bed Load Formulas. Technical report, Agricultural Research Services, USDA, Rep. No. ARSSCW-1, Agricultural Research Services, USDA, Washington, 1968.
- Simons, D. B. and Sentuerk, F. *Sediment transport technology*. Fort Collins, Colo. : Water Resources Publications, 1977.
- Sinnakaudan, S. K., Ghani, A. A., Ahmad, M. S., and Zakaria, N. A. Multiple Linear Regression Model for Total Bed Material Load Prediction. *J. Hydraul. Eng. ASCE*, 132(5):521–528, 2006.
- Smart, G. M. and Jaeggi, M. Sedimenttransport in steilen Gerinnen . Sediment transport on steep slopes. *Mitteilung Nr. 64 der Versuchsanstalt fuer Wasserbau, Hydrol. und Glaziologie, ETH, Zuerich*, 1983.
- Smith, A. and Gefland, A. Smith - Bayesian Statistics without tears: A Sampling-Resampling Perspective. *Am. Stat.*, 46(2):84–88, 1992.
- Sutherland, A. Hiding functions to predict self-Armoring. In *Int. Semin. Grain Sorting*, Zuerich, Switzerland, 1992. Mitteilungen Nr. 117 der Versuchsanstalt fuer Wasserbau, Hydrologie und Glaziologie.
- Suzuki, K. and Hano, A. Grain Size Change of Bed Surface Layer and Sediment Discharge in Rivers with Gravel and Sand Mixture. *Proc. Hydraul. Eng.*, 35:411–416, 1991. 10.2208/prohe.35.411.

- Talmon, A., Struiksma, N., and Van Mierlo, M. Laboratory measurements of the direction of sediment transport on transverse alluvial-bed slopes. *J. Hydraul. Res.*, 33(4):495–517, 1995. 10.1080/00221689509498657.
- Tassi, P. Sisyphé v6 . 3 User Manual. 33(1), 2014.
- Tatang, M. A., Pan, W., Prinn, R. G., and McRae, G. J. An efficient method for parametric uncertainty analysis of numerical geophysical models. *J. Geophys. Res. Atmos.*, 102(D18): 21925–21932, 1997. 10.1029/97JD01654.
- Toffaletti, F. B. Definitive Computation of Sand Discharge in Rivers. *J. Hydraul. Div.*, 95(1): 225–248, 1969.
- van Rijn, L. C. Sediment Transport, Part I: Bed Load Transport. *J. Hydraul. Eng.*, 110(10): 1431–1456, 1984. 10.1061/(ASCE)0733-9429(1984)110:10(1431).
- Van Rijn, L. C. Sediment transport: bed load transport. *J. Hydraul. Eng.*, 110(10):1431–1456, 1984.
- Vanoni, V. A. *Sedimentation Engineering*. American Society of Civil Engineers, Reston, VA, classic ed edition, mar 2006. 10.1061/9780784408230.
- Villadsen, J. and Michelsen, M. L. *Solution of differential equation models by polynomial approximation*. Prentice- Hall, Englewood Cliffs, 1978.
- Villaret, C., Hervouet, J. M., Kopmann, R., Merkel, U., and Davies, A. G. Morphodynamic modeling using the Telemac finite-element system. *Comput. Geosci.*, 53:105–113, 2013. 10.1016/j.cageo.2011.10.004.
- Webster, M. D., Tatang, M. A., and McRae, G. J. Application of the probabilistic collocation method for an uncertainty analysis of a simple ocean model. *MIT Jt. Progr. Sci. Policy Glob. Chang. Rep.*, 4, 1996.
- White, W., Milli, H., and Crabbe, A. D. Sediment transport: an appraisal of available methods. *UK Hydraul. Res. Station. Wallingford, UK*, Rep. 119, 1973.
- Wilcock, P. R. Experimental investigation of the effect of mixture properties on transport dynamics. *Dyn. Gravelbed Rivers*, John Wiley:109–139, 1992.
- Wilcock, P. R. The flow, the bed, and the transport: interaction in flume and field. *Gravel-Bed Rivers V. NZHS, Wellington, NZ*, pages 183–219, 2001.

- Wong, M. and Parker, G. Reanalysis and correction of bed-load relation of Meyer-Peter and Müller using their own database. *J. Hydraul. Eng.*, 132(11):1159–1168, 2006. 10.1061/(ASCE)0733-9429(2006)132:11(1159).
- Wu, W. *Computational River Dynamics*. Taylor & Francis, 2008. ISBN 978-0-415-44961-8.
- Wu, W., Wang, S. S., and Jia, Y. Nonuniform sediment transport in alluvial rivers. *J. Hydraul. Res.*, 38(6):427–434, 2000. 10.1080/00221680009498296.
- Wurms, S. and Schröder, M. Evaluation of strategies for the acceleration of morphodynamic simulations against the background of waterways maintenance. In *River Flow 2012 - Int. Conf. Fluv. Hydraul.*, pages 1235–1241, San Jose, Costa Rica, 2012. London: Taylor & Francis.
- Yalin, M. An Expression for Bed-Load Transportation. *J. Hydraul. Eng. ASCE*, 89(3):221–250, 1963.
- Yalin, M. S. *Mechanics of sediment transport*. Oxford : Pergamon Press, 2d ed edition, 1977. ISBN 0080211623.
- Yalin, M. S. and Scheuerlein, H. *Friction factors in alluvial rivers*. H. Blind, 1988.
- Yang, C. T. and Wan, S. Comparisons of selected bed-material load formulas. *J. Hydraul. Eng.*, 117(8):973–989, 1991.
- Yen, C.-I. and Lee, K. T. Bed Topography and Sediment Sorting in Channel Bend with Unsteady Flow. *J. Hydraul. Eng.*, 121(8):591–599, aug 1995. 10.1061/(ASCE)0733-9429(1995)121:8(591).